Design, Construction and Commissioning of a Cryogenic Undulator for Laser-Plasma Based Free Electron Lasing at Lux

by

Maximilian Trunk

A Thesis Submitted to the Faculty of

Mathematics, Informatics and Natural Sciences

Department of Physics

for the Degree of

DOCTOR RERUM NATURALIUM

Universität Hamburg

July 2022

Gutachter der Dissertation:	Dr. Andreas R. Maier
	Prof. Dr. Wolfgang Hillert
Zusammensetzung der Prüfungskommission:	Prof. Dr. Jochen Liske
	Dr. Markus Tischer
	Prof. Dr. Nina Rohringer
	Dr. Andreas R. Maier
	Prof. Dr. Wolfgang Hillert
Vorsitzende der Prüfungskommission:	Prof. Dr. Jochen Liske
Datum der Disputation:	11.11.2022
Vorsitzender des Fach-Promotionsausschusses Physik:	Prof. Dr. Wolfgang J. Parak
Leiter des Fachbereichs Physik:	Prof. Dr. Günter H. W. Sigl
Dekan der Fakultät MIN:	Prof. Dr. Heinrich Graener

Eidesstattliche Versicherung / Declaration on oath

Hiermit versichere ich an Eides statt, die vorliegende Dissertationsschrift selbst verfasst und keine anderen als die angegebenen Hilfsmittel und Quellen benutzt zu haben.

Die eingereichte schriftliche Fassung entspricht der auf dem elektronischen Speichermedium.

Die Dissertation wurde in der vorgelegten oder einer ähnlichen Form nicht schon einmal in einem früheren Promotionsverfahren angenommen oder als ungenügend beurteilt.

Hamburg, December 9, 2022 _____

Maximilian Trunk

Abstract

In this thesis, the design and commissioning of the cryogenic in-vacuum undulator Frosty is presented, which will be used to demonstrate a possible free electron lasing with a laser plasma accelerated beam at the Lux facility. The design of Lux follows a decompression scheme to reduce the effective energy spread in the FEL, which requires a tunable and taperable gap up to 5 %/m. The machine provides 130 Periods with 15 mm period length and could reach a K parameter of 2.84 at a gap of 2 mm when cooled below 77 K of temperature. Due to the cooling, thermal gradients and mechanical stresses occur which are compensated by an adequate layout of the tolerance chain and the design of the machine. Especially thermally induced deformations of the gap will cause a high phase advance which is discussed in detail. A measurement bench with an active laser-based closed loop regulation is built to characterize and tune the undulator field. To commission the undulator, fundamental measurements of the spontaneous undulator radiation are presented.

Zusammenfassung

Diese Arbeit behandelt Design, Vermessung und Inbetriebnahme des Tieftemperaturundulators Frosty. Mithilfe dieser Maschine soll ein Freier Elektronen Laser mit Laser-Plasma beschleunigten Elektronen aus dem Lux Beschleuniger nachgwiesen werden. Das Konzept von Lux beinhalted eine Dekompressionssektion um der die effektive Energieverteilung und deren Einfluss auf das Lasing reduziert werden soll. Dafür muss das Spaltmaß des Undulators verstellbar und um 5 %/m verkippbar sein. Der Undulator besteht aus 130 Perioden mit einer jeweiligen Länge von 15 mm und kann einen K Wert von 2.84 bei einem nominellen Spaltmaß von 2 mm erreichen, wenn die Maschine auf unter 77 K gekühlt wird. Das Tieftemperaturverhalten der Maschine erzeugt Temperaturgradienten wodurch mechanische Verspannungen hervorgerufen werden, welche durch eine geschickte Gestaltgebung der Toleranzkette abgefangen werden können. Der thermische Verzug des nominellen Spaltmaßes erzeugt einen Phasenvorschub des abgestrahlten Lichts und wird detailliert behandelt. Zur Vermessung und Optimierung des Magnetfelds wurde eine selbstregulierende, laserbasierte Messbank gebaut. Zum Abschluss der Inbetriebnahme wurden erste grundlegende Eigenschaften der spontanen Undulatorstrahlung vermessen.

Contents

List of Figures

List of Tables

1 Introduction

Free electron Lasers (FELs) are machines which produce coherent light pulses with highest brilliance. In contrast to conventional lasers, the emitted wavelength range of FELs is tunable from the millimeter range down to the hard x-ray regime, which makes FELs versatile light sources for a broad variety of applications [2, 17, 18, 1, 19]. FELs are built out of several sections. At the beginning of the machine an electron bunch is generated and accelerated towards highly relativistic energies. After the acceleration a transport beam line guides the electron bunch into an undulator section. Undulators are magnetic devices which force traversing relativistic electrons onto an oscillatory motion around their main path of propagation due to which a high brilliant x-ray pulse is emitted. Depending on the number of oscillations, the observed radiation bandwidth can reach into a sub-% range. Due to the periodic oscillation of the electrons inside the undulator a resonant condition can build up in which the emitted radiation interacts back onto the emitting electron beam. By exploiting this condition the radiated power is amplified about several orders of magnitudes compared to the case without interaction and a laser-like x-ray pulse with coherent properties is emitted. The central wavelength and divergence of the light pulse depend on the kinetic energy of the electrons and the central wavelength is tunable over a broad range. This makes those machines a versatile and indispensable tool for modern x-ray spectroscopy in many fields of natural sciences like microbiology, medicine, chemistry, or physics, as FELs grant access to investigate matter down to its atomic structures and resolute ultra fast processes due to the short pulse duration [2, 17, 18, 1, 19]. The state of the art flagship of free electron lasers (To the date of this thesis) is the European XFEL located in Hamburg, Germany [20]. Its operational wavelength range reaches down to 0.05 nm with a bandwidth of 0.1% and pulse durations below 100 femtoseconds with 27000 shots per second. With this FEL it should be possible to measure and film the formation of molecules out of single atoms with a resolution on the order of the atomic length scale, which is, for example, required to research and optimize chemical catalysts used in industry [20].
Modern state of the art FEL institutes like the European Xfel, Flash and LCLS are driven by conventional linear accelerators and operate facilities with several hundreds to thousands of meters in length [21, 20, 22]. The complexity of these machines and the accompanying costs to build and maintain them restrict the number of available FEL facilities in the x-ray regime to a few world wide, whereas the user demand of coherent x-ray radiation is increasing [23]. So, alternative concepts are required.

A promising candidate to reduce the overall length of FEL facilities are laser plasma accelerators. With the invention of the chirped pulse amplification lasers with peak powers in the terrawatt regime are accessible [24, 25]. When such a laser is guided into a gas channel a plasma is ignited along its path and in the wake of the laser electrons are accelerated with the electrical field of the atomic cores, orders of magnitudes higher than the acceleration field in conventional accelerators [26–28].
Due to the reduced acceleration length the overall size and cost of a laser plasma driven FEL facility has the potential to shrink drastically. In contrast to the small and localized number of conventional FELs, the compactness of laser plasma accelerators would allow to build a comprehensive network out of compact x-ray sources which would de-centralize scientific research. It could be possible to bring the FEL to the user experiments and not vice verca which would enrich the scientific landscape significantly. While laser plasma accelerators are still a young field of research and the electron beam qualities in terms of energy stability and repeatability are not yet comparable with those of conventional accelerators, it was already demonstrated that the parameter space and stability required to drive an FEL are accessible [27–34, 3]. Also, the start up of a free electron lasing using a laser plasma accelerated bunch was demonstrated [35].

One of the facilities at which this novel technology is under research is the Lux accelerator located at the DESY campus in Hamburg, Germany [36, 37]. The main focus of the facility is to built a reliable and compact laser plasma based electron source with a high repeatability of stable electron beam parameters to demonstrate the start up of the free electron lasing [37, 38, 4, 39].
The idea of laser plasma based FELs is to construct overall smaller machines. So, also the required undulator follows a novel compact concept which allows to increase the FEL acceptance of deviations in the electron parameters [40, 4, 41]. The undulator built for Lux is a short period cryogenic in-vacuum machine with a tunable and taperable gap, codenamed Frosty. The desing of the undulator is adjusted such that it fits to the requirements of laser plasma accelerated electron beams at Lux. Frosty was developed in a close collaboration between the Helmholtz Zentrum Berlin (HZB), namely Johannes Bahrdt and Bodo Schulz, and the Lux team. For this machine, a novel magnetic alloy was developed with which it is possible to increase the magnetic field of the undulator when it is cryo cooled [42, 6].

Thesis Overview

This thesis focuses on the design, assembling and commissioning of the Frosty undulator in detail. To do so, the important basics of undulator radiation are presented in Sec. 2 and the concept to demonstrate a possible free electron lasing with the laser plasma accelerator Lux is reviewed in Sec. 3. For the design and construction of the undulator a deep understanding of the mechanics is of major importance. Besides the mechanical stresses due to the acting forces onto the support structure, also the cryo cooling concept does have an impact onto the mechanics and the magnetic field of the machine, as it introduces thermal gradients along the device, see Sec. 4. A Helmholtz coil is built around the undulator chamber. A detailed analysis how the coil field is amplified in the undulator's pole material is shown in Sec. 5. To tune the undulator field a measurement bench is built and characterized in detail, see Sec. 6 with which the magnetic field of the machine is optimized, see Sec. 7. To complete the commissioning of the undulator it is installed in the Lux accelerator and the spectral near field properties of the emitted radiation are analyzed with an x-ray spectrometer, see Sec. 8 and Sec. 9.

2 Concept of Free Electron Lasers

Free electron lasing (FEL) is a self amplifying resonant condition which builds up due to an interaction between an electron bunch and its emitted light field, while the bunch is traveling through a periodic magnetic field generated by machines called undulators. Due to this resonance, a high brilliance peak builds up at the resonant wavelength and a coherent photon pulse with a narrow bandwidth is emitted.
When relativistic electrons enter the undulator field, they perform energy dependent periodic oscillations around their main path of propagation. As they receive a continuous deflection along the undulator the electrons also continuously emit radiation into the orbit, which is called spontaneous synchrotron radiation. Along the mean path of propagation the emitted light front from one undulator period travels faster than the electron bunch, because of the electron's oscillatory detour and mass and a characteristic periodic slippage between the light front and the electron bunch will occur. As the radiation emitted in each undulator period will interfere with the light of the subsequent period only wavelengths which are very close or equal to the length of this slippage will interfere constructively and the resulting bandwidth decreases the more transverse oscillations are performed by the electron bunch. The outcome is a high intensity radiation pulse with a tunable wavelength and an intrinsically small bandwidth.
The electrical field component of the emitted light field can interact back onto the electron bunch and transfer energy. Depending on the relative phase between the particles and the electrical field, the electrons are either accelerated or decelerated, due to which an energy modulation is imprinted into the bunch on the period length of the electrical field. This interaction scales with large beam currents in the kA range which increase the intensity of the electrical field. Also, when the electron beam sizes are matched to the size of the light cone, the energy exchange between the light field and the electrons is increased as the photon field covers the full cross section of the bunch, which leads to a stronger energy modulation.
The electrons are traveling on energy dependent trajectories, so this energy modulation will result in a particle sorting which slowly builds up while the bunch is traveling through the undulator. Electrons with a higher momentum are more rigid against the transverse deflection of the magnetic field whereas decelerated electrons perform oscillations with an increased amplitude. So, relative to their initial position inside the bunch, accelerated electrons will move forward and decelerated ones fall behind due to the path length difference and the imprinted periodic energy modulation will result in

a density modulation which is also periodic with the emitted wavelength.
These high density peaks build up by time and are called micro bunches, a substructure inside the electron bunch, which are periodically separated by the wavelength. These micro bunches have now a fixed phase relation to the light and emit coherent radiation which, again, is re-acting onto the bunch and causes an even stronger energy modulation and so on. This self-amplifying process is then called free electron lasing and produces a coherent peak at the central wavelength which is orders of magnitudes above the reachable synchrotron radiation brightness.
The resonance can only build up when several requirements are fulfilled. For example, if the initial electron energy deviation is too high it would wash out the energy modulation imprinted by the light which would suppress the lasing. Also, when the undulator field is too distorted the resonant wavelength would change from undulator period to period which would drive a majority of the emitted light into destructive interference which would also suppress the energy modulation. So, to achieve a lasing the electron beam parameters and the quality of the undulator parameters have to match.
In this chapter, the electron dynamics inside an undulator field and the resulting radiation characteristics are explained.

As the core of this thesis is the design and commissioning of the undulator the description of the electron dynamics is linked to characteristic quantities of the magnetic field which are measurable and tunable in the laboratory and form the basis for all radiation properties, see Sec. 2.1 and Sec. 2.2. These measurable quantities are then applied to the undulator structure in Sec. 2.3 and the resulting radiation characteristics are discussed in the following sections. Intensive simulations were done to find a parameter space in which a lasing can be demonstrated [4]. From those simulations, also the main undulator parameters were derived, which will be shortly discussed in Sec. 2.4.

2.1 Beam Dynamics of Relativistic Electrons

The electron trajectory inside a magnetic field, excluding radiative emission and absorbtion processes, can be derived and expressed in terms of integrals. These integrals are of major role for tuning the undulator in the laboratory, as they do not depend on electron beam properties, but on the deflecting device itself. By measuring and tuning those integrals the trajectory of the electrons can be predicted and shaped. When a relativistic electron with a total energy above its rest energy $\gamma = \mathrm{E}/\mathrm{E}_0 \gg 1$ enters a magnetic field $\vec{\mathrm{B}}$ with a velocity $\vec{\beta}\mathrm{c}$ it is forced onto a curved trajectory perpendicular to the magnetic field. This motion is described by the Lorentz force [1, 17]

$$\mathrm{m}_e \gamma \ddot{\vec{\mathrm{x}}}(\mathrm{t}) = -e\vec{\beta}\mathrm{c} \times \vec{\mathrm{B}}$$

where m_e is the rest mass of the electron e its charge and c the speed of light. Restricting to a static vertical field $B_y(z)$ and assuming that $\vec{\beta} \approx 1$, the equations can be expressed in terms of the longitudinal position along the device instead of the time dependency by exchanging $d/dt \approx c \cdot d/dz$ [1, 17]:

$$x'' = \frac{e}{\gamma m_e c} \cdot B_y(z),$$

from which the equations of motion can be derived:

$$x' = \frac{e}{\gamma m_e c} \cdot J_1 + x'_0 \tag{2.1}$$

$$x = \frac{e}{\gamma m_e c} \cdot J_2 + x'_0 \cdot z + x_0 \tag{2.2}$$

with the field integrals

$$J_1(z) = \int_0^z B_y(z')dz' \qquad\qquad J_2(z) = \int_0^z J_1(z')dz'. \tag{2.3}$$

Magnetic fields conserve the momentum of a particle, so a transverse acceleration causes a longitudinal deceleration. As the total velocity stays constant ($\beta_0 = \sqrt{1 - \frac{1}{\gamma^2}}$ = const.) the change of the longitudinal velocity β_z is expressed in terms of the transverse velocity:

$$\beta_z = \sqrt{\beta_0^2 - x'^2} = \sqrt{1 - \frac{1}{\gamma^2} - x'^2} \approx 1 - \frac{1}{2\gamma^2} - \frac{x'^2}{2}.$$

Integrating β_z along the path z yields the total traveling distance of the electron. Subtracting the integration path z gives the detour length of the electron:

$$s(z) = z - \int_0^z \beta_z dz = \frac{z}{2\gamma^2} + \frac{1}{2}\int_0^z x'^2 dz$$

$$s(z) = \frac{z}{2\gamma^2} + \frac{1}{2}\left(\frac{e}{\gamma m_e c}\right)^2 J_{ph} \tag{2.4}$$

With the phase integral

$$J_{ph} = \int_0^z J_1^2 dz. \tag{2.5}$$

So, the change in longitudinal position of the electron depends on the detour the electron takes due to the magnetic field which is expressed by the phase integral J_{ph}. All three field integrals J_1, J_2 and J_{ph} are quantities which only depend on the shape of the magnetic field (B(z) and z) and not on properties of the electron bunch itself like initial offsets or collective effects like energy fluctuations. By measuring the magnetic field and calculating these integrals the electron trajectory can directly be obtained

with the equations above. That means that these field integrals are of major importance for tuning the performance of the undulator, as they give a direct measure of the behavior of an electron inside the machine. As all photon beam properties depend on the electron motion, those integrals are the fundamental tuning set to also calculate the emitted field in terms of central wavelength, photon phase space, bandwidth, photon flux and so on for a given electron energy.

2.2 Radiation from Relativistic Electrons

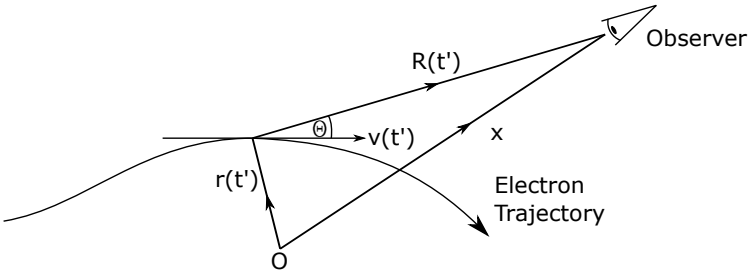

Figure 2.1 – Geometry to calculate the observed electrical field for an arbitrary electron trajectory. The sketch is inspired by [1].

Due to the deflection inside a magnetic field, relativistic electrons start to emit an electromagnetic field which could be received by an observer. In Fig.2.1 this geometry is sketched. The electron travels with a velocity $\vec{v}(t')$ through the magnetic field and emits a photon at the emission, or retarded time t'. This photon arrives at the observation time t at the observer, while it traveled along the straight path $\vec{R}(t') = \vec{x} - \vec{r}(t')$. So, observed and emitted time relate to $t = t' + |\vec{R}(t')|/c$. If a particle radiates for a certain time interval dt' the ratio between the observed and retarded time is [1, 17]

$$\frac{dt}{dt'} = 1 - \vec{n}(t')\vec{\beta}(t') = 1 - \beta\cos(\theta).$$

Here, $\vec{n}(t) = \vec{R}(t)/R(t)$ is the normalized unity vector pointing from the source to the observer along $\vec{R}(t)$. That means that the emission time is squeezed into a much shorter time frame at the observer. The maximum time squeezing is given when $dt/dt' \to 0$, so for highly relativistic particles with $\gamma >> 1$ and small observation angles of $\theta << 1 << \gamma^{-1}$. In this approximation the time ratio gets [1, 17]

$$\frac{dt}{dt'} \approx \frac{1}{2\gamma^2}\left(1 + \gamma^2\theta^2\right). \tag{2.6}$$

When a highly relativistic electron emits wavelengths on a scale of $dx' \approx c \cdot dt'$ the observed length dx of the radiation is contracted about $dx = \frac{1}{2}(1/\gamma^2 + \theta^2)dx'$ and the

field is maximal within a radiation cone of $\theta << \gamma^{-1}$. So, the time squeezing in Eq. 2.6 is the main mechanism to produce intense x-ray beams with small opening angles from relativistic electrons which propagate through cm long magnetic structures, like undulator periods. The emitted electromagnetic field at time t' which is received at the observer at time t can be evaluated by Liénard–Wiechert fields at the emitted time. If the retarded velocity and retarded position of the electron are known the field at the observation time can be calculated from this [1]:

$$\begin{aligned} \vec{\mathrm{E}}(\mathrm{t}) &= \frac{e}{4\pi \mathrm{c}\varepsilon_0}\left(\vec{\mathrm{E}}_\mathrm{c}(\mathrm{t}) + \vec{\mathrm{E}}_\mathrm{r}(\mathrm{t})\right)_{\mathrm{t}'} \\ \vec{\mathrm{B}}(\mathrm{t}) &= \frac{\vec{\mathrm{n}} \times \vec{\mathrm{E}}(\mathrm{t})}{\mathrm{c}} \end{aligned} \tag{2.7}$$

with:

$$\begin{aligned} \vec{\mathrm{E}}_\mathrm{c}(\mathrm{t}) &= \left(\frac{\mathrm{c}(1-\beta^2)(\vec{\mathrm{n}} - \vec{\beta})}{\mathrm{R}^2(1 - \vec{\mathrm{n}} \cdot \vec{\beta})^3}\right)_{\mathrm{t}'} \\ \vec{\mathrm{E}}_\mathrm{r}(\mathrm{t}) &= \left(\frac{\vec{\mathrm{n}} \times \left(\left(\vec{\mathrm{n}} - \vec{\beta}\right) \times \dot{\vec{\beta}}\right)}{\mathrm{R}\left(1 - \vec{\mathrm{n}} \cdot \vec{\beta}\right)^3}\right)_{\mathrm{t}'} \end{aligned}$$

where ε_0 is the vacuum permittivity. The electrical field consists out of two components: $\vec{\mathrm{E}}_\mathrm{c}(\mathrm{t})$ is the Coulomb field of the moving particle and becomes $\vec{\mathrm{E}} = e\vec{\mathrm{n}}/(4\pi\varepsilon_0\mathrm{R}^2)$ when the electron is stationary ($\vec{\beta} = \dot{\vec{\beta}} = 0$). Due to the $1/\mathrm{R}^2$ dependency the amplitude rapidly decays with increasing distance to the observer and stays in the vicinity of the electron. So it can be neglected in far distance observations.
$\vec{\mathrm{E}}_\mathrm{r}(\mathrm{t})$ describes the radiated field due to an acceleration, deflection or deceleration and is the main contribution of synchrotron radiation due to its $1/\mathrm{R}$ dependency.
The observed frequency spectrum $\Delta\omega/\omega_0$ of the observed pulse length $\Delta\mathrm{t}$ can be expressed by Heisenberg's uncertainty principle [43]

$$\Delta\omega \propto \frac{1}{\Delta\mathrm{t}}. \tag{2.8}$$

So, the longer the observed wave train the smaller is the bandwidth of the pulse.

2.3 Spontaneous Undulator Radiation

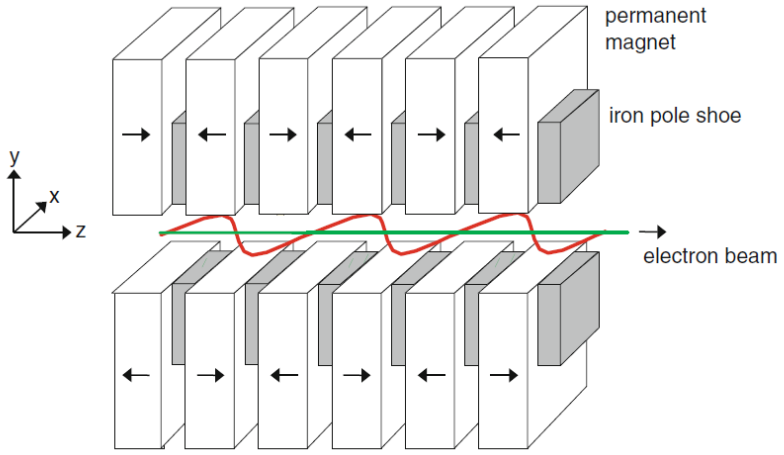

Figure 2.2 – Schematic sketch of the undulator lattice following the Halbach configuration. In this design the magnetic field direction of neighboring magnets is alternating but parallel to the undulator length as indicated by the black arrows. Small metal plates between the magnets act as poles and guide the field vertically towards the gap. Along the green line, the center of the gap, an alternating vertical magnetic field is created with this setup. The resulting sine like electron trajectory is colored in red inside the undulator gap. Picture from [2].

In Fig. 2.2 a schematic sketch of an undulator structure is shown. The device consists out of two magnetic arrays, which are parallel and with a gap in between. This magnetic assembly is arranged such that it creates a sinusoidal vertical magnetic field along its longitudinal axis.
The magnetization axis of the magnets is alternating along each array and the polarity of the magnets in the opposing array is shifted such, that two facing magnets have an anti-parallel magnetization, which is indicated by the arrows in the figure above. Between neighboring magnets iron plates are mounted which act as a guidance for the magnetic field towards the gap. On axis, so along the green line in the picture, a vertical sinusoidal magnetic field with a period length λ_u with N_u periods and a total length of $L_u = N_u \cdot \lambda_u$ is created. The observable magnetic field near the gap center (close to the green line in Fig. 2.2), is described by hyperbolic functions [2, 17, 1], which can be expanded up to the second order to:

$$\vec{B}(x,y,z) = -B_0 \begin{pmatrix} -k_x^2 \cdot x \cdot y \sin(k_u \cdot z) \\ \left(1 - \frac{(k_x \cdot x)^2}{2} + \frac{(k_y \cdot y)^2}{2}\right) \sin(k_u \cdot z) \\ k_u \cdot y \cdot \cos(k_u \cdot z) \end{pmatrix} \tag{2.9}$$

with the wave number $k_u = 2\pi/\lambda_u$ and the wave number relation $k_u^2 = k_y^2 + k_x^2$. Directly on the magnetic axis x = y = 0 this field reduces to a pure sinusoidal function:

$$\vec{B}(z) = -B_0 \cdot \sin(k_u \cdot z) \cdot \vec{e}_y. \tag{2.10}$$

2.3.1 Electron Trajectory

For the sinusoidal field the particle trajectory is derived by solving the field integrals in Eq. 2.3:

$$\begin{aligned} x'(z) &= +\frac{K}{\gamma}\cos(k_u \cdot z) + x'_0, \\ x(z) &= +\frac{K}{\gamma k_u}\sin(k_u \cdot z) + x'_0 \cdot z + x_0, \end{aligned} \tag{2.11}$$

with the dimensionless K-parameter

$$K = \frac{eB_0}{m_e c k_u} \approx 0.94 \cdot B\ [\mathrm{T}] \cdot \lambda_u\ [\mathrm{cm}]. \tag{2.12}$$

The longitudinal motion from Eq. 2.4 is:

$$s(z) = z\left(1 - \frac{1}{2\gamma^2}\left(1 + \frac{K^2}{2}\right)\right) - \frac{K^2}{8\gamma^2 k_u} \cdot \sin\left(2 \cdot k_u \cdot z\right) \tag{2.13}$$

2.3.2 Radiation Properties

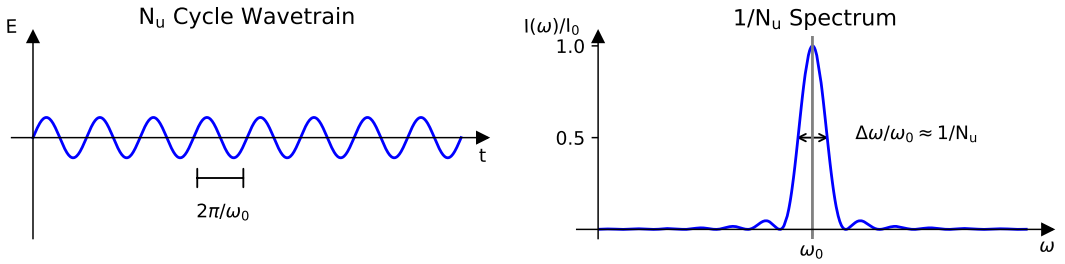

Figure 2.3 – Emitted wavetrain with $N_u \cdot \lambda$ oscillations on the left. The spectral intensity on the right is the square of the Fourier transform and follows a Sinc^2 like function. The bandwidth decreases with the number of oscillations like $1/N_u$.

The detour due to the transverse oscillation causes the particle to fall back with respect to a straight line about

$$\lambda = \frac{\lambda_u}{2\gamma^2}\left(1 + \frac{K^2}{2}\right) \tag{2.14}$$

per undulator period, see Eq. 2.13. While the electron continuously emits radiation into the orbit, only wavelengths which are equal to λ can interfere constructively into the forward direction. So, Eq. 2.14 gives the fundamental wavelength of the emitted undulator radiation. When the observation is not on axis the angular dependency of the observed wavelength from Eq. 2.6 has to be taken into account which increases the off axis wavelength to [1, 17]

$$\lambda = \frac{\lambda_\mathrm{u}}{2\gamma^2}\left(1 + \frac{\mathrm{K}^2}{2} + \gamma^2\theta^2\right).$$

For the fundamental wave train the observed bandwidth from Eq. 2.8 scales reverse with the number of undulator periods [17, 1], see Fig. 2.4

$$\frac{\Delta\lambda}{\lambda} \approx \frac{1}{\mathrm{N_u}}. \tag{2.15}$$

and due to the interference of the single waves, the majority of the photons are observed within a narrow light cone with an rms opening angle (half of the full opening angle) of [1]

$$\sigma_{\mathrm{r}'} = \sqrt{\frac{\lambda}{\mathrm{L_u}}} = \frac{1}{\gamma}\sqrt{\frac{1 + \mathrm{K}^2/2}{2\mathrm{N_u}}} \tag{2.16}$$

and a source size of [1]

$$\sigma_\mathrm{r} = \frac{1}{4\pi}\sqrt{\lambda \mathrm{L_u}} = \frac{\lambda_\mathrm{u}}{4\pi\gamma}\sqrt{\frac{\mathrm{N_u}}{2}\left(1 + \frac{\mathrm{K}^2}{2}\right)}. \tag{2.17}$$

The source size and the initial opening angle are summarized in their product called the photon beam emittance, so the phase space area for a single photon is then the product $\sigma_\mathrm{r}\sigma_{\mathrm{r}'} = \lambda/4\pi$ [1].

2.3.3 Flux

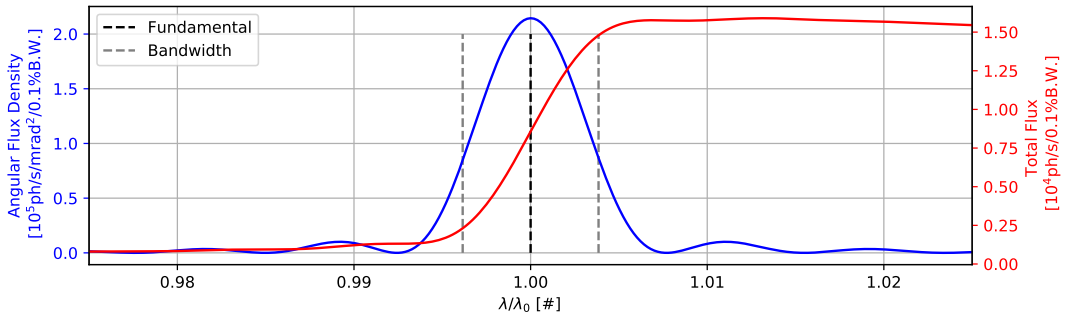

Figure 2.4 – Simulation of the angular flux density and the integrated flux for an undulator with N_u=130 periods, K=0.45, lu=15 mm and a 300 MeV electron beam with 5 pC charge. The central wavelength and the bandwidth $1/N_u$ are marked as dashed lines.

The emitted spectrum of the radiation is retrieved by calculating the Fourier transformation of the electric field $E(\omega) = \int E(t)e^{i\omega t}dt$, which gives the spectral angular flux distribution often called flux density which denotes the number of photons N emitted into a solid angle $d\Omega d\theta$ within a small bandwidth $\Delta\omega/\omega$. As the EM field depends on the sinusoidal magnetic undulator field with N_u periods the angular distribution has a sinc-shape function which scales with $1/N_u$ due to the Fourier transformation, see Fig. 2.4. Integrating the flux density over all emission angles of the undulator radiation gives the total flux, also called integrated flux, so the total number of photons emitted by the undulator, which can be expressed in practical units of photons per second per 0.1% bandwidth. The peak of the total flux in the central cone for the first harmonic is [1]

$$\dot{N} = 1.43 \cdot 10^{14} N_u I_b Q(K) \left[\frac{\text{photons}}{s \cdot 0.1\%\text{B.W.}}\right] \tag{2.18}$$

with the on-axis flux function

$$\begin{aligned} Q(K) &= \left(1 + K^2/2\right) F(K) \\ F(K) &= \frac{K^2}{(1 + K^2/2)^2} \left(J_1\left(Y(K)\right) - J_0\left(Y(K)\right)\right)^2 \\ Y(K) &= \frac{K^2}{4(1 + K^2/2)} \end{aligned} \tag{2.19}$$

which depends on the Bessel-functions $J_{(n\pm1)/2}$ of the K parameter and the harmonic n of the radiation [1]. An example of the integrated flux for the fundamental wavelength is shown in Fig. 2.4.

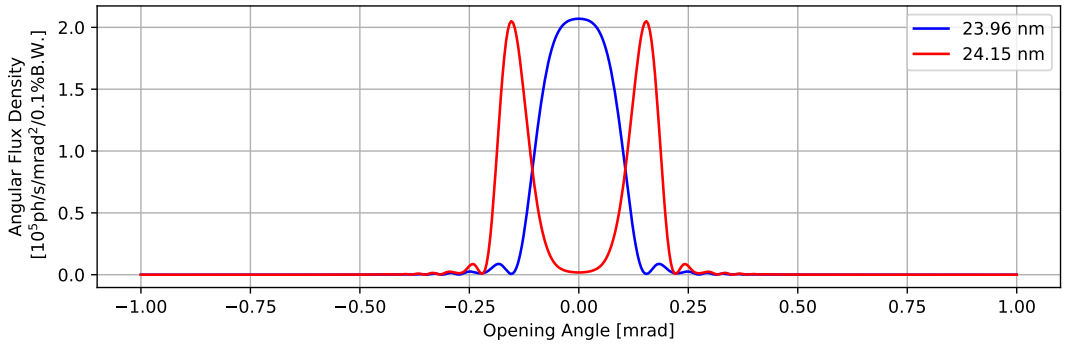

Figure 2.5 – Angular Flux distribution for the exact harmonic wavelength of 23.96 nm. The peak flux is red shifted about $1/(1-1/\cdot \mathrm{N_u})$ to a wavelength of 24.15 nm. Here the flux is doubled compared to the exact harmonic due to the higher angle contributions. Parameters from Fig. 2.4 are used.

The maximum flux is not directly at the fundamental but shifted about $1/(1-1/\cdot \mathrm{N_u})$ and a factor 2 higher than the flux on the fundamental due to higher angle contributions: Looking into the emitted spectrum of one half oscillation the fundamental will only appear once when the electron points towards the observer at the peak of the undulator period. The observed photons before and after the peak are slightly red shifted about the same amount, which leads to the doubled flux for at the slightly red shifted wavelength [1, 17]. A simulation of the angular flux distribution for the exact harmonic and the red-shifted peak flux are shown in Fig. 2.5.
The opening angle on the exact harmonic is reduced in comparison to the opening angle of the radiation cone of Eq. 2.16 by a factor of $\sqrt{2}$ [1, 17]. So, the source size and divergence at the exact harmonic are

$$\sigma_{r'} = \sqrt{\frac{\lambda}{2\mathrm{L_u}}} = \frac{1}{\gamma}\sqrt{\frac{1+\mathrm{K}^2/2}{4\mathrm{N_u}}}$$
$$\sigma_{r} = \frac{\lambda_u}{4\pi\gamma}\sqrt{\mathrm{N_u}\left(1+\frac{\mathrm{K}^2}{2}\right)}. \tag{2.20}$$

The integrated flux is of special interest at Lux, as it is directly measurable with the installed spectrometer.

2.4 Free Electron Lasing

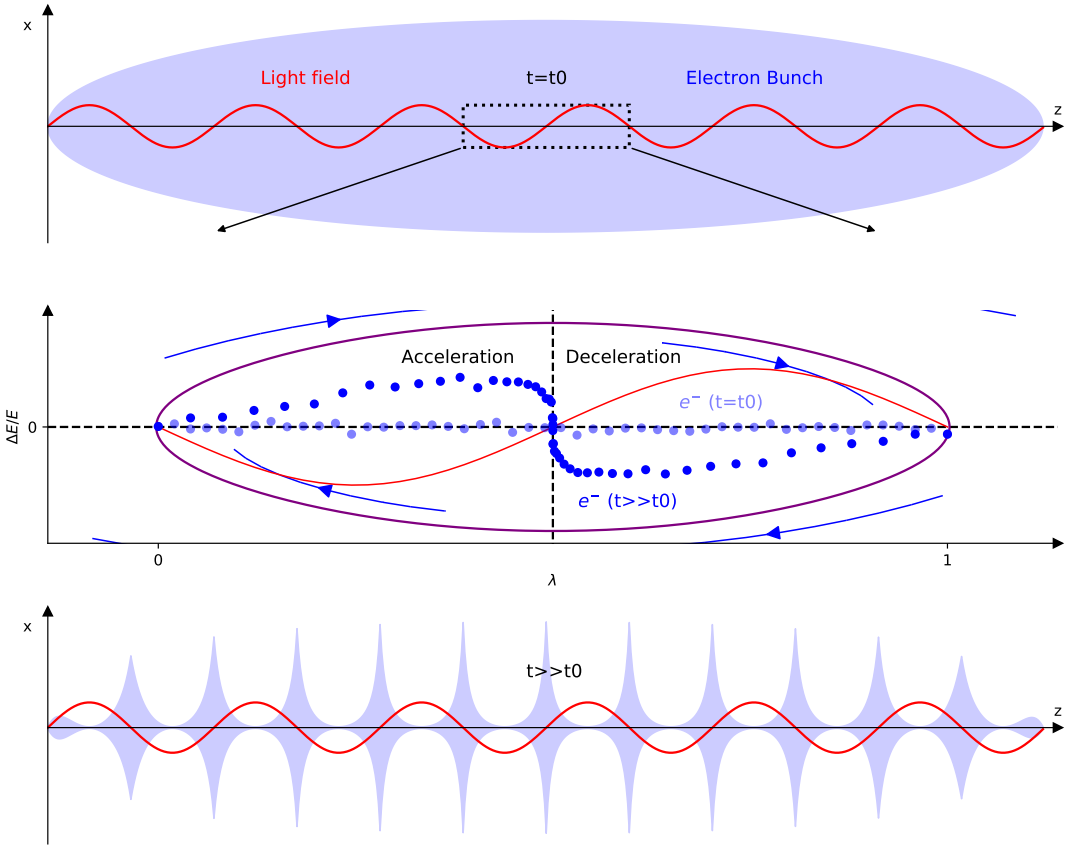

Figure 2.6 – A sketch of the FEL process. On top, the light field generated inside the undulator which propagates through the electron bunch. The electric field component of the light accelerates or decelerates the electrons (middle picture) depending on their relative positions to the emitted wavefront due to which they start to rotate in the phase space, indicated by the arrows. So, an energy modulation occurs which is transformed into a density modulation by the dispersive undulator. These micro bunches with lengths smaller than the emitted wavelength have a defined distance and emit coherently as macro charges.

The lasing process evolves when the generated photon field of the electron bunch inside the undulator interacts back onto the electrons and modulates the energy of the particles on the length scale of the wavelength such that a micro bunching of the electron pulse appears which causes a coherent emission. A sketch of this process is shown in Fig. 2.6. In a simplified picture, the energy transfer dI/dt between the light field and an electron is proportional to the electric field amplitude E_x of the light and the transverse velocity of the oscillating particle v_x, so $dI/dt \propto E_x \cdot v_x$.

The field amplitude itself depends on the square root of the pulse intensity. The energy transfer is proportional to $I^{1/2} \cdot v_x$ [44]. The micro bunching occurs because the vertical magnetic field amplitude of the photon pulse B_w causes an additionally longitudinal acting Lorentz force due to the transverse motion of the electrons inside the undulator field, which itself also depends on the square root of the intensity, $B_w \propto I^{1/2}$, which leads to $v_x \propto I^{1/2}$. This causes an electron in a decelerating phase of the electric photon field to fall behind relative to the center bunch position until it reaches an accelerating photon phase and vice versa, (middle in Fig. 2.6) [44]. Following from this the electrons will gather at specific locations inside the bunch relative to the emitted wavelength and a density modulation occurs on the length scale of the central wavelength (bottom in Fig. 2.6). These micro bunches have a fixed phase relation to the photon field and emit coherently. This leads to an energy transfer rate which is proportional to the intensity of the light pulse $dI/dt = A \cdot I$, with A = constant, so, to an exponential scaling of the emitted power due to the micro bunching [44]. Setting $A = u/L_g$ leads to the exponential intensity scaling [44, 45]

$$I = I_0 \exp\left(\frac{u \cdot t}{L_g}\right) = I_0 \exp\left(\frac{z}{L_g}\right) \tag{2.21}$$

along the undulator length z, which depends on the gain length L_g, the distance after which the field amplitude increased about a factor of e^1.
An advanced and more accurate calculation of the particle-light interaction results in a third order equation which is in its simplest form $E_x''' = i\,\Gamma^3\,E_x$ with $\Gamma = 1/(\sqrt{3}L_g)$ [2, 17]. The analytical solution of the third order equation gives the electrical field component of the FEL wave [2, 17]:

$$\frac{E_x(z)}{E_{in}} = \frac{1}{3}\left[e^{(i+\sqrt{3})\Gamma \cdot z/2} + e^{(i-\sqrt{3})\Gamma \cdot z/2} + e^{-i\Gamma \cdot z}\right]. \tag{2.22}$$

The resulting power gain $G(z) = |E_x(z)|^2/E_{in}^2$ of the emitted light pulse is then [46]:

$$\begin{aligned} G(z) &= \frac{1}{9}\left[1 + 4 \cdot \cosh\left(\frac{\sqrt{3}}{2} \cdot \Gamma \cdot z\right) \cdot \left(\cosh\left(\frac{\sqrt{3}}{2} \cdot \Gamma \cdot z\right) + \cos\left(\frac{3}{2} \cdot \Gamma \cdot z\right)\right)\right] \\ &= \frac{1}{9}\left[1 + 4 \cdot \cosh\left(\frac{1}{2}\frac{z}{L_g}\right) \cdot \left(\cosh\left(\frac{1}{2}\frac{z}{L_g}\right) + \cos\left(\frac{\sqrt{3}}{2}\frac{z}{L_g}\right)\right)\right] \end{aligned} \tag{2.23}$$

and its scaling with the gain length L_g is shown in Fig. 2.7. For $z \gg L_g$, the power scales like $G(z) \propto \frac{1}{9}e^{z/L_g}$.

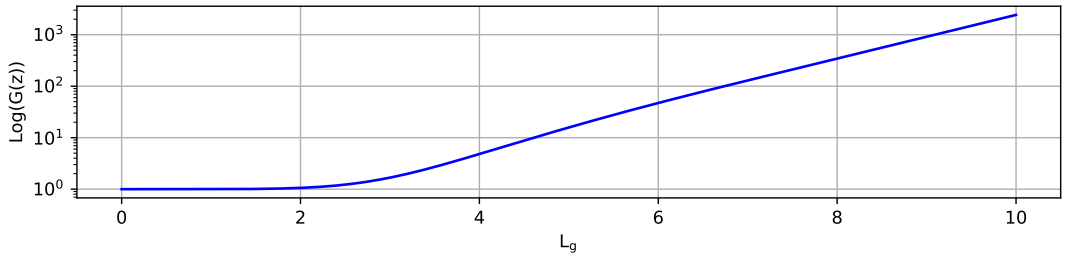

Figure 2.7 – The power gain Eq. 2.23 of the FEL process plotted for the start up regime, so for the first 10 gain lengths.

This process is called Self-amplified spontaneous emission (SASE) and exponentially increases the amplitude of the emitted power up to several orders of magnitudes due to the micro bunching process [2, 17, 44, 45].
The gain length is a measure for the amplification process and characterizes the requirements for the lasing. It depends on the undulator period length and the efficiency with which the FEL amplification is building up:

$$L_g = \frac{1}{4\pi\sqrt{3}} \frac{\lambda_u}{\rho}. \tag{2.24}$$

Here, the efficiency is expressed by the Pierce parameter ρ which is one of the fundamental parameters to describe FEL physics:

$$\rho = \frac{1}{\gamma} \left[\frac{I_b}{I_a} \frac{\lambda_u^2}{2\pi\sigma_x\sigma_y} \frac{(K[JJ])^2}{32\pi} \right]^{1/3} \tag{2.25}$$

with the Alfvén current $I_a = 17$ kA and the Bessel functions [JJ]=$J_0(Y_0(K))$-$J_1(Y_0(K))$ and $Y_0(K)$ as defined in Eq. 2.19. With those two parameters, ρ and L_g, some basic estimates for the lasing can be made [2, 17]:

- Power amplification scaling $P/P_0 \propto e^{z/L_g}$
- Radiation peak power in saturation $P_{sat} \approx 1.6 \cdot \rho \cdot P_{beam}$
- Laser saturation after $L_s \approx 20\ L_g \approx \lambda_u/\rho$
- FWHM bandwidth of FEL light $\Delta\lambda/\lambda \approx \rho$
- Electron energy spread acceptance $\sigma_\gamma/\gamma \leq \rho/2$
- Cooperation length, the slippage of the photon field within one gain length with respect to the electron bunch $l_c \approx \lambda \frac{L_g}{\lambda_u}$

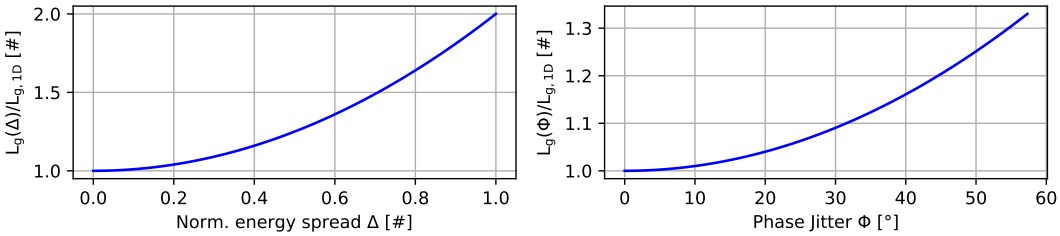

Figure 2.8 – Elongations of the 1D gain length of Eq. 2.24 with normalized energy spread of Eq. 2.26 and phase jitter of Eq. 2.27.

3D effects, like the electron beam dimensions along the undulator length, the energy spread and undulator field errors elongate the 1D gain length of Eq. 2.24. The individual scaling factors are derived by Xie [47]. To understand the concept of the laser plasma driven FEL and the design of the undulator two major scaling factors, the energy spread and the undulator phase jitter are of interest. A detailed discussion about all scaling parameters and their influence onto a possible lasing can be found in [4]. In a simplified picture, the elongation due to a Gaussian distributed energy spread σ_γ depends on the normalized energy spread $\Delta = \sigma_\gamma/\rho$ like [4]:

$$\frac{\mathrm{L_g}(\Delta)}{\mathrm{L_{g,1D}}} \approx (1 + \Delta^2). \tag{2.26}$$

The undulator phase jitter summarizes the degradation of the radiation phase of the emitted light due to magnetic field errors in the magnetic lattice. It is a measure for the power degradation and increases the gain length like [48]

$$\frac{\mathrm{L_g}(\Phi)}{\mathrm{L_{g,1D}}} \approx \left(1 + \frac{\Phi^2}{3}\right). \tag{2.27}$$

2.5 Conclusion

Within this chapter the basic physics of undulator and FEL radiation are shown. With hindsight to the thesis, which focuses onto the construction and characterization of the used undulator, the beam dynamics of electrons inside a magnetic field are linked to measurable properties of the undulator field in Sec. 2.1 namely to the first, second and phase integral. The radiation properties of undulator radiation, which depend on those integrals, are derived in Sec. 2.3 and the basic principle of the self amplifying process of the observable radiation, the free electron lasing, is presented in Sec. 2.4.

3 The LUX facility

LUX is a laser plasma driven undulator x-ray light source built at the DESY campus in Hamburg, Germany and dedicated to develop and improve laser plasma accelerators towards reliable electron sources for free electron lasers [36, 39]. Lux is driven by the Angus Ti:Sa laser system [49] which uses the chirped pulse amplification technology to produce pulses with 100 TW and 1 Hz repetition rate [24, 25]. Within the recent years the performance and stability of the Angus system and the plasma acceleration process were pushed to a state in which a 24 hour operation with $>$ 100000 consecutive shots with a mean energy of 368 MeV, an rms energy deviation of 4% and 25 pC average charge was demonstrated [34]. Until then, the plasma target development pushed the energy stability of the electrons further down towards and below the 1% rms energy spread mark, see Fig. 9.8 and to $\approx$ 50 pC of charge ($\approx$ 3 kA) [3], which opens access to the parameter space required to drive free electron lasers.
As already mentioned in Sec. 2.4, the free electron lasing is an exploit of a resonance condition which builds up when electrons are emitting synchrotron radiation while oscillating along their main path of propagation inside an undulator. The resonance frequency depends on the kinetic energy of the electrons and any statistical energy deviation inside the electron bunch acts as a damping of the resonant amplitude, which suppresses the amplification. So, to run an FEL, uncorrelated electron energy spreads smaller than the FEL efficiency are required [17, 2], which is a general challenge for laser plasma accelerators. At Lux, a decompression scheme is used to imprint a correlation of energy and longitudinal position into the electron bunch distribution, which grants access to manipulate the electron beam phase space such that its impact onto a possible lasing is reduced [39, 4].
Within this chapter, the basic motivation of the decompression scheme of Lux is presented. The fundamental physics of laser plasma acceleration and the implementation at Lux is shortly summarized in Sec. 3.2. The decompression scheme mainly consists out of a magnetic chicane to stretch the beam and a taperable undulator which is briefly derived in Sec. 3.3. The undulator design, which is a consequence from the Lux FEL design, will be discussed in Sec. 3.4.

3.1 Beam Line Overview

An overview of the Lux beamline is shown in the sketch on the next page. The laser (only final focusing section shown) is guided into a gas capillary target and generates an electron bunch using the ionization injection scheme [3]. A quadrupole doublet captures the electron beam and additional corrector dipoles steer the electron bunches downstream towards the chicane, in which the bunch can be decompressed. Behind the chicane the stretched bunch is focused with five quadrupoles (a quintet) into the undulator Frosty and the emitted radiation is measured with two spectrometers. The VUV spectrometer is used for wavelengths between 20 and 120 nm, see Sec. 8, whereas the VIS spectrometer records wavelengths above 200 nm. To diagnose the electron beam energy properties, two electron spectrometers are installed along the beam line. In total four beam position monitors record the center of mass of passing electron bunches and six screen stations are installed as beam profile monitors.

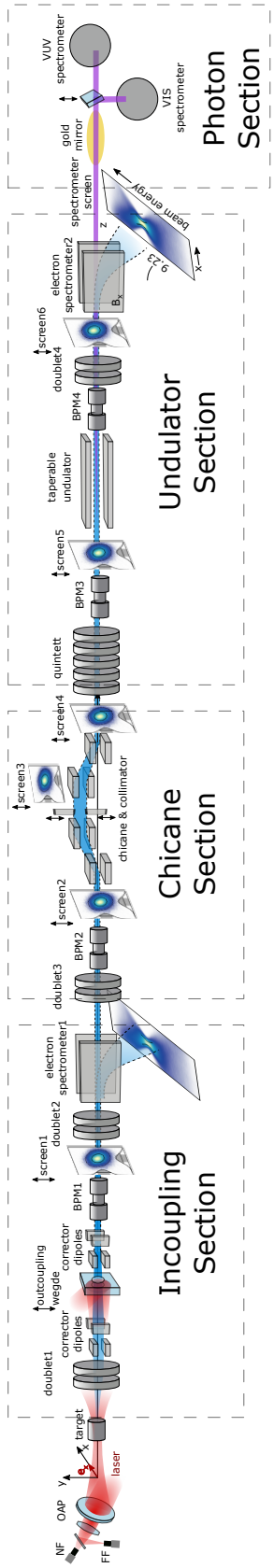

Figure 3.1 – Lux Beamline Overview. The Angus laser (red) is focused into the gas target with an off axis parabola (OAP) and generates an electron bunch (blue). Subsequent magnetic lenses (marked as doublet or quintet) and corrector dipoles capture and focus the divergent electron beam downstream towards the decompression chicane, in which the bunch is stretched and then focused into the undulator. The emitted light is analyzed with spectrometers. To measure the electron beam parameters four beam position monitors, two electron spectrometers and six screen stations are installed along the beamline. The laser is coupled out of the accelerator beamline with a wedge for further diagnostics. Picture Courtesy: Paul Winkler.

3.2 Laser Plasma Acceleration at Lux

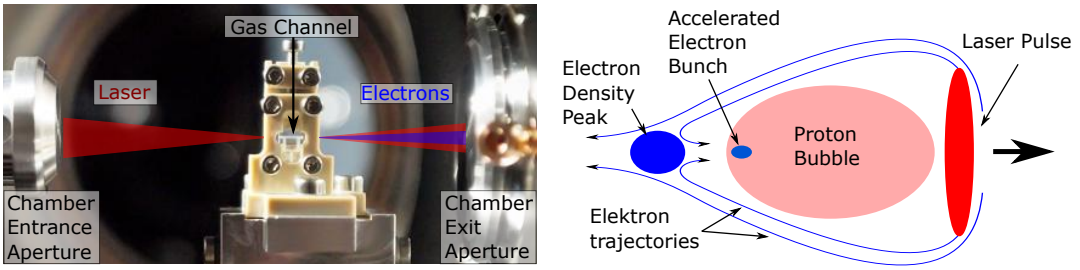

Figure 3.2 – Close up of the Lux plasma source and a sketch of a self injection laser wake field acceleration process. The intensity of the laser pulse expels the electrons inside the gas away from the laser axis, whereas the protons remain in position and a plasma wave is created behind the laser front. The expelled electrons gather behind the wave and can scatter into the laser direction where they enter the accelerating electrical field of the plasma wave. Photo: University of Hamburg, Niels Delbos.

The interaction between the laser and the plasma electrons depends on the ponderomotive force $\vec{F}_p = -mc^2\nabla\vec{a}_0^2/2$ which evacuates nearly all plasma electrons from the laser axis when the normalized laser vector potential $a_0 \approx 0.85\ \lambda\ [\mu m]\ \sqrt{I_0\,[10^{18}\,W/cm^2]} >> 1$ [29]. So, when a short pulsed laser with a wavelength λ and a high intensity I_0 is focused into a plasma with density n_e it creates a plasma wave which propagates behind the laser through the plasma. This plasma wave acts as a cavity with a length $\lambda_p\,[\mu m] \approx 3.3 \cdot 10^{10}\sqrt{n_e\,[cm^{-3}]}^{-1}$ in which an accelerating electrical field up to $E_0\,[V/m] = 96\sqrt{n_e\,[cm^{-3}]}$ could build up. For gas densities of 10^{18} cm^{-3} the accelerating gradient can reach orders of 100 GV/m, in which electrons from the background plasma can be trapped and accelerated up to several hundreds of MeV within some millimeters of acceleration length [29]. The self injection scheme illustrated in Fig. 3.2 is a statistical process in which electrons can scatter continuously into the plasma wave. The acceleration process is limited by the following phenomenons [29]:

- Laser depletion - As energy is transferred from the laser to the electrons the wake field can only be sustained over a certain distance
- Laser diffraction - The laser diameter widens by distance and the pulse intensity drops below the threshold to drive the wake field
- Dephasing - As the electrons inside the bubble are accelerated they can overtake the accelerating phase of the electrical field and run into the decelerating phase.
- Beam loading - Due to the Coulomb field of the trapped electrons the accelerating field is reduced until it completely vanishes.

Due to the continuous injection of electrons into the bubble and the linear acceleration gradient inside the wakefield the electron beam quality suffers from high energy spreads. Electrons injected at the beginning of the target receive a longer acceleration time as electrons injected close to the end of the target. Two particles captured at the same time, but at different longitudinal potions will receive the same acceleration time, but reach a different final energy due to the linear acceleration gradient inside the wake. This causes a correlation of the energy distribution with the bunch length, called energy chirp, and increases the projected energy spread. The localized electron beam charge produces an electrical field which counteracts the acceleration gradient along the electron bunch, which limits the amount of charge which can be accelerated.
With an adequate bunch shape, this effect offers the opportunity to alter the acceleration gradient inside the wakefield such that the electron bunch receives a close to constant acceleration along the whole current profile, which results in a constant acceleration of all particles and, therefore, in a high quality electron beam. With the localized ionization injection scheme used at Lux the beam loading can be adjusted to its optimum, see Fig. 3.3 [50, 3].

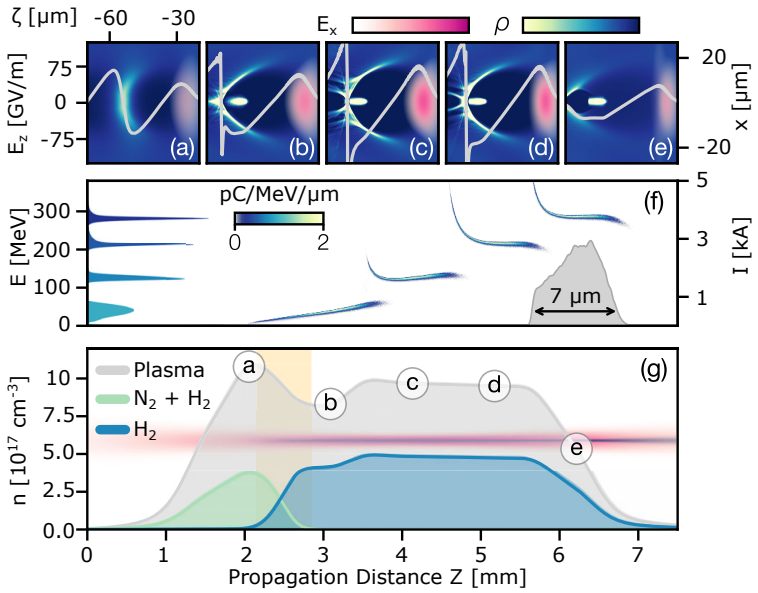

Figure 3.3 – Particle in cell simulations of the electron injection and acceleration shown in [3]. In the lower plot, the gas density distribution inside the target and the resulting plasma density is shown. The vertical red line represents the laser. At the locations (a)-(e) snapshots of the plasma wave, electron bunch and the laser are shown in the upper plot with the charge density ρ, the laser envelope E_x and the on-axis longitudinal wakefield E_z [3]. The center plot shows the evolution of the longitudinal energy distribution from (b) to (e). Picture taken from [3].

In the localized ionization injection scheme two different gases stream into the capillary, see lower plot in Fig. 3.3. A nitrogen doped hydrogen mix (90% H_2 10% N_2) is infused at the beginning of the target and pure hydrogen (90% H_2) at the end. When the laser is guided into the gas channel it starts to ionize the outer electron shells of the nitrogen and the plasma wave evolves, see snapshot (a) in the upper plot. Due to the high binding energy of nitrogen, the electrons of the inner shells are not yet expelled. When the laser reaches higher intensities also those electrons are set free directly inside the cavity, which is additionally shortly elongated in the density downramp, see snapshot (b). Due to the following density upramp the tail of the captured electron bunch is cut off and an isolated bunch is accelerated along the pure hydrogen plateau, see snapshots (c) and (d). Due to the depletion and diffraction of the laser intensity the acceleration field inside the plasma wave decreases and is eventually compensated by the beam loading of the electron bunch which results in a uniform acceleration and a flat energy distribution inside the core of the bunch, see (e) and (f). A strong beam loading overcompensates the acceleration field and causes a acceleration of the tail of the bunch, leading to a negative energy chirp. A low beam loading would cause a positive energy chirp. Both effects increase the projected energy spread with the charge from the optimum, see right plot in Fig. 9.10 and [3]. For the optimum beam loading, the acceleration field is completely compensated which results in beams with low energy spreads close to 1%, see Fig. 9.8 and bunch lengths of 7 μm with $\approx$ 50 pC and $\approx$ 3 kA peak current [3].

3.3 Decompression Concept

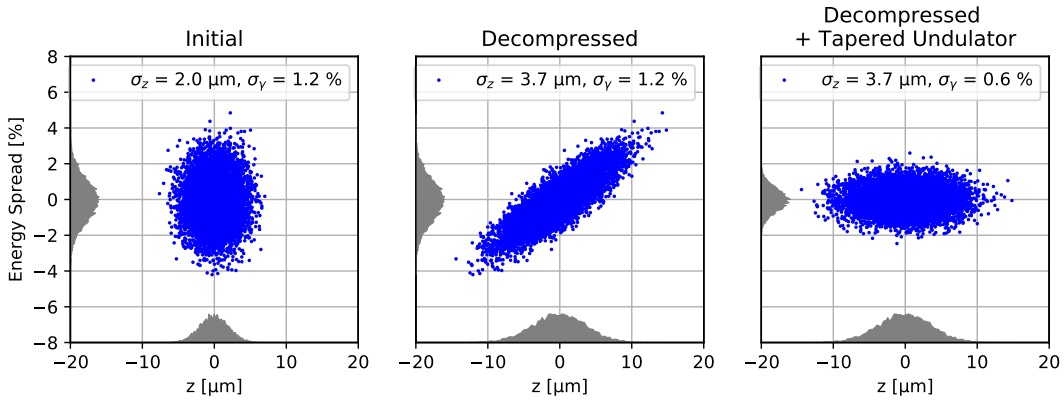

Figure 3.4 – Decompression concept used at Lux. A high current, high energy spread beam (left) is stretched in time using a magnetic chicane (middle plot with parameters from Fig. 3.5) which imprints an energy chirp. The undulator field is tapered such, that it compensates the chirp which results in an effective reduction of the energy spread contribution to the FEL process (right).

To compensate the 1% energy spread, a high-as-possible Pierce parameter above the 1% level is required to reduce the elongation of the gain length for the FEL below a factor of 2, see Eq. 2.26 and Fig. 2.8. A high Pierce parameter would lead to long gain lengths and overall long undulator sections. As the spirit of laser plasma accelerators is to build compact FEL sources, also the undulator section has to shrink in size, leading to a desirable short gain length in contrast. A balancing between the energy spread acceptance and a reasonably short machine length is the decompression concept used at Lux [39, 4]. Here, the high current and high energy spread electron beams are decompressed in time with a magnetic chicane, leading to a beam with a moderate current profile and a correlation between electron energy and position inside the bunch, see left and center plot in Fig. 3.4. As the total energy spread is conserved, the chirp results in a reduced slice energy spread. This energy chirp is compensated by linearly changing the undulator peak field amplitude along the device such, that the emitted wavelength, see Eq. 2.14, within the cooperation length is kept constant while the electron bunch travels along the undulator. That means that the wavelength emitted by the bunch tail at the beginning of the undulator is equal to the wavelength emitted by the head of the bunch at the end of the undulator. This combination of a decompression chicane and a tapered undulator reduces the effective energy spread of the electron bunch, see right in Fig. 3.4 [51, 39, 4]. In a simplified example with linear scales, a stretching of the bunch about a factor of $\mathrm{n} = 2$ would half the energy spread and the current. The Pierce parameter scales with $\mathrm{I}^{1/3}$ and would change about $\mathrm{n}^{-1/3} \approx 0.8$, see Eq. 2.25, whereas the energy spread decreases close to linear about $\mathrm{n}^{-1} = 0.5$. This reduces the initial normalized energy spread $\Delta = \sigma_\gamma/\rho$ about $\Delta(n) = \mathrm{n}^{-2/3}\Delta \approx 0.63\,\Delta$ and would change the gain length elongation of Eq. 2.26 to $\left(\mathrm{L_g}(\Delta) - \mathrm{L_g}(\Delta(n))\right)/\mathrm{L_{g,1D}} \approx (1 - n^{-4/3}) \cdot \Delta^2 \approx 0.6 \cdot \Delta^2$. Due to this reduction it is possible to reduce the overall machine length, which is required to demonstrate the start up of the lasing process with high energy spread electron beams [39, 4].

Bunch Decompression with a Magnetic Chicane

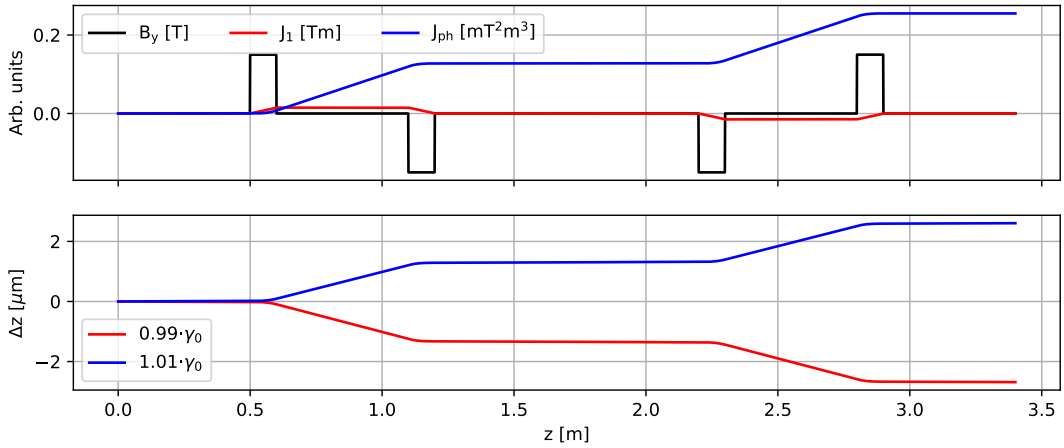

Figure 3.5 – The upper plot shows the magnetic field distribution and the phase integral of a chicane with $B_0 = 0.15$ T, $L_{mag} = 0.1$ m and $L_d = 0.5$ m. The energy dependent longitudinal displacement for two particles is shown in the lower plot. The central energy is $\gamma_0 = 600$.

The magnetic C-shaped chicane used at Lux consists out of a symmetric arrangement of four transverse deflecting dipole magnets with same amplitudes B_0 and a + - - + polarity. The magnetic field of such an assembly is shown in Fig. 3.5. The magnets have a magnetic length of L_{mag} and the distances between the magnets are L_d - L - L_d. Due to this setup the energy dependent transverse deflection of the electrons causes different path lengths and a longitudinal sorting inside the bunch. The longitudinal position change due to a magnetic field can directly be calculated by solving the phase integral from Eq. 2.5 for the described assembly:

$$J_{ph} = 2 \cdot B_0^2 \cdot L_{mag}^2 \cdot (L_{mag} \cdot 2/3 + L_d).$$

The resulting path length difference Δs for two energies of γ_1 and γ_2 after the chicane is given by Eq. 2.4:

$$\Delta s = \frac{1}{2}\left(\frac{1}{\gamma_1^2} - \frac{1}{\gamma_2^2}\right)\left(z + \left(\frac{e}{m_e \cdot c}\right)^2 \cdot J_{ph}\right) = \frac{1}{2}\left(\frac{1 - d\gamma^2}{\gamma_1^2}\right)\left(z + \left(\frac{e}{m_e \cdot c}\right)^2 \cdot J_{ph}\right)$$

with $d\gamma = \gamma_1/\gamma_2$. So, higher energetic electrons will move forward with respect to the bunch center and lower energetic electrons fall back, which leads to a longitudinal energy position correlation, see Fig. 3.5.

Chirp Compensation

By adjusting the magnetic field of the chicane, the bunch is stretched approximately linear about a factor n to a length of $\sigma_z(n) \approx n \cdot \sigma_{z,0}$, which directly leads to a reduction of the current to $I(n) \approx I_0/n$. While the overall projected energy spread is unaffected by the decompression, the local energy spread is reduced about n and an energy chirp of the form

$$\frac{d\eta}{dz}(n) \approx \frac{1}{n}\frac{\sigma_\gamma}{\sigma_z}$$

is imprinted into the beam profile, see middle plot in Fig. 3.4. When the undulator field linearly changes along the undulator length s like

$$\frac{dK}{ds} \approx \frac{\left(1+\frac{K^2}{2}\right)^2}{K\gamma^2}\frac{d\eta}{dz},$$

the chirp is compensated and the projected overall energy spread effectively reduced about n, see right plot in Fig. 3.4, [51, 39].

To further increase the energy spread acceptance the undulator provides a high K-value close to 3 and a short period length of 15 mm, which decreases the FEL gain length and increases the Pierce parameter up to the one percent level. It was shown in [39, 4] that this concept is capable to demonstrate the start up of an FEL for energy spreads of 1% which are decompressed with a chicane to 0.25% and than guided into an undulator with a K = 3.3 and a taper of 5.3%/m. The study showed that the FEL power is ≈ 60 times the spontaneous radiation power, which is enough to clearly identify the start up.

3.4 Undulator Parameter Choice

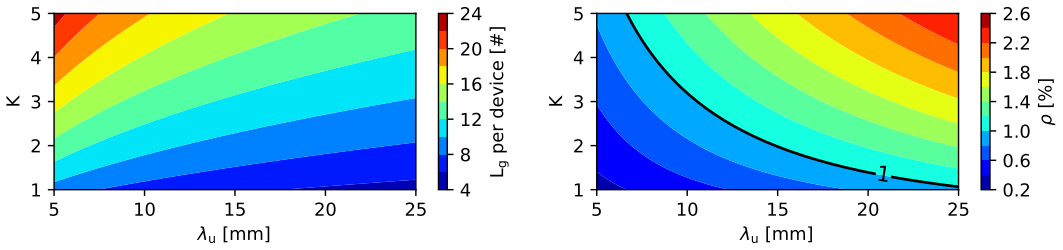

Figure 3.6 – 1D Pierce Eq. 2.25 and the number of 1D gain lengths Eq. 2.24 (per 2 m device length) scaling with the undulator period and K-value. A $\gamma = 600$, $\sigma_x = \sigma_y =$ 30 μm, I_b=3.6 kA were used, which are taken from [4].

The undulator design was a consequence of the beam parameter space obtainable with laser plasma accelerated electron beams and was analyzed in full detail in [4]. The FEL process is a complex mechanism with a lot of contributions from electron beam parameters onto the gain length, which all requires additional corrections. As the focus of this thesis is to build and characterize the undulator and not the FEL physics, the full 3D description would be beyond the scope, so only a short motivation within a 1D approximation will be presented. All details can be found in the PhD thesis of Thorben Seggebrock, which was dedicated to this topic [4].
The main criterion for the maximum undulator length was, that the available space in the former laboratory for which the machine was originally designed for, was limited to two meters [12]. So, a balancing between a high number of gain lengths and a high Pierce had to be found. An advantage which has to be mentioned here is, that the Lux accelerator is dedicated to research the technology itself and not to produce light for user experiments. This allows to chose a parameter space for the FEL demonstration without the boundary to lase at a specific wavelength. Also, to demonstrate the FEL only the start up has to be shown and not a full saturation. This allows to shrink the number of required gain lengths.

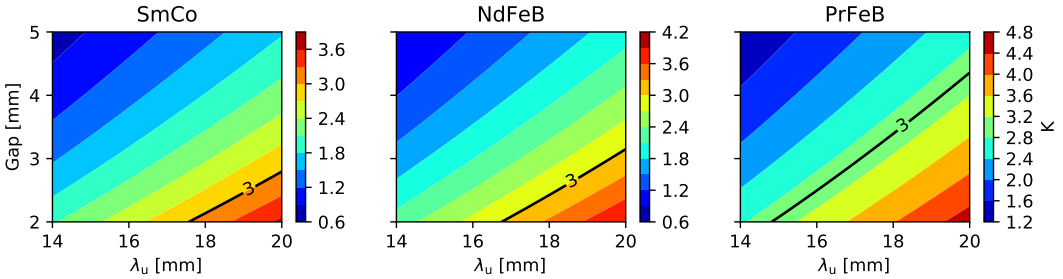

Figure 3.7 – Achievable K values Eq. 2.12 for different permanent magnet materials. The fit parameters for Eq.4.1 are a = 3.33 b = -5.47 c = 1.8 for CmSo (at 293 K) [1], a = 3.44 b = -5.08 c = 1.54 for NeFeB (at 293 K) [1] and a = 3.598 b = -3.840 c = 0.631 for PrFeB (at 77 K) [5].

The gain length Eq. 2.24 and the pierce parameter Eq. 2.25 scale both with the period length λ_u and the K-value of the undulator. A high number of gain lengths per machine and a high Pierce can be achieved by choosing a short λ_u and a high K, as illustrated in Fig. 3.6. Those parameters can not be chosen arbitrary, as the K value depends on the undulator period, Eq. 2.12, and on the peak field, which itself is gap and period dependent, see Eq.4.1. Fig. 3.7 shows a comparison of the achievable K-values for different magnet alloys available for the undulator design: CmSo, NdFeB at room temperature and PrFeB in a cryogenic state, which was developed in a collaboration between Lux, HZB and the company Vacuumschmelze [42]. A cryogenic undulator based on PrFeB allows to reduce the period length down to 15 mm, implementing a

total of 130 periods and produces a K of 3 at a 2 mm gap which would result in a Pierce parameter of 1% and a high number of gain lengths per device, see Fig. 3.6. So, the cryogenic technology was chosen for the undulator which was then codenamed Frosty.

3.5 Conclusion

Within this section the Lux accelerator beamline and the decompression concept, which is used to demonstrate a possible start up of an FEL is presented in Sec. 3.3. From the prior FEL simulations the important parameters for the undulator design in terms of technology and period length, were recapitulated, see Sec. 3.4.

4 On the Design of Frosty

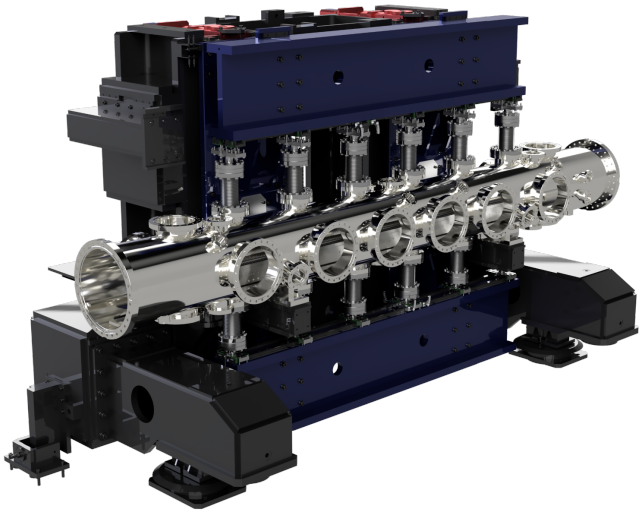

This is Frosty.

The heart of the free electron lasing is the undulator which provides the sinusoidal magnetic field in which the electron oscillation and the subsequent radiation and resonant amplification takes place.
Although the theoretical relevant description of Frosty reduces to a simple sinusoidal, see Eq. 2.10, the mechanical and physical realization of it is a rather complex topic of its own. Just as an example: Within one period are four magnets kept in position with two clamps and two screws each, and four poles with two adjustment screws each, so a total of 32 components per period. That makes 4160 components for 130 periods which have to be positioned with a micrometer / micro Tesla accuracy. As the created on-axis field depends exponentially on the positioning it is hardly possible to achieve a pure sinusoidal field if the design of the support structure is not capable of positioning the components with that accuracy, or if the repelling forces of the magnets bend the support structure about several tenths of micrometers. The additional cooling of the undulator amplifies the influence of positioning errors in several ways.

First, the temperature sensitive magnets will produce a different on axis field if the cooling is inhomogeneous and second, a local hot spot would cause a local thermal expansion of the support structure, so a bulking due to which magnets of the opposing girders will have a different distance and create a different on-axis field.
Following from this, it is absolutely mandatory to gain insight into the impact of the different error influences onto the on-axis undulator field and layout the design of the machine in a way to minimized those effects. This will be achieved in two ways. First, with an adequate dimensioning of the magnet keepers in the girders which requires to set up a tolerance chain of the fabricated components. With this it is possible to reduce global errors over the whole machine. Second, by implementing a tuning method of the undulator field. This allows to actively correct for local field errors.
In this chapter, the main design of Frosty is presented. At first a general overview onto the machine is presented in Sec. 4.1 to understand the subsequent design criteria and definitions. For Frosty, a special magnet alloy is used which allows an increase of the on-axis field with decreasing temperature. This temperature change also affects the demagnetization resistance. Both effects are the main reason to cool the undulator to cryogenic temperatures. The magnetic properties like the on-axis field and resulting forces will be discussed at first in Sec. 4.2.
Due to the cooling also the support structure will contract. As different materials are used it is important to layout the tolerance chain between the individual components such, that a possible clamping and high stresses are prevented. Otherwise they could cause a burst of the girders. The cooling concept consists out of two cold heads which are connected to the girder ends. From those localized cooling spots a thermal gradient will arise along the device which will affect the field of the magnets and the thermal contraction of the support structure which will be evaluated in Sec. 4.3.
From those design considerations the mechanical layout of Frosty is derived and the impact of the finished design onto the undulator field properties will be discussed in Sec. 4.4.

4.1 Design overview

Frosty is designed as an in-vacuum cryogenic planar hybrid undulator which can be tapered. The hybrid structure means, that an alternating arrangement of hard magnetic permanent magnets and soft magnetic pole plates is used to achieve a high on axis field. This field can be further increased by cooling the magnets down to cryogenic temperatures, which can only be done inside a vacuum tank. The magnetic structure is kept in position by a mechanical letter case, also called comb structure, with a period length of 15 mm in the cryo state and 15.08 mm at room temperature. In total 130 periods are mounted on one Frosty girder.

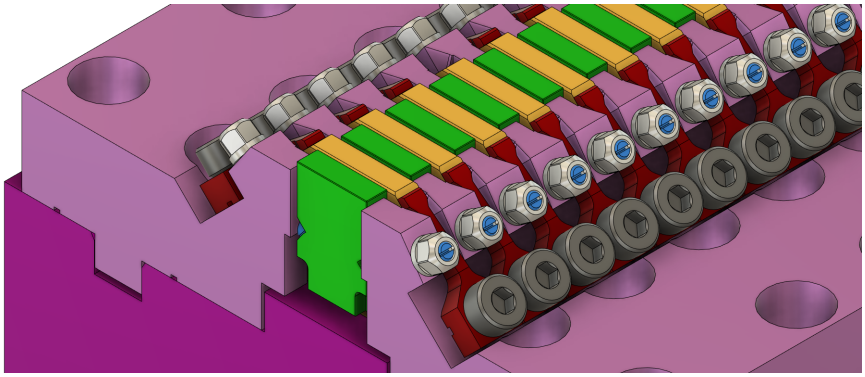

Figure 4.1 – Close up onto the magnetic array of one girder. The color code represents the different components.

Fig. 4.1 shows the girder assembly. The poles are indicated in green and the magnets in yellow. The surrounding comb structure (light pink) forms the letter case which defines the period length. The comb structure is mounted on top of a long girder (dark pink) which is responsible for the stiffness of the structure. The magnetization axis of the individual magnets points parallel to the girder and is alternating between neighboring magnets. The magnets are blocked in position with clamps which are colored in red. To adjust local field errors the poles can be slightly changed in position by turning one of the two blue adjustment screws, which form the pole suspension.

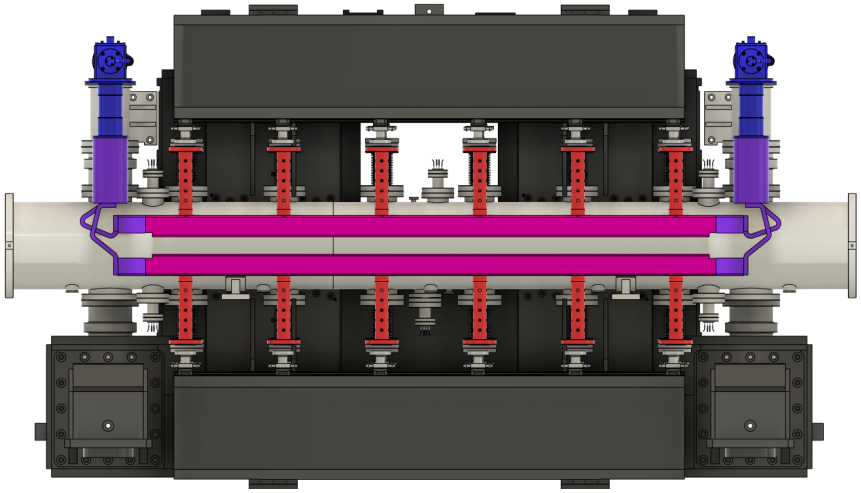

Figure 4.2 – A side view onto the Frosty design with a transparent undulator chamber (gray) to see the in-vacuum girders. The color code represents the individual sections of the machine.

Fig. 4.2 shows the full assembly of Frosty. Two girders (pink) are mounted such that the magnets inside them are facing each other. Inside the gap between the two girders

the magnetic undulator field forms along the undulator axis (from left to right in the picture) which reduces to a sinusoidal field at the center of the gap. On each girder end, a copper band (purple) reaches to a cryo cooler (blue) to establish the cooling chain. Each girder is mounted on a total of six pillars (red) which are connected to the out of vacuum undulator frame (black), also called back bone. This back bone compensates the attractive forces between the gap.

4.2 Magnet Technology

When talking about permanent magnets two major quantities are of interest: the remanence of the magnetic material and the coercivity.

Remanence $\mathbf{B_r}$

When a ferromagnetic material is exposed to an external magnetic field, the remanent magnetization, or residual flux density B_r is the field which remains in the ferromagnetic material after the external field is switched off. When the magnetic field is measured while the two magnetic poles of the magnet are not connected via a magnetic conductor one would measure a comparably weak remanence called open remanence. When the loop between the poles is closed the remanence develops its maximum which is called closed remanence, or simply remanence and is the specified quantity when ordering permanent magnets.

Coercitivities $\mathbf{H_{cB}}$ & $\mathbf{H_{cJ}}$

When a permanent magnet is exposed to an external magnetic field, with opposing field strength, the magnet can be demagnetized. The applied magnetic field strength which is necessary to compensate the remanence of the magnet is called the coercivity H_{cB}. For a much higher applied field the magnetic polarization starts to annihilate, which leads to the total destruction of magnetic properties. The value for the coercivity at which the magnet starts to degrade is called H_{cJ}. So, the coercivity of a magnetic material represents its resistance versus external fields and also against radiation damages.

The higher the remanence B_r the more magnetic field can be guided towards the undulator axis which allows higher K values for the same gap. Unfortunately, the remanece and the coercivity are linked over the constant magnetic energy density $(BH)_{max} \approx B_r \cdot H_{cB}/4$, which means it is not possible to increase B_r and H_{cB} simultaneously arbitrarily high and a trade off is required.

4.2.1 Specifications of the used Magnets

Magnet Material	VACODYM 131 DTP [52]
Dimensions x,y,z (mm)	18 x 21 x 3.7
Remanence B_r at 293 K / 77 K	1.41 T / 1.62 T
Coercivity H_{cJ} at 293 K / 77 K	1640 kA/m / 6251 kA/m
Pole material	VACOFLUX 50 [53]
Dimensions x,y,z (mm)	12 x 18 x 3.6

Table 4.1 – Magnetic design parameters of the Frosty undulator.

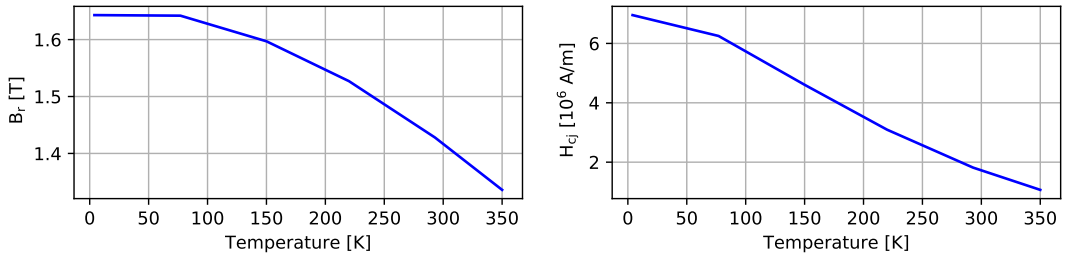

Figure 4.3 – Temperature curve of the remanence and coercitivity of VACODYM 131 DTP [6].

The used magnetic material VACODYM 131 DTP is a $Pr_2Fe_{14}B$ alloy developed in a collaboration between the LMU Munich, HZB Berlin and the company Vacuumschmelze [40]. One characteristics of this material is, that it does not show a spin reorientation transition at 130 K which occurs for NdFeB magnets [6]. The characteristics of this material are, that the typical remanence field increases from 1.41 T to 1.62 T when they are cooled from 20 deg. down to -196 deg. and the coercivity increases from 1640 kA/m up to 6251 kA/m [6]. The temperature curve and characteristics are shown in Fig. 4.3. Inside the undulator the magnets will be assembled with an alternating magnetic polarization, so neighboring magnets will always repel each other in a way that their fields B_r are always counter acting to the neighbor's H_{cJ}. A demagnetization will appear when the induced coercivity from the neighboring magnet $H = B_r/\mu_0$ ($\mu_0 =$ vacuum permeability $= 4\pi \cdot 10^{-7}$ N/A^2) is above the H_{cJ} threshold. Especially during the assembling of the magnets even higher coercivities can be generated inside the already installed magnets, which requires a safety factor of 1.5 for the minimum H_{cJ}, so $H_{cJ} = 1.5 \cdot H$ at room temperature. So, for the remanence of 1.41 T a $H_{cJ} = 1683$ kA/m at room temperature is demanding which can be achieved by treating the magnets with a grain boundary diffusion process as described in [6].

4.2.2 Heat Induced Demagetization

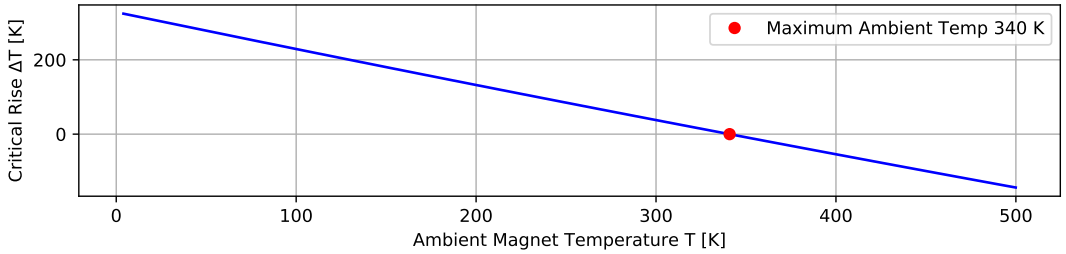

Figure 4.4 – Maximum local temperature rise before demagnetization due to ambient magnetic fields will occur.

The design electron beam parameters for the LUX FEL case are a beam with a diameter between 30 μm and 100 μm, with 300 MeV electron energy and up to 50 pC charge. Due to the small minimum gap of 2 mm the girders are very close to the design electron beam envelope and a possible impact of emitted radiation or electrons can happen which degrades the remanence field of the magnets. As the resistance versus electron impact is linked to the coercivity of the material a cooling of the magnets has the favorable side effect to suppress those damages as well. If the incoming electron beam is misaligned, or has a diameter larger than the gap of the undulator, electrons from the outer region of the bunch can hit the magnets and depose their energy inside of the material. To estimate this impact a prototype was built on which those measurements and the varieties of electron - matter interactions are researched and published in [41]. One aspect which is still missing is the temperature rise inside the magnets due to the electron energy loss. Those local hot spots will reduce the local coercivity H_{cJ} of the magnets. If the reduction is so strong, that the coercivity of the neighboring magnets H is above H_{cJ}, a local demagnetization will occur. To estimate the critical temperature jump the curves in Fig. 4.3 are used to determine the critical local temperature jump ΔT at an ambient temperature T, which is required to fulfill $H_{cJ}(T + \Delta T) = B_r(T)/\mu_0$, see Fig. 4.4. If the ambient temperature exceeds 340 K the undulator starts to demagnetize itself without external "help". Another limit is the maximum operation temperature of a single magnet which is at $\approx$ 383 K [52], above which the magnet starts to loose its field. This limit will be neglected as it is above the 340 K limit.
To discuss the heat induced demagnetization the temperature dependent heat capacity of the magnet material and also the energy loss of the electrons inside the material have to be found. To do so, a simplified model will be used. The aim of the approximation is to estimate how good the electron beam has to be aligned through the undulator to not cause any harm to the magnetic field. In the spirit of this machine protection it is valid to overestimate the impact, which will be done by several assumptions:

1. The energy loss of the electrons will be completely converted to heat. Matter anti-matter creations, star events and all mechanisms which can occur will be neglected as they are already described in [41].
2. The internal heat diffusion of the magnets takes orders of magnitudes more time than the heat deposition. So, the heat is generated instantaneously in a certain volume.
3. Particle scattering and a subsequent increase of the beam diameter will be neglected and it is assumed, that all particles within a certain cross section will stay within the cross section.
4. The calculations are all done for particles entering the magnets within a cross section of 1 μm $\times$ 1 μm and the electron energy loss is released within a volume of 1 μm^3.

Heat Capacity of VD 131 DTP

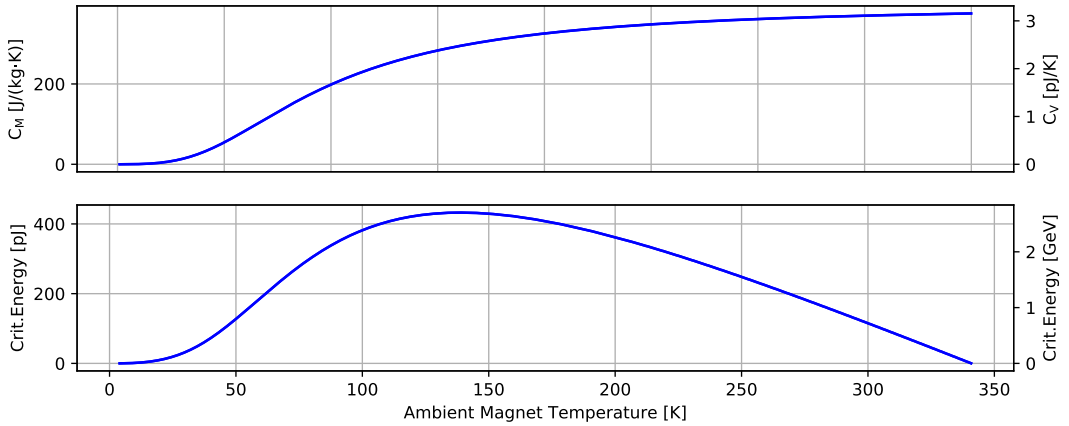

Figure 4.5 – Temperature dependent heat capacity and critical energy of $Pr_2Fe_{14}B$.

The amount of energy which is required to heat up one kg of material about one degree is described by the heat capacity of the material which itself is a temperature dependent quantity and can be described by the Debye function [54]:

$$C_M(T) = 9\frac{NR}{m_{mol}}\left(\frac{T}{T_D}\right)^3 \int_0^{T_D/T} \frac{x^4 \cdot e^x}{(e^x-1)^2} dx$$

Here, $m_{mol} \approx 1074.5$ g/mol is the molar mass of $Pr_2Fe_{14}B$, N is the number of atoms per chemical formula (for $Pr_2Fe_{14}B$ follows N = 17), $R \approx 8.3\frac{J}{mol \cdot K}$ is the universal gas constant and $T_D \approx 400$ K the Debye temperature of the magnets [54].

Using the density $\rho_{VD} = 8.4\,g/cm^3$ of the magnets [15] and the assumed volume of $V = 1\,\mu m^3$, the heat capacity C_M can be rearranged to get $C_V = C_M \cdot \rho_{VD} \cdot V$, the amount of Joules to heat up the defined unit volume about one degree. Combining C_V with the critical temperature rise from Fig. 4.4 allows to estimate a critical energy dose in the unit volume before demagnetization occurs, which is shown in Fig. 4.5.
While the heat capacity increases towards room temperature the critical energy reaches a maximum at 140 K at which 2.7 GeV can be deposed in the unit volume. Due to the subsequent decreasing critical temperature also the critical energy is decreasing again. For example, the critical energy at 293 K and 51 K are equal at 0.84 GeV. This is caused by the low heat capacity at 51 K and the low allowed critical temperature rise at 293 K. These two temperatures are of major interest, as they are close to the lowest and highest temperature at which Frosty will operate.

Energy Loss of Electrons in the Magnetic Array

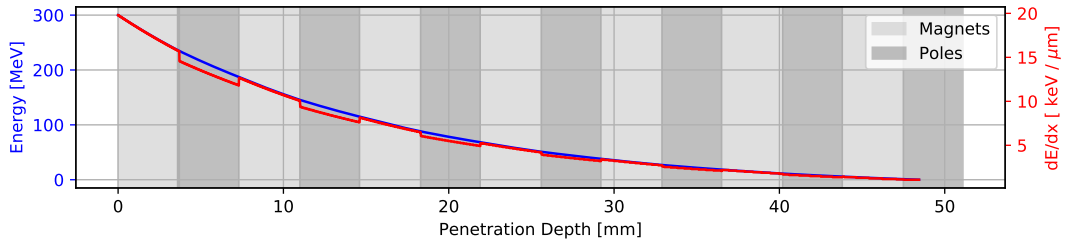

Figure 4.6 – Energy loss of a 300 MeV particle within the magnetic undulator array.

The complex mathematics behind the energy loss of relativistic electrons in matter is described by the theory of Bethe [55], [56] and its corrections evaluated by Sternheimer [57],[58]. For the sake of simplicity, those calculations were left over to the online data bank of E-Star [59], an online tool which includes all corrections to the Bethe formulas and is bench marked with experimental data.
The energy loss of a single electron inside the undulator array with an energy of 300 MeV is shown in Fig. 4.6. Assuming a frontal impact the electron would penetrate roughly 3.5 undulator periods with an initial energy loss of $dE/dx_{max} \approx 20\ keV/\mu m$ at the entrance of the first magnet. Using this value and the critical energy of 848 MeV at 293 K or 51 K, the maximum charge density allowed to enter the unit cross area is $\rho_q \approx 6.8 \cdot 10^{-15}\ C/\mu m^2$.
The Lux accelerator will operate in a so-called traveling focus scheme with local beam diameters down to 35 μm with ≈ 50 pC of charge. Assuming a transverse Gaussian bunch shape it is possible to calculate the peak current density within the bunch profile and to estimate the minimum beam size above which the magnets could withstand a direct single impact, see Fig. 4.7.

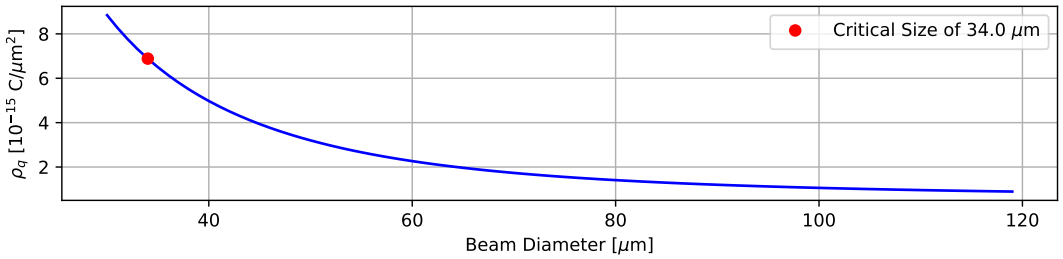

Figure 4.7 – Peak charge density for different bunch diameters and a total charge of 50 pC.

When the beam size is above 34 μm the charge density is too low to increase the temperature above their critical level as long as the ambient temperature is kept between 51 K and 293 K. So, within the limits of this thermal simplified model, the undulator is save for a singe impact of a 300 MeV electron beam with 50 pC and a diameter above 34 μm.

4.2.3 On-axis Undulator Field

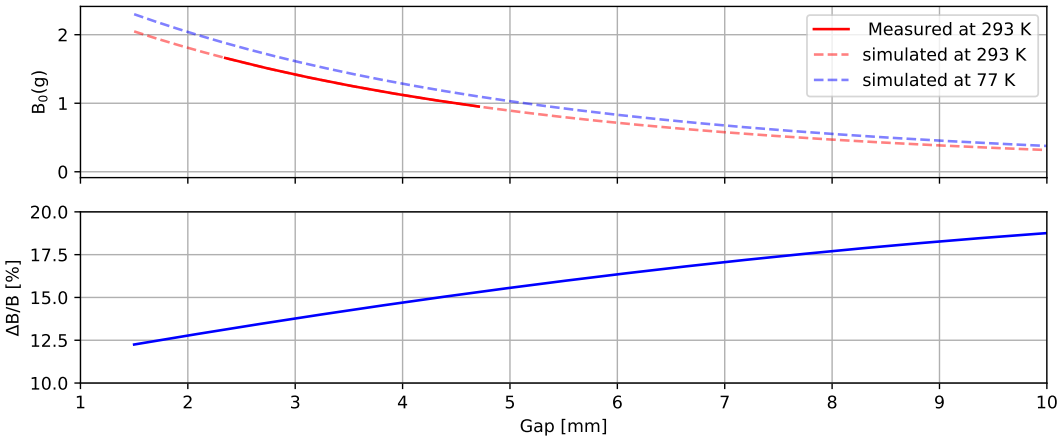

Figure 4.8 – Simulated gap scans for warm and cold undulator condition. In the lower plot is the ratio of the field increase due to cooling.

The gap dependent on-axis field of a planar undulator with period length λ_u follows an exponential function of the form [1]

$$B_0(g) = a \cdot \mathrm{Exp}\left(b \cdot \frac{g}{\lambda_u} + c \cdot \left(\frac{g}{\lambda_u}\right)^2\right). \tag{4.1}$$

The fit parameters are evaluated by simulations using CST [60] for the warm and the cold remanence field of the magnet material, see Tab. 4.1 and are summarized in Tab. 4.2.

B_{Magnet}[T]	T [K]	a	b	c	B_0 (g=2 mm) [T]	K (g=2 mm)
1.41	293	3.007	-3.944	0.833	1.81	2.55
1.62	77	3.325	-3.786	0.757	2.04	2.86

Table 4.2 – Fit parameters for the warm and cold condition of Frosty. The simulation was done for gaps from 2 mm to 40 mm.

The simulated gap scan in the upper plot of Fig. 4.8 is congruent with a reference measurement of the real undulator field in the warm state. In the lower part the ratio between the simulated warm and cold field is plotted. As the magnets increase their field about $\approx 15\%$ when cooled, also an increase of the $B_0(g)$ field on the same level is expected. The field increase is on the 15% level for gaps above 4 mm and decays for smaller gaps due to saturation effects of the pole material and is only around 12% at the nominal gap of 2 mm.

4.2.4 Taper

To taper the peak field amplitude $B_0(g)$ the magnetic arrays are mechanically tilted towards each other and a mechanical gap gradient $\eta = \Delta g/g_0/L_k$ occurs along the undulator. g_0 is defined as the nominal gap at the undulator center. $L_k = 1.87$ m is the distance between the two gap measurements systems with which the taper is adjusted and Δg the adjusted gap difference between these two measurement points. This linear gap change along the device, $g(z) = g_0\ (1+\ \eta{\cdot}z)$ with $g(z = \text{center}) = g_0$, causes an exponential field change of the on-axis undulator field, see Eq. 4.1 and Tab. 4.2:

$$B_0(g_0, \eta, z) = a \cdot \text{Exp}\left(b \cdot \frac{g_0}{\lambda_u}\,(1 + \eta \cdot z) + c \cdot \frac{g_0^2}{\lambda_u^2}\,(1 + \eta \cdot z)^2\right)$$

For small gradients, so $\eta^2 \cdot z^2 \approx 0$, the change of the field amplitude along the girder is approximately

$$B_0(g_0, \eta, z) \approx B_0(g_0) \cdot \text{Exp}\,(d \cdot \eta \cdot z)$$

with $d = b\frac{g_0}{\lambda_u} + 2c\frac{g_0^2}{\lambda_u^2} < 0$. A Taylor expansion up to the second order of the exponential function gives the approximate taper dependent field change:

$$B_0(g_0, \eta, z) \approx B_0(g) \cdot \left(1 + d \cdot \eta \cdot z + \frac{1}{2}d^2 \cdot \eta^2 \cdot z^2\right)$$

A positive mechanical taper $\eta > 0$ will lead to a decrease of B_0 along the girder and can be used to compensate a negative electron energy chirp (higher energetic tail). A negative mechanical taper $\eta < 0$ leads to an increase of B_0 along the machine which compensates a positive electron energy chirp (higher energetic head).

4.2.5 Attractive Forces

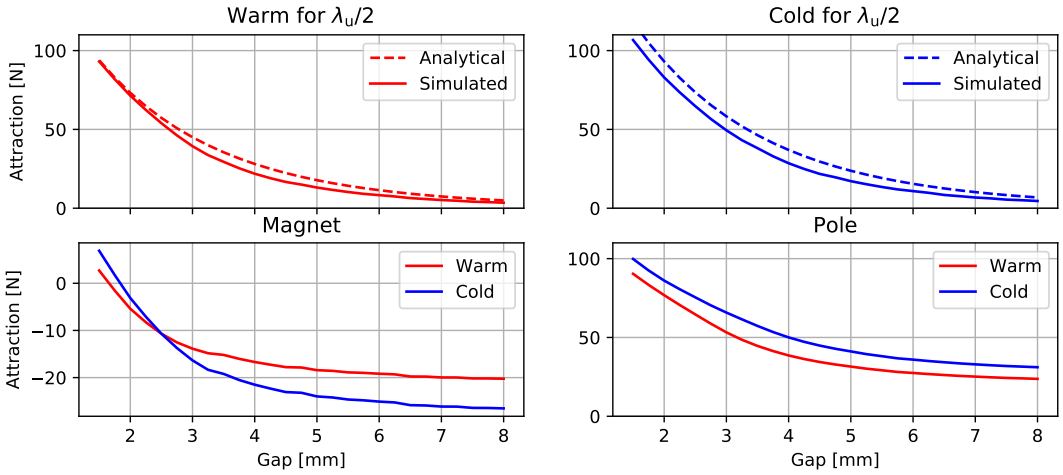

Figure 4.9 – Gap dependent forces acting onto a half period and onto the individual components, the pole and the magnet.

The magnetic field inside the gap creates an attractive force onto the poles towards the gap and a repelling force onto the magnets away from the gap. This force is calculated by the magnetic energy density stored in a volume $\frac{dE}{dV} = \frac{d^3E}{dxdyds} = \frac{B^2}{2\mu_0}$ (μ_0 is the vacuum permability) and integrating over the center gap plane [1]

$$F = \int\int \frac{(B_0 \sin(k_u \cdot z))^2}{2\mu_0} dxdz = \frac{B_0^2 LW}{4\mu_0} \approx 22.86\,N \cdot K^2 \cdot N_u.$$

L is the undulator length and $W \approx \lambda_u$ the horizontal width of the field. The forces can also be expressed in terms of the operating K value and the number of periods N_u. At 2 mm gap the acting force will reach ≈ 19.2 kN at warm temperature and ≈ 24.2 kN due to cooling.
Besides the force acting onto the whole girder structure it is of interest how much force is acting onto one half period and onto the poles and magnets specifically. An easy estimate to get the force per half period is by dividing the equation above by the number of half periods inside the undulator which is shown in the upper plots of Fig. 4.9 and would result in 77 N (warm, 1.84 T) and 94 N (cold, 2.05 T) per half period.

Within the half period, the average force is split into an attractive force onto the pole towards the gap and a counteracting force onto the magnet which have individually higher amplitudes. In the lower part of Fig. 4.9 the forces of the upper plots are split up for the individual components. While the force onto the pole is always into the same direction and above the average force for gaps higher than 1.8 mm, the force onto the magnet will change the direction for gaps below 1.8 mm. So, the magnets will be pushed towards the gap, if they are not locked in position.

4.3 Design Considerations

For the design of the undulator structure several aspects play a major role which are briefly explained here. The accelerator beam line and the undulator underlie a high vacuum standard which restricts the allowed materials for the design. For those materials it is important to know their temperature behavior in terms of conductivity and geometrical contraction to predict the temperature distribution inside the undulator when it is cooled. When a steady state temperature is reached remaining thermal gradients inside the structure will affect the geometry of the support structure and the remanence of the magnets. Both effects will have an impact onto the field quality.

4.3.1 Material Specifications

Component	Material
Poles	Vacoflux 50 (CoFe)[53]
Magnets	Vacodym 131 DTP (Pr_2 $Fe_{14}B$)[52]
Pillars	Stainless Steel (316 LN)[61]
Girder and combs	Aluminum (EN AW-5083)[62]
Screws	Titan Grad 5 (TiAl6V4)[14]
Copper Connectors	CU-HCP [63]

Table 4.3 – Materials used for the Frosty undulator.

Frosty and the LUX accelerator are operated at the DESY campus in Hamburg, Germany. The facility has a long lasting experience in terms of accelerator operation and developed a standard for all materials and components which should operate in a vacuum system attached to an accelerator [64]. This standard was developed to prevent the machines from damages due to long carbon molecules evaporated by fat inside the chambers which would act as lightning rods in conventional cavities, or would bake to optics causing interference rings in a laser system which guides high energies. This standard includes a complex cleaning process and a restriction to the

variety of materials which are allowed to operate inside the vacuum chambers attached to accelerators. The materials allowed and used for Frosty are given in Tab. 4.3.

4.3.2 Temperature Dependent Mechanical Characteristics

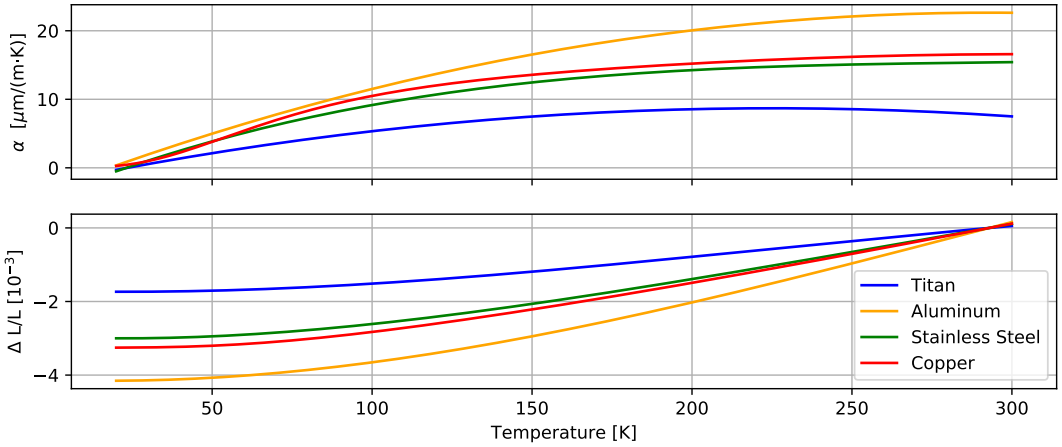

Figure 4.10 – Temperature dependent expansion coefficients for the used materials listed in Tab. 4.3. The data is provided by [7].

As the hole undulator structure shrinks due to the cooling, one central aspect for the design is the tolerance chain between components out of different materials as they have different coefficients of thermal expansion called α. A wrong design would lead to material stress and pressure between the contact surfaces of touching materials which could cause an irreversible deformation or a burst of the structure. The temperature dependent thermal expansion coefficients and the relative length change of the used materials are all listed in [7] and are plotted in Fig. 4.10.
To estimate the temperature dependent tolerance chain between components it is only important to know the thermal contraction between room temperature and the design temperature (77 K). Taken only those two data points into account, the non-linear behavior of the thermal contraction coefficient and the relative length scale shown in Fig. 4.10, 4.11 can be linearized to the values given in Tab. 4.4. The expansion coefficients for the poles and magnets were measured by cooling the materials down from 293 K to 73 K [5]. Due to the manufacturing process, the magnets have a different contraction coefficient for the direction parallel to the undulator (z axis) and perpendicular (x/y axis) to it.

Material	α [10^{-6}/K]	Δ L/L [10^{-3}]
Poles	-7.0	-1.54
Magnets $\parallel$	-3.5	-0.77
Magnets $\perp$	-1.5	-0.33
Stainless Steel	-12.96	-2.8
Aluminum	-18.0	-3.89
Titan	-7.52	-1.62
Copper	-14.09	-3.04

Table 4.4 – Linearized thermal expansion coefficients for the in-vacuum materials of Tab. 4.3 for a temperature difference between room temperature 293 K and the design temperature of 77 K. The data for the poles and magnets was provided by [5], all others are taken from [7].

For the design of the support structure the Young's modulus of the aluminum and stainless steel is of major importance, which will increase with decreasing temperature, leading to a stiffer and more robust support structure, see Fig. 4.11.

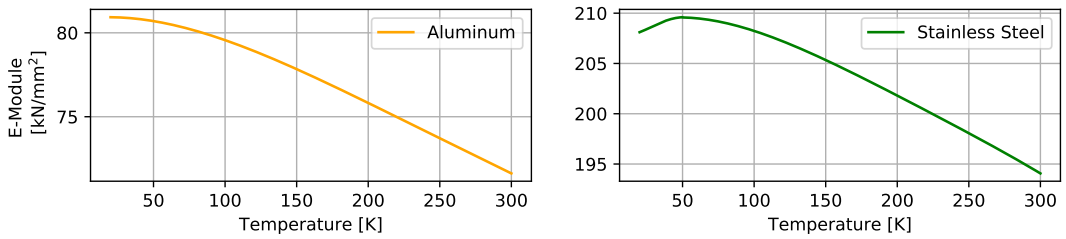

Figure 4.11 – Young's modulus for the used aluminum and stainless steel alloys [7].

Material	E-mod (293 K) [kN/mm^2]	E-mod (77 K) [kN/mm^2]
Stainless Steel	194.66	209.12
Aluminum	71.91	80.18
Titan	114	–
Magnets	155	–

Table 4.5 – E-Modulus for the aluminum and stainless steel of Tab. 4.3 for a temperature difference between room temperature 293 K and the design temperature of 77 K. Data taken from [7], Titan data from [14], Magnets data from [15].

This is beneficial as also the acting magnetic forces will increase with lower temperature. For a conservative design the E-module at room temperature is taken into account to create a safety factor of $\approx 7\%$ for the aluminum bending and $\approx 11\%$ for the stainless steel calculations. Doing so will yield to a slight overestimation of the bending in the cold state.

4.3.3 Thermal Conductivity

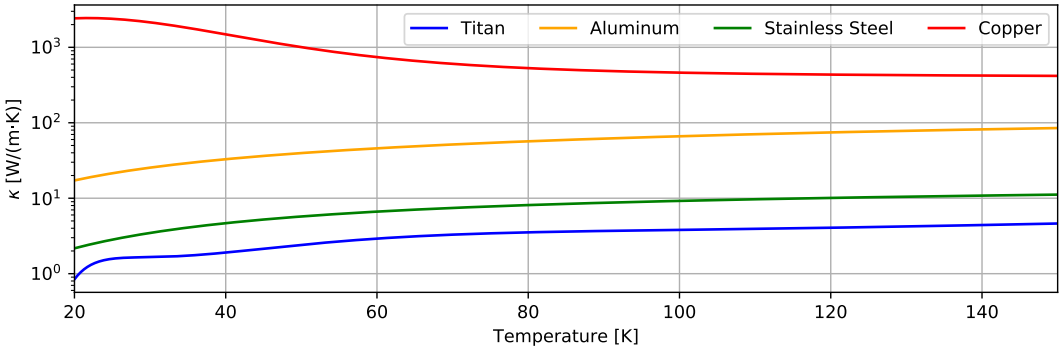

Figure 4.12 – Thermal conductivity k for the used materials [7].

To estimate the steady state temperature the heat load into the system has to be known, which depends on the thermal conductivity k of the materials. As the thermal resistance scales with $\propto 1/k$ a high conductivity is desired for the cold head and its copper connector to the girders, whereas the pillars should have a low conductivity to act thermally insulating. The thermal conductivities are plotted in Fig. 4.12 with data from [7]. For aluminum and stainless steel the functions for the curves above are given as [7]

$$\begin{aligned}\log k(\mathrm{T}) =& \mathrm{a} + \mathrm{b}(\log \mathrm{T}) + \mathrm{c}(\log \mathrm{T})^2 + \mathrm{d}(\log \mathrm{T})^3 + \mathrm{e}(\log \mathrm{T})^4 \\ &+ \mathrm{f}(\log \mathrm{T})^5 + \mathrm{g}(\log \mathrm{T})^6 + \mathrm{h}(\log \mathrm{T})^7 + \mathrm{i}(\log \mathrm{T})^8\end{aligned}$$

and for copper[7]

$$\log k(\mathrm{T}) = 10(\mathrm{a} + \mathrm{cT}^{0.5} + \mathrm{eT} + \mathrm{gT}^{1.5} + \mathrm{iT}^2)/(1 + \mathrm{bT}^{0.5} + \mathrm{dT} + \mathrm{fT}^{1.5} + \mathrm{hT}^2)$$

with the fit parameters

	Range[K]	a	b	c	d
Aluminum	4-300	-0.90933	5.751	-11.112	13.612
Stainless steel	1-300	-1.4087	1.3982	0.2543	-0.6260
Copper	4-300	2.2154	-0.47461	-0.88068	0.13871
	e	f	g	h	i
Aluminum	-9.3977	3.6873	-0.77295	0.067336	0
Stainless steel	0.2334	0.4256	-0.4658	0.1650	-0.0199
Copper	0.29505	-0.02043	-0.04831	0.001281	0.003207

4.3.4 Operating Temperature

At room temperature, mechanical errors and magnetic deviations inside the undulator can easily be compensated by tuning the poles in position, as long as the deviations are not to strong. In contrast to this is the influence of temperature gradients inside the undulator which occurs after the cooling. Those gradients will distort the electron beam trajectories between warm and cold state and cause two main issues for the design:

1. The magnets are temperature sensitive, so a thermal gradient will cause a magnetization gradient along the girder which will shift the phase error between the warm and cool state, which was demonstrated with a prototype, see [65].
2. The thermal contraction of the materials is also temperature sensitive and a the thermal gradient will lead to a mechanical gradient along the gap which will exponentially affect the undulator peak field.

So, the impact of a thermal gradient will lead to magnetic and mechanic gradients along the machine, which will deform the on axis undulator field and cause a systematic change in the phase integral which manifests in a phase advance compared to a state without gradients. Both cases and their impact onto the phase integral will be discussed here. As a figure of merit a phase advance of $\approx 5°$ is plotted as a reference, which corresponds to a intensity reduction of 1%. This is an acceptable change, as it is typically below the statistical phase errors which can be achieved by tuning the magnetic field. Also one has to mention here, that the phase advance has to be interpreted as a systematical error and has a different impact onto the emitted radiation than statistical errors. A discussion about the handling of the phase advance is at the end of Sec. 4.4.7. Nevertheless, for the design it is important to know and minimize the impact of systematic errors onto the performance.

Temperature Gradient

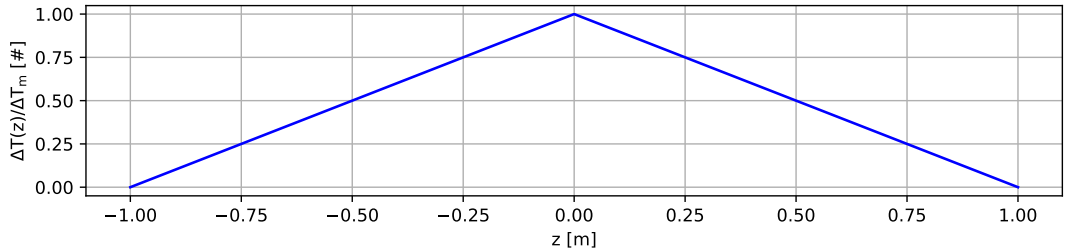

Figure 4.13 – Relative temperature change along the girder with heat sinks at the ends.

Frosty will operate in a small tunnel without an integrated cooling line. For personal safety, cold heads with a fixed coolant volume have to be used, which are mounted at the ends of each girder, see Fig. 4.46. From this geometry the heat will flow from warm to cold, so from the center towards the ends and a thermal gradient $G_T = \Delta T/\Delta L > 0$ will arise with a maximum temperature at the center of the undulator, so at $z = 0$ and minima at the girder ends $z \approx \pm 1\,m$. This behavior follows a triangular function with the maximum temperature change $\Delta T_m = G_T$ at the center of the undulator, see Fig. 4.13:

$$\Delta T(z) = \Delta T_m - G_T|z|. \tag{4.2}$$

Magnetization Gradient

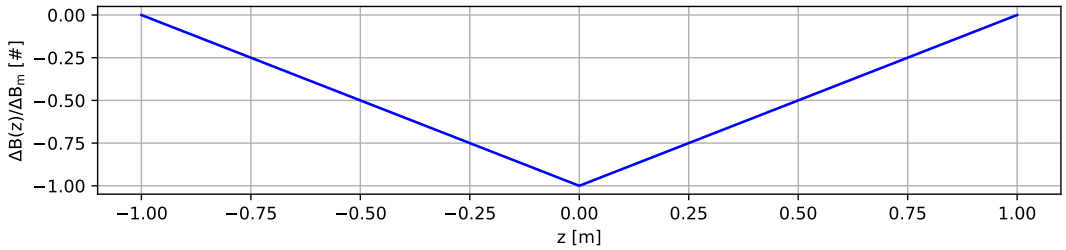

Figure 4.14 – Relative magnetic field change due to a temperature gradient along the girder.

Due to the temperature dependent magnetization, the thermal gradient causes a magnetic gradient, as indicated in Fig. 4.3. Here, the magnetic field decreases with increasing temperature, so with a negative gradient $G_B = \Delta B/\Delta T < 0$ in units of [T/K]. Combining this gradient with the positive temperature gradient G_T leads to the magnetic gradient $G = G_B \cdot G_T < 0$ in units of [T/m] along the girder which is also represented with a triangular function, see Fig. 4.14:

$$\Delta B(z) = \Delta B_m - G|z|$$

with $\Delta B_m = G < 0$. This linear field variation leads to an additional term of the sinusoidal undulator field:

$$B_{err}(z) = (B_0 + \Delta B(z)) \sin(k_u \cdot z) = (B_0 + \Delta B_m) \sin(k_u \cdot z) - G|z| \sin(k_u \cdot z) \tag{4.3}$$

The change of the field amplitude does change the second and first field integrals in a similar way. That means, that the amplitudes of the field integrals also increase and decrease linear according to the magnetic field amplitude variation. This is in contrast to the phase integral which depends quadratically on the first field integral, see Eq. 2.5. The impact onto the phase error will not vanish over the whole machine.

To estimate the impact, the first integral has to be evaluated. To easier analyze the field, the change of sign due to |z| is shifted to G like G·|z|=(s(z)· G)·z:

$$J_1(z) = -\frac{(B_0 + B_m)\cos(k_u z)}{k_u} + s(z) \cdot G \left(\frac{z\cos(k_u z)}{k_u} - \frac{\sin(k_u z)}{k_u^2} \right) \tag{4.4}$$

Evaluating the phase integral $J_{ph} = \int J_1^2 dz$ will lead to a complex expression which is split up into three terms for a better readability:

$$T_1 = \frac{(B_0 + B_m)^2(2k_u z + \sin(2k_u z))}{4k_u^3}$$

For B_m=0 this term is the standard result for the phase integral without a heat gradient and only changes the amplitude but does not affect the shape.

$$T_2 = -\frac{s(z) \cdot G}{4k_u^4} \left[(B_0 + B_m)(2k_u z(k_u z + \sin(2k_u z)) + 3\cos(2k_u z))\right]$$

The amplitude of T_2 is proportional to $s(z)G/k_u^2$ and still has the sign dependency from the absolute value |z|. So, this term will change the shape along the integral.

$$T_3 = \frac{G^2}{24k_u^5} \left[3\left(2k_u^2 z^2 - 5\right)\sin(2k_u z) + 2k_u z\left(2k_u^2 z^2 + 9\cos(2k_u z) + 6\right)\right]$$

The sign dependency vanishes again due to the square of $(s(z)G)^2$=G^2. This term will also only cause a shift of the amplitude.
The temperature gradient G_T is expected to be in the range of -10^2 K/m and the magnetic gradient G_B in the range of 10^{-5} T/K, when the ambient temperature is below 77 K, see Fig. 4.3. Following from this, G would be in the range of -10^{-3} T/m. As the amplitude of T_3 scales with G^2/k_u^2 its effect would be in the 0.1% range of T_2 and would only have an impact for high gradients. From the phase integral the radiation phase Φ_n from Eq. 6.2 will be calculated as

$$\Phi_n(z,G) = \frac{k_u}{1 + \frac{K_0^2}{2}} \left(z + \left(\frac{e}{m_0 \cdot c} \right)^2 \cdot (T_1 + T_2 + T_3) \right)$$

The resulting phase advance is then the difference to the ideal case

$$\Phi_{MAG}(z,G) = \Phi_n(z,G) - \Phi_n(z,0) \tag{4.5}$$

An example how a thermal gradient impacts the field shape and the phase is shown in Fig. 4.15. For the simulation a magnetic gradient of -1 mT/m was assumed with a peak field of B_0=1.838 T at 2 mm gap and an ambient temperature of 77 K. The first plot shows the linear field gradient along the device calculated in Eq. 4.3.

As discussed, the shape variation of the magnetic field amplitude (first plot of Fig. 4.15) is directly translated to the field integrals see second plot of Fig. 4.15, where Eq. 4.4 is shown. The last plot shows the influence onto the phase error of Eq. 4.5, which does not vanish over the machine and already reaches 20° for a magnetic gradient of -1 mT/m. A thermal gradient with a higher temperature in the undulator center and lower temperature at the girder ends will induce a positive phase error along the machine.

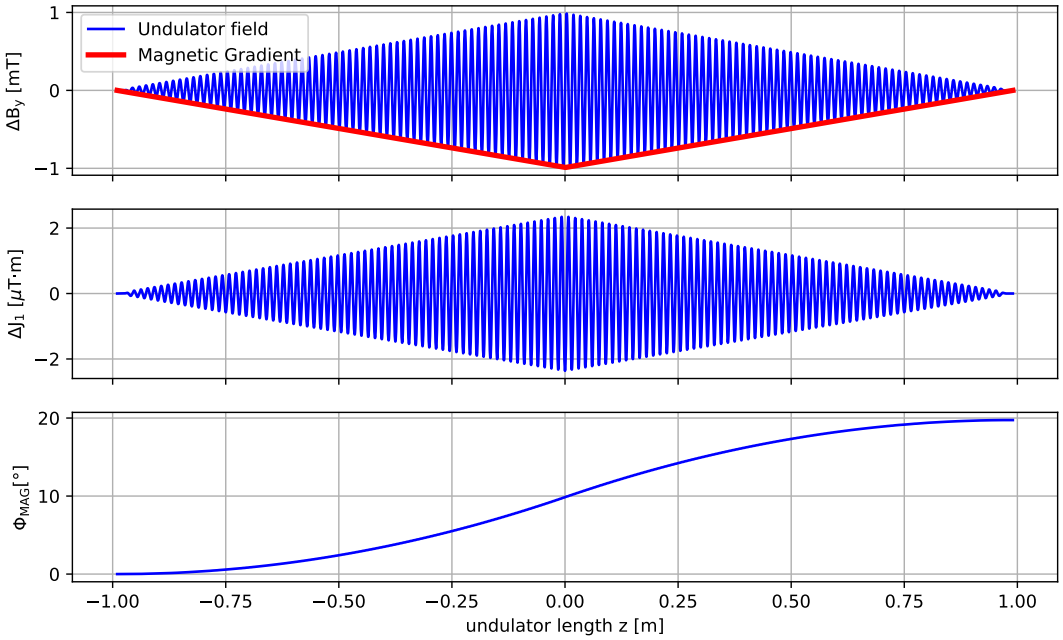

Figure 4.15 – Influence of a gradient of - 1 mT/m onto the magnetic field, the first field integral and the phase advance.

Fig. 4.16 shows the phase advance for different gaps and magnetic gradients. To keep the phase error below 5° the gradient G has to stay below - 240 μT/m. For an average temperature below 77 K, the magnetic gradient is G_B = -13.7 μT/m, which would give a maximum temperature gradient of $G_T = G/G_B$ = 17.3 K/m.

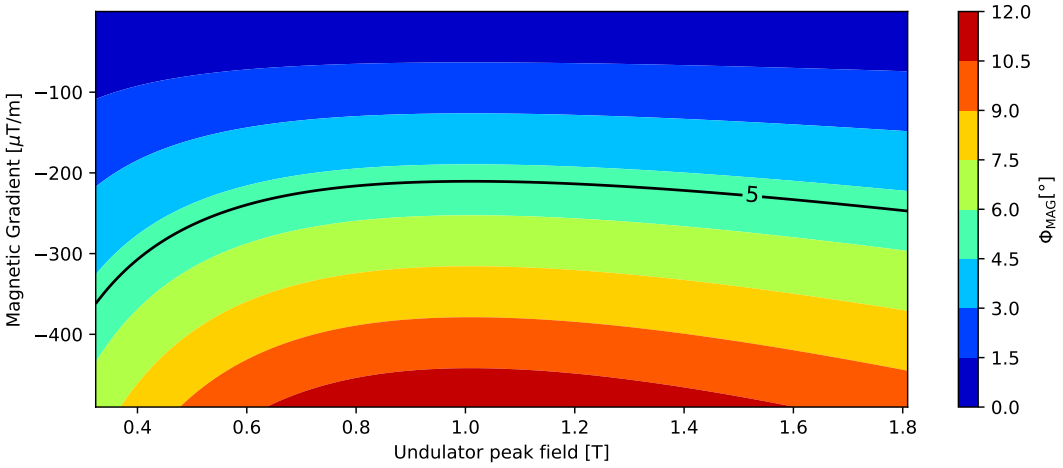

Figure 4.16 – Change of the phase advance with a variable magnetic gradient G.

Mechanical Gradient

Due to the cooling process the whole undulator structure will contract. As the girders are mounted on pillars which are connected to the out-of-vacuum frame, also those will change their length according to the temperature difference between the out-of-vacuum connection and the cryo cooled girder. So, the thermal gradient described in Eq. 4.2 will not only affect the remanence of the magnets but also cause a different thermal contraction of the individual pillars which, in turn, will directly lead to mechanical gradients along the girder. To estimate the impact onto the gap the distance between the gap and the out-of-vacuum connectors has to be known.
The two relevant parameters here are the pillar length d_p with the thermal expansion coefficient α_p and the distance between the gap-sided surface of the aluminum girder and the pillar connection inside the bayonet lock called d_{al} with α_{al}, see Sec. 4.4.5 and Sec. 4.4.2. Combining both will lead to a maximum variation of a single girder of dy=$(d_{al} \cdot \alpha_{al} + d_p \cdot \alpha_p)$. Now one have to pay attention: The maximum girder deformation dy is reached in the center of the undulator, as the girder is warmer in this region which leads to longer pillars. This means, that the gap between both girders at the center is reduced about a factor of -2·dy, which results in a gap variation of -2dyΔT(z) with the temperature gradient of Eq. 4.2 and is expressed as

$$\Delta g(z) = \Delta g_m - g_T \cdot |z|. \tag{4.6}$$

$g_T = -2 \cdot dy \cdot G_T$ is the thermal expansion gradient in units of m/m, so expanded height per undulator length with the maximum of $\Delta g_m = g_T$ at the center.

According to Eq. 4.1 this linear gap change will cause an exponential field change of the on-axis undulator field:

$$\mathrm{B(z,g,g_T)} = \mathrm{a} \cdot \mathrm{Exp}\left(\mathrm{b} \cdot \frac{\mathrm{g}}{\lambda_\mathrm{u}}\left(1 + \frac{\Delta\mathrm{g(z)}}{\mathrm{g}}\right) + \mathrm{c} \cdot \frac{\mathrm{g}^2}{\lambda_\mathrm{u}^2}\left(1 + \frac{\Delta\mathrm{g(z)}}{\mathrm{g}}\right)^2\right) \tag{4.7}$$

Δg(z) describes the material expansion due to a heat gradient. Looking onto Tab. 4.4 the thermal expansion coefficients for the aluminum girder per degree is $\alpha_\mathrm{al} \approx 24$ μm/(m $\cdot$ K) and for stainless steel $\alpha_\mathrm{p} \approx 13.4$ μm/(m $\cdot$ K). Assuming a contracted length of 0.2 m for both materials and using the defined upper limit for the heat gradient, which was calculated before to be $\mathrm{G_T} \approx 17\,\mathrm{K/m}$, one can estimate that $\mathrm{g_T} < -2(\alpha_\mathrm{p} + \alpha_\mathrm{al}) \cdot 0.2\ \mathrm{m} \cdot \mathrm{G_T} \approx -0.3$ mm/m. So, the maximum value for Δg(z), $\Delta\mathrm{g_m} = \mathrm{g_T}|\mathrm{z}|_{\mathrm{z=center}}$ can be estimated to be ≈ -0.3 mm. Following from this, and assuming a g = 3 mm nominal gap, the contribution of the $(\Delta\mathrm{g(z)/g})^2$ term is then roughly 5% of the $2 \cdot \Delta\mathrm{g(z)/g}$ term and will be neglected in Eq. 4.7. Eq. 4.6 can now be inserted and the exponent can be rearranged into an easier expression:

$$\ln\left(\frac{\mathrm{B(z,g,g_T)}}{\mathrm{a}}\right) =: \mathrm{c_1} + \mathrm{c_2} - |\mathrm{z}| \cdot \mathrm{c_3}$$

with the constants:

$$\begin{aligned}
\mathrm{c_1} &= \mathrm{b} \cdot \frac{\mathrm{g}}{\lambda_\mathrm{u}} + \mathrm{c} \cdot \left(\frac{\mathrm{g}}{\lambda_\mathrm{u}}\right)^2 \\
\mathrm{c_2} &= \frac{\Delta\mathrm{g_m}}{\mathrm{g}}\left(\mathrm{b} \cdot \frac{\mathrm{g}}{\lambda_\mathrm{u}} + 2 \cdot \mathrm{c} \cdot \frac{\mathrm{g}^2}{\lambda_\mathrm{u}^2}\right) \\
\mathrm{c_3} &= \frac{\mathrm{g_T}}{\mathrm{g}}\left(\mathrm{b} \cdot \frac{\mathrm{g}}{\lambda_\mathrm{u}} + 2 \cdot \mathrm{c} \cdot \frac{\mathrm{g}^2}{\lambda_\mathrm{u}^2}\right)
\end{aligned}$$

$\mathrm{c_1}$ describes the expression of an undisturbed undulator peak field amplitude $\mathrm{B_0(g)}$, see Eq. 4.1, so the exponential function of Eq. 4.7 can now be re-written as

$$\mathrm{B(z,g,g_T)} \approx \mathrm{a} \cdot e^{\mathrm{c_1}+\mathrm{c_2}-|\mathrm{z}|\cdot\mathrm{c_3}} = \mathrm{B_0(g)} \cdot e^{\mathrm{c_2}} \cdot \mathrm{e}^{-|\mathrm{z}|\cdot\mathrm{c_3}}. \tag{4.8}$$

The resulting variable undulator field $\mathrm{B(z,g,g_T)} \cdot \sin(\mathrm{k_u} \cdot \mathrm{z})$ can now be integrated to calculate the first field integral. Because of the absolute value |z| in the exponent, a case-by case integration for the region of $\mathrm{z} \leq 0$ and $\mathrm{z} > 0$ will be done (z=0 is the longitudinal center of the undulator, see Fig. 4.13):

$$\mathrm{J_1(z,g,g_T)} = \frac{\mathrm{B_0(g)} \cdot e^{\mathrm{c_2}}}{\mathrm{c_3^2} + \mathrm{k_u^2}} \cdot \begin{cases} e^{\mathrm{c_3 z}}(\mathrm{c_3}\sin(\mathrm{k_u z}) - \mathrm{k_u}\cos(\mathrm{k_u} \cdot \mathrm{z})) & \mathrm{z} \leq 0 \\ -e^{-\mathrm{c_3 z}}(\mathrm{c_3}\sin(\mathrm{k_u z}) + \mathrm{k_u}\cos(\mathrm{k_u} \cdot \mathrm{z})) & \mathrm{z} < 0 \end{cases}$$

From the first field integral the phase integral is evaluated to be:

$$\begin{aligned}
\mathrm{J_{ph_1}}(\mathrm{z} \leq 0, \mathrm{g}, \mathrm{g_T}) = \frac{\mathrm{B_0(g)}^2 \cdot e^{2\mathrm{c_2}} e^{2\mathrm{c_3 z}}}{4\mathrm{c_3}\left(\mathrm{c_3^2} + \mathrm{k_u^2}\right)^3} \Big(& \left(\mathrm{c_3^2} + \mathrm{k_u^2}\right)^2 \\
& - \mathrm{c_3^2}\left(\mathrm{c_3^2} - 3\mathrm{k_u^2}\right)\cos(2\mathrm{k_u z}) + \mathrm{c_3 k_u}\left(\mathrm{k_u^2} - 3\mathrm{c_3^2}\right)\sin(2\mathrm{k_u z})\Big) \\
\mathrm{J_{ph_2}}(\mathrm{z} > 0, \mathrm{g}, \mathrm{g_T}) = \frac{\mathrm{B_0(g)}^2 \cdot e^{2\mathrm{c_2}} e^{-2\mathrm{c_3 z}}}{4\mathrm{c_3}\left(\mathrm{c_3^2} + \mathrm{k_u^2}\right)^3} \Big(& - \left(\mathrm{c_3^2} + \mathrm{k_u^2}\right)^2 \\
& + \mathrm{c_3^2}\left(\mathrm{c_3^2} - 3\mathrm{k_u^2}\right)\cos(2\mathrm{k_u z}) + \mathrm{c_3 k_u}\left(\mathrm{k_u^2} - 3\mathrm{c_3^2}\right)\sin(2\mathrm{k_u z})\Big)
\end{aligned}$$

The integration constants, which were not discussed in the equations before, have to be chosen such, that $\mathrm{J_{ph_1}}(-1, \mathrm{g}, \mathrm{g_T}) = 0$ and $\mathrm{J_{ph_2}}(0, \mathrm{g}, \mathrm{g_T}) = \mathrm{J_{ph_1}}(0, \mathrm{g}, \mathrm{g_T})$. From the phase integral the phase can than be calculated using

$$\Phi(\mathrm{z}, \mathrm{g}, \mathrm{g_T})_n = \frac{\mathrm{k_u}}{1 + \frac{\mathrm{K_0^2}}{2}} \left(\mathrm{z} + \left(\frac{\mathrm{e}}{\mathrm{m_0 \cdot c}} \right)^2 \cdot \mathrm{J_{ph}}(|\mathrm{z}|, \mathrm{g}, \mathrm{g_T}) \right)$$

and the resulting phase advance is again the difference to the ideal case

$$\Phi_{\mathrm{MEC}}(\mathrm{z}, \mathrm{g}, \mathrm{g_T})_n = \Phi(\mathrm{z}, \mathrm{g}, \mathrm{g_T})_n - \Phi(\mathrm{z}, \mathrm{g}, 0)_n. \tag{4.9}$$

To evaluate the equation above, the assumption was done that quadratic influences in the exponent are negligible. So, in a first cross check the phase error is numerically calculated by integrating Eq. 4.7 directly over the parameter space of interest and comparing it to the results of Eq. 4.9 which is plotted in Fig. 4.17. The error increases for higher gradients and higher gaps because the neglected term $(\Delta \mathrm{g(z)}/\mathrm{g})^2$ increases into this direction and will have a higher contribution. As the gradient should be kept low and the relative gap deformation would have a higher impact for the interesting gaps below 5 mm one can state, that the approximation is valid and that the error of $< 1\%$ is acceptable for the analytical expression.

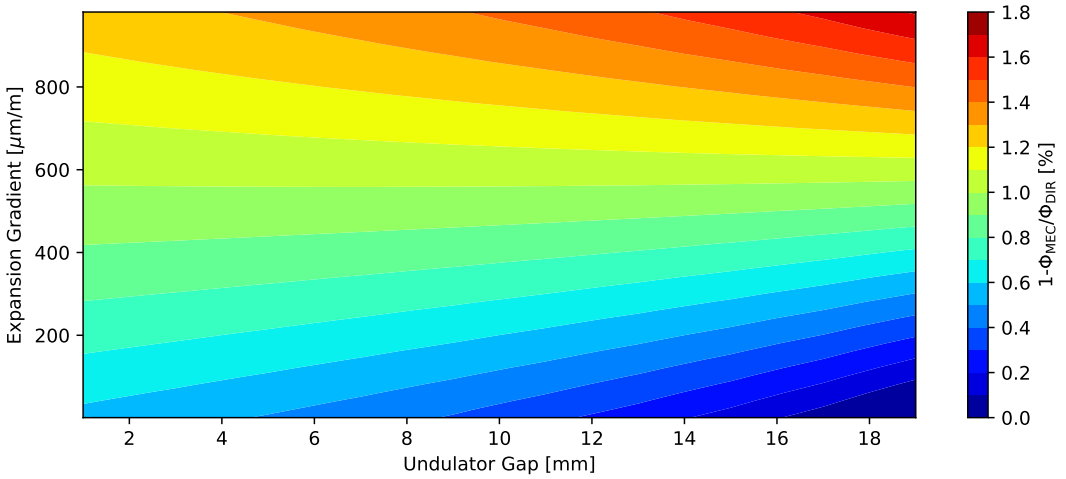

Figure 4.17 – Error of the phase advance calculation using a numerical method for direct integration of Eq. 4.7, denoted as Φ_{DIR}, and the approximated analytical expression Φ_{MEC} from Eq. 4.9.

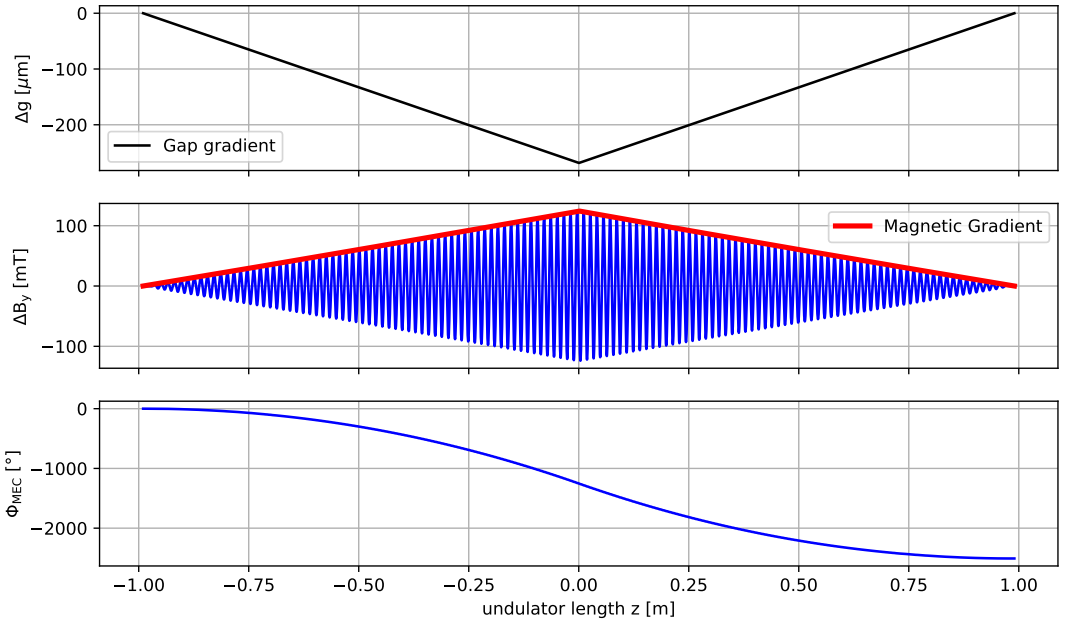

Figure 4.18 – Induced phase advance for a thermal gradient of 17 K/m and the resulting gap variation along the girder with a nominal gap of 2 mm.

Fig. 4.18 shows Eq. 4.6 for the prior estimated expansion gradient of $g_T \approx$ -0.3 mm/m with a nominal gap of 2 mm at 77 K. The decreasing gap causes a field increase of the on-axis undulator field according to Eq. 4.8 up to 150 mT in the center.

Due to this change, the phase advance of Eq. 4.9 is in the range of two thousands of degrees between the warm and cold state which is plotted in the last picture.

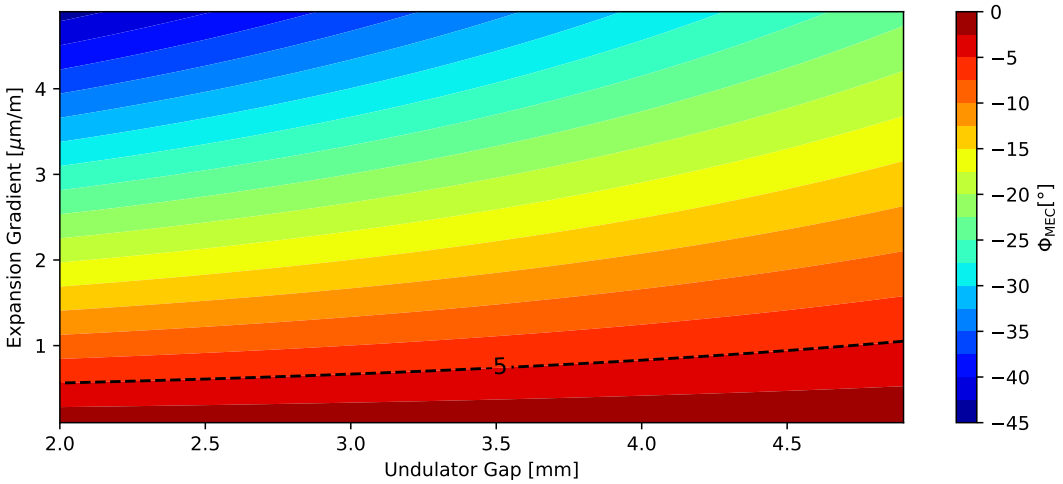

Figure 4.19 – Generated phase advance due to a thermal gradient and the following mechanical deformation of the undulator.

In Fig. 4.19 the gap dependent phase error of Eq. 4.9 for different expansion gradients g_T is shown. The color bar indicates the phase advance between the warm and the cold state. For the design gap of 2 mm the maximum expansion gradient has to stay below $\Delta g_m < 0.6\ \mu m/m$ to not increase the phase error about more than -5°. At the beginning of this sub chapter the expression $g_T < 2(\alpha_p + \alpha_{al}) \cdot 0.2m \cdot G_T$ was used to estimate an upper limit for g_T from the upper temperature gradient limit G_T. The limit for G_T was chosen such, that the heat induced magnetic field degradation does not introduce a phase advance above 5°. By rearranging the mentioned expression into $G_T < \Delta g_m/(2(\alpha_p + \alpha_{al}) \cdot 0.2\ m)$, an upper limit for the temperature gradient is estimated to be 80 mK/m. With this temperature gradient, the gap deformation would lead to a phase advance of -5°. This limit is now orders of magnitudes small than the estimated 17 K/m for the magnetic gradient change.
For the Frosty cooling system, which consists out of two cold heads mounted at the ends of the girders, it is impossible to cryo-cool the undulator and to hold the temperature gradient below the estimated threshold of 80 mK/m. As mentioned, the phase advance is not a statistical fluctuation but a systematical error, which means it can be compensated. To get the phase advance into a reasonable limit the magnetic field can either be shimmed at room temperature with the inverse mechanical gradient, which is then canceled out by the cooling, or shimmed in the cryo state by changing the pillar lengths according to the local gap deviation.

4.3.5 Manufacturing Tolerances

The main core of the undulator is the magnetic array inside the girders which defines the physical behavior of the machine and is, therefore, a central aspect for the design. Following from that, the geometrical and magnetic characteristics of the magnets and poles have to be known. The lead time of the magnets depends on the specified tolerances onto the geometry and the magnetic field and is typically on the half a year to year scale. So, the magnets were ordered in an early stage of the project when the magnetic field simulations where completed. This gave the advantage to take their manufacturing tolerances into account while designing the girder structure.
To produce the magnets, a grain powder is filled into a casting mold and heated to 800 degrees under high pressure. An external magnetic field is applied to the magnets while they are cooled down again to room temperature. Subsequent, a grain boundary diffusion treating is applied to the magnets which increases the coercitivity of the magnet's surface. In a final step the magnets are coated with a 2 - 3 μm thick Titanium nitride (TiN) layer. This layer prevents out gassing of the materials inside the magnets while they are in a vacuum environment and the coating also eases the handling of the magnets during installation. From the 700 delivered magnets 91 ($\approx$ 13%) were measured at 293 K to get the average dimensions and their deviations which are listed in Tab. 4.6. On average, the produced magnets are smaller than the design values, but their deviations stay within a $\pm\,5\,\mu$m range in each dimension which would cause a maximum change in the magnetic volume below 0.2%, which is acceptable. The maximum length deviations are below or equal to the design values in height and thickness. The maximum width is $4\,\mu$m over the design value. The structure has to be several $50\,\mu$m to $100\,\mu$m bigger than the magnet dimensions to ensure an easy installation. Therefore, the 4 μm maximum offset of the magnets is negligible.

	Width (x)	Height (y)	Thickness (z)	Unit
Mean	17.993	20.994	3.686	mm
Std	0.005	0.004	0.005	mm
Min	17.980	20.977	3.675	mm
Max	18.004	21.000	3.694	mm
Design	18.000	21.000	3.700	mm
Design-Mean	-7.0	-6.32	-14.14	μm

Table 4.6 – Sample analysis of the ordered magnets.

The magnets were specified to have an absolute accuracy of the main component up to 0.3% from the mean and the orientation errors have to stay below 0.3°. All magnets were measured and the deviation is plotted in Fig. 4.20.

The relative error is 0.22%, which means that the generated amplitudes in the undulator would also stray about 0.22%. This is compensated by changing the positions of the poles inside the magnetic array to get the field integrals flat.

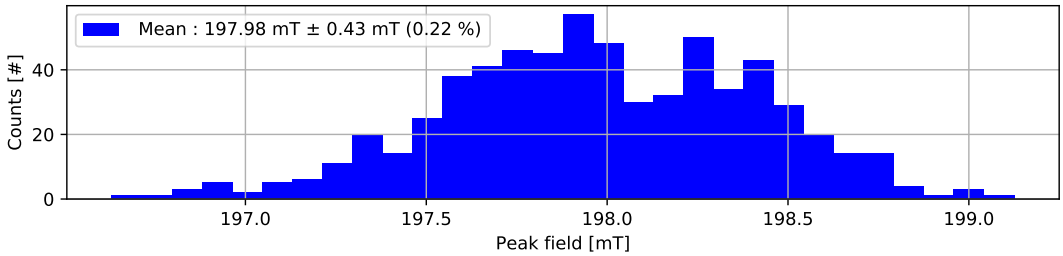

Figure 4.20 – Measured open remanence fields of all permanent magnets.

The poles will be heat treated after the manufacturing to optimize their magnetic properties. Remaining geometrical deviations were reduced with a proper surface grinding of the materials. So, their dimensions are close to the design, see Tab. 4.7.

	Width (x)	Height (y)	Thickness (z)	Unit
Min	11.985	17.98	3.55	mm
Mean	12.000	18.00	3.58	mm
Max	12.015	18.02	3.60	mm
Design	12.000	18.00	3.60	mm
Design-Mean	0	0	-2	μm

Table 4.7 – Measured tolerances of the ordered poles.

Manufacturing Tolerances for the Support Structure

Besides the errors in the peak field also geometrical errors in the longitudinal positioning of the magnets have an influence onto the generated field. If the comb structure in the upper and the lower girder are shifted the on-axis field would not be parallel to the vertical axis but tilted. If the periodicity along the magnetic array differs, also the emitted wavelength would differ. For the design it is important to keep the undulator period as constant as possible. Their error influence can also be compensated by tuning the poles but only within a certain limit. The periodicity should be kept constant with a maximum error of one tenth of the design peak field deviation, so 0.03 %. For a period length of 15.08 mm this means a standard deviation of 4.5 μm which is challenging to manufacture and to measure.
The comb structures are mounted onto one 2 m long aluminum girder which also acts as a mechanical stop for the magnet installation to have them all on the same level.

When the combs are mounted on both sides of the girder they form a case in which the magnets will be mounted. Surface deviations of the girder will cause a global vertical shift of the magnets in several periods which will distort the generated on-axis field in the undulator. Due to the manufacturing tolerances of the magnet's height this effect will already occur locally within the undulator period. As the standard deviation of their height is ≈ 5 μm a maximum offset above ≈ 10 μm within one undulator period is possible. This limit should not be exceeded by the surface deviation of the girder, so the surface should stay flat about 10 μm over the 2 m length. Keeping an accuracy of 10 μm over a two meter long device is an enormous task on its own which is also hardly measurable with coordinate measuring machines as these required tolerances are close to, or below the accuracy limits of those machines.
Aluminum is a comparably soft metal and threads inside it would be worn out after a screw is tightened the fourth or fifth time in it. The adjustment screws of the poles have to be moved and tightened some orders of magnitudes more than that and it is more than likely that the undulator has to be re-adjusted several times within the next ten to twenty years of operation. To increase the lifetime of the threads additional thread inlets out of a strong copper alloy are inserted into every thread inside the vacuum system without exception. Those inlets have a reduced wear and can easily be exchanged in case they are worn out.

4.3.6 Forces

In the cryo state poles get attracted with ≈ 100 N at 2 mm gap, see Fig. 4.9. The pole hanging has to be designed such, that the forces can be forwarded into the girder structure without deforming or bursting the brittle pole material, or deform the adjustment screws. The acting forces onto the magnets are pointing towards the girder until a gap of 1.8 mm is reached, below which the magnets are dragged towards the undulator axis with a force below 10 N. The magnets need to be fixed to not drop out of the structure.
In total a force of 24 kN is acting on each girder which will cause them to bend towards each other. This effect has to be minimized by a suitable thickness of the girders.

4.3.7 Geometrical Constrains

For the tuning it is relevant that the measurement setup fits into the gap when the machine is closed to the design gap of 2 mm. Following from that, the gap has to accessible from the side. To tune the magnetic field the poles have to be shifted and or rotated in position. To do so, also the adjustment screws have to be accessible at minimum gap to perform a real time tuning of the individual poles. As the magnetic pointing strays up to 0.3° (5 mrad), also the poles need enough space to be rotated

about the same angle. The rotation center of the poles is 11 mm below their surface which shows towards the gap. Following from that, the poles need an additional horizontal space above 60 μm to compensate the rotation. This number has to be hold in the cryo state.
Due to the cooling the girders will shrink in length about 1 cm which would create torques onto the pillars which connect the cryo undulator with the warm frame and could lead to a burst of those pillars. To prevent this, the pillars have to be mounted on sliders to also change their longitudinal position according to the length of the girders. As these in-vacuum pillars will also be cooled and shrink due to that, the security and gap measurement systems of the undulator frame have to hold for both temperature states.
In contrast to conventional undulators with some 3 - 4 meters in height, the Frosty frame has to fit in the accelerator tunnel with 2.2 meters in height and 2 meters in width.
Last but not least, the design should be effective in terms of purpose, lead time and manufacturing cost and it has to be possible to assemble the designed components.

4.4 Mechanical Design

The mechanical design for Frosty follows the considerations presented in Sec. 4.3, where the main focus lies on the contraction of all materials due to the cooling. So, the design criteria are applied to the cold state and then derived for the warm state. For the undulator it is important to restrict the bending due to the 24 kN acting onto the girder within a low micro meter range which can only be achieved by an accurate mechanical design of the support structure. This bending is inverse proportional to the material specific elasticity modulus, called Young's modulus E or simply E-modulus, and the area moment of inertia I (also known as second moment of area) which describes the geometrical resistance against an acting torque. Assuming a rectangular cross section, vertical height h and horizontal width b, the second moment is $I = \frac{b \cdot h^3}{12}$ [16]. For Frosty, three bending types are of major importance, which are pictured in Fig. 4.21. A cantilever beam with the force concentrated at the free end (left side) which is fixed on the other end, a uniformly distributed load $\omega = F/l$ (center) and a beam fixed on both ends with a uniformly distributed load on the right. The maximum deflection of the three shown setups are given in Tab. 4.8.

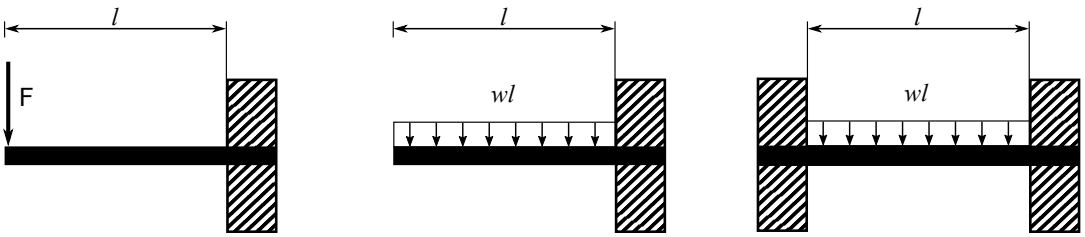

Figure 4.21 – Bending types used to estimate deformations in the Frosty design.

Type	Maximum Deflection	Δ_{max}
Cantilever Beam - Concentrated Load	at free end	$Fl^3/(3EI)$
Cantilever Beam - Uniform Load	at free end	$\omega l^4/(8EI)$
Fixed Beam - Uniform Load	at center	$\omega l^4/(384EI)$

Table 4.8 – Maximum Deflections for the three setups with the force per unit length ω [16].

4.4.1 Undulator Period

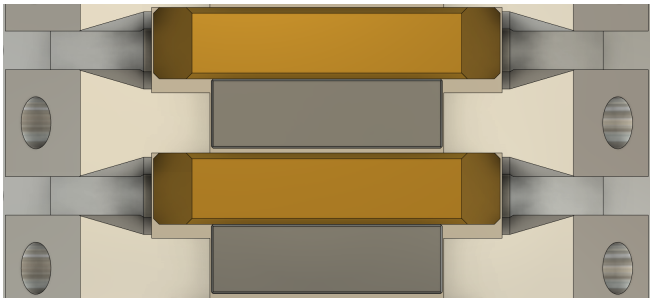

Figure 4.22 – Top view onto the girder with the magnets in yellow and the poles in dark gray. They are kept in position with the comb structure on the left and right.

The comb structure forms a periodic letter case and defines the geometrical period length. A top view onto this letter case can be seen in Fig. 4.22. The comb structure is colored in light grey, the magnets in golden and the poles in dark grey.

Horizontal Dimensioning

For the installation of the magnets and the poles the comb dimensions have to be some 100 μm wider than the pole and magnet dimensions, otherwise the components could block during the installation. To rotate the poles about the maximum specified angle deviation the minimum increase should be 50 μm in the cold state on both sides, leading to 100 μm in total. Cold, the poles have an average width of 11.98 mm,

leading to a desired bag width of 12.08 mm. Warmed up, this results in 12.145 mm which is rounded to 12.14 mm for easier manufacturing, which again would result in an acceptable 94 μm play for the poles in the cold state.
The magnets should have a play of 50 μm on each side in the cold state, leading to an increase of 100 μm. The cold magnet width is 17.994 mm leading to a cold bag width of 18.094 mm, which is 18.190 mm warmed up. This quantity is also rounded for easier manufacturing to 18.2 mm in the warm state, which results in a play if 110 μm in cold for the magnets.

Longitudinal Dimensioning

In the longitudinal direction the undulator period shrinks about 80 μm from warm to cold, leading to a design period length of 15.00 mm. Crucial here is the different expansion coefficient between the aluminum ($5.28 \cdot 10^{-3}$) comb and the magnets ($0.77 \cdot 10^{-3}$), see Tab. 4.4. A clamping of the magnets with the combs could cause a burst of the magnets. Besides that, a bigger gap eases the installation of the magnets as they will be pushed away from the already installed magnets. So, for the purpose of an easier installation, the dimension was set to 4.4 mm in the warm state which is 4.376 mm cold.

Suspension Dimensioning for the Magnets

Figure 4.23 – Front view onto one magnet mounted in the girder.

In Fig. 4.23 one can see a single magnet mounted in the comb structure. The magnet sits on the girder (lower dark grey box) and is kept in position by two clamps from the sides which are mounted under a 55° angle with respect to the girder plane, the horizontal axis. The titanium clamps are designed such, that they flush with the height of the magnet and do not reach into the gap. Under this angle, the vertical distance between the head of the clamp (which blocks the magnet) and its base (at which it is connected to the comb structure) is 12.430 mm and the clamp is screwed to the comb structure at a vertical design distance of 7.443 mm with reference to the girder

surface. This results in a total height of 19.873 mm. When the structure is cooled, the total height shrinks about 18.52 μm (Ti)+ 39.3 μm (Al) = 57.8μm whereas the magnet only shrinks about 6.6μm. This height difference of 51.3μm will lead to an additional pressure onto the magnets.
Under the assumption of no mechanical deformation the created pressure due to cooling can be estimated by adding the thermal expansion coefficients $\alpha_{Al} + \alpha_{Ti} - \alpha_{VD}$ ($6.4{\cdot}10^{-3}$) and multiplying it with the average Young's modulus of the aluminum comb, the titanium clamp and the magnet material (114 GPa). This results in a pressure of 732 MPa in the contact region which is above the compressive strength limit of 600 MPa for the magnets [15] and would fracture the magnet. To reduce the occurring pressure the clamps have to be designed flexible enough to allow a travel of $\Delta_{\max} \approx 50\,\mu$m but also stiff enough to hold the magnet in position when the force orientation onto the magnets flip for smaller gaps, see Sec. 4.2.5.

Clamp Design

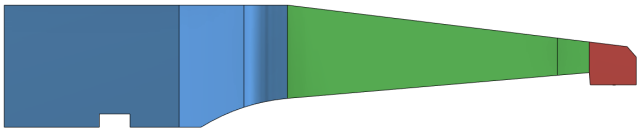

Figure 4.24 – Side view of the clamp design with the functional sections colored.

Fig. 4.24 shows a side view of the clamp. It consists out of three colored sections. The blue section holds the M4 through hole for the screw with which the clamps are connected to the girders. The red section is the head of the clamp which is in direct contact to the magnet. The green section is a lever which reaches to the magnets. This lever is critical for the design as its geometry defines its stiffness against bending forces. This lever has to be thin enough to reach towards the magnets without blocking the space for the pole hanging. While the thickness of the lever is constant at b= 1.8 mm the height varies linearly from the blue to the red section from h = 3 mm to h = 1 mm. This allows a high flexibility close to the red region while the stiffness close to the blue region is increased, where higher torques are acting. The total length from the end of the blue area to the touching point in the red area is l=10.634 mm. The momentum of inertia varies along the clamp and is on average $I_{AVG} \approx 1.49$ mm^4, which would correspond to a constant height of 2.15 mm. Using the first equation of Tab. 4.8 the required force to bend the clamp about 50 μm can be estimated to be F $\approx$ 21 N.

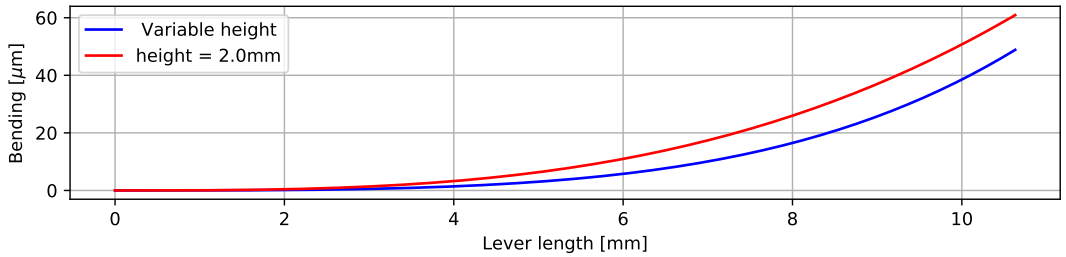

Figure 4.25 – Bending of the clamp for different heights.

In Fig. 4.25 the bending along the clamp is plotted. As a comparison to the chosen variable height design also a bending curve with constant height of 2 mm is plotted. In contrast to the constant height, the variable solution does not deform more than 10 μm on the first 7 mm but gets more flexible towards the head of the clamp and bends about 20 μm on the last mm. Due to this design the clamp is strong enough to keep the magnet in position, but flexible enough to deform such that the remaining pressure onto the magnet is kept small and that mounting errors like a shifted magnet or fabrication errors of the clamp can easily be compensated.

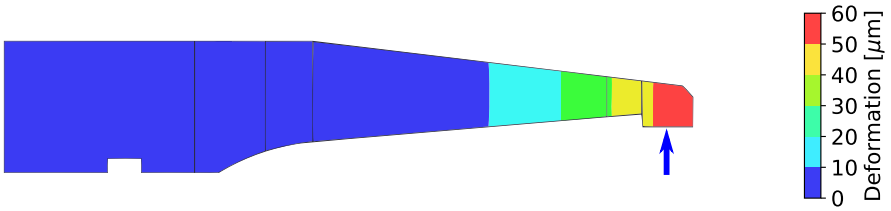

Figure 4.26 – FEM simulation of the clamp design. The blue arrow indicates the direction of the acting force F=21 N. The head of the clamp changes its position about 50 μm.

In Fig. 4.26 a bending simulation of the clamp is shown. The center of the through hole is kept fix and a force of 21 N is applied to the center of the head (marked with the blue arrow) which causes a displacement of about 50 μm, as predicted.
The clamp head is designed as a cylinder with a radius r_c = 8 mm and a length l_c= 3 mm which creates a linear contact and prohibits a punctual load onto the magnet which would cause a high pressure peak. When a force is acting between clamp head and the plane magnet surface, a flattening of the cylinder will occur which causes an increased contact area, so a reduced pressure. The pressure in the contact region can be estimated with the Hertzian contact theory [66]:

$$P_{max} = \frac{F}{2\pi r_c l_c} \cdot \frac{E}{1-\nu^2}$$

where E (see Tab. 4.5) and $\nu \approx 0.3$ are the Young's modulus and the Poisson number of the materials and

$$\frac{1-\nu^2}{\mathrm{E}} = \frac{1}{2} \cdot \left(\frac{1-\nu_1^2}{\mathrm{E}_1} + \frac{1-\nu_2^2}{\mathrm{E}_2} \right).$$

In a steady state in which the clamp is bent with 21 N, the resulting contact pressure is $\approx$ 144 MPa which is in a good agreement with simulations, see Fig. 4.27 and far below the compressive strength limit of 600 MPa, [15].

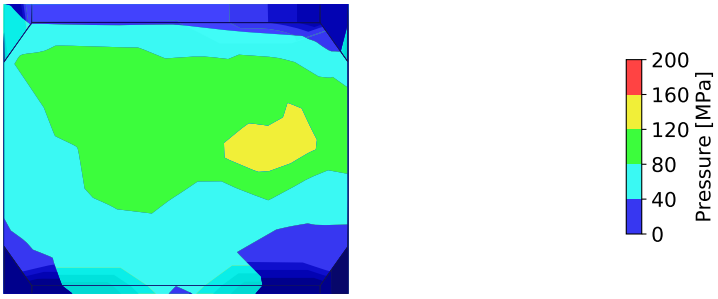

Figure 4.27 – Contact pressure distribution on the magnet's surface in the contact region of the clamp. The average pressure is below 150 MPa.

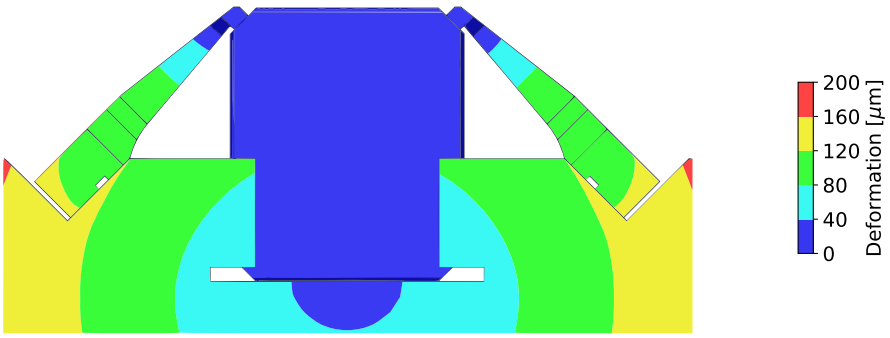

Figure 4.28 – Displacement due to cooling and a shrinking of the structure, the fix point is centered below the magnet.

The full displacement of the magnet mount is simulated and shown in Fig. 4.28. The fix point was set to the surface of the girder right below the magnet and the structure was cooled about 220 degrees. The simulation shows that the deformation is completely absorbed by the clamps.

Suspension Dimensioning for the Poles

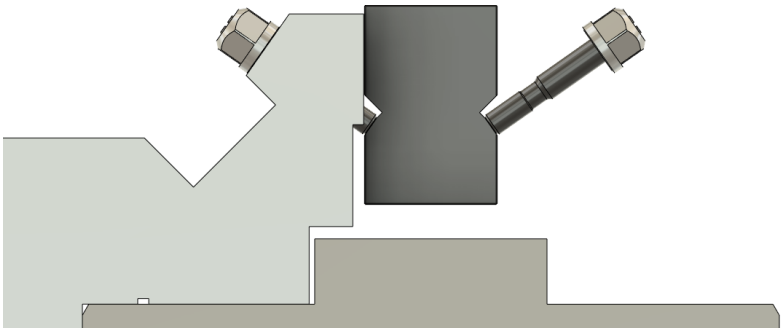

Figure 4.29 – Front view onto the pole suspension of Frosty with the pole in the center. The right comb is not shown to see the screw.

The front view onto the pole suspension system is sketched in Fig. 4.29. Due to the acting magnetic forces, see Sec. 4.3.6, the pole will always be pushed towards the gap (up in the picture) and has no contact to the girder. The screws are mounted in the upper region of the comb structure and point down under an angle of $\alpha = 55°$ with respect to the vertical axis into the cutouts of the pole. The angle is chosen such that the screws are flushing with the design pole height and do not reach further into the gap. The screws are designed as stud screws with a 2.5 mm thread and a l_s= 6.9 mm long shaft with a diameter of 2.2 mm. The shaft has a point support at the end with a radius of 8 mm. Each screw is locked in position with a small nut.
A 2.5 mm thread is normed after ISO 4762 with a travel of 450 μm for a full turn leading to 1.25 μm/°. Considering the rotation of the screw with respect to the vertical axis about the angle α, this leads to a vertical position shift of ≈ 0.72 μm/°. The pole hangs free and is only blocked in movement by the adjustment screws, so, a cooling of the structure would cause the screws to guide the pole downwards towards the girder but does not create remarkable stresses. Critical here are the forces acting inside the suspension system due to the magnetic attraction of the opposing girders.

Force on Adjustment Screws

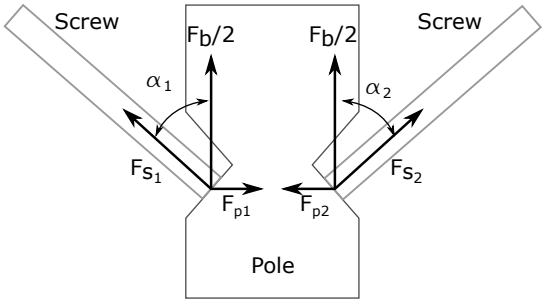

Figure 4.30 – Sketch of the acting forces in the pole suspension.

In the cryo state at 2 mm gap F_b = 100 N are acting onto one pole which have to be compensated by the adjustment screws, see Sec. 4.2.5. Important here is, that the deformation due to changes in the applied force are on a low μm level to guarantee a reproducible field amplitude after several gap scans or cooling cycles. Due to the symmetry of the suspension, see Fig. 4.30, the magnetic force F_b will induce a torque onto the screws with a counter clockwise rotation for the left and a clockwise rotation for the right one. Following from this, the sketched forces F_{p1} and F_{p2} are counteracting, of same magnitude and cancel each other out. So, the sum of all torques in the system becomes zero and the screws act as a clamp and keep the pole in position. The expected deformations are small and will mainly come from an elastic contraction of the titanium screws, as its Young's modulus is almost half of the one from the pole material, see Tab. 4.5. Each screw has to handle half the total force, so $F_b/2$= 50 N. The resulting force acting along the screw axis is then $F_s = F_b/(2\cos(\alpha))$=87.2 N and creates a pressure of $P_s = F_s/(\pi r^2)$=22.96 MPa onto the cross section of the shaft, which is then squeezed in length about $d=l_s \cdot P_s/E_{tit} \approx 1.4$ μm.

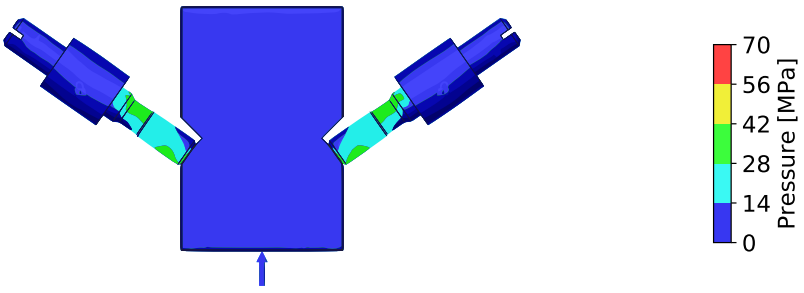

Figure 4.31 – Pressure distribution of the suspension system. The pressure is well below the critical yield strengths of the materials and between 40 MPa and 20 MPa inside the screw.

Calculating this into a vertical and horizontal displacement gives $dx = d \cdot \sin(\alpha) = 1.14$ μm and $dy = d \cdot \cos(\alpha) = 0.8$ μm. As the screws are mounted with an angle of 55 degrees with respect to the vertical axis, the contact surface in the cutout section of the pole has an angle of $\beta = 35°$ with respect to the horizontal axis. So, moving the screw about dx in the horizontal direction gives an extra vertical travel for the pole of $dy_2 = dx/\tan(\beta) \approx 1.6$ μm. Following from this, a total vertical displacement in the range of $dy_{tot} = dy + dy_2 \approx 2.4$ μm is expected. The vertical displacement is checked with a simulation, see Fig. 4.32 and within a good agreement to the estimated 2.4 μm offset.

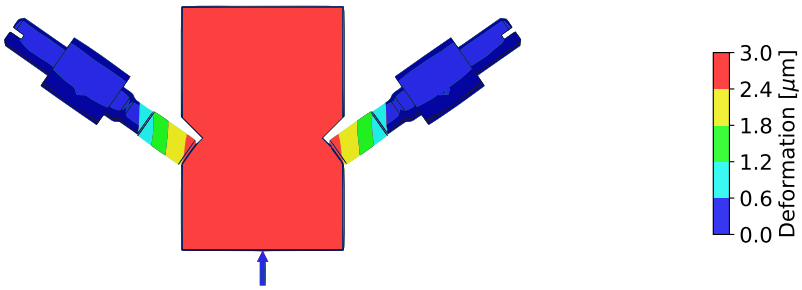

Figure 4.32 – Displacement simulation of the pole hanging. 100 N are applied to the pole which is indicated by the blue arrow. The blue cylinders indicate the threads of the adjustment screws, which are fixed in position.

4.4.2 Girder Design

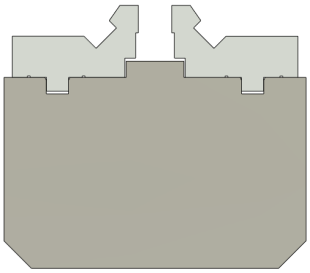

Figure 4.33 – Front view onto the cross section of the girder which can be approximated by a rectangle with dimensions of ≈ 106.57 mm times 84.50 mm.

The girder is the base frame on which the comb structure is mounted and the main support structure to keep the magnetic array stiff. When driving the gap and changing the acting forces with that, the structural bulking of the girder has to be kept within a known low one digit μm range. With an adequate layout of the girder design, this is easy to achieve. The shown layout of the girder in Fig. 4.33 ia approximated by a

rectangle with a cross section of 106.57 mm x 84.50 mm for an easier calculation of the bending.

Girder Deformation

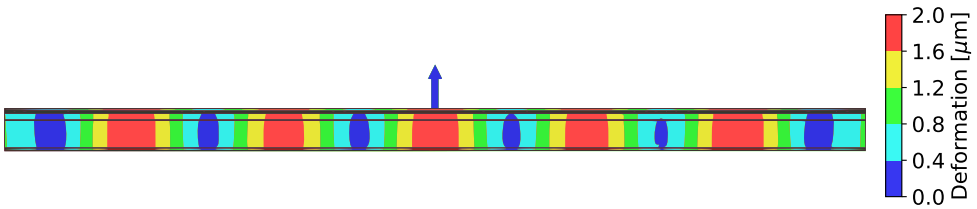

Figure 4.34 – Simulation of the girder bending for 24 kN (@ 77 K) acting onto the gap sided surface, indicated by the blue arrow. The bulking of the upper surface is $\approx$ 1.6 μm from the mean. The fix points are at the locations were the pillars are connected to the girder, see Fig. 4.2.

At room temperature, the girder has a total length of 2010.7 mm, whereas the relevant magnetic structure is 1963.7 mm long. In the simplified approximation the cross section is 106.57 mm in width and 84.50 mm in height resulting in an area moment of inertia of $5.36{\cdot}10^6$ mm^4. Each girder is connected with the outer undulator frame with six pillars, where the distance between the pillars is $d_1 = 345.84$ mm and the outer pillars have an offset of $d_2 = 140.75$ mm from the girder ends. Using Eq.3 from 4.8 and assuming an acting force of 20 kN for the warm state, the maximum deflection is $\Delta_{max} \approx 1.03\,\mu$m, which is cross checked with a simulation in which the maximum deformation is in the range of $\approx 1.3\,\mu$m, so in a good agreement. In the cold state, the dimensions of the girder shrink to a width of 106.2 mm, a height of 84.24 mm and a length of 2002.9 mm, leading to I=$5.25{\cdot}10^6$ mm^4 and a structural bulking of 1.24 μm, which is close to the simulated value of 1.6 μm, see Fig. 4.34.

Pillar Connectors

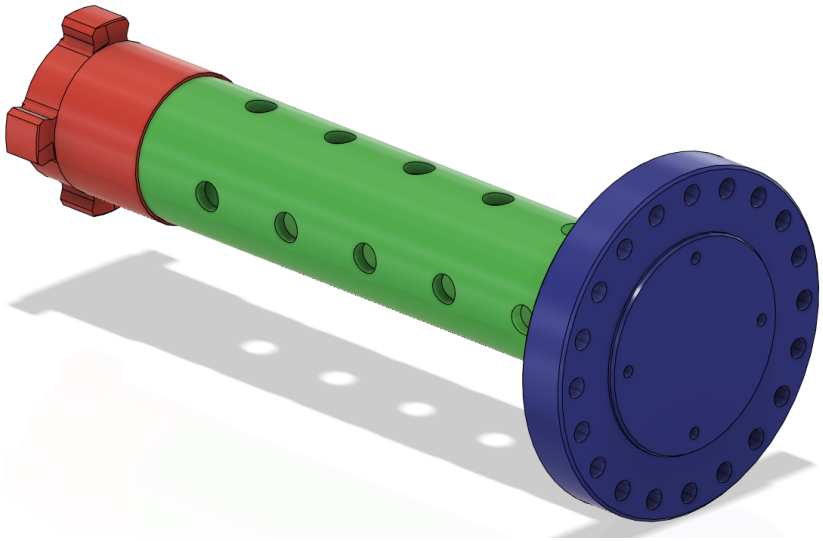

Figure 4.35 – CAD model of the pillar with the frame connection in blue, the green extension pipe and the red bayonet lock.

Fig. 4.35 show a CAD model of one of the twelve stainless steel pillars which connect the in-vacuum girders with the out-of-vacuum frame. The pillar is colored into three sections. The blue flange is the connection of the pillar to the mechanical on-air support which is on the frame. The green extension tube reaches towards the red head, which locks inside the girder and establish a play-free and reproducible connection. The pillar length and position define the initial straightness of the girders and can be shimmed to tune the gap. This tuning has to be conserved when the pillars are unplugged, for example when the chamber is installed, which can be achieved using a bayonet lock as a pillar head. This lock has to be rigid. If the connection has a too high manufacturing tolerance and is loose due to that, the lower girder could start to jump while closing the gap because attractive magnetic forces compensate the gravitational forces. Opening the gap again, the girder would drop onto the pillars which could cause a shift of the poles inside the structure.
Besides the mechanical forces also the main heat flux into the vacuum system goes through the pillars. To reduce the thermal conductivity it is important to reduce the contact surfaces and the diameter of the pipe.

Bayonet Lock

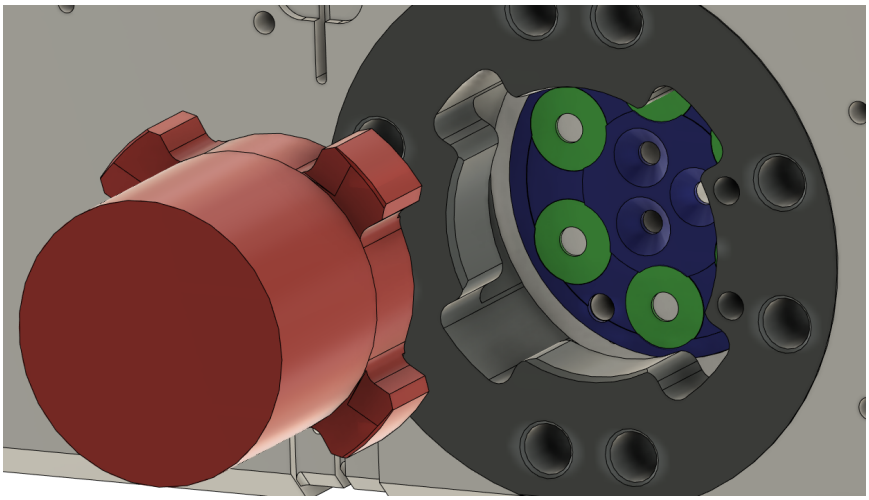

Figure 4.36 – Full assembly of the bayonet lock with the pillar head in red, the receptor in dark gray and the spring system in blue with green springs.

A bayonet lock is a mechanical fastening mechanism to connect two components play-free together. In Fig. 4.36 the full assembly of the bayonet lock is shown. The lock consists out of one male connector with radial pins and a female receptor with the inverse shape, which acts as a contact surface. Inside the receptor is a spring mechanism to push the male part into position. The male connector is the red head of the pillars, the receptor is an inlet into the bottom side of the girders and colored in dark gray. The blue cage system holds the green cup springs. During the assembling the pillar is pushed through the receptor and against the springs. Then, the pillar is rotated about 45 °, such that the pins of the head are centered onto the contact area of the female receptor. The springs push the pins against the contact area and the pillar is locked in position.

Forces onto the Pillar Head

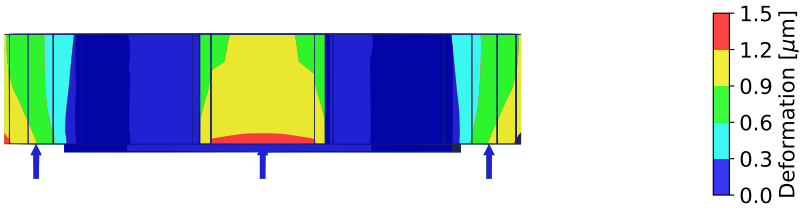

Figure 4.37 – Simulated bending of the lock pins. 1 kN was applied to all contact surfaces inside the bayonet locks, marked with arrows. The simulation was done for the full bayonet lock assembly, but only the top part of the male connector and its pins are shown.

Assuming a uniformly distributed force of 24 kN onto the girder in the cold state, each of the 6 bayonet locks have to withstand 4 kN, so 1 kN per pin. The contact area is approximated with a width of 13.1 mm and a length of 7.15 mm, which leads to an area of ≈ 94 mm^2 and a pressure of ≈ 11 MPa. In the contact area the thickness of the stainless steel pins is 13.5 mm, which leads to an area moment of inertia of $I_s \approx 2686$ mm^4. For the aluminum receptor the thickness is 15 mm and assuming the same width, this would lead to $I_s \approx 3695$ mm^4. The length of the contact area between the pin and the receptor can be assumed as a cantilever beam with a uniform load, see Tab. 4.8. From this, the deflection of the pin is 0.35 μm and of the receptor 0.72 μm which sums up to a total vertical deflection of 1.1 μm of the tip of the pin. Fig. 4.37 shows the FEM simulation of the displacement for the acting setup described above. The shaft of the head extends about 0.33 μm and the tip of the pin about 1.56 μm which results in a bending of 1.23 μm, which is in a good agreement of the estimated 1.1 μm displacement.

Spring System

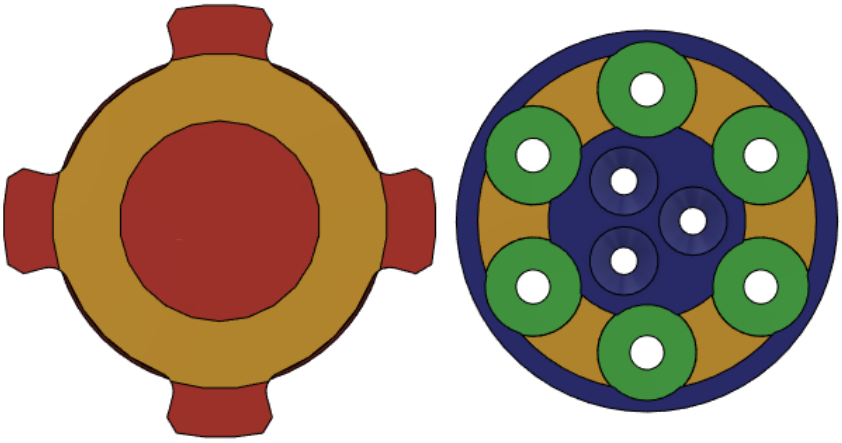

Figure 4.38 – Close up onto the spring system (right) and pillar head (left). Cup springs in green. The yellow rings mark the contact regions.

To reduce the heat flow into the girder the contact surface inside the bayonet lock should be minimized but controllable and uniform for all pillars. One crucial aspect for the design is to prevent a so-called gap breathing, which is an effect which occurs when the pillar head looses contact inside the bayonet lock during the cooling process. This can happen when the pillars are not of same length, or when the tolerances of the bayonet lock are too large.
For example it is possible that five pillars are rigid inside the lock and No.6 is loose, as the pillar is some 50 μm longer than the others. When the undulator is cooled pillars 1 to 5 shrink and the bayonet lock of No.6 receives contact due to which the pillar also start to shrink. When pillar 1 to 5 reach their thermal steady state and the contraction stops, pillar 6 will lose its contact and starts to heat up again. No. 6 will now expand until it reaches the opposite side of the bayonet lock and starts to push against the cooled girder due to which the gap starts to bulk. At this point the pillar receives cooling contact again, contracts and the bulking in the gap vanishes until the pillar lost its contact and is heating up again. This gap breathing will happen on a time scale of several hours and strongly deforms the trajectory of the electrons inside the magnetic field, which makes the undulator impact onto the FEL unpredictable and, therefore, unusable.
Following from this the design of the lock have to be carefully chosen. On the one hand, the lock should be as tight as possible to reduce the probability of a possible gap breathing. On the other hand the tolerances have to be kept big enough to not stress the materials due to different thermal contractions which would lead to a burst. In each case it has to be possible to compensate manufacturing and mounting tolerances. A solution for this issue is the installed spring system which is indicated in blue in

Fig. 4.36 and Fig. 4.38, which holds up to six cup springs (green). This system has two tasks:

1. Guarantee a contact closure at any times
2. Compensate gravitational forces at any times, such that the lower 70 kg heavy girder does not jump when the magnetic attraction is higher than the gravitational force

In Fig. 4.38 is a close up of the contact area between pillar head (red) and spring system (blue). The cage is mounted in a fit inside the girder. For the connection it is important to have a defined contact region, so the ring on top of the pillar head is extruded about 1 mm, whereas the corresponding deepening inside the spring cage is only 0.2 mm. Assuming the 70 kg weight of the girder, the load on each of the six springs inside each of the 6 bayonet locks is ≈ 20 N. The springs are normed (DIN 2093) and have an outer diameter of 15 mm, an inner diameter of 5.2 mm, a thickness of 0.7 mm and a total height of 1.1 mm. When mounted, they are 0.4 mm above the contact area. The spring develops a counter force of 214 N when squeezed about 0.1 mm, so, assuming a linear relation, the weight of the girder is compensated after a spring travel of 10 μm. Following from that, the minimum distance between the stainless steel pillar head and the aluminum spring cage is 0.39 mm in the warm state. Due to the cooling and the different thermal contraction coefficients this distance will decrease and further squeeze the spring. If the spring would be squeezed to 100 % the spring would permanently loose its effect and would become a normal plate which would not develop the required restoring force to push against gravitation. The relevant distance for the cooling is the 0.39 mm gap between the pillar head and the cage. When cooled, this distance decreases to 37 μm, so 90 % of the spring height.
For the installation in the laboratory it could be very difficult to squeeze all springs about the same amount. If this is not possible an alternative back up solution is to replace the springs with shimming plates and to reduce the play inside the lock close to zero. This can only be done to a certain extend and depends on the thickness of the shimming plates. So, using this technique a small jump below 10 μm has to be expected, which has to be tolerated.

Frame Connection

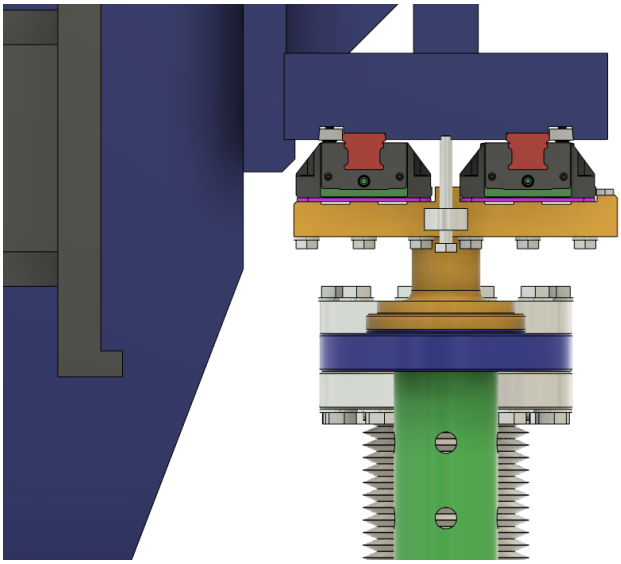

Figure 4.39 – Front view onto the pillar - frame connection. The vacuum components are shown in grey and cut out to see the connection. The air - vacuum interface is between the yellow stamp and the blue flange of the pillar and the stamp is connected to the black sliders which can move into the longitudinal direction (into the picture) to compensate thermal contractions of the girder. Shimming plates (pink) can be inserted between slider and stamp to change the length of the pillars.

The full assembly of the frame connection can be seen in Fig. 4.39. The blue flange of the pillars fulfills two functions at once. The lower side is the vacuum interface. Here, a bellow will be connected which is indicated in light gray in the picture. For a better visibility the bellow was switched transparent to see the mechanics. The upper part is the on-air interface which is a defined plane surface on which the yellow stamp is settled. The stamp is surrounded by a clamping ring (indicated in gray in the picture) which squeezes the pillar to a defined and reproducible position relative to the stamp. So, this connection can be opened and closed without losing the previous adjusted gap. When the undulator is cooled it contracts about 1 cm in length, so the pillars need to be able to change their position. This is done with the black sliders which can move along the red rails. Between the connector and the slider shimming plates can be inserted, marked as purple, to change the length and a tilt of the pillar. These shimming plates will not be removed when the pillar is unplugged, so the shimmed undulator field is conserved. The sliders are ball monorail guidance systems with a dynamic load rating of 13 kN and a static load of 27 kN, so they can withstand the acting forces of 4 kN through the pillars.

4.4.3 Frame Design

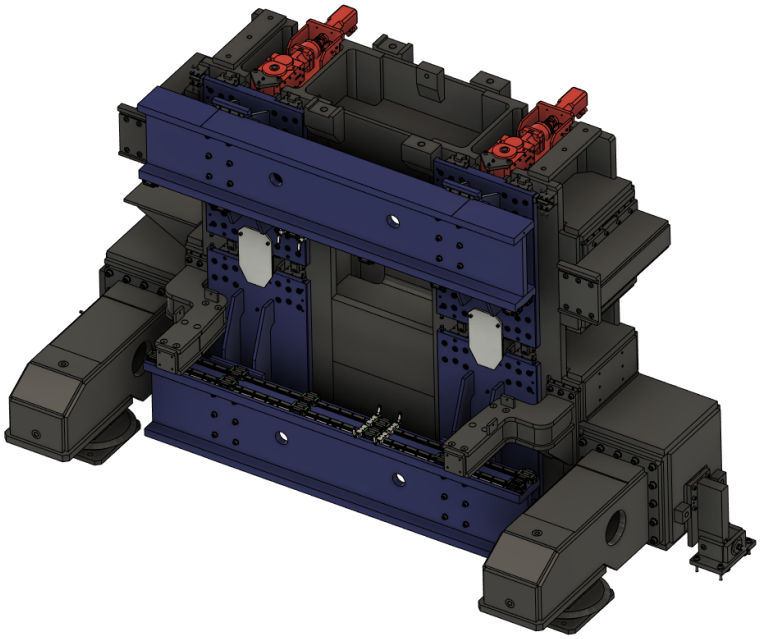

Figure 4.40 – View onto the undulator frame. The drive trains are colored in red and are housed within the black backbone. The girder is connected to the blue steel beams which can be moved.

The frame is responsible to compensate the attractive magnetic forces and consists out of three major components which are colorized in Fig. 4.40. The black backbone is the base frame. The motorization chain is shown in red and the mechanics to drive the gap are blue. The frame is 1.8 m in height and 1.6 m in width to fit inside the Lux accelerator tunnel. As the on-axis field grows exponentially with the gap, the accuracy and reproducibility of the motorization has to be on the μm level. Due to the cooling the absolute gap size would roughly increase about 2 mm which has to be actively monitored and sent as a feedback to the control system. Otherwise the motors would drive to an arbitrary position which does not correspond to a known gap. The mechanical layout has to be stiff enough to compensate the magnetic forces, but also flexible enough to allow a mechanical taper of the girders. As the backbone can only be mounted on one side to grant access to the magnetic array from the other, a so called C-shaped bending will inevitably occur. This bending will be gap dependent, as the gap defines the acting force.

Driving Units and Reproducibility

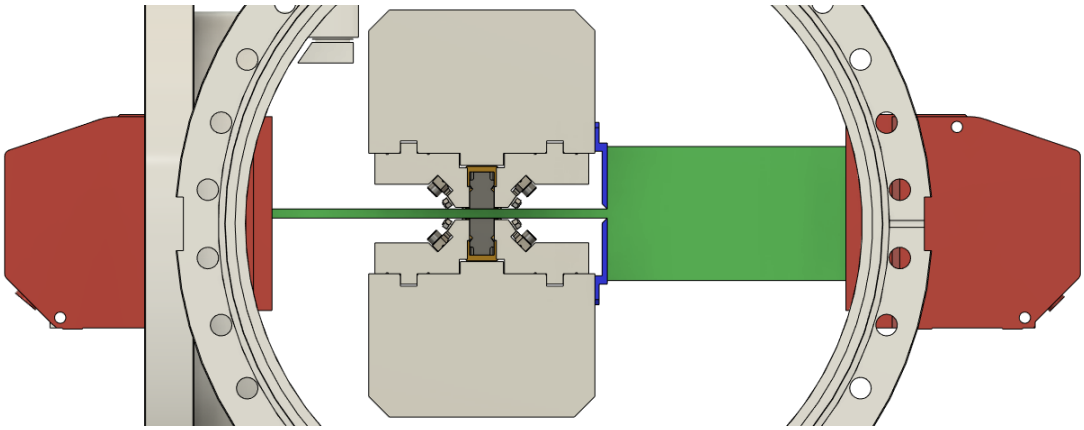

Figure 4.41 – Front view onto the gap measurement system. The light emitter and receiver are colored in red and mounted outside on a window flange to the chamber (not shown). The blue blades mounted on the right side of the girder cut out a defined window of the light beam which relates to the magnetic gap.

When the gap is closed, 24 kN are acting on each girder which have to be compensated to drive the undulator gap open again. To do this, two drive trains are used which are 0.55 m before and behind the longitudinal center of the undulator, see red blocks in Fig. 4.40. Each drive train consists out of a precision rolled ball screw with a left / right thread to symmetrically move both girders into the opposite direction [67]. The dynamic load for each ball screw section is 35.5 kN and they can withstand 101.6 kN at rest. Each ball screw has a slope of R = 5 mm per full rotation and is connected to a bevel-helical gear unit with a gear ratio of 1:48 [68]. Between the gear unit and the motor is an additional shaft coupling. With the gear, the total slope is 104.2 μm per full motor rotation. In contrast to stepper motors servo motors are not limited by a minimum steps size. So, servo motors will be used for Frosty to regulate the gap with a resolution far below 0.3 μm /°. The limitation of the system is the software communication with the motor boxes. Taking this into account the motors can be driven with a minimum resolution of 0.13 μm/step or 7.5 steps for 1 μm.
Two digital Keyence ls 7070 micrometers [69] are installed 1.87 m apart at the beginning and the end of the undulator to permanently measure the gap. The systems are out of vacuum and the light cone is sent through window flanges into the chamber. The light beam is cut with two blades mounted on the side of the girder as shown in Fig. 4.41 and received on the opposite chamber side. The repeatability of the system is in the $\pm 0.2\,\mu$m range and the measurement accuracy $\pm 3\,\mu$m. With this measurement setup and the accuracy of the servo motors the undulator gap can actively be measured and stabilized up to the uncertainty of $\pm 3.2\,\mu$m [69].

One motor has a power of ≈ 300 W and creates a torque of ≈ 0.9 Nm [70]. The efficiency of the gear unit is 93.5%, which results in an effective torque of $M_g = 40.4\,Nm$ per ball screw axis [68]. The ball screws themselves have an efficiency of 82%, so the created lifting force can be estimated to be $F_l = 0.82 \cdot 2 \cdot \pi \cdot M_g/R \approx 41.6$ kN. In the cold state, this limit is reached when the gap is at 1.08 mm, so below the design gap of 2 mm.

Taper

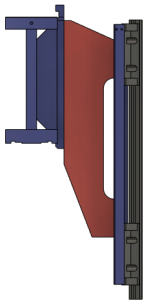

Figure 4.42 – Front view onto the driving unit with the red girder hangings.

To taper the magnetic field the girders need to be tilted which requires a certain flexibility within their hanging. If a torque M_t is acting onto a body with a torsional moment of inertia $I_T = \frac{1}{3}\left(1 - \frac{0.630}{h/b} + \frac{0.052}{(h/b)^5}\right) \cdot h \cdot b^3$, it will start to twist around its central axis about an angle ϕ [66]:

$$\phi = \frac{M_t \cdot l}{G \cdot I_T}. \tag{4.10}$$

The bending depends on the length l of the body and its shear modulus G which is connected to the Young's modulus E via the Poisson number ν like $G = E/(2 + 2 \cdot \nu)$. The girder is connected to the driving units with 4 metal plates, two on each motor axis, which are colored in red in Fig. 4.42. The connection between the left side, so between blue steel beam and the red plates has a height of h=415 mm and the plates are b = 15 mm thick. The distance between the blue steel beams on the left and the right is l = 144 mm. The rotation centers are located at the motor axis, which are 1.1 m appart from each other. To estimate the torque the Young's modulus of steal, 210 GPa, and a Poisson number of 0.3 is assumed. Using those values the twist angle of a single plate, see Eq. 4.10 can be calculated for an acting force of the motors. To get the rotation angle around the undulator center the torsion momentum has to be

doubled as two plates are on each motor side. From this angle, the height change dx can be calculated for an acting motor force F to be

$$\mathrm{dx} \approx \mathrm{l} \cdot \sin\left(271 \frac{\mu\mathrm{rad}}{\mathrm{kN}} \cdot \mathrm{F}\right). \tag{4.11}$$

As the geometry is far more complex than it can be described with Eq. 4.11, it is compared to a FEM simulation. The relative error between the described approach and the FEM is plotted in Fig. 4.43 and shows an overestimation up to $\approx 6\%$, which is acceptable.

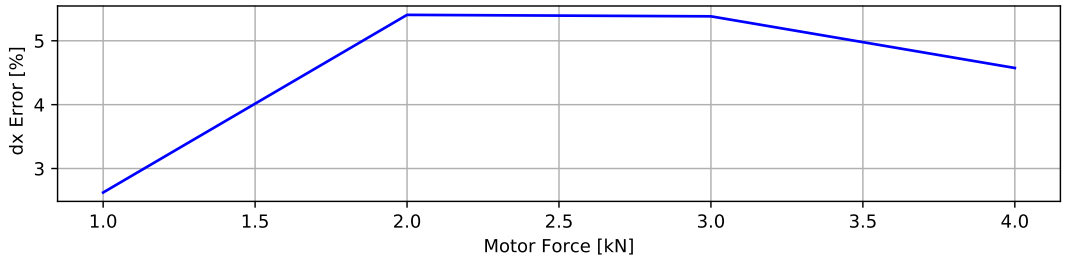

Figure 4.43 – Relative error between the analytical approach of Eq. 4.11 and a FEM simulation for the resulting height change dx for to an acting force of one motor.

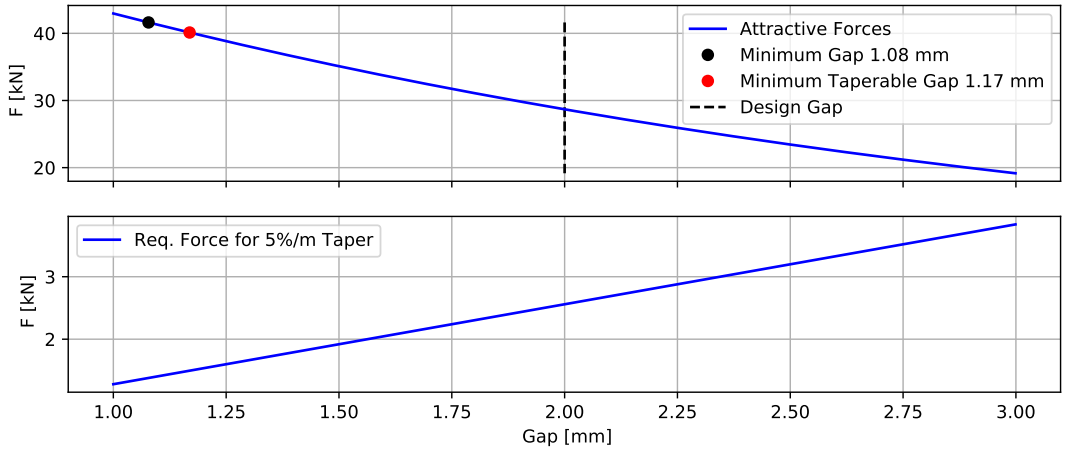

Figure 4.44 – The upper plot shows the acting forces onto one motor axis due to the magnet's attraction (at 77 K) for different gaps. The motors can hold a minimum gap of 1.08 mm and can produce a taper of 5% for a minimum gap of 1.17 mm. The lower plot shows the required motor force to generate a 5%/m taper onto the machine.

Using this overestimation the minimum gap can be calculated at which one can still drive a taper of 5%/m which is at 1.17 mm and also well below the design gap of 2 mm, see Fig. 4.44.

C-shaped Bending

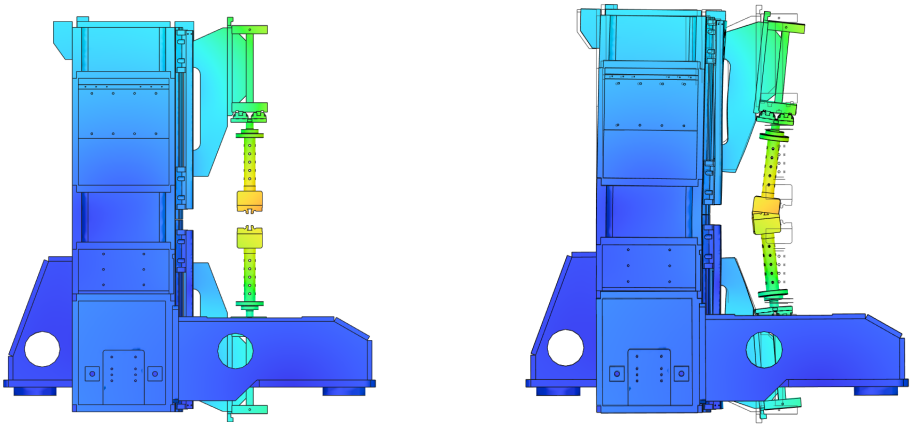

Figure 4.45 – C-shaped bending of the structure due to the attractive magnetic forces between the girders. Left with real scale, right magnified to see the deformation.

Due to the acting forces and the single sided support structure a torque around the longitudinal axis will arise which will cause the frame to bend in the transverse plane towards the gap. An illustration of this bending type can be seen in Fig. 4.45. In a simplified manner the front view onto the undulator frame can be perceived as a c-shape with the open part being the gap, which gives the bending its name. As the torque is a rotational force, the structure will deform around a rotation center. This will cause a translation and rotation of the girders which will manifest in a gap gradient along the horizontal axis, so transverse taper. By closing or changing the gap a deformation of the frame is expected, which induces a gap change and a transverse gradient. The reduced gap can easily be measured and compensated by the active gap measurement feedback, so this will not be noticed. The gap dependent transverse gradient can not be actively compensated and needs to be estimated.
Simulations show, that one girder will rotate around the longitudinal undulator axis about an angle of $\phi_{sb} \approx 250\,\mathrm{nrad/kN \cdot F}$, where F is the acting force. At the design gap of 2 mm roughly 50 kN are acting, which will rotate a single girder about 12.5 μrad and will cause a transverse gap gradient of 25 μrad. Following from this the 12 mm wide poles will have an edge-to-edge offset of $\approx 0.3\,\mu$m and an offset of $\approx 50\,$nm within the good field region of the magnetic field, so within $\pm 1\,$mm from the axis. Compared to the 10 times higher girder deformations (see Fig. 4.4.2) this effect is negligible.

The horizontal translation reaches $\approx 50\,\mu$m, which is also small compared to the mentioned good field region.

4.4.4 The Cooling System

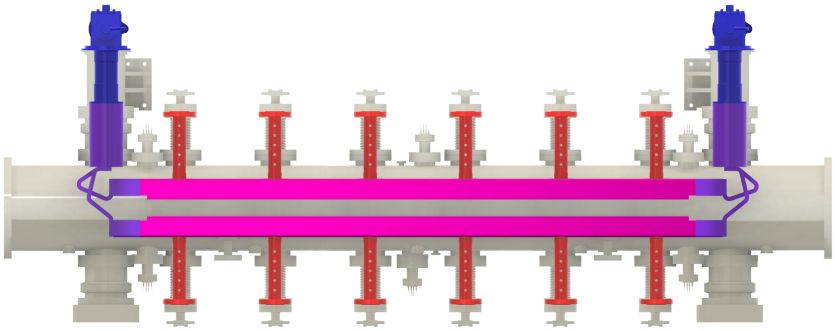

Figure 4.46 – Overview of the cooling system for Frosty. The vacuum chambers can be seen in gray and the color scheme indicates the heat flow of the system from warmest in red, to coldest in blue.

In Fig. 4.46 the cooling system installed in the Frosty vacuum chamber is shown. The color scheme indicates the heat flow in the system which is blue at its minimum and red where heat enters the system through direct contact. The chamber is shown in gray. Two SRDK-400B cooling heads [8], indicated in blue, are connected above the chamber and can cool down to 30 K. A big copper cylinder (purple) is mounted on the cooling head from the inside of the vacuum system and serves as a temperature buffer. The connection to the girder is established with copper bands (purple) which are connected to copper blocks (purple) at the front sides of the girders. These bands create a flexible joint between the cooling head and the girders, which is required as the cooling system is static but the girders will be moved up and down to change the gap. The pillars (red) hold the girders (pink) in position and are connected to the frame. This connection reaches out of the vacuum system and is a main contributor for the external heat load into the system. Besides the heat transmission through mechanical contact, also heat radiation from the chamber walls will warm up the girders.

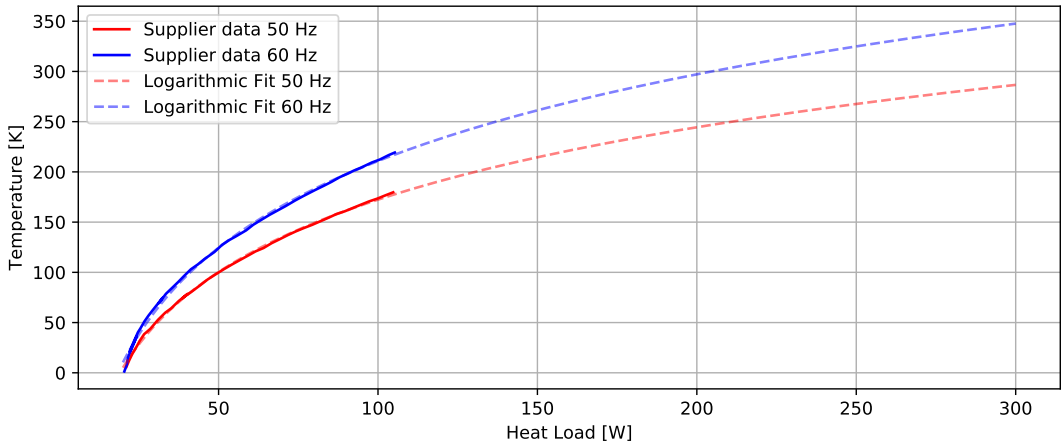

Figure 4.47 – Cooling curves [8] of one cold head which will be installed at Frosty.

For the cooling of the girders two SRDK-400B cold heads [8] are used, which operate in a 50 Hz or in a 60 Hz mode. The heat load curves of the cooling heads are plotted in Fig. 4.47. The blue and red lines are the information provided by the supplier on which a logarithmic fit was done:

$$\begin{aligned} \dot{Q}_{cs50\mathrm{Hz}} &\approx -306.3\mathrm{W} + 103.95\mathrm{W} \ln\left(\frac{\mathrm{T}}{[\mathrm{K}]}\right) \\ \dot{Q}_{cs60\mathrm{Hz}} &\approx -362.7\mathrm{W} + 124.53\mathrm{W} \ln\left(\frac{\mathrm{T}}{[\mathrm{K}]}\right) \end{aligned} \tag{4.12}$$

As the cooling capacity decreases with temperature but the heat load into the system increases with decreasing temperature, see Eq. 4.13, a thermal equilibrium establishes depending on the loads. To estimate the temperature distribution, the heat load into the girders have to be known. The heat load will have two main sources: through the pillar connection to the outside called $\dot{Q}_s$ and thermal radiation $\dot{Q}_r$. The thermal radiation will result in a uniform heating along the girder surface, whereas the heat loads through the pillars is localized. To estimate the impact of both effects the thermal resistances inside the undulator have to be known first.

4.4.5 Thermal Resistances

Due to the symmetric mount of the cooling system only half of one girder has to be analyzed to quantify the thermal gradients. To get insight how the temperature distribution behaves an analytical estimate with the 1D approximation is used. After the setup is analytically expressed in 1D, 3D FEM simulations are done to see the real temperature distribution.

A heat flux will arise inside a body if a temperature gradient $\Delta\mathrm{T}/\Delta\mathrm{L}$ over the length of the body occurs. The heat flux is the amount of energy transported through a cross section per time and is described by Fourier's law for heat transport [71]:

$$\dot{q}_\mathrm{s} = k\frac{\Delta\mathrm{T}}{\Delta\mathrm{L}}$$

where k is the material specific thermal conductivity in units of W/(m·K) and $\Delta\mathrm{T}$ the temperature difference over the length $\Delta\mathrm{L}$. The total heat flow rate $\dot{Q}_s$ through the cross section A of the intersection between the two bodies is then

$$\dot{Q}_s = \dot{q}_s \cdot \mathrm{A} = \Delta\mathrm{T} \cdot k \cdot \frac{\mathrm{A}}{\mathrm{L}} \tag{4.13}$$

and gives the total amount of energy transported per second [71]. The mathematics used to describe heat currents through a system are equivalent to those used to describe electrical currents, so it is convenient to summarize the geometrical factor and the conductivity to a thermal resistance

$$\mathrm{R} = \frac{\mathrm{L}}{k \cdot \mathrm{A}}.$$

The resistances along the cooling chain is calculated for a simplified design which neglects chamfers, bore holes, complex geometries and contact resistances.
Contact resistances between the components actually play a major role. As the name suggests these resistances will occur between the contact surfaces of components. The contact highly depends on the roughness and the contact pressure with which the parts are screwed together. If the surfaces are very rough, the contact will be reduced which will lead to a reduced heat transport. If components are screwed rather loose, small bumps in the surfaces will create the contact but the majority of the surfaces do not touch. Here, it is important to know if air or vacuum is in between the gap, which would also change the heat flow. Following from those examples it is hardly possible to analytically estimate the real contact resistance, even if approaches exist [72]. Especially the temperature dependence of those contacts are unknown. So the true resistances have to be found experimentally by assembling the machine, cooling it down and measure the temperature distribution along the girder. They will be neglected for the temperature calculations presented here.

Thermal Resistance of the Frame Connector

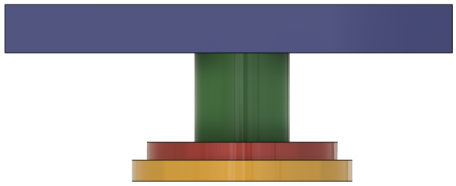

Section	**Area** [mm^2]	**Length** [mm]
Blue	7800	16.2
Green	804.248	29.90
Red	3216.991	6.0
Yellow	4300.84	7.1

For the calculation also the frame connection has to be taken into account to estimate if a possible condensation of water from the surrounding air on the pillar could happen. The room temperature will be defined onto the area which is attached to the sliders, marked in pink in Fig. 4.39 and is the top surface of the blue body in the simplified design shown below.

Thermal Resistance of the Pillar

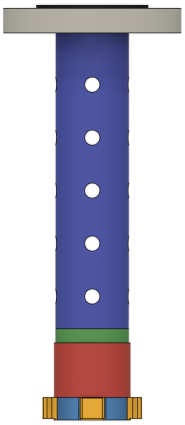

Section	**Area** [mm^2]	**Length** [mm]
Black	4300.84	2
Grey	10824.954	16.3
Dark blue	563.013	195.5
Green	1832.248	9.4
Red	2002.962	36
Light Blue	1924.422	14.00
Yellow	274.814	8.15

For the pillar the holes inside the pipe are neglected for the 1D approach. Nevertheless, the holes will have a contribution to the resistance of the pipe as they reduce the diameter within a certain section and increase its resistance. The heat flow will go through the black top part which is connected to the frame connector and flows through all sections. The yellow pins are the bayonet lock and are in contact to the girder with their upper surface. The listed values are for individual components and are always taken to the perpendicular surface to the next body going from black to yellow.

Thermal Resistance of the Girder

Section	**Area** [mm^2]	**Length** [mm]
Blue	6412.09	23.51
Yellow	8967.20	87.99
Green	7212.2	58.50
Red	8967.20	287.34
Black	8967.20	143.62

The sections between the pillars have equal length, but the part which is connected to the cooling head is reduced. To easier handle the changing cross section due to the cut outs in the bayonet locks their circular shapes are approximated by a rectangular cross section with a width and length of 58.5 mm and depth of 30 mm. This cut out is subtracted from the girder dimensions.

Thermal Resistance of the Copper Connector

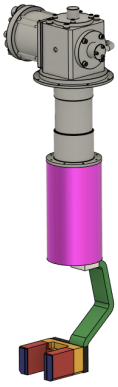

Section	**Area** [mm^2]	**Length** [mm]
Blue	1482.0	2.0
Red	1594.00	66.0
Yellow	6536.00	30.0
Black	6360.00	15.0
Green	675.00	235.0
White	2025.00	15.0
Magenta	12271.846	230.0
Grey	5026.548	150.0

In the image the copper cooling chain from one girder end to the cryo cooler is shown. Two girders are connected to one cold head, but as the chain is the same for both girders only one is shown. The copper block has one cut out in which a foil spanning system is mounted, so the girder is connected to two arms shown in red which will then go into one big copper block shown in yellow. This block is connected to the magenta colored copper block with a copper band which is divided into three colored sections. The cold head is shown in grey.

4.4.6 Contact Heat Transport Calculations

The heat current calculations are identical to electrical current calculations which follow the Ohm's law U=R·I [71], where I is the (heat or electrical) current in the system, R the thermal/electrical resistance and U the change of the thermal/electrical potential. Following from this, the heat flow $\dot{Q}$ corresponds to the current I and the temperature change ΔT to the change in voltage U. Also, series and parallel circuits are treated identical [71]. Within a series circuit the current is constant for all resistances whereas the voltage and the resistances are summed ($U=U_1+U_2...$, $R=R_1+R_2...$). In parallel circuits the voltage is constant and the current is summed ($I=I_1+I_2...$, $1/R=1/R_1+1/R_2...$).

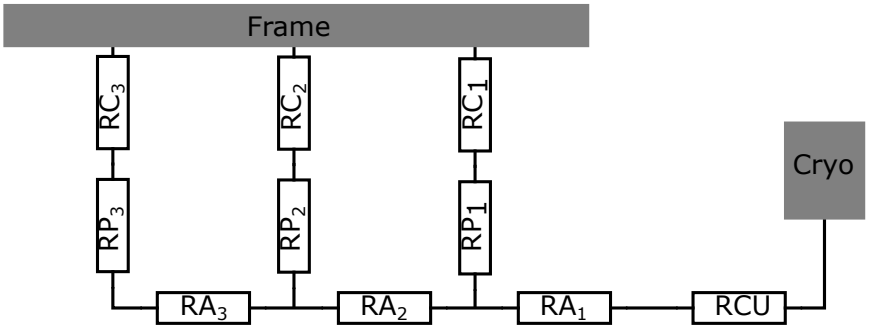

Figure 4.48 – Thermal resistance diagram of the cooling chain.

Fig. 4.48 shows the resistances of one half girder which includes all in-vacuum components and the out-of-vacuum frame connectors. The frame connectors are called RC_i (i is index of the pillars) through which a current I_i streams into the system. the resistances of the pillars are called RP_i. The aluminum girder is divided into three sections RA_i. Each section includes one bayonet lock. The copper connectors to the cryos are called RCU. For the calculation only the total current $I_c=\sum_i I_i$ at the cold head is a known variable (Eq. 4.12) whereas the current contribution of the individual pillars are unknown because the incoming current depends on the girder's temperature at the height of the girder which changes from pillar to pillar. So, the total resistance of the undulator has to be calculated first to estimate the total current. After, the individual currents of the pillars can be calculated. The sketch in Fig. 4.48 can further be simplified by adding the resistances $R_3=RC_3+RP_3+RA_3$, $R_2=RC_2+RP_2$ and $R_1=RC_1+RP_1$. With this simplification the total resistance of the undulator is

$$R_{ges} = RCU + RA_1 + \frac{R_1 \cdot \left(RA_2 + \frac{R_2 \cdot R_3}{R_2+R_3}\right)}{R_1 + RA_2 + \frac{R_2 \cdot R_3}{R_2+R_3}}.$$

The current contribution from each pillar is calculated for a known I_{ges} to be

$$I_1 = I_{ges} / \left(1 + \frac{R_1}{RA_2 + \frac{R_2 \cdot R_3}{R_2 + R_3}} \right)$$
$$I_2 = \frac{I_{ges} - I_1}{1 + \frac{R_2}{R_3}}$$
$$I_3 = I_{ges} - I_1 - I_2$$

Constant Conductivity Approach

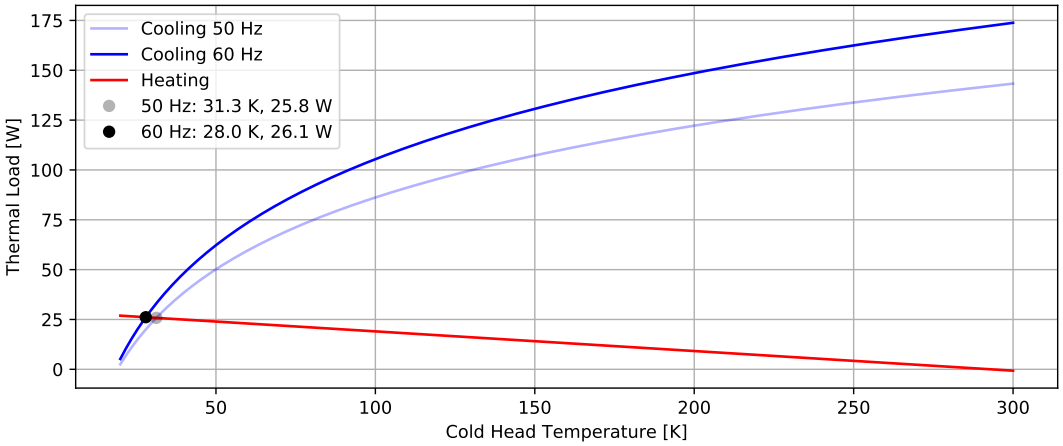

Figure 4.49 – Heat contribution through the pillars vs cooling capacity of one cold head for constant thermal conductivities.

To check the validity of the analytical model, constant thermal conductivities are used which are calculated with the functions given in Sec. 4.3.3 for 293 K.

Material	λ [W/(m· K)]
Copper	401
Aluminum	125
Stainless steel	16.3

With this, the resistances are $RC_i \approx 2.62\,K/W$, $RP_i \approx 23.74\,K/W$, $RA_1 \approx 0.17\,K/W$, $RA_2 = RA_3 \approx 0.32\,K/W$ and $RCU \approx 1.004\,K/W$. The total resistance of the system is $R_{ges} \approx 10.142\,K/W$. With the known total resistance, the heat load into the system for a variable temperature difference $I_{ges} = \Delta T / R_{ges}$ can be calculated versus the cooling curve of one cold head, which is shown in Fig. 4.49.

Here, only half the cooling capacity has to be used, as only the resistance of one half girder was calculated. The cooling of the cold heads is compensated by the heat income when a cooling power of $\approx 26\,\mathrm{W}$ is reached, which corresponds to a cold head temperature of 28 K for the 60 Hz and 31.3 K for the 50 Hz mode.

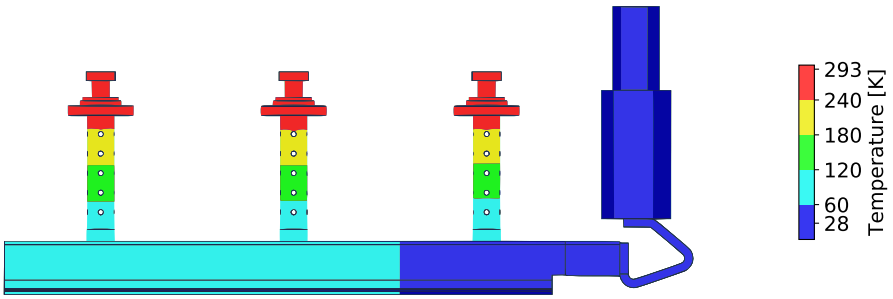

Figure 4.50 – Thermal distribution simulation of one half girder with the calculated temperature of 28K at the cold head in the 60 Hz mode.

With the known total current the temperature along the cooling chain is calculated backwards in the 1D approximation. The model is compared to a 3D simulation, see Fig. 4.50, and the values are listed in Tab. 4.9. The current splits up like $I_1 \approx 34.0\%\, I_{ges}$, $I_2 \approx 33.2\%\, I_{ges}$, $I_1 \approx 32.8\%\, I_{ges}$.

	1D [K]	3D [K]	ΔT [K]
Cold Head	28	28	0
Cu Connector	54.23	53.53	0.7
B. Lock 1	58.74	58.89	-0.15
B. Lock 2	64.28	64.64	-0.36
B. Lock 3	67.03	67.25	-0.22
Pillar 1	269.69	266.2	3.49
Pillar 2	270.24	266.7	3.54
Pillar 3	272.99	267.7	5.29

Table 4.9 – Predicted and simulated temperatures along the cooling chain.

To estimate the temperature distribution along the girder the 1D approximation and the 3D simulation are in a good agreement, whereas the temperature change along the pillar deviates about some degrees. In the simulation also gradients along the contact surfaces appear which are not modelled with the 1D approximation. Also, the simplified 1D model does not consider the holes inside the pipe. Besides that, the 1D model is in a good enough agreement with the simulation to estimate the temperature along the girder. This model is used to calculate the temperature distribution with a varying thermal conductivity in the next section.

Variable Conductivity Approach

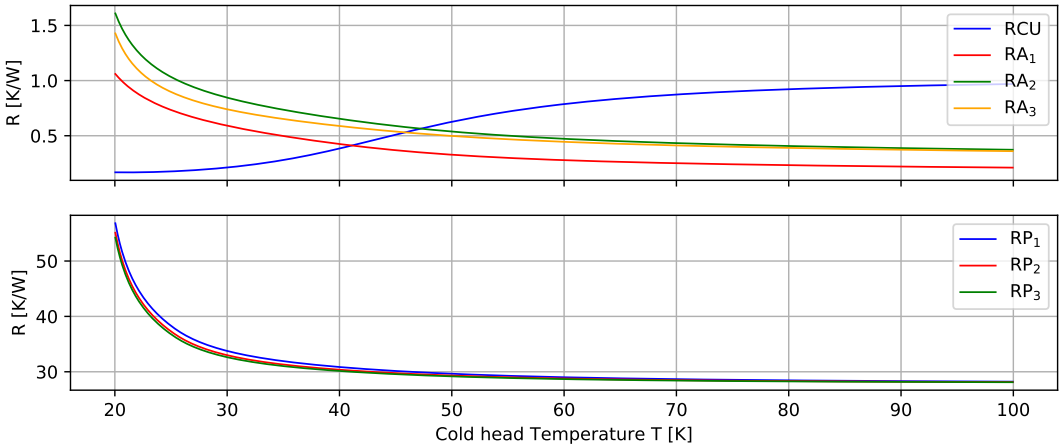

Figure 4.51 – Temperature dependent change of the thermal resistances.

The variable heat conductivities shown in Sec. 4.3.3 can now be implemented into the analytical description shown before. As the total resistance will now vary with temperature the calculation can only numerically be solved by assuming a fixed but variable set for the heat load I_0 and temperature T_0 from Eq. 4.12 at the cold head and than calculating along the resistance chain. In Fig. 4.51 the thermal resistance versus the mentioned sets are plotted. The resistance of the copper connector decreases which allows a high conductance between the girders and the cold head, and that the resistance of the pillars strongly increases at low temperatures which result in a higher insulation and a reduced heat contribution into the system. The resistance of the aluminum girder sections also increase about different amounts due to their different length and different currents transported through the sections. From this, a varying but constant gradient between the sections is expected.

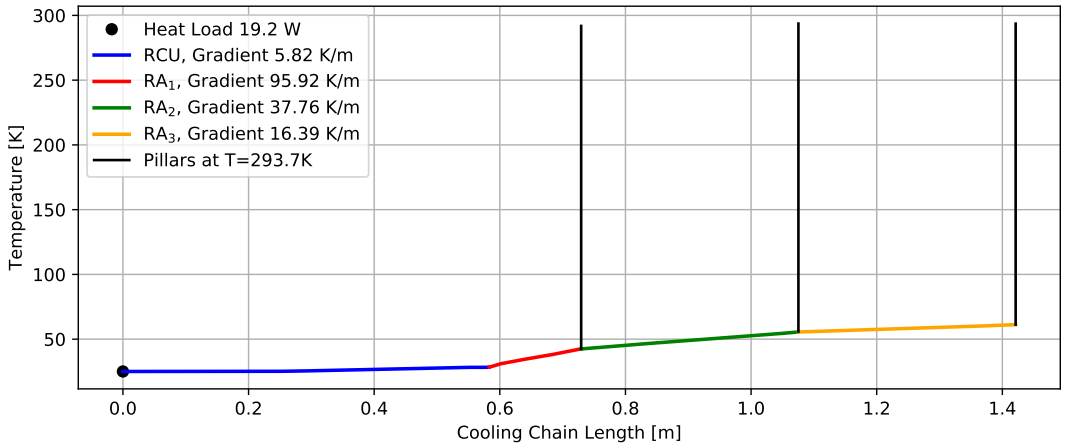

Figure 4.52 – Thermal distribution along the cooling chain with variable thermal resistances of the components.

Using these resistances the temperature distribution along the girder is found and is shown in Fig. 4.52. The heat load into the system is compensated when the cold head reaches a temperature of ≈ 25 K with a heat load of ≈ 19.2 W. The temperature at the contact area between the copper connectors and the girders rises about ≈ 3.4K due to the low resistance of the copper. The first girder section, which reaches from the copper blocks to the center of the first bayonet lock, heats up about 14 K which leads to a gradient of ≈ 96 K/m. The second section has a temperature rise about 13 K with respect to section one, which gives a gradient of 38 K/m. The last section heats again about 5.7 K, so a gradient of 16.4 K/m. These temperature changes can now be transformed into a length variation using the thermal expansion coefficients shown on Fig. 4.10. The variation of the stainless steel components depends on the length of the pillar $L_P \approx 259.20$ mm (The distance between the pins in the bayonet lock to the frame connector has to be used) and the length of the frame connector $L_{FC} \approx 59.20$ mm:

$$L_{VS} = (1 + \Delta L/L_{Steel}(T)) \cdot (L_P + L_{FC}) \approx 318.40\text{mm} \cdot (1 - \Delta L/L_{Steel}(T)).$$

For the variation of the aluminum girder the distance $L_G \approx 81$ mm from the contact surface in the bayonet lock to the gap sided end of the comb structure has to be used to calculate the girder variation

$$L_{VA} = 81\text{mm}(1 + \Delta L/L_{Al}(T)).$$

The total length is then $L_{tot} = L_{VA} + L_{VS}$. The values are listed in Tab. 4.10.

	T [K]	ΔT [K]	L_{tot} [mm]	ΔL_{tot} [μm]
Cooler	28.4	0	398.118	0
Lock 1	42.5	14.1	398.121	3.2
Lock 2	55.5	27.1	398.141	23.8
Lock 3	61.2	32.8	398.153	35.5

Table 4.10 – Temperature and Length changes along the undulator with respect to the undulator end value at the cooler.

As the heat load was calculated for one fourth of the undulator, the total heat load into the system is expected to be ≈ 77 W.

4.4.7 Temperature Induced Phase Advance Estimate

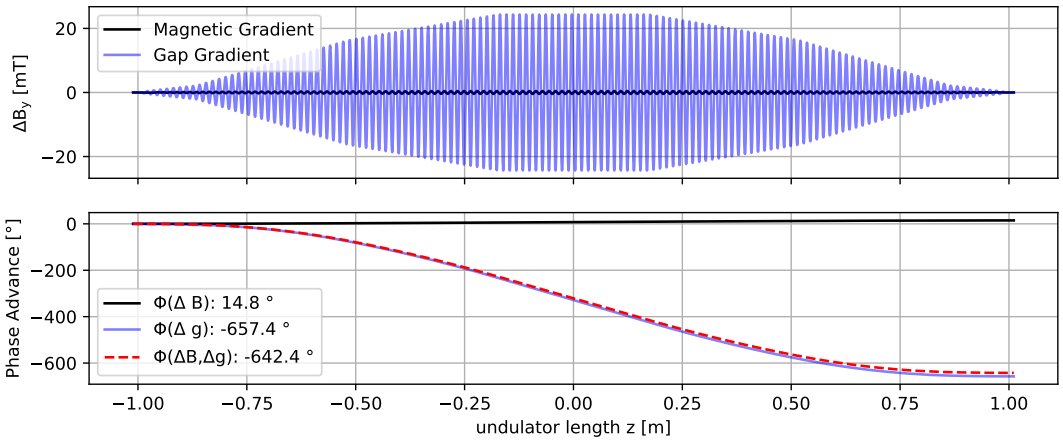

Figure 4.53 – The top picture shows the magnetic field change due to a temperature dependent magnetization in black (see Eq. 4.5) and a magnetic field change due to a mechanical deformation induced by a temperature gradient (Eq. 4.9) in the undulator in blue. The lower picture shows the respecting phase advance. A nominal gap of 3 mm in the cryo state with a nominal peak field of $B_0 = 1.41$ T ($K = 2$) is used.

Using the values in Tab. 4.10 and the thermal magnetization dependency shown in Fig. 4.3, the field change is calculated with Eq. 4.5 and Eq. 4.9 and is plotted in Fig. 4.53. As already shown in Fig. 4.15 and Fig. 4.18 the phase changes are counter acting but the total phase change due to a mechanical gradient is dominant about orders of magnitudes. The impact of the change in magnetization is plotted in black and the change of the gap in blue. The total phase is the red dotted line and reaches -642.4 °.

Discussion

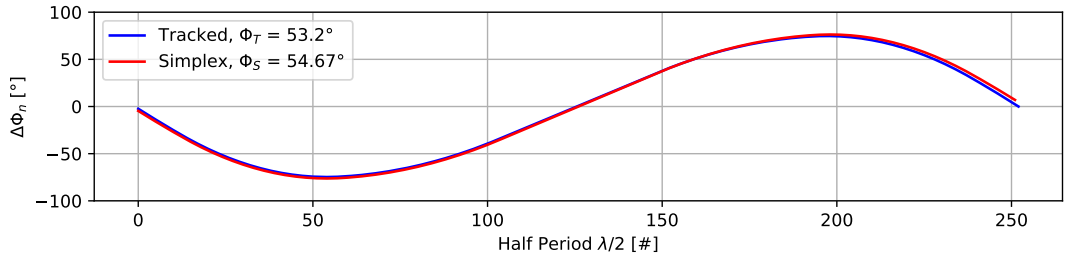

Figure 4.54 – Phase distribution of the emitted light by an undulator field affected with a thermal gradient shown in Fig. 4.53. Data evaluated with the Simplex code [9] and by calculating the phase as described in Sec. 6.1.

As already mentioned in the introduction of Sec. 4.3.4, the phase advance is a systematic effect and has a different impact onto the emitted radiation, than a statistical fluctuations.
The phase advance shown in Fig. 4.53 is calculated with respect to the emitted wavelength of the first undulator period, which is the shortest emitted wavelength in the spectrum. Due to the thermal gradient along the device the average on axis undulator field is higher than the field of the first undulator period. So, the average emitted wavelength is red shifted. To calculate the phase with respect to the average wavelength, a linear regression has to be subtracted from the phase advance shown in Fig. 4.53 [73, 74]. Here, the average phase advance is calculated by using a particle tracking (see J_{ph} calculation in Sec. 6.1), which is validated with the phase error calculations of the FEL code Simplex [9], see Fig. 4.54.
To the average wavelength the phase advance of Fig. 4.53 manifests as a phase error of $\Phi = 54°$, which is roughly a factor of 10 smaller than the phase advance shown in Fig. 4.53 and would increase the gain length about $\Delta L_G/L_G = \Phi^2/3 \approx 30\%$ [48]. The maximum difference of the phases is 150 ° between pole 50 and 200 in Fig. 4.54. For the FEL physics, see Sec. 2.4, a constant phase relation between the emitted light and the electrons is required to efficiently transfer kinetic energy of the bunch to the light field. To do so, a majority of the electrons should stay in the decelerating area, see Fig. 2.6.
Due to the phase change of 150 ° along the undulator, the decelerating electrons could be forced into an accelerating phase and vice versa and the prior amplification of the light could be,to some extend, reversed, which should be avoided.

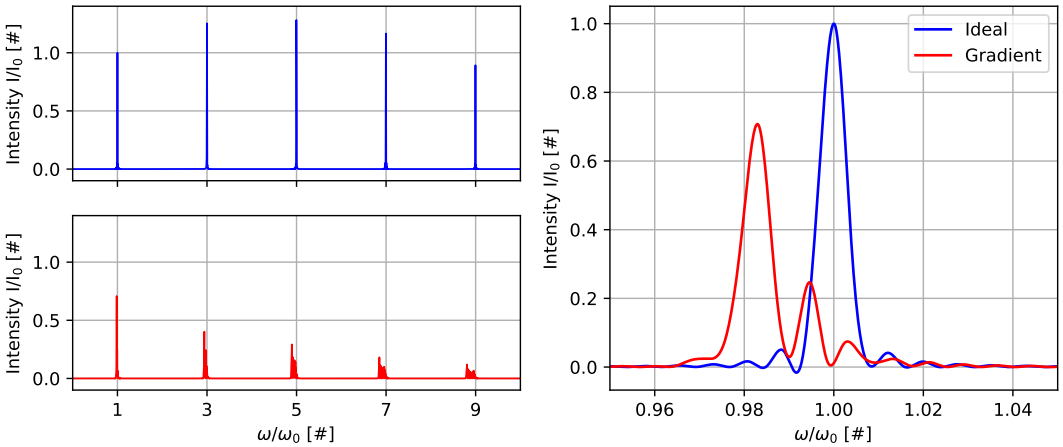

Figure 4.55 – Intensity distributions of the light emitted by an ideal undulator field with a K = 2 (blue) and a field with the thermal gradient (red) from Fig. 4.53. The intensities of the radiation for each harmonic wavelength is plotted on the right and normalized to the fundamental of the ideal undulator radiation in the upper left plot. On the right, the spectra of the first harmonics are shown with respect to the fundamental frequency ω_0 of the ideal radiation.

The spectral properties of the radiation emitted by an undisturbed undulator field and a field affected by a thermal gradient, as shown in Fig. 4.53, are plotted in Fig. 4.55. The left pictures show the intensities of the higher radiation harmonics normalized to the fundamental of the ideal field. The intensities of the disturbed field are strongly reduced. The peak of the first harmonic is red shifted about 1.7% and has a reduction about 30% in intensity compared to the peak of the undisturbed field. At the fundamental ω_0 of the undisturbed field the intensity of the disturbed field vanishes, as the power ratio $R = e^{-\cdot\Phi^2} \approx 0$ for the phase advance of Φ = -644.5° shown in Fig. 4.53 [1, 17].

These effects would impact the lasing process and would make the undulator the dominant degradation factor of the FEL performance. To make the undulator operational the field has to be tuned again for the cryo state. This can be done by comparing the field measurements before and after the cooling process and calculate the gap deformation from that. This gap deformation can now be inverted ($\Delta g_{cold} \longrightarrow -\Delta g_{warm}$) and shimmed into the warm undulator. Doing so, will cause a phase advance in the warm state to look like the lower plot in Fig. 4.53 but with a change of sign. Cooling would now cause the phase to go to zero. Due to those mechanical conversions the shimming process is highly error-prone as all mechanical contacts between girders and frame have to be opened and closed to de/install the vacuum chamber and the measurement bench, which potentially changes the thermal contact resistances. Alternatively,

the pillars can be shimmed in length when the machine is cooled to get the phase close to flat again.

4.4.8 Thermal Radiation Heat Transport Calculations

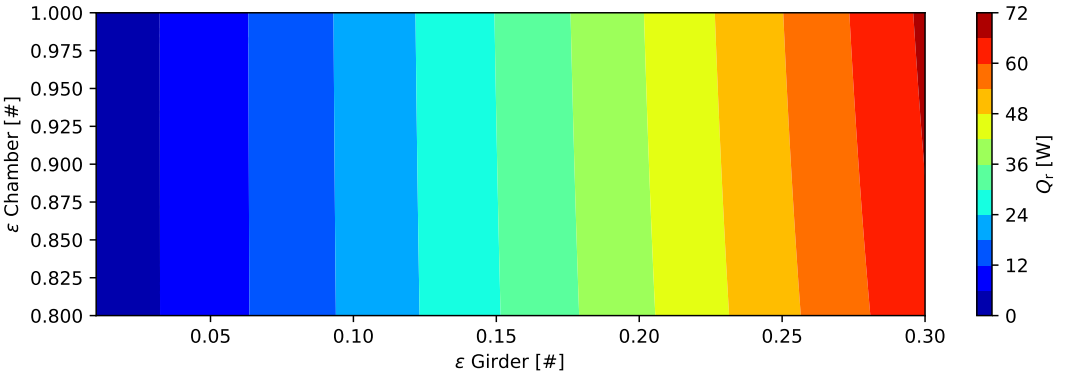

Figure 4.56 – Radiation heat load for different emissivities. The ambient temperature was set to 293 K and the girder temperature to 20 K.

Besides the energy transport through contact, energy is also transported through thermal radiation. The radiation based heat flux follows the Stefan-Boltzmann law [71]:

$$\dot{q}_r = \mathrm{F}_\epsilon \cdot \sigma \cdot \left(\mathrm{T}_1^4 - \mathrm{T}_2^4\right)$$

with the Stefan-Boltzmann constant $\sigma = 5.67 \cdot 10^{-8} \frac{\mathrm{W}}{\mathrm{m^2 K^4}}$. $\mathrm{T}_{1,2}$ are the temperatures of the bodies and F_ϵ describes the exchange coefficients of the materials. This coefficient depends on the emissivities $\epsilon_{1,2}$ of the materials surface and their enveloping surfaces $\mathrm{A}_{1,2}$ [71].

$$\mathrm{F}_\epsilon = \frac{1}{\frac{1}{\epsilon_1} + \frac{\mathrm{A}_1}{\mathrm{A}_2}\left(\frac{1}{\epsilon_2} - 1\right)} = \frac{\mathrm{A}_2\epsilon_1\epsilon_2}{\mathrm{A}_2\epsilon_2 + \mathrm{A}_1(\epsilon_1 - \epsilon_1\epsilon_2)}$$

The heat flow rate between the bodies through the surface of the body A_2 is now

$$\dot{Q}_r = \dot{q}_r \cdot \mathrm{A}_2 = \mathrm{A}_2 \cdot \mathrm{F}_\epsilon \cdot \sigma \cdot \left(\mathrm{T}_1^4 - \mathrm{T}_2^4\right) \tag{4.14}$$

The thermal radiation $\dot{Q}_r$ is calculated with Eq. 4.14 for which the emissivity values have to be known which depend on the surface qualities of the materials. All emissivity values discussed in this chapter are taken from [75]. Due to the milling process, the aluminum surfaces of the girders are highly reflective and close to polished, which would give an emissivity of $\epsilon_{2\mathrm{a}} = 0.05$. Some components have to be coated due to which the polished surface becomes rougher, which gives $\epsilon_{2\mathrm{b}} = 0.275$. The tube has a rough surface and is fabricated out of stainless steel for which an emissivity between

$\epsilon_{1a} = 0.85$ and $\epsilon_{1a} = 1$ is assumed. To calculate the inner surface of the vacuum chamber it is approximated as a cylinder with a diameter of 300 mm and a length of 3 m. The shell surface of this cylinder and the area of both flanges is then A_1=2.97 m^2. The girders are approximated with a rectangular shape and have a surface of A_{2a}=1.56 m^2 for both girders. Fig. 4.56 shows the impact of the emissivities onto the radiation heat load into the system. For the expected values of $\epsilon_2 \approx 0.1$ and $\epsilon_1 \approx 0.85$ the radiation heat load would be $Q_r \approx 20$ W when cooling the machine from 293 K to 20 K. To reduce the heat load a heat shield made out of polished aluminum with an $\epsilon_3 < 0.05$ could be installed. This heat shield could consist out of a thin aluminum cylinder or simple foil which is directly connected to the inner surface of the chamber. Assuming emissivities of 0.1 and 0.05 the heat load is reduced to ≈ 11 W. To further decrease the radiation impact the heat shield could be cooled to 200 K as the radiation heat load scales with $\propto T^4$. This would cause the thermal heat load to drop to $Q_r \approx 2.4$ W. So, with an adequate and simple shielding the heat load due to radiation can be strongly suppressed and would only introduce a uniform temperature increase in the 10% range of the contact heat transport.

4.5 Conclusion

The newly developed magnets out of $Pr_2Fe_{14}B$ increase their remanence field about 15 % when cooled down to 77 K, which leads to an increase of the undulator on-axis field at a 2 mm gap of 11.3 %, see Sec. 4.2.1 and pushes the acting forces onto each girder from 19 kN up to 24 kN, see Sec. 4.2.5.
As the cooling will also reduce the heat capacity a high and localized temperature jump could arise when an electron beam is dumped into the structure. It was shown in Sec. 4.2.2, that the magnetic array can withstand an impact of a Gaussian shaped electron beam with 300 MeV, 50 pC charge and a rms beam size of 35 μm.
To design a cryogenic undulator the different temperature dependent contractions and thermal conductivities of all components inside the cooled system have to be known, which are shown in Sec. 4.3.2 and Sec. 4.3.3. For Frosty, a localized cooling scheme at the ends of the girders is used. Following from the simple ansatz that heat is transported from warm to cold, a mathematical model was derived to estimate the thermal gradient which will arise inside the undulator structure with localized heat sinks, see Sec. 4.3.4. This thermal gradient will systematically affect the temperature sensitive remanence field of the magnets and also deform the gap along the undulator as the contraction of the support structure is temperature dependent. It was shown that both effects will affect the phase, but in an opposite direction and that the impact of the mechanical deformation is orders of magnitudes higher than the change in the remanence field. To change the systematic phase advance about 5°, just by taking a magnetic gradient into account, a thermal gradient of 17 K/m is acceptable. The same

phase advance would arise with a thermal gradient of 80 mK/m for just taking the mechanical deformation into account. So, thermal gradients should either be completely avoided or the mechanical structure has to be tunable enough to correct for it.
The chosen Frosty undulator design is explained in Sec. 4.4. The geometrical design constrictions of one undulator period are shown in Sec. 4.4.1 with the primary focus on the mechanical tolerance chains arising between the cold and warm undulator state. It was shown that the mechanics will deform such, that the poles receive a tolerable shift of $\approx 2.5\,\mu$m towards the gap when it is closed to 2 mm with respect to no forces acting. Due to the acting forces also the girder will bend and a maximum deformation up to $\approx 1.6\,\mu$m is expected which is explained in Sec. 4.4.2. The girder is connected with pillars to the frame, which have to compensate the acting forces. In Sec. 4.4.3 the girder design is presented. It was shown that the backbone can compensate the attractive forces of the magnets even when a taper is implemented in the structure. Assuming a tapered gap of 5%/m, the motorization is strong enough to drive a minimum gap of 1.2 mm, which is well below the minimum design gap of 2 mm.
The design of the cooling chain is presented in Sec. 4.4.4. The heat load into the system is separated into two main contributors: through mechanical contact and through radiation. To estimate the heat distribution along the device due to mechanical contacts the thermal resistances of the individual components are calculated in Sec. 4.4.5 and the heat circuit diagram was solved in Sec. 4.4.6. It was found that a total heat load of 77 W (through contact) goes into the system and causes thermal gradients between 16 K/m and 96 K/m along the undulator. Those gradients cause a phase advance of the radiation phase, see Sec. 4.4.7, up to -644.5 °, which has a contribution of +14.9 ° due to the magnetic gradient and -659.5 ° from the mechanical gradient along the device. In the warm state the undulator field has to be tuned such, that this systematic error vanishes for all gaps when the machine is cooled. This can be done for example by introducing a phase advance of +644.5 ° in the warm state which is then canceled out by the cooling, or by shimming the pillars in the cold state again.
The impact of the thermal radiation is discussed in Sec. 4.4.8. The radiation highly depends on the surface quality of the chamber walls and the aluminum girders, which have to be found experimentally. Besides that it was shown, that a simple shielding between the chamber and the girder will lead to a decrease of the absorbed heat by the undulator. An additional cooling of the shielding could suppress the incoming heat load down into the low one digit Watt range.

5 Assembling of the Undulator

In this chapter, some major topics for the assembling of the undulator are presented. To reduce the impact of the magnet's remanence field fluctuations onto the undulator field the magnets are sorted in advance and the effect is shown in Sec. 5.1. The average periodicity of the combs is measured in Sec. 5.2 and their alignment on the girder is shown in Sec. 5.3. Due to acting forces during the assembly of the magnets, the girders start to bulk, see Sec. 5.4, which has to be compensated with a later pillar shimming. During the installation of the girders inside the vacuum chamber, the rail system inside the chamber malfunctioned, see Sec. 5.5, and the undulator was exposed to vibrations. This deformed the field integrals, which required the installation of a compensation coil around the chamber, see Sec. 5.6. The cryo installation is discussed in Sec. 5.7.

5.1 Magnet Sorting

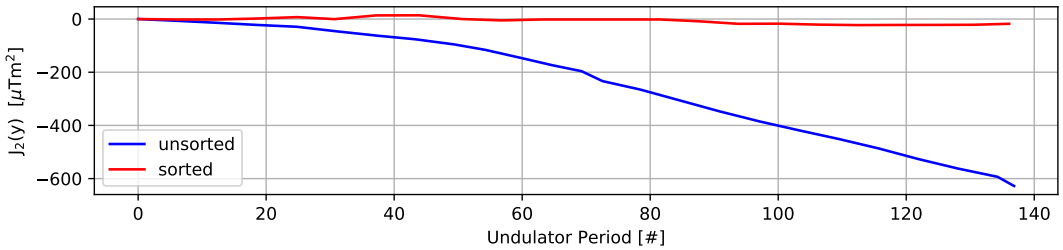

Figure 5.1 – Calculated effect of the magnet sorting onto the second field integral. The blue curve would be one result if the magnets would have been installed in random order. The red curve shows the result of a sorted installation which reduces the field integral. The data is provided by HZB [5].

Due to manufacturing processes the magnets can vary in size, field strength and direction of the magnetic field. These effects can be reduced by the manufacturer, but after a certain threshold these deviations can only be further reduced by an overproduction and subsequent hand sorting to get the desired magnets. Nevertheless, the remaining deviations of the magnetic field strength can be up to the order of 1% and the direction of magnetization up to 1 degree.

After the magnets are assembled in the girder and the girders are mounted in the frame, the shimming of the on-axis undulator field can start in which the poles are shifted in their vertical position to change the peak field. To reduce the amount of the required corrections a magnet sorting is done before the installation. The magnetic field for each individual magnet was measured and the magnets were sorted such, that the influence of their deviations onto the undulator field are minimized. With this sorting each magnet receives a unique position in the girder and it is possible to reduce the fluctuations of the second field integrals. In Fig. 5.1 is a field integral calculation for the unsorted field and the sorted field plotted to demonstrate the advantage of the sorting technique. For Frosty, the measurement of the individual magnets and the subsequent sorting list was provided by HZB [5].

5.2 Period Length

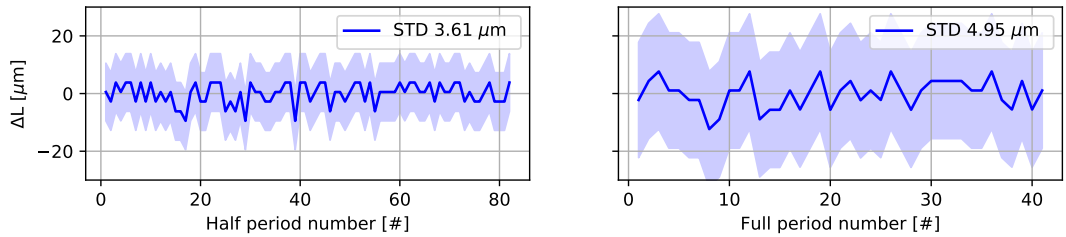

Figure 5.2 – Measured length deviation from the mean of the half periods on the left and the calculated error for the full period. The systematic error of the single measurement is 10 μm and plotted as the light blue background.

The comb structure is longitudinally subdivided into 3 sections with a hook system close to the intersections to link them up. The shortened structural length allows an easier manufacturing. The 6 combs of the lower girder and their facing comb in the upper girder are identical in construction and the pairs only differ in the hooking system at their ends. This allows to produce the holding structure of the magnets and poles within one machining run for all combs. Doing so causes machining errors to appear in all combs at the same positions, so the magnets and poles are only shifted in position along the longitudinal axis but not rotated. This shift causes an increase in the period length and a variation in the field integrals, which could be compensated by changing the peak field. To stay within the estimated standard deviation of 4.5 μm for the undulator periods all half periods of the combs were measured three times with a caliper gauge at 20 ° ambient temperature. The measurement accuracy for the single measurement of the caliper is given as 10 μm over 150 mm by the manufacturer. This error basically comes from the missing display for the 1 μm range.
An example of such a measurement is shown for one comb in Fig. 5.2. For the calculated

undulator period the systematic measurement error from two half periods ad up to 20 μm. The undulator period length over all combs at room temperature is determined to be

$$\lambda_u = 15080.56\,\mu\text{m} \pm 5.44\,\mu\text{m}\,(\text{S}) \pm 20\,\mu\text{m}\,(\text{M}).$$

This is, within the measurement error, acceptably close to the allowed statistical fluctuations (S) of $\pm$ 4.5 μm. The comparably high systematical error (M) for the single measurement of 20 μm arises from the measurement inaccuracy of the calipers and can be interpreted as the summed maximum worst case fluctuation of a single measurement of two half period which could occur. The given measurement accuracy of 10 μm for the single measurement is given by the lowest digit number on the tool. The measurements where repeated several times and the average was taken, so the real error will be well below 20 μm.

5.3 Comb Alignment

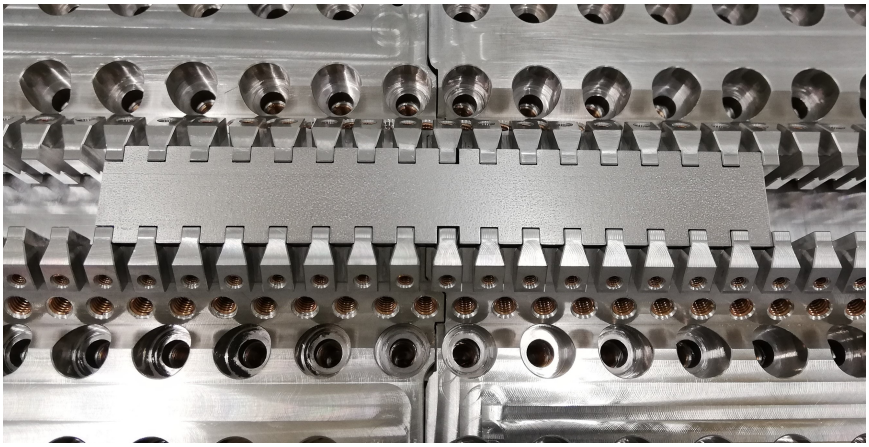

Figure 5.3 – A close up onto the alignment tool inserted into the comb structure of one girder. The increased bag for the tooth at the intersection comes from a machining error of the tool and not from the combs.

To align the combs to each other a negative of the magnetic structure was machined and inserted at the intersections. A close up onto the alignment tool can be seen in Fig. 5.3. The tool has one machining error at the center at which the cut out for the comb's tooth is too big. With this tool the combs can be adjusted in the longitudinal position and the horizontal spacing for the magnets and poles can be referenced. As mentioned before the combs have a hook system at their ends. The purpose of it is to connect all combs together such that they can only be moved as one unit. The design of the hooks was done such that they have a wrong contact between each other

when assembled which leads to a jack up of one comb. The resulting step from comb to comb is visible in Fig. 5.4. The left picture shows the offset between the first and second comb, the right shows the offset between second and third comb.

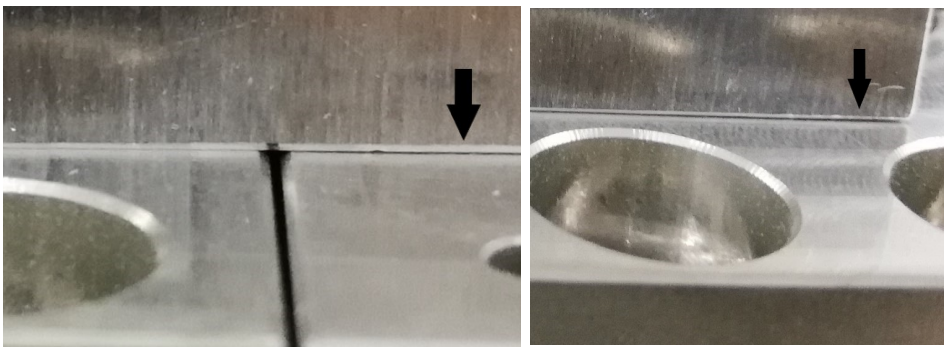

Figure 5.4 – Height offset between the combs at the intersections.

The relative height change of the comb surface with respect to the girder was measured with a laser scanner with 1 μm accuracy from the company Micro Epsilon [76] and is shown in Fig. 5.5.

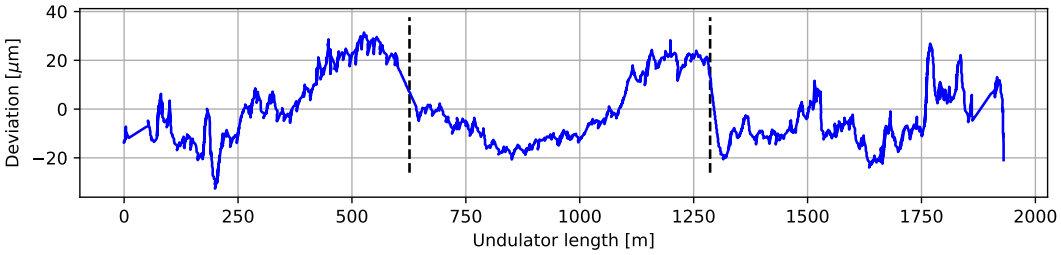

Figure 5.5 – Relative displacement of the comb surface along the undulator. Clear jumps around the intersections between the combs is visible.

The first comb bulks up about 30 μm towards the intersection as the comb sits on the second comb and not on the girder. The same happens between the intersection of the second and third comb with a jump of 40 μm. This deviation has no effect on the magnet position as they are directly blocked in position by the girder. But it affects the nominal position of the poles as the pole screws are mounted gap sided in the combs and their position follows the offset. The offset has an effect onto the cooling as the combs do not have a uniform contact surface over the full length.

5.4 Girder Bulking

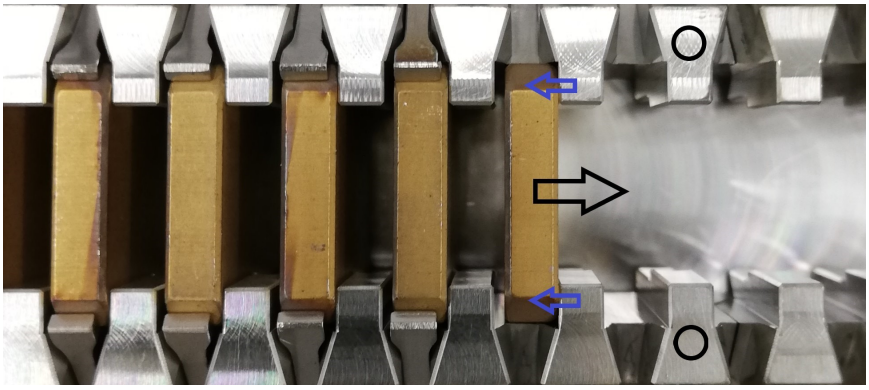

Figure 5.6 – Close up onto the magnet structure during the assembling. The black arrow indicates the direction of the repelling force onto a newly installed magnet which comes from the already installed magnets. The blue arrows indicate the force direction of the initial pre-load when subsequent magnets are installed and an equilibrium of the magnetic forces is reached. The black circles are reference points to measure the girder bulking.

When assembling the magnets inside the comb structure, stresses arise which cause a bulking of the girder. These stresses are caused by the repelling force between the magnetic structure and the newly installed magnet called M_a, which is pushed away from the already installed magnet lattice. A sketch of the acting force on M_a is indicated with the black arrow in Fig. 5.6. In the figure, the magnet is pushed towards the right side of its bag and induces a pressure on it. The new magnet M_a will now be fixed in position with a certain mechanical pre-load against the combs due to the repelling forces of the neighboring magnets. When the subsequent magnets are installed their repelling force onto M_a will act from the opposite direction and an equilibrium state for the longitudinally acting forces F_{z_i} will arise at M_a such that the sum of F_{z_i} becomes zero. What is left is now the initial pre-load with which the magnet was fixed in position. This initial stress will now counteract onto the combs in the direction of the blue arrows in Fig. 5.6 and produces a longitudinal pressure which will manifest in an elongation of the gap-sided surface. Due to this, the girder will bulk similar to a bi-metal strip which is warmed up on one side. The acting force between two magnets with magnetic field amplitudea B_i, cross sections A_i and a distance d can be calculated analogue to the Coulomb force and simplified for identical magnets to:

$$F = \frac{1}{4\pi\mu_0}\frac{B_1A_1 \cdot B_2A_2}{d^2} = \frac{1}{4\pi\mu_0}\frac{B^2A^2}{d^2}$$

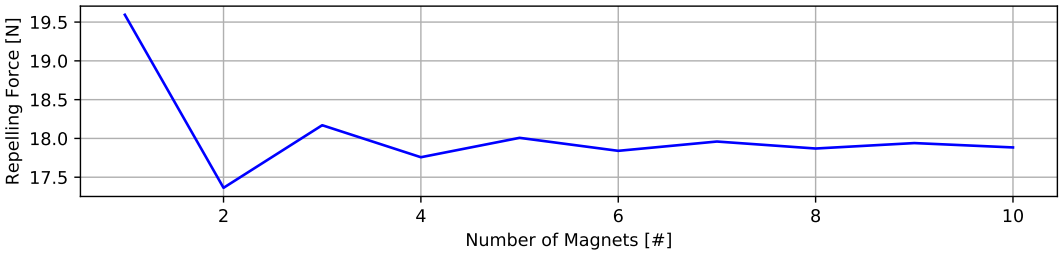

Figure 5.7 – Total repelling force onto one magnet for different numbers of magnets taken into account.

As the magnets are always assembled such that two neighboring magnets are flipped in the magnetic axis, the direct neighbor will push M_a, the next one will pull M_a and so on. This will lead to a reduced effective force acting onto M_a compared to just taking one neighbor into account, which has to be calculated first. The magnets are edged and also have cut outs at the edges which reduces the effective dimensions to $\approx$ 20 mm x 17 mm, so a cross section of 340 μm^2. As no poles are installed during the magnet assembly the amplitude of the open remanence field B $\approx$ 198 mT (see Fig. 4.20) has to be used. The distance between two neighboring magnets is 3.84 mm and increases about half a period (7.54 mm) per magnet.
Fig. 5.7 shows the repelling force onto one newly inserted magnet which changes for the number of magnets taken into account. The force settles around 17.72 N which will push against the comb structure and will act as a pre-load for each magnet during the assembling. Due to the alternating direction of the field amplitude, this pre-load is always pointing into the same direction. Summed over all 154 installed magnets in one girder this leads to a total force of F_{tot}= 4567 N acting into the longitudinal direction of the comb structure. To calculate the resulting bending from this force Eq. 1 from Tab. 4.8 is used and it is assumed, that the longitudinal acting force can be converted into a perpendicular acting force at the girder end. To measure the bulking of the girders they were put onto tables with the bulking pointing up. So, the gravitational force onto the 70 kg girder has to be considered to estimate the bending, as it acts against the bulking. The girder height is measured at the top surface of the comb structure, marked with black circles in Fig. 5.6, at 27 different positions along the girder. The measurement error is 0.1 mm. The measured bulking of both girders and the analytical estimate calculated here are shown in Fig. 5.8. The analytical expression fits good with the measured bulking of girder 2, but differs for girder 1. This is because the magnetic lattice inside girder 1 had to be built in and out several times as some magnets cracked and had to be replaced. This changed the pre-load in this region and also the deformation. The bulking up to 450 μm has to be shimmed out with the pillars when the girders are installed inside the frame. The ends of the girders, which overhang from the last pillars, will still be bent which has to be compensated by tuning the poles.

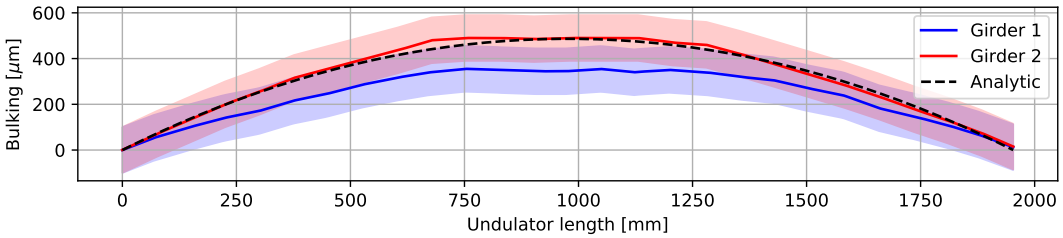

Figure 5.8 – Bulking of both girders and the analytical estimate described in the text. The colored regions are the measurement uncertainties.

5.5 Girder Installation

Figure 5.9 – The girder package on wheels moving into the chamber.

After the on-air shimming of the undulator field is done, see Sec. 7.2.4, the chamber has to be installed. For this the girders have to be removed. To preserve the shimmed field the girders are packed and bolted together to one girder package which is rolled on a rail system into the chamber, see Fig. 5.9. During the installation it turned out that the rail system was undersized to withstand the weight load of the 150 kg girder package. It started to bent such that the mounting bracket of the wheel touched the rail and drilled itself into the aluminum. This caused the whole system to be stuck in position. To shift the girders to its final position a certain momentum was required to overcome the friction which caused heavy vibrations of the package and a damaging of the rail system, see Fig. 5.10.

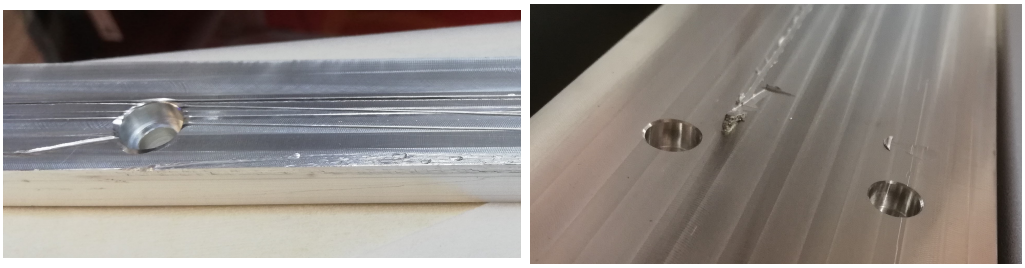

Figure 5.10 – Damaged rail system after the undulator was installed inside the chamber.

After the girders where in place again it turned out that the outer diameters of the pillars were too big to fit through the bellows of the chamber. They had to be reworked and cleaned after. During the machining and cleaning, the pillars were heated up to almost 100°. This heating caused inner tensions in the material to be released and bent the pillars. The consequence was, that the shimmed pillars were lost as reference marks for the girder installation and with that, the measured magnetic field.

5.6 Compensation Coils

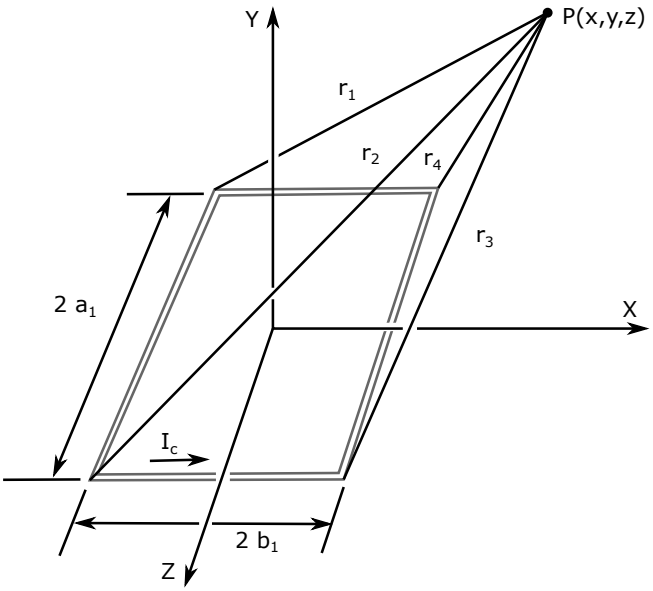

Figure 5.11 – Schematic sketch for the coil geometry in the coordinates of the undulator. The longitudinal axis goes along z, horizontal along x and vertical along y. The picture is from [10].

Electromagnetic coils around the undulator chamber are used to create an additional on-axis magnetic field with which errors in the trajectories, or the background field in the tunnel can be compensated. Pure air-core coils scale linear with the applied current, whereas the poles inside the undulator structure also amplify the field of the compensation coil. So, the field increase is also a gap dependent quantity and does not purely scale with the applied current. As the pole material starts to saturate for gaps smaller than 4 mm the amplification of the coil field would also decay for smaller gaps. This effect has to be simulated. For the compensation of field errors two coils with the geometry shown in Fig. 5.11 are mounted symmetrically above and below the undulator chamber with $x = 0.22\,m$ width and $z = 2.5\,m$ length. The coils are 0.38 m apart from each other and centered around the undulator gap. So, each coil is $y = 0.19\,m$ away from the gap. Both coils are powered such that the created magnetic field points into the same direction, similar to a Helmholtz coil. For one rectangular air-core coil analytical expressions to calculate the field at specific coordinates as shown in Fig. 5.11 are given in [10]. The coordinate system of the coil is aligned to the undulator, meaning y is pointing vertically, x horizontally and z into the longitudinal undulator direction. The magnetic field components created by the coil at one specific point P(x,y,z) are given as:

$$B_y = \frac{\mu_0 I_c N_c}{4\pi} \sum_{\alpha=1}^{4} \left[\frac{(-1)^\alpha d_\alpha}{r_\alpha [r_\alpha + (-1)^{\alpha+1} C_\alpha]} - \frac{C_\alpha}{r_\alpha [r_\alpha + d_\alpha]} \right]$$

$$B_x = \frac{\mu_0 I_c N_c}{4\pi} \sum_{\alpha=1}^{4} \left[\frac{(-1)^{\alpha+1} \cdot y}{r_\alpha [r_\alpha + d_\alpha]} \right]$$

$$B_z = \frac{\mu_0 I_c N_c}{4\pi} \sum_{\alpha=1}^{4} \left[\frac{(-1)^{\alpha+1} \cdot y}{r_\alpha [r_\alpha + (-1)^{\alpha+1} C_\alpha]} \right]$$

with

$$C_1 = -C_4 = a_1 + z \qquad C_2 = -C_3 = a_1 - z$$

$$d_1 = d_2 = x + b_1 \qquad d_3 = d_4 = x - b_1$$

$$r_1 = \sqrt{(a_1 + z)^2 + (x + b_1)^2 + y^2} \qquad r_2 = \sqrt{(a_1 - z)^2 + (x + b_1)^2 + y^2}$$

$$r_3 = \sqrt{(a_1 - z)^2 + (x - b_1)^2 + y^2} \qquad r_4 = \sqrt{(a_1 + z)^2 + (x - b_1)^2 + y^2}$$

Due to superposition of magnetic fields the on-axis field of both coils is double the field of one coil. The field distribution at the center axis along the z coordinate is plotted in Fig. 5.12 and is almost constant in the inner region of the coil where the undulator is positioned.

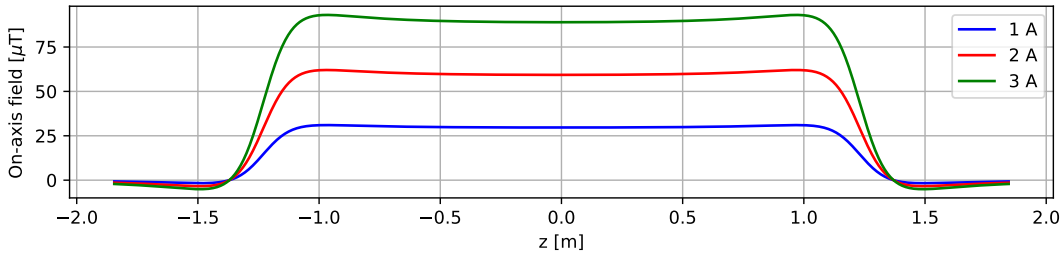

Figure 5.12 – Current dependent on-axis field generated by a coil pair in vacuum

For the center of the coil ($z = y = x = 0\,m$) the linear dependency between the applied current I and the generated vertical field is

$$B_y[\mu T] = 29.65 \cdot I[A] \tag{5.1}$$

The undulator poles are used to guide the field of the permanent magnets towards the gap, but they will also amplify the field generated by the coil. This amplification strongly depends on the saturation of the poles which increases with smaller gaps. As soon as the saturation starts, the amplification would decay compared to the not saturated regime. In contrast to the high on-axis field of up to 2 T generated by the permanent magnets, the amplified field of the coils is in the range of below 1 mT. That means, for one fixed setting, so one fixed gap with one fixed saturation point one would still expect a linear behavior between coil current and additional on-axis field without the influence of saturation effects, as the generated field is far below the 0.1 % range of the peak field, see Fig. 5.19. That means, the amplification for one setting is constant and by scanning the peak field for different gaps and coil currents one could extract a gap dependent amplification curve which gives the linear ratio between the coil field in-vacuum and the amplified field through Frosty.

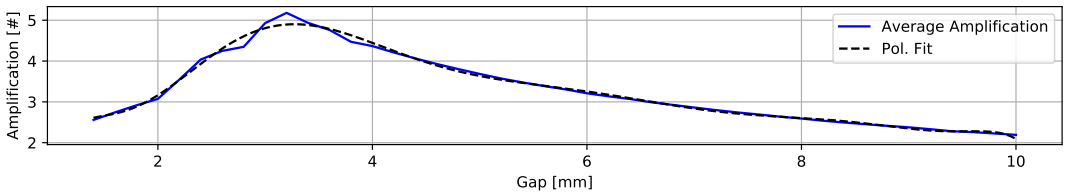

Figure 5.13 – Gap dependent amplification of the coil field through the poles.

The amplification of the coil field through the poles is scanned in CST by using one half period of the undulator and the coil in its full dimensions as given in the beginning of the section. The undulator field is simulated for different gaps and for different coil currents. For each setting the on axis field inside the half period is calculated.

These scans where done for coil currents between 0 A and 6 A in 1 A steps. The 0 A simulation is a reference for the undisturbed undulator field. To calculate the amplified coil field the 0 A measurement is subtracted from all other measurements. To get the amplification factor, the amplified coil field is divided by the estimated peak field of an air-core coil given in Eq. 5.1. The resulting average amplification is plotted in Fig. 5.13 which shows an exponential increase of the amplification with smaller gaps down to ≈ 3 mm, which is expected as the undulator peak field follows an exponential behavior and, therefore, also the amplification follows this behavior. For smaller gaps the poles start to saturate which decreases also the amplification factor within this region. One have to note here that the small bend in the distribution between 2 mm and 4 mm gap are generated by the meshing of the used model and are unphysical. A 10th order polynomial $A(g) = \sum_i h_i \cdot g^i$ is fit to the gap dependent amplification with the fit parameters

i	0	1	2	3	4	5
h_i[1/mm]	-62.469	192.565	-238.207	161.02	-65.837	17.18
i	6	7	8	9	10	
h_i[1/mm]	-2.929	0.325	-0.023	$9.01 \cdot 10^{-4}$	$-0.156 \cdot 10^{-4}$	

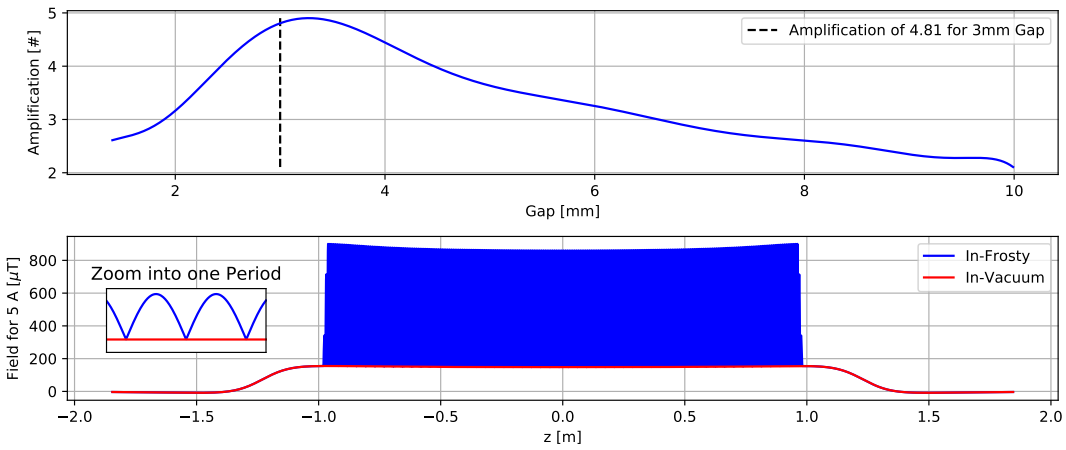

Figure 5.14 – Coil field in-vacuum and amplified for 3 mm undulator gap and 5 A coil current.

Using this function it is possible to determine the amplified coil field on the undulator axis which is shown in Fig. 5.14. Outside the undulator, the field follows the behavior of an air-core coil (red) whereas the field gets amplified in the presence of the pole material (blue). The amplified field is homogeneous in the range from z = -0.5 m to 0.5 m and start to increase towards the fringes of the coil.

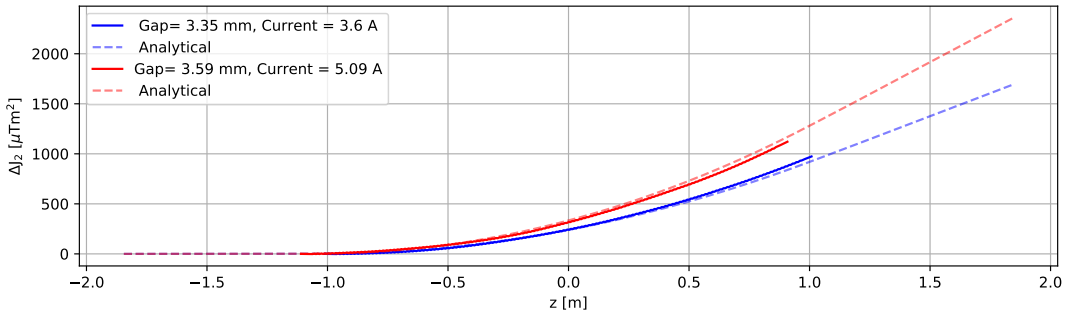

Figure 5.15 – Change of the field integrals due to an applied coil current.

To validate this empirical model the magnetic field along the undulator was measured at different gaps for different coil currents. The measured change of the field integral and the estimated change due to the coil are shown in Fig. 5.15. The curves are close, but not perfectly matching. The analytical curve overestimates the change for higher gaps. The reasons for the difference are diverse. The model assumes a perfect undulator with a constant gap along the machine and a coil pair which is mounted symmetrically around the gap without any sagging of the cables. In reality the poles were tuned before so the gap is not constant and the coil gets amplified about different amounts at different pole positions. Also, the coils are only attached to the vacuum chamber of the undulator and are not referenced to the undulator on-axis field itself. The chamber is mounted on eight height adjustment units which were adjusted such that the chamber does not wiggle in position, but the chamber could be off to the magnetic axis about one cm or 3 degrees in angle. A picture of the upper coil (the gray cable winded around the flange in the center) is shown in Fig. 5.16. A sagging of the wire along the undulator chamber is visible which results in a disturbed field distribution along the machine.

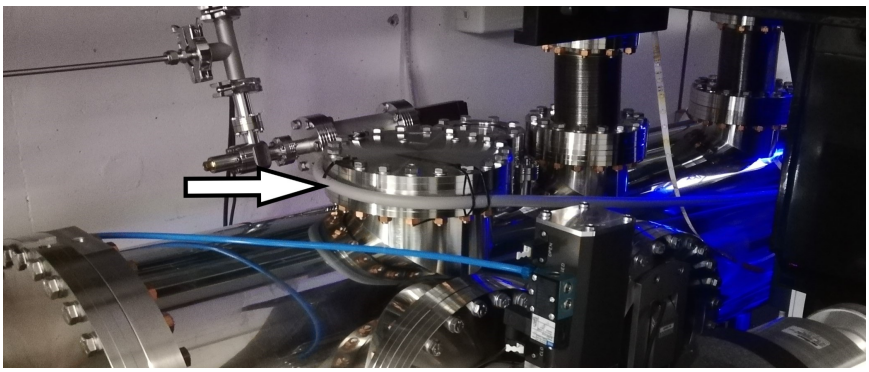

Figure 5.16 – The grey cable strapped to the flange in the middle is the upper coil to tune the on-axis field.

Besides these influences the model is still valid as a good approximation to tune the field integrals closer to zero for a given gap. The final measurements of the undulator field, which will be discussed in Sec. 7.2.5 can now be used to estimate the required coil current to get either J_1 or J_2 to zero. The case $J_1 = J_2 = 0$ would correspond to an undisturbed sinusoidal undulator field and is hardly achievable. Under the assumption, that all undulator field errors scale linear with the peak field Eq. 4.1 is used to rescale the field integrals depending on the gap.

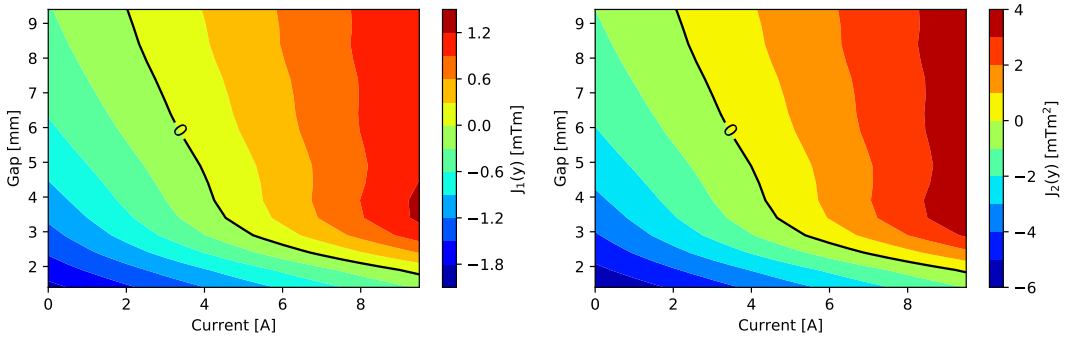

Figure 5.17 – Required coil current to compensate first and second field integral errors of the final field, see Sec. 7.2.5. The amplitude is rescaled with Eq. 4.1. The black curve marks the setting to reduce the integrals to zero at a distance of 2.07 m after the undulator.

In Fig. 5.17 the required current to tune the first or second field integral of the final undulator field are shown. The current is not constant for all gaps, as the amplification of the coil signal follows an exponential behavior and distorts in the saturation region of the poles, see Fig. 5.13. The black curves in Fig. 5.17 mark the current to get the respective field integral at a certain gap and after a certain distance to zero. The distance here was chosen to be 2.07 m after the undulator exit because in the beamline a screen station is installed after that distance, at which the transverse position of the electron beam can be monitored. Those curves are close to identical and only deviate about a small offset. The reason for this is rather simple. When the first field integral is fully compensated, electrons leave the undulator only with an offset dx, but not with a kick, so dx'=0. To compensate the second field integral such that it becomes zero after a certain distance l, only a small change of the coil current is required to produce an additional kick dx' such that the electron beam is steered back to the axis until $dx' \cdot l = 0$. The longer this distance is the smaller the current needs to be.
To estimate the coil current which is required to compensate the respective gap dependent field integral error both black curves are expressed by 10th order polynomials $A_{J_1}(g)$ and $B_{J_2}(g)$ with the fit parameters:

i	0	1	2	3	4	5
a_i[A/mm]	-114.393	286.897	-269.758	138.306	-43.954	9.175
b_i[A/mm]	-118.231	296.178	-278.472	142.822	-45.417	9.489
i	6	7	8	9	10	
a_i[A/mm]	-1.286	0.12	$-71.993 \cdot 10^{-4}$	$2.507 \cdot 10^{-4}$	$-0.039 \cdot 10^{-4}$	
b_i[A/mm]	-1.331	0.125	$-74.74 \cdot 10^{-4}$	$2.607 \cdot 10^{-4}$	$-0.04 \cdot 10^{-4}$	

An example of the integral compensation for a 7 mm gap is shown in Fig. 5.18. When the first field integral is compensated (red) the particle would leave the undulator field without an additional kick and only with an offset. Increasing the coil current about 110 mA would cause an overcompensation of J_1 which leads to a kick and a resulting J_2 compensation at a certain position after the undulator, marked as the dashed line. If one would like to compensate both integrals a second coil at the end of the undulator would be required. Then, the first coil would compensate J_2 such that it is zero right after the undulator and the second coil would compensate for a leftover kick.

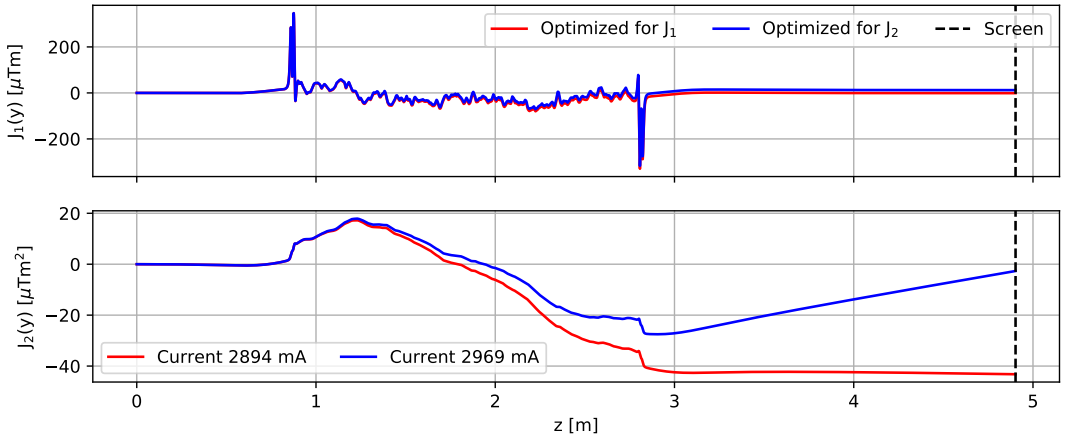

Figure 5.18 – Integral compensation with the coil for an 7 mm gap. The compensation is either for the first, or the second field integral. The dash line represents the plane at which the second field integral should be zero. The integrals are averaged to suppress the oscillation.

In Fig 5.19 the effect of a gap variation with constant coil current and vice versa is shown. The left pictures show representative second field integrals and the right ones full range scans evaluated on a screen plane behind the undulator. Assuming a 300 MeV electron beam the field integrals can directly be converted to position offsets like $1\,\mu\text{Tm}^2 \approx 1\,\mu\text{m}$. If a constant current is applied to the coil the exponential field increase and especially the saturating poles dominate the field error and cause a

deflection while driving the gap. When the gap is fixed the coil current causes a linear deflection of an electron beam with the applied coil current, as explained earlier.

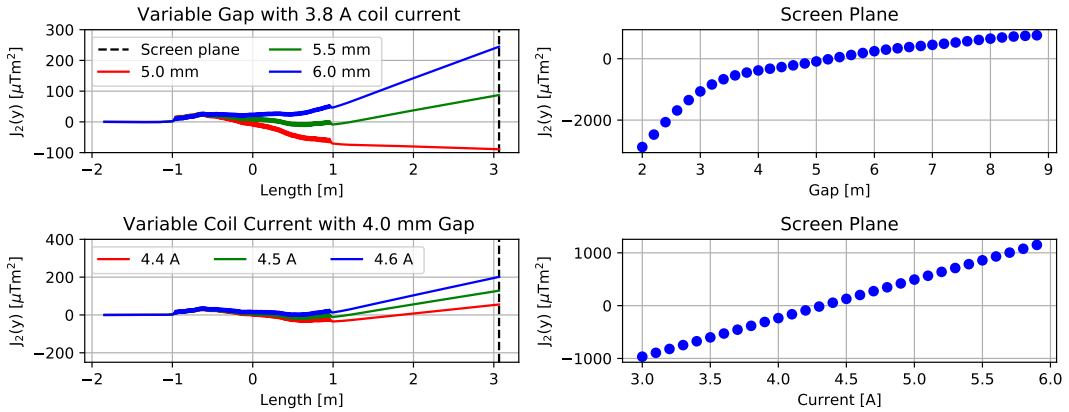

Figure 5.19 – Deflection of the undulator for different coil currents and gaps. In the upper plots a constant coil current is applied and the deflection of the second field integral is shown on a screen 2.07 m after the undulator. In the lower part the gap is set constant and the coil current varies which results in a linear deflection.

The validity of the derived model above has its limits. First, the simulations on how the coil current affects the on-axis field was limited to a range between 1.5 mm and 10 mm which also limits the derived polynomials. Second, it was assumed that the field errors linearly scale with the amplitude of the peak field B_0 over the whole gap range because the respective magnetic field component scales with the peak field, see Eq. 2.9. This is only true within a small range around the measured gap. As shown in Fig. 5.7 a single magnet interferes with all magnets within the neighboring 10 undulator periods. So, also the local measured undulator field is a superposition of those ten periods which are all affected by a local exponential gap dependency and positioning errors. This superposition, which consists out of exponential functions, will only change linear within a small range, but most likely not over the full gap range between 2 mm to 40 mm.

5.7 Cryo Cooler

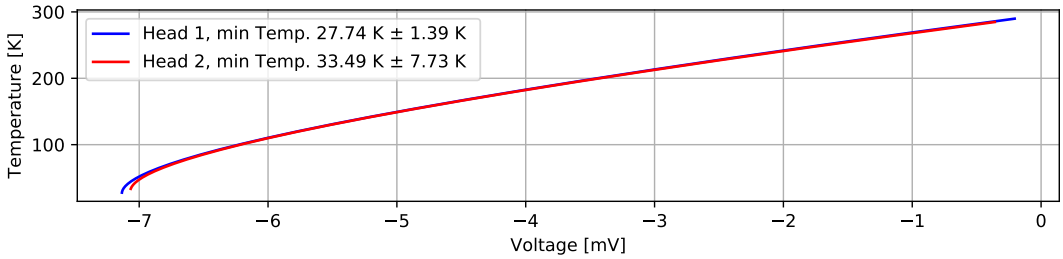

Figure 5.20 – Temperature curve of the cryo heads vs voltage readout of the sensors.

The temperature curves of the used cryo heads are first cross checked to estimate the minimum reachable temperature, as they are only specified to reach temperatures below 40 K with 54 W on cooling power [8]. To do so, 10 temperature sensors were connected to the cryo head and their voltage curve vs. temperature was recorded, see Fig. 5.20. The voltage output goes strictly linear with temperature. A change in voltage is recalculated to a temperate change. The minimum temperature reached by cold head 1 is $27.74\,\mathrm{K} \pm 1.4\,\mathrm{K}$ and by cold head 2 is $33.5\,\mathrm{K} \pm 7.7\,\mathrm{K}$, so both reach their specified temperature below 40 K. The high difference in the error can come from the connection between the sensors and the cold heads and or systematic errors of the temperature sensors and their read out electronics.
The original design of Frosty included the cryogenic cooling of the magnets to increase the undulator peak field and push the K - parameter close to 3. In parallel to the manufacturing of the undulator, simulations, optimizations and improvements were performed by my group members to get a deeper insight into the laser plasma based free electron lasing at Lux. With the available parameter space at Lux, an optimum for the lasing was found for a K-parameter close around two. This K- range is easily accessible even in the warm state of the undulator, see Sec. 4.2.3, and renders a cooling unnecessary. In addition, the cooling concept of Frosty will have a complex influence onto the phase, see Sec. 4.4.7, which is quite delicate to manage. So it was decided to skip the cooling in a first run, which means that the cooling chain was not installed into the undulator. If it turns out that the cooling is required, it can be upgraded on demand.

5.8 Conclusion

The sorting of the magnets, see Sec. 5.1, decreases the initial second field integral close to zero which means that the pole tuning has to be done about some one digit μm and

not about several hundreds of μm. The geometrical period length of the combs was determined to be

$$\lambda_u = 15080.56\,\mu\text{m} \pm 5.44\,\mu\text{m} \pm 20\,\mu\text{m}$$

with a statistical error of 5.44 μm and a systematic error of 20 μm, see Sec. 5.2. The combs were installed onto the girder and their distance between the girder and the gap sided comb surface was measured. It was found, that the ends of the combs lie on top on each other which causes a bulking of the surface up to 30 μm, see Sec. 5.3.
When assembling magnets inside the combs, repelling forces create a longitudinal stress along the girder. This stress results in a bulking up to 450 μm in the middle which has to be compensated by an adequate adjustment of the pillars, see Sec. 5.4.
Due to a malfunction of the rail system, see Sec. 5.5, which was used to install the girders inside the vacuum chamber, they were exposed to vibrations during the installation which lead to a deformation of the field integrals, see Sec. 7.2.5.
To adjust errors in the field trajectory, a compensation coil is installed around the undulator chamber. The field of the coil is also amplified by the poles of the magnetic array, where the gap dependent amplification factor was found by simulations. The model was cross checked with measurements and is in a good agreement. As the undulator poles start to saturate below 4 mm gap, also the coil amplification will change and a higher current is required. The required polynomial to convert the gap value into a current to compensate for first, or second field integral errors was found and presented in Sec. 5.6. In Sec. 5.7 the temperature curves of the cryo coolers were measured. For the FEL process, the desired K-value range changed to a region which is also accessible at warm temperatures which is why the cryo coolers were not installed.

6 The Measurement System

After the assembling and geometrical tuning of the undulator, the magnetic field has to be flattened to reduce the disturbances of the electron trajectories. To do so, it is necessary to derive thresholds for the alignment as it is hardly possible to tune a machine in the laboratory such that it is congruent with the theoretical description of a pure sinusoidal field. As the tuning takes place in the absence of any electron source all radiation characteristics of the undulator radiation have to be linked and expressed in terms of quantities which are accessible in the laboratory. The three figures of merits here are the first field integral (expresses the deflection of particles), the second field integral (represents the position) and the phase error which gives the gain length increase of the FEL [48]. Those three quantities are directly calculated from magnetic field measurements and adequately manipulated to shape the trajectory, see Sec. 2.1. The boundaries can be derived in two ways.
First, out of the one particle undulator theory, see Sec. 2.3. Here, the undulator is the only error source which degrades the light quality. This results in intrinsic limitations which are independent of all electron beam parameters like energy spread, diameter, initial position / divergence, focusing and so on. Those limits can be very tight and disproportionately strict comparing them to the influences of the electron beam parameters mentioned.
A more reasonable approach is, to also take the electron beam into account and to derive balanced limits for the individual error sources out of FEL simulations. For Frosty, those simulations were done by Thorben Seggebrock and published in his PhD thesis [4] in 2015.
Due to extensive developments at the Lux beamline the electron beam gained in quality over the years which relaxed and changed the working point for the lasing in comparison to [4], so also the derived limits in [4] have to be checked again.
In this chapter, the boundaries for the tuning from both ansatzes are discussed in Sec. 6.1. Besides just knowing the boundaries to which the field integrals have to be tuned, it is also important that the accuracy and reproducibility of the measurement bench actually allows measurements within those limits. So, to get qualified statements from the measured field profiles it is mandatory to drive the Hall probe along a reproducible path through the undulator. To do so, an active regulation of the transverse Hall probe position onto a laser line is installed. To estimate the performance of the bench the error influence of each measurable quantity is described and discussed in detail in Sec. 6.2 and cross checked with reproducibility scans.

6.1 Field Integral and Alignment Tolerances

As the free electron lasing depends on the interaction between the light field and the electrons it is easy to understand that the maximum performance is achieved when the phase space volume of the electron beam and the photon field are equal and do overlap.
In a first assumption this can be achieved, when the angular deflection of the electrons is always below the natural divergence of the photons and the transverse position of the electrons always within the light cone. With a decreasing overlap, the FEL performance will also decrease until the amplification is lost. So, the FEL degradation is a fluent transition and does not simply interrupt at a certain threshold. Therein lies an issue for the undulator tuning: It is hardly possible to tune the field to such a quality, that it corresponds to the mathematical definition of a sinusoidal field. So, fixed upper limits for the field integral deviations are required, which have to be evaluated by extensive FEL studies, as done by Thorben Seggebrock for the Frosty undulator [4]. The derived limits of the study are linked to electron beam parameters which, in the case of the Lux facility, gained in quality since the publication of [4] which means, that also the limits for the undulator field deviations have to be evaluated again. As it is expected that the quality of the electron beam parameters at Lux will further increase in the future [12], it is recommended to use measures which are independent of the FEL process and the electron beam quality.
A reasonable approach is to link the field integrals to intrinsic limits from the one particle theory described in Sec. 2.3.2 and Sec. 2.3.3, namely the opening angle and source size of a single emitted photon. Here, one have to keep in mind, that different mathematical definitions of the undulator radiation exist (see Eq. 2.16, Eq. 2.17 and Eq. 2.20) which either refer to the exact harmonic wavelength, or to the peak wavelength and differ about a factor of $\sqrt{2}$, see Sec. 2.3.3 [1, 17]. Following from this, also the intrinsic limits will vary for the field integrals, which have to be evaluated first. To distinguish those limits, they will be denoted as J_p for the peak wavelength and J_e for the exact harmonic and discussed after.
As an alternative limit for the maximum position deviation it is also valid to define the oscillation amplitude as an upper boundary, as this one is in any case smaller than the radiation cone of the light. On the downside, this limit can be very tough to achieve and more strict than necessary.
As already stated, those limits are not clear boundaries at which the FEL immediately collapses but should be interpreted in the sense that it could be possible to observe undulator related degrading effects, when the field errors are far above the limits and electron beam errors like the energy spread are close to zero and could be neglected.

J_1 Limit

As stated, the angular spread error onto Eq. 2.2 should be smaller than the natural divergence of the single photon beam, see Eq. 2.16 and Eq. 2.20, so $\Delta x' \leq \sigma_{r'}$. It follows for the upper limits for the first field integral J_1:

$$\begin{aligned} J_{1,p} &\leq \frac{m_e c}{e}\sqrt{\left(1+\frac{K^2}{2}\right)\cdot\frac{1}{2\cdot N_u}} \\ J_{1,e} &\leq \frac{m_e c}{e}\sqrt{\left(1+\frac{K^2}{2}\right)\cdot\frac{1}{4\cdot N_u}} \end{aligned} \tag{6.1}$$

J_2 Limit

To keep the electron inside the radiation cone $\Delta x \leq \sigma_r$, see Eq. 2.2, Eq. 2.17 and Eq. 2.20, the second field integrals have to stay below

$$\begin{aligned} J_{2,p} &\leq \frac{m_e c}{e}\frac{\lambda_u}{4\pi}\sqrt{\frac{N_u}{2}\left(1+\frac{K^2}{2}\right)} \\ J_{2,e} &\leq \frac{m_e c}{e}\frac{\lambda_u}{4\pi}\sqrt{N_u\left(1+\frac{K^2}{2}\right)} \end{aligned}$$

whereas the maximum oscillation amplitude is at

$$J_{2,h} = \pm\frac{B_0}{k_u^2}$$

Beam Wander Limit

Due to disturbances inside the first field integral it is possible that the electron trajectory stays within the J_2 limit but bounces between the limits. This will most likely appear in those periods in which the field was tuned such that the trajectory will be kicked back on axis. There, the mean trajectory will have a small curvature which causes the particles to radiate into different directions, so a red shift compared to the ideal radiation will occur, which decreases the performance due to deconstructive interference of the light. The figure of merit here is the rms deviation from the mean path of

propagation, called beam wander, which is the standard deviation of the cumulative second field integral $\Delta J_{2,n}$ [77, 4]:

$$J_{2,bw} = \sqrt{\frac{1}{2N_u} \sum_{n=1}^{2N_u} (\Delta J_{2,n})^2}$$

The beam wander describes the rms overlap between the electron bunch and the emitted light field, so it also has to stay within the light cone:

$$J_{2,bw} \leq J_2$$

J_{ph} limit

The longitudinal motion of the electron given in Eq. 2.4 determines the central wave train emitted by the undulator and the longitudinal synchronization of the FEL. Small errors in the trajectory cause phase shifts between the waves emitted in the individual periods. Those phase errors will lead to destructive interference and a power loss. The radiation phase is [1, 17]:

$$\begin{aligned} \Phi_n &= \frac{\pi}{\lambda} \left(\frac{z}{2\gamma^2} + \frac{1}{2} \int \beta_x^2 dz \right) \\ &= \frac{k_u}{1 + \frac{K_0^2}{2}} \left(z + \left(\frac{e}{m_e \cdot c} \right)^2 \cdot J_{ph} \right) \end{aligned} \tag{6.2}$$

In the one particle theory, in which the undulator field is the only degradation effect of the emitted power, the ratio R of the power loss scales with the rms phase error, called phase jitter Φ as [1, 17]

$$R \approx e^{-n^2 \cdot \Phi^2} \tag{6.3}$$

where n is the higher harmonic of the emitted radiation. The fast degradation of the power at a certain wavelength harmonic is plotted in in Fig. 6.1.

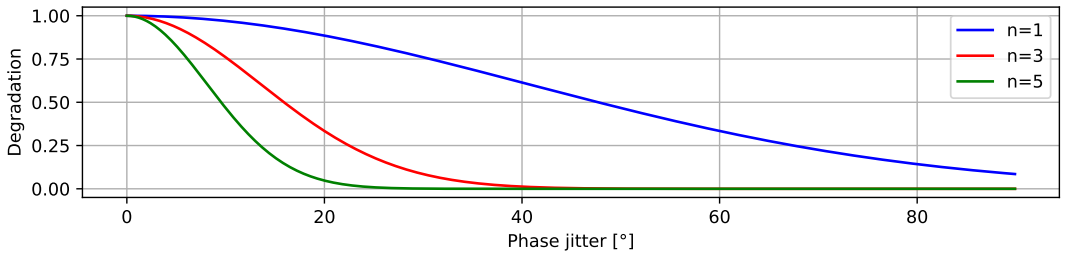

Figure 6.1 – Power degradation of the nth harmonic for different phase jitters.

The phase jitter Φ is a crucial quantity because it increases the gain length of the FEL process like $\Delta L_G/L_G = \Phi^2/3$ [48]. From this equation the phase error can be estimated at which the gain length is increased about a factor of the FEL bandwidth ρ:

$$\Phi = \sqrt{3 \cdot \rho}$$

To calculate the phase error several options are available:

1. Using the change of the K-parameter as this would represent the wavelength change from each half period. This method assumes that the undulator has only errors in the magnetic field and that the peaks are equidistant, so geometrical errors can not be be represented with this method and the evaluated phase error would be an under estimation of the real error.

2. Using the phase integral which describes the slippage of a particle along the device with respect to the emitted wavefront. This is a 1D approximation which can directly be retrieved from the measured data but does not consider 3D effects from the electron trajectory or the observation point of the radiation.

3. By tracking a particle through the measured 3D magnetic field, calculating the observed electrical field (see Eq. 2.7) of the light pulse and retrieving the phase error from that. With this method, all possible effects like initial electron beam divergence, the observation point relative to the whole 3D magnetic undulator field and collective undulator errors are taken into account and is therefore closest to reality and will be used here.

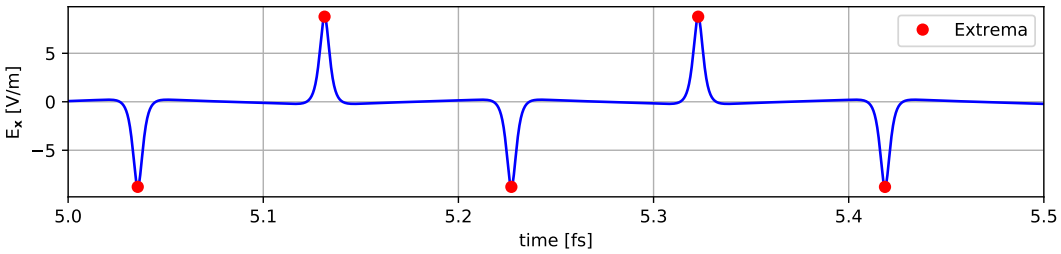

Figure 6.2 – Observed horizontal electrical field component of the photon wave train in a distance of z= 100 m for a K of 1.9, λ_u= 15 mm and an electron energy of 300 MeV. The red dots mark the extreme which are used for the phase error evaluation.

In Fig. 6.2 the observed electrical field is shown which was calculated by a measured magnetic field and an observer distance of 100 m away from the undulator. The blue line gives the amplitude of the observed electrical field and the red dots mark the extreme, which are used for the phase error calculation. The distance between two red dots is one half period $\lambda_{1/2}(i)$ of the emitted wavelength of period i.

The phase error of the i-th half period with respect to the average length of a half period $\lambda_{1/2}$ is calculated with

$$\Delta\Phi_\mathrm{i} = \pi \frac{\lambda_{1/2}(\mathrm{i}) - \lambda_{1/2}}{\lambda_{1/2}}.$$

The phase error at the n-th undulator half period is the sum over all individual phase errors, so $\Delta\Phi_\mathrm{n} = \sum_{\mathrm{i}=1}^{\mathrm{n}} \Delta\Phi_\mathrm{i}$ and the figure of merit is, to get the rms phase error, the phase jitter Φ, small:

$$\Phi = \sqrt{\frac{1}{2\mathrm{N_u}} \sum_{\mathrm{n}=1}^{2\,\mathrm{N_u}} \Delta\Phi_\mathrm{n}^2}$$

The measured field has to be up sampled to increase the resolution of the calculated electrical field of the wave train which will cause an additional error induced by the simulation. This error is estimated by calculating the phase jitter for a perfect sinusoidal field with the same number of grid points and marked as (S) in the following to distinguish it from the measurement error marked as (M). An example for the error introduced by the simulation is plotted in Fig. 6.3. The systematic error is in the range of $\approx 0.02°$. Phase errors are expected to be in the one digit degree range, so this error is negligible small, but has to be mentioned.

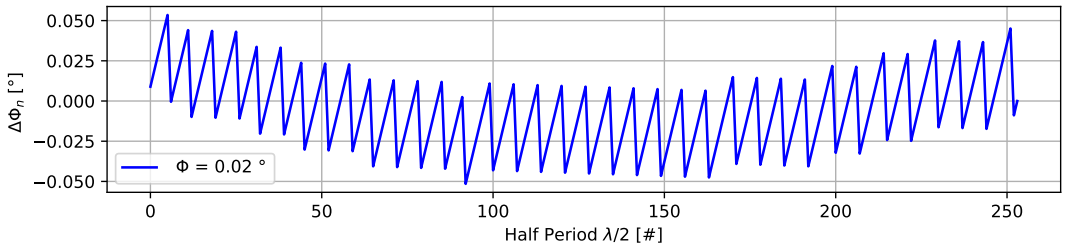

Figure 6.3 – Phase error of the simulation code for an ideal on-axis undulator field.

Discussion

K	1	2	3
ρ [10^{-3}]	4.9	7.1	9.0
$J_{1,p}$ [μTm]	129	184	250
$J_{1,e}$ [μTm]	91	130	176
$J_{2,p}$ [μTm^2]	20	28	38
$J_{2,e}$ [μTm^2]	28	40	54
$J_{2,h}$ [μTm^2]	$\pm$4	$\pm$8	$\pm$12
Φ [°]	6.9	8.4	9.4

Table 6.1 – Tuning limits for the integrals out of the one particle theory for different K values of the undulator. The relevant limits are marked in green. For the Pierce parameter (see Eq. 2.25) a beam diameter of $\sigma_x = \sigma_y = 30$ μm, λ_u= 15 mm, a current of I_b=1.2 kA and a γ = 600 are assumed.

As mentioned earlier, extensive FEL simulations were done to estimate the impact of undulator field errors onto the FEL performance when a real beam is sent through the machine, see [4]. The tolerances were simulated by evaluating the power ratio of the FEL at a K-value of 3.3 as a function of the error source and are defined such, that the FEL degradation is below 5% for all combined undulator errors. For the tuning of the undulator, the limits for the beam wander and the phase jitter are of major interest, which were found to be ≈ 34 μTm^2 and 17.8° [4]. So, if the undulator has a beam wander and a phase jitter on this level, the FEL power would decrease about 5%. The simulated limit for the beam wander is on the same scale as the one particle beam wander limit for the peak wavelength, see Tab. 6.1, whereas the simulated phase jitter is roughly double in value. So, when staying below the limits in Tab. 6.1, the influence of field errors onto the FEL performance is assumed to be in the low one-digit % range. To ensure this, always the smallest value for the integral limit of Tab. 6.1 is chosen as a figure of merit and marked as green.
The design K value of Frosty changed from the 3.3 in [4] to a value close to 2 with a peak field of B_0=1.42 T, which means that the first field integral should stay below $J_1 = 130\,\mu$Tm. J_2 and the beam wander should stay below $28\,\mu$Tm^2 and the phase error below 8.4°.
The hard limit for the second field integral allows a deviation of $J_{2,h} \pm 8$ μTm^2, which is difficult to achieve, as it challenges the accuracy of the measurement bench:
Assuming $J_{2,h}$ as the maximum allowed measurement uncertainty over 130 undulator periods, a maximum measurement uncertainty of $J_{2,hp} \approx 63$ nTm^2 within a single undulator period is allowed, so a maximum cumulative position uncertainty of $\pi \cdot J_{2,hp}/B_0/\lambda_u \approx 9\,\mu$m for one period. Assuming 20 measurement points per period, the accuracy of a single measurement has to be in the range of 0.45 μm. To measure with this accuracy over several meters requires a full understanding and characterization of

the used measurement bench down to this level, which will be discussed in full detail in Sec. 6.2.
Despite the difficulty to measure with an accuracy better than described above, the integral limits should be chosen such that the remaining deviations have close to no impact onto the performance. So, for the second field integral deviations $J_{2,h}$ is targeted, whereas $J_{2,e}$ is set as a goal.

Alignment Accuracy

Besides the tuning limits it is also important to align the measurement bench within a certain precision to the undulator. This becomes of major importance if the undulator axes of an already tuned field have to be found again. A good quantity for the alignment limit is the so-called good field region which defines the distance in the transverse direction after which the undulator peak field changed about a certain value $\Delta B/B$. This change of the amplitude can be directly converted into a transverse position or angle from Eq. 2.9:

$$y,x = \sqrt{2\frac{\Delta B}{B}}/k_{x,y} \qquad\qquad y', x' = x, y/L_u$$

where L_u is the undulator length of 2 m and $k_{x,y}$ the respective periodicity in x or y, which have a maximum for $k_{x,y} = k_u = 2\pi/\lambda_u$. Typically, the good field region is defined as the region in which the field amplitude does not vary about more than 10^{-3} which would give an upper limit for the required alignment accuracies. To stay below this threshold a good field region of 10^{-4} is chosen to increase the reproducibility of the alignment procedure. Assuming this good field region and also using the maximum values $k_{x,y} \approx 416\ m^{-1}$ gives alignment limits of

$$y, x = 34\,\mu m \qquad\qquad y', x' = 17\,\mu rad$$

for the Hall probe to the magnetic axes. For a later alignment of the electron beam to the undulator field it is a reasonable demand that the beam orbit should stay within a good field region of 10^{-3}, which would give a required electron beam alignment accuracy of $\approx 100\ \mu m$ in position and $\approx 50\ \mu rad$ in angle.

6.2 The Measurement Bench

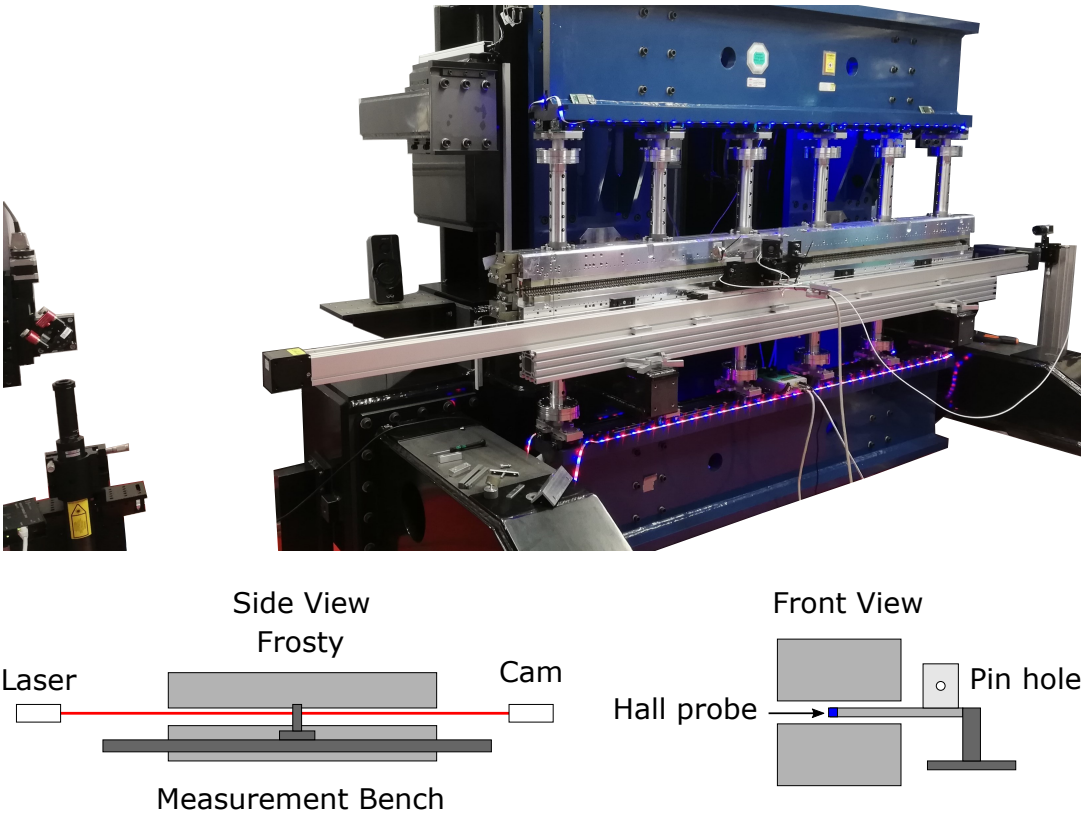

Figure 6.4 – Picture of the measurement setup on top and a sketch on the bottom. A reference laser goes from the left to a camera on the right through a pinhole mounted on the slider (center). The slider carries the Hall probe while it is driving along the measurement bench.

To characterize the undulator field, a so-called SAFALI system (self aligned field analyzer with laser instrumentation) is built, which needs to be characterized in terms of measurement accuracies. In this section all involved components are presented and their individual alignment to the magnetic axes of the undulator and their influence onto the measured field are described. In Fig. 6.4 the actual setup and a sketch of the main components is shown. The measurement bench consists out of a motorized 3 m long stage (long silver block in front of the undulator) which is aligned parallel to the girders. The stage carries a slider on which the measurement setup is mounted. The longitudinal position is recorded with an interferometer (Not in the picture). On the slider the Hall probe is connected to a carrier with 3 piezo stages and a pin hole. A laser is aligned parallel to the magnetic axis through the pinhole and the profile is measured with a camera on the other side. When the center of mass on the camera changes

above a certain threshold the piezo stages actively regulate the pinhole (and the probe) in position. With this setup the transverse accuracy of the probe is regulated actively in a closed loop. The hole bench measures in a step-by-step mode to simplify the data synchronization of the individual measurement systems. As the stage was a work in progress project during the installation of the undulator, the setup changed frequently to improve the bench. In this section only the final version is presented but different setups are shown along the pictures.
To get an insight how strong a measurement error may influence the field integrals a small simulation is done:
For each quantity the rms measurement error is added as a noise fluctuation with Gaussian distribution to an ideal sinusoidal magnetic field with a peak field of $B_0 = 1.2\,\mathrm{T}$ and a period length of $\lambda_u = 15.08\,\mathrm{mm}$. The noise quantities $B_n = (B_{nx}, B_{ny}, B_{nz})$, x_n and y_n are added to Eq. 2.10 like :

$$\vec{B}_{noise}(x,y,z) = B_n - B_0 \begin{pmatrix} -k_x^2 \cdot (x + x_n) \cdot (y + y_n) \sin(k_u \cdot z) \\ \left(1 - \frac{(k_x \cdot (x+x_n))^2}{2} + \frac{(k_y \cdot (y+y_n))^2}{2}\right) \sin(k_u \cdot z) \\ k_u \cdot (y + y_n) \cos(k_u \cdot z) \end{pmatrix} \tag{6.4}$$

and z_n is added to the integration path as $s = z + z_n$ only. For the periodicities the measurements of Tab. 7.1 are used.

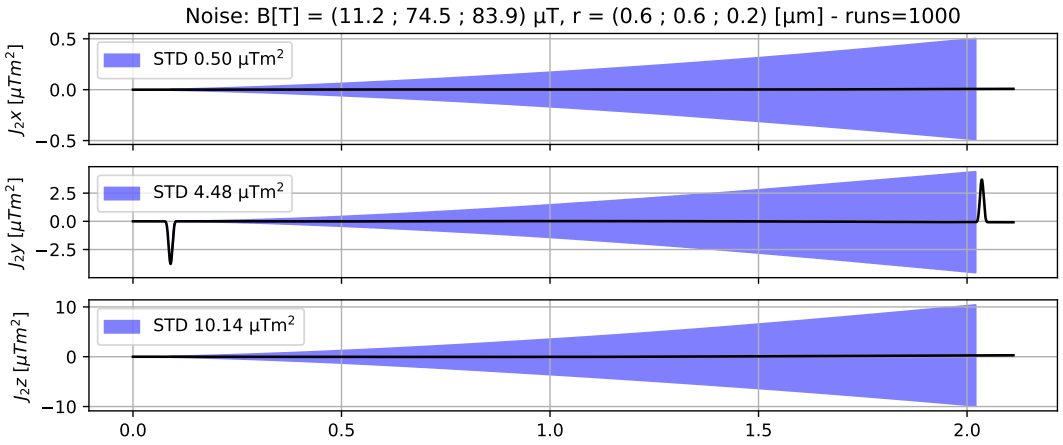

Figure 6.5 – An example plot of Eq. 6.4 for added noises in the magnetic field. A moving average over the second field integrals is plotted. The two black peaks are the coupling periods.

For the error influence only the deviation from the sinusoidal oscillation is of interest and not the oscillation by itself, so a rolling average over one undulator period is applied to the data which averages out the oscillation term and only the error is left over. The resulting standard deviation of the simulation is used as a measure to determine the

influence of the respective error. In Fig. 6.5 is an example, how the moving average over the second field integral looks like. The two peaks close to $z = 0\,m$ and $z = 2\,m$ in $J_2(y)$ represent the in and out coupling periods which have different amplitudes between their half periods. The moving average becomes non-zero and the peaks rise. The standard deviations are always evaluated at the end of the undulator.

6.2.1 Longitudinal Positioning

Component	Manufacturer	Type
3 m Stage	Rose and Krieger	Douline Z 60 clean
Stepper motor	Nanotec	PD6-N8918
Interferometer	Hewlett Packard (now Keysight)	5517B (Laser),5507B

Table 6.2 – Positioning and measurement equipment for the longitudinal coordinate.

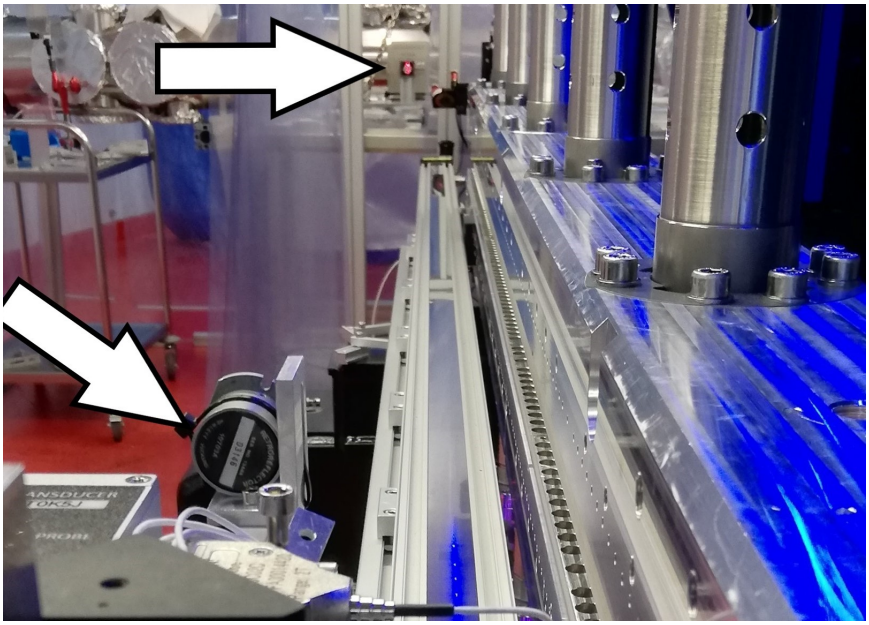

Figure 6.6 – A view from the slider towards the interferometer. The upper arrow indicates the laser and the lower arrow the reflector which is mounted on the slider.

For the longitudinal positioning a linear stage is used which is moved by a stepper motor. The motor has an internal regulation which counts the lost steps while driving and corrects the lost path length. The motor has 200 full steps per revolution which can be divided into up to 64 micro steps per full step, so a total of 12800 micro steps per rotation. The mechanical gear transmission of the bench allows to drive the slider

about 165 mm per revolution which gives a minimum step width of 12.89 μm per step. The motor is mounted at the end of the stage and connected to the slider by a timing belt. The 335 mm long slider holds the measurement setup and carries the reflector unit of an interferometer which measures the longitudinal position, see Fig. 6.6.

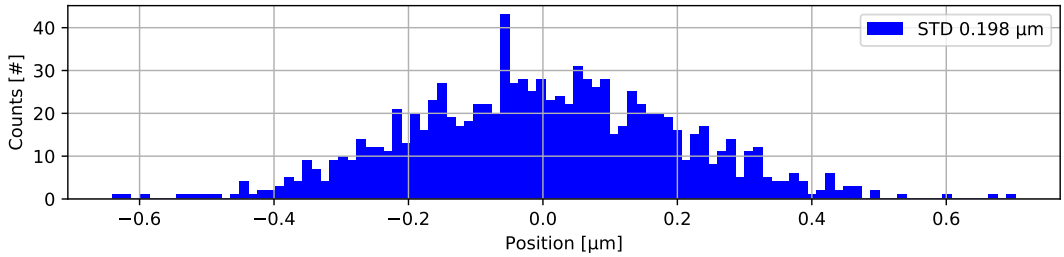

Figure 6.7 – Histogram of the Interferometer data over 1000 shots. The noise level is 0.2μm.

To measure the noise level of the interferometer 1000 subsequent shots were recorded. For the interferometer a noise level 0.2 μm was measured, which gives a lower limit onto the measurable longitudinal position, see Fig. 6.7.

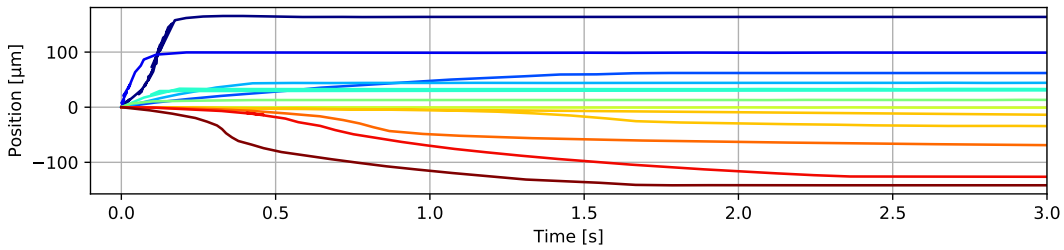

Figure 6.8 – Slider slippage after the motor stops for 11 measurements.

Inside the linear stage a timing belt connects the slider with the motor. The belt is made out of rubber which means it is elastic and can deform under tension. When the motor drives a small amount of steps it can happen that the tension onto the belt is too low to overcome the friction of the slider. Following from that, it can happen that the motor drove steps, but the slider position did not change, which is an unpredictable error source. In addition, the tension inside the rubber can decrease over time which results in a slow crawling of the slider position. As the belt is connected on both sides of the slider this tension release is arbitrary. For the measurement it is necessary to determine the longitudinal position with highest accuracy at it is the integration axis. To test the slider movement the motor is moved about some distance into one direction and the slider position is measured after the motor stopped. This was done eleven times and the data is plotted in Fig. 6.8.

When the motor stops, the slider is still moving for several seconds. Within one measurement the slider was still moving after 8 seconds. Even the additional traveled distance is not constant. To compensate this error the longitudinal position of the slider is measured before and after the magnetic field is recorded. If the difference was higher than 0.5 μm the measurement is repeated, else it is saved. The limit of 0.5 μm is experimentally chosen, a smaller limit is too close to the noise level which leads to several iterations before a measurement is recorded. Greater values limit the accuracy of the measurement. As this limit is still afflicted with the noise of the interferometer, the errors are added up to a total measurement error of 0.7 μm. Using this uncertainty for the error function of Eq. 6.4, the error of the longitudinal position measurement would result in a measurement inaccuracy of $\approx 10\,\mu\mathrm{Tm}^2$ for $\mathrm{J}_2(\mathrm{y})$, which is above, but very close, to the strict limit given in Tab. 6.1.

6.2.2 Magnetic Field Measurement System

Component	Manufacturer	Type
Teslameter	Senis	3MH6
3-Axis Hall Probe	Senis	I3C-03C05L

Table 6.3 – Measurement equipment for the magnetic field.

For the measurement of the magnetic field a high-accuracy and high resolution Teslameter and a 3D probe from the company SENIS is used. The System is calibrated within a range of $\pm\,2\,\mathrm{T}$ with an accuracy better than 0.01 % at 2 T peak field [78]. This would lead to an error of $\approx 120\,\mu\mathrm{T}$ while measuring a 1.2 T peak field.

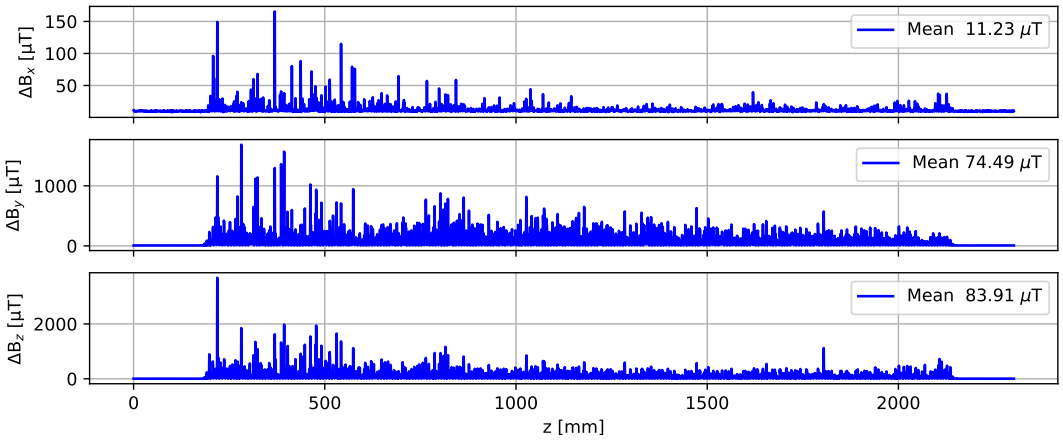

Figure 6.9 – The Measurement error along the undulator field.

For the measurements the device was programmed such that it averages over 100 shots and returns the mean and standard deviation, which are always recorded. The performance of the probe inside the laboratory was tested by measuring the magnetic field and its standard deviation along the undulator, see Fig. 6.9. The measurement errors are not constant over all axes and have higher fluctuations at the beginning of the undulator compared to its end. For B_z the measured error is close to the estimated error, whereas the B_y component is below the estimated noise and B_x has lowest noise of 13 μT.
Assuming those noise levels hold for all measurements, the measurement uncertainties for the field integrals are, according to Eq. 6.4, $J_2(x) \approx 0.5\,\mu\mathrm{Tm}^2$, $J_2(y) \approx 3\,\mu\mathrm{Tm}^2$ and $J_2(z) \approx 4\,\mu\mathrm{Tm}^2$.

6.2.3 Transverse Positioning

Component	Manufacturer	Type
Laser	Thorlabs	HNL210LB (attenuated to 20 μW)
Laser stages	Owis	LTM-60
Piezo mirror	Newport	8816-6, Controller: newfocus 8742
Pinhole	inhouse	0.7 mm Diameter
Piezo stages	Smaract	SLC-2460s
Camera	Basler	acA1920-40gm

Table 6.4 – Positioning and measurement equipment for the transverse coordinates.

A transverse offset would result in a quadratic deviation from the ideal sinusoidal undulator field, see Eq. 2.9. As the measurement bench is not flat nor the slider movement perfectly longitudinal on a μm scale, it is necessary to correct the transverse position of the Hall probe to get reproducible measurements. To do so, an active feedback regulation of the probe onto a laser line is installed, which is aligned to the magnetic axis of the undulator. The laser line is shown in Fig. 6.4. The laser is on the left side of the picture and the camera is 3.5 m away from the mirror on the right side. The setup stands on its own feet and is not connected to the stage to reduce the impact of possible vibrations coming from the stepper motor.

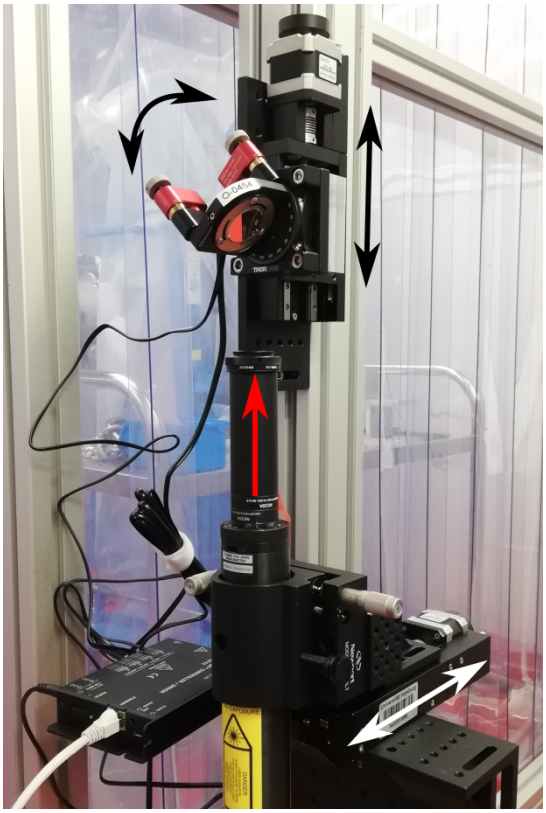

Figure 6.10 – Laser line positioning system. The laser points up (red arrow). Two linear stages handle the transverse displacements, the motorized mirror mount the tip / tilt of the light axes.

The setup for the laser line positioning is shown in Fig. 6.10. The laser is pointing up and is bend with a mirror into the horizontal plane towards the undulator. To align the laser to the magnetic axes a completely motorized setup was chosen. This allows to automatize the alignment routine and to improve the reproducibility of the alignment. For the horizontal positioning a linear stage is attached to the laser, for the vertical positioning a stage attached to the mirror. Both stages are calibrated such, that a travel of 0.3 μm/step is possible. The motorized mirror mount allows a minimum step size of 0.7 μrad/step, but it is not equipped with encoders, so the alignment has to be done in several iterations. An additional filter was mounted directly on the camera to suppress the surrounding stray light.

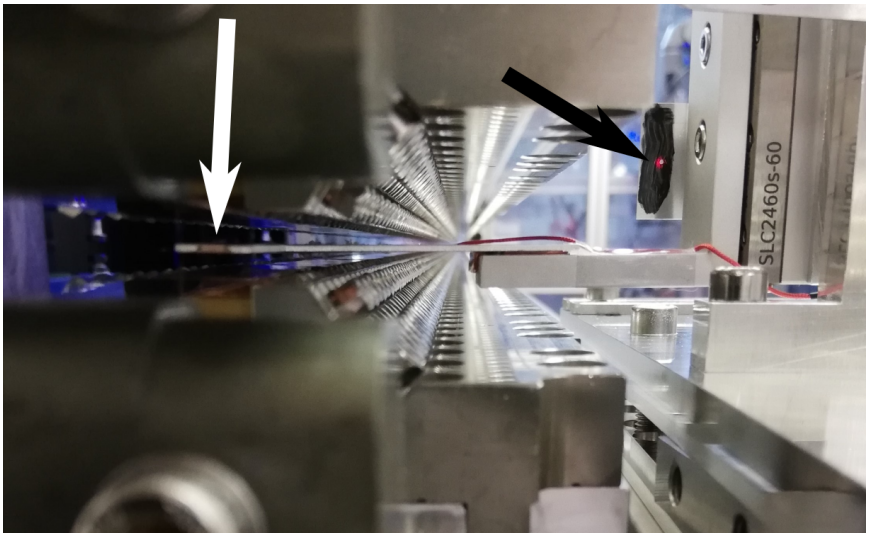

Figure 6.11 – Front view onto the Hall probe holder (white arrow) inside the gap. On the right upper side is the black painted pin hole with the red laser spot on it (black arrow).

The laser line is guided through a pinhole attached to the Hall probe holder, see Fig. 6.11. On the left side is the undulator structure with the Hall probe inside the gap. The probe is mounted on a cantilever which reaches out of the structure and is attached to the measurement setup. On the same cantilever is also the pinhole to have a fixed relationship between laser line and Hall probe position. The area around the pinhole with a diameter of 0.7 mm is painted black to reduce the stray light in the laboratory. The laser is in the center of the black area as a red dot.

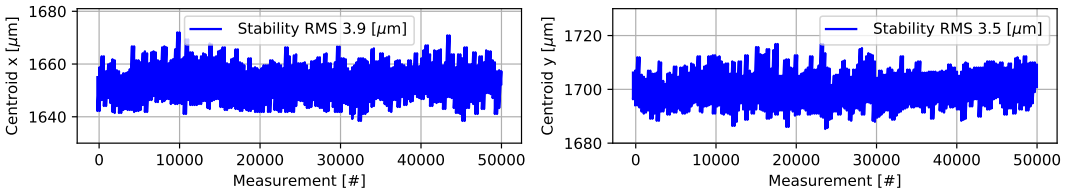

Figure 6.12 – Camera centroid stability plot of the laser line.

For this setup the laser centroid was measured over 50 thousand shots with 50 Hz to estimate the measurement error of the transverse position. As the bench is designed to measure in a step-by-step mode this measurement was done while the setup stood still. The stability of the centroid is ± 3.9 μm in the horizontal plane and ± 3.5 μm in the vertical, see Fig. 6.12. The pixel size of the camera is 5.86 μm, so the errors are below one pixel.

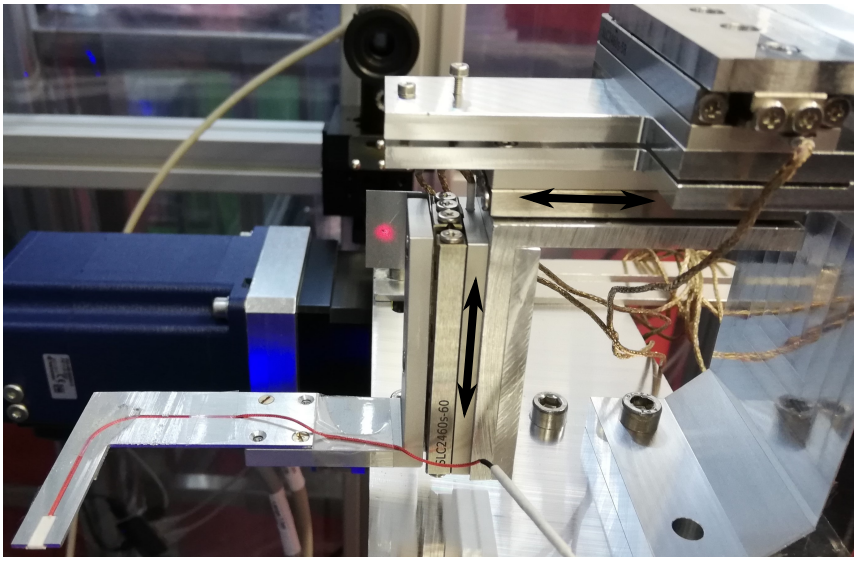

Figure 6.13 – A close up onto the regulation setup. On the left is the cantilever with the white Hall probe (small white box). In the middle is the laser spot on the pinhole and the camera in the background. Attached to the pinhole are two stages for the active feedback.

Offsets of the pinhole change the centroid positions on the camera, which are directly corrected by two Piezo stages attached to the pinhole, see Fig. 6.13. The regulation works in a closed loop: When the centroids change above a threshold, the stages correct the position deviations and a subsequent comparison between the encoder values of the Piezo stages and the distance which should have been corrected guarantees that the driven distance is correct. This whole process runs in the background with 20 Hz to have a permanent regulation of the Hall probe position. The threshold for the active feedback was experimentally chosen and was a balancing between the accuracy of the transverse positioning and the required time for the regulation. At the end a threshold of 0.1 pixel, so 0.6 μm was chosen. To test the reliability, the regulation was recorded for 25 consecutive measurements over the undulator structure.

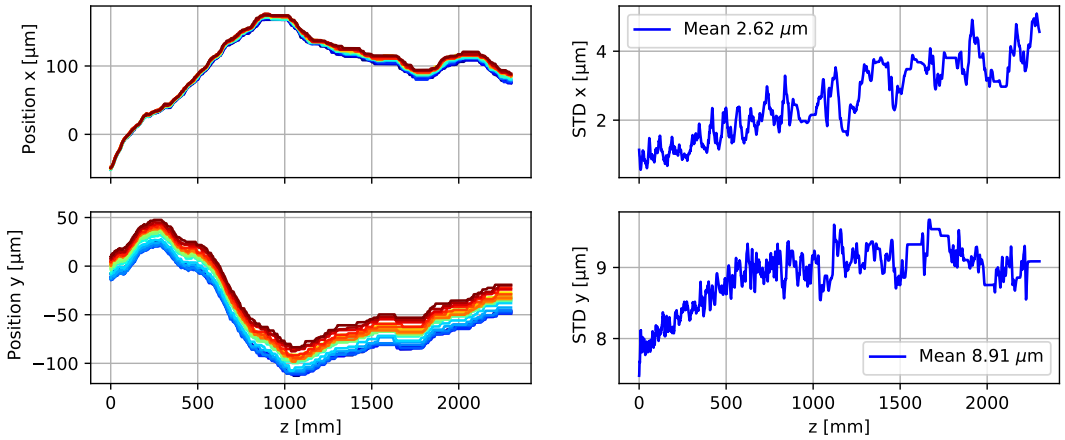

Figure 6.14 – Piezo encoder values for 25 consecutive measurements.

The Piezo encoder values from each run are on the left in Fig. 6.14 and their deviations on the right. The shape of the regulated distances is similar between the runs, but a sagging between the signals is visible which leads to offsets up to 50 μm between the first and last measurement. The overall accuracy decreases with the distance between pinhole and camera. This is counter intuitive, as the resolution should increase with smaller distance. One possible explanation for this effect is, that the camera pixels go into saturation with decreasing distance to the pinhole and that saturated pixels falsify the estimated centroid position. The sensitivity of the camera had to be balanced such, that a centroid can be detected when the pinhole is at the opposite end of the measurement bench (4 m distance) and in front of the camera (0.5 m distance). Due to the distance of 3.5 m between those two points and the divergent laser beam (1.15 mrad), the spot size on the camera chip varies between 4.7 mm and 1.3 mm, which does also change the irradiance of the camera chip about a factor of 13.
A solution to reduce the offsets is to drive the pinhole to a defined "point zero" (further called P_0) in front of the undulator while the regulation was turned off and switched on after. With this method the reproducibility is increased, but still small offsets will occur which worsen the accuracy. To quantify this error source the probe was driven again 10 times through the undulator with the P_0 regulation turned on. Before the measurement started the bench was rebuilt and realigned to the undulator which is why the profile shapes between Fig. 6.14 and Fig. 6.16 look different. The centroid of the camera and the encoder values of the stages were recorded and the data is plotted in Fig. 6.15 and Fig. 6.16. The standard deviation is calculated for all 10 measurements and are plotted on the right side of the figures.

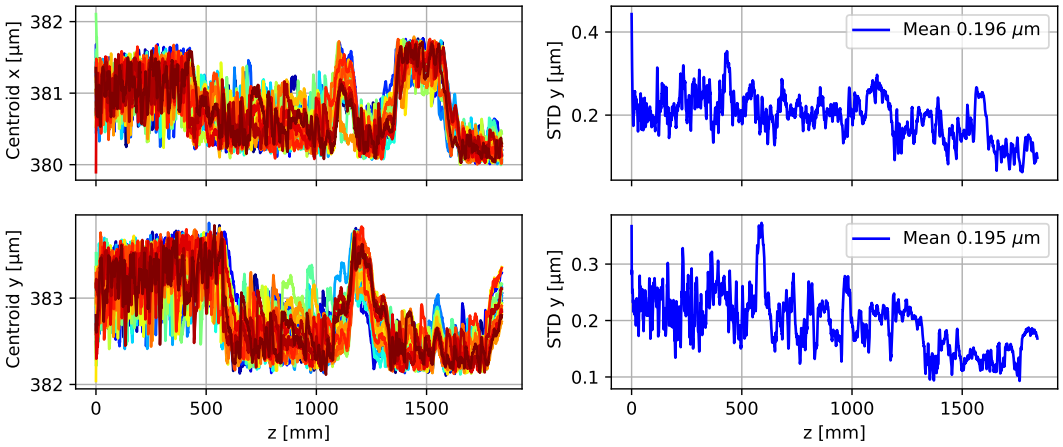

Figure 6.15 – The centroids on the camera for 10 consecutive measurements with active P_0 regulation.

The individual centroid positions with the active feedback and the P_0 regulation are shown in Fig. 6.15. An upper limit of 0.6 μm was set as a threshold for the regulation. The individual centroids deviate about 0.43 μm in x and y along the measured length. The fluctuation over all 10 measurements is $\approx$ 0.2 μm in x and y. Summing both errors up will end in an uncertainty of $\approx$ 0.63 μm which is the threshold of the regulation and an intrinsic check that the regulation works correctly. So, the probe is guided along the laser line with a transverse accuracy of 0.6 μm over the 3.5 m measurement length during a single measurement.

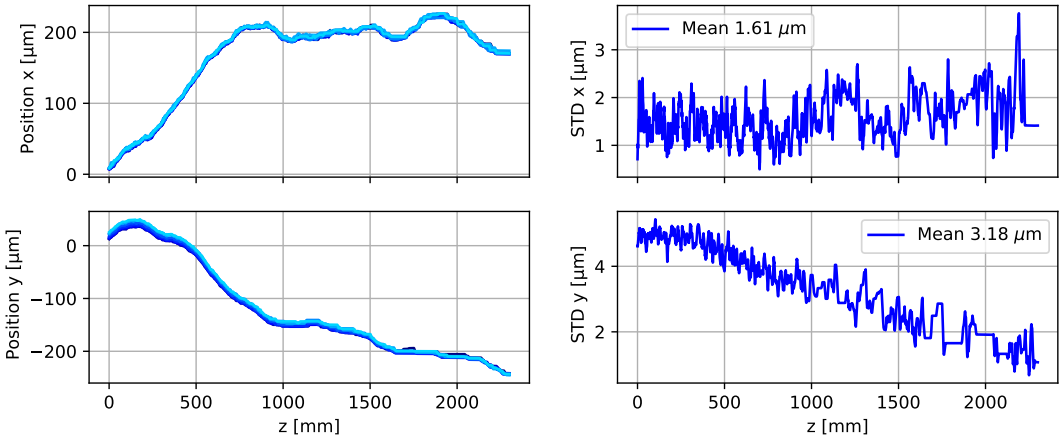

Figure 6.16 – The positions of the Piezo stages for 10 consecutive measurements with active regulation. The data is plotted on the left, on the right is the standard deviation over all measurements.

The regulated distances of the piezo stages are plotted in Fig. 6.16. The settings of the camera were adjusted to handle the saturation effects. The standard deviation of the horizontal position is almost constant around 1.6 μm and the slope on the signal vanished. In contrast to the data plotted in Fig. 6.14, the vertical deviation increases now linearly with the distance between pinhole and camera and is 3 μm on average. With the new regulation scheme the reproducibility was increased by a factor of 3 in the vertical plane and 2 in the horizontal one. At the beginning of the measurement the pin hole was driven to a fixed position in space, while the regulation was turned off. Without the active positioning feedback, the initial starting positions do vary about a small amount and is the main cause for the deviations in the horizontal plane, which is 1.6 μm for all ten measurements. In the vertical plane, the sagging of the initial position does still occur, but with a reduced deviation between the measurements. The still higher error in the vertical plane comes from the regulation itself:
The Piezo stages can only lift a small amount of weight as a tradeoff for the small step size and the Hall probe holder is so heavy that the vertical stage is close to its load limit. When the stage has to regulate downwards the weight will lead to an additional push and causes an overshoot of the regulated distance. In contrast to this downward movement is the slow regulation upwards as the stage has now to work against the load. So, the time to regulate is different for the directions. Combining this with the decreasing resolution of the laser centroid by distance, an overshoot due to a false centroid measurement is more likely and takes more time to be compensated. This will manifest in a slow sagging of the pin hole position by time and is also the effect which caused the high vertical offsets in the scans shown in Fig. 6.14.
This effect does not appear in the horizontal direction as the stage does not need to work against gravity which is the reason why the standard deviation is close to constant, see Fig. 6.16.

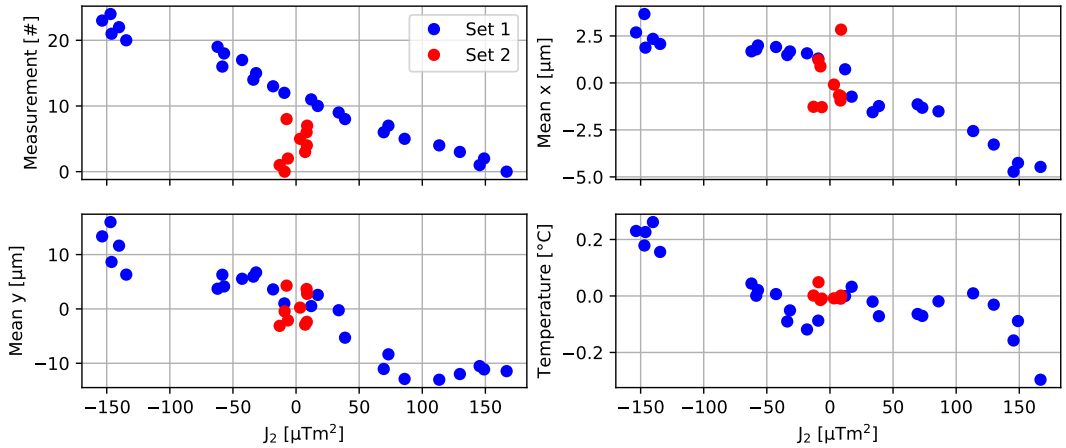

Figure 6.17 – Correlations between the measured field integrals and the average offsets of the Piezo stages and the temperature during the measurement. Blue shows the data before heat shielding and without P_0 regulation. The red data shows the results after.

The improvement of the P_0 regulation is shown in Fig. 6.17. The measured data of the run without the P_0 regulation is Set 1 (blue) and Set 2 (red) is the recorded data with the regulation switched on. To make the data comparable, only the deviations from their means are shown. Due to this new regulation scheme the overall fluctuations of the field integrals due to initial position changes is decreased about a factor 7. The remaining fluctuations are caused by the uncertainty of the regulation due to overshooting of the Piezo stages, as explained on the page before. Besides the impact of the positioning also the temperature in the laboratory is of interest. During the previous test a temperature change over time was measured and an additional temperature shielding of the lab was installed to suppress cold air streaming through some holes in the ceiling to the building. In addition the power of the flow boxes was reduced during the measurements as they produce a heat gradient in the lab. This decreased the temperature fluctuations inside the laboratory down to $\pm 0.2\,°C$. This is mainly important for the used magnetic material. As the peak field changes about $\approx 10^{-3}/°C$ a fluctuation of $0.4\,°C$ would change the measured amplitudes about $0.04\,\%$. If this would happen during one measurement it would falsify the data which is used to tune the machine. The deviation of the field integrals is dominated by the fluctuations in the mean y position. The additional heat shielding reduced the temperature fluctuations almost to zero.
With the evaluated positioning accuracies of $1.6\,\mu m$ in x and $3.2\,\mu m$ in y, see Fig. 6.16 and using Eq. 6.4 the influence of positioning errors onto the second field integrals are $J_2(x) \approx 0.01\,\mu Tm^2$, $J_2(y) \approx 0.05\,\mu Tm^2$ and $J_2(y) \approx 53\,\mu Tm^2$. The influence on $J_2(x)$ is close to zero, because both errors are multiplied and end up in a small contribution to the field, see Eq. 6.4. For $J_2(y)$ the error is also close to zero, as the magnetic field

depends quadratically on the error sources. So, small deviations will have a small impact. $J_2(z)$ has a linear correlation between vertical error and peak field which is why the influence is several orders of magnitude higher just due to the positioning errors in the vertical plane. The high error in the $J_2(z)$ component is acceptable, as this field component should be close to zero and impacts from it can be compensated by additional Helmholtz coils around the chamber.

6.2.4 Angular Displacement

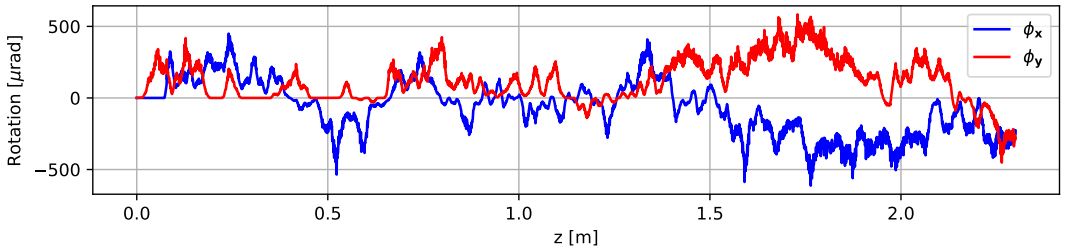

Figure 6.18 – Angular rotation of the pinhole due to the transverse displacement.

With the laser regulation it is only possible to actively correct the probe for displacements during the measurements but not for rotations, as no angular measurement system nor correction system is installed. The pinhole has to be regulated up to 200 μm while driving along the undulator (see Fig. 6.16) which means, that the bench is not flat, nor parallel to the regulated axis. It is certain that the probe also receives a small rotation around the vertical and horizontal axis. From the compensated transverse distance per measurement step it is possible to estimate the rotation angle like $\phi_x = \Delta x/\Delta z$ and $\phi_y = \Delta y/\Delta z$ which is plotted in Fig. 6.18. The rotation is within a range of up to $\pm\,400\,\mu$rad. Following from this, two things will happen to the Hall probe:

1. The probe will be displaced from its origin in all three coordinates
2. Due to the rotated Hall probe chip the magnetic field components get mixed up

To estimate the impact rotation matrices around the horizontal and vertical axes are used:

$$R_x = \begin{bmatrix} 1 & 0 & 0 \\ 0 & \cos(\phi_x) & \sin(\phi_x) \\ 0 & -\sin(\phi_x) & \cos(\phi_x) \end{bmatrix} \qquad R_y = \begin{bmatrix} \cos(\phi_y) & 0 & -\sin(\phi_y) \\ 0 & 1 & 0 \\ \sin(\phi_y) & 0 & \cos(\phi_y) \end{bmatrix}$$

The probe has an offset of $\vec{D}_0 = (dx, dy, dz)$ with dx = 68.031 mm , dy = -17.65 mm and dz = 27.5 mm compared to the pinhole. To calculate the position the rotation

matrices are applied to the estimated angles in Fig. 6.18 like $\vec{D} = R_x R_y \vec{D}_0$ and the resulting displacement $\Delta\vec{D} = \vec{D}_0 - \vec{D}$ is plotted in Fig. 6.19. The small angle deviation changes the Hall probe position about several tens of μm.

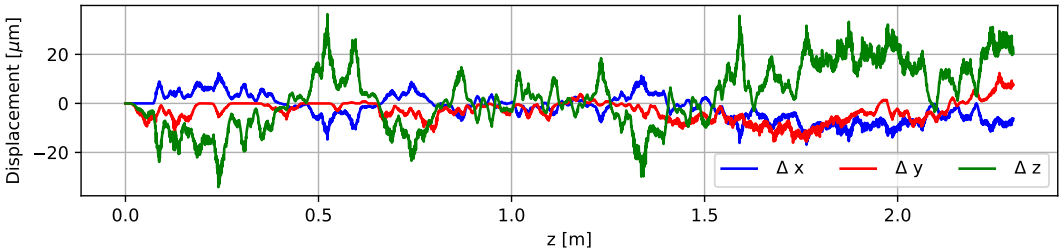

Figure 6.19 – Hall probe displacement due to angular rotations of the cantilever around the pinhole.

The influence onto the field integral is shown in Fig. 6.20. The shift of the Hall probe would cause a change of up to 100 μTm^2 of the second field integral.

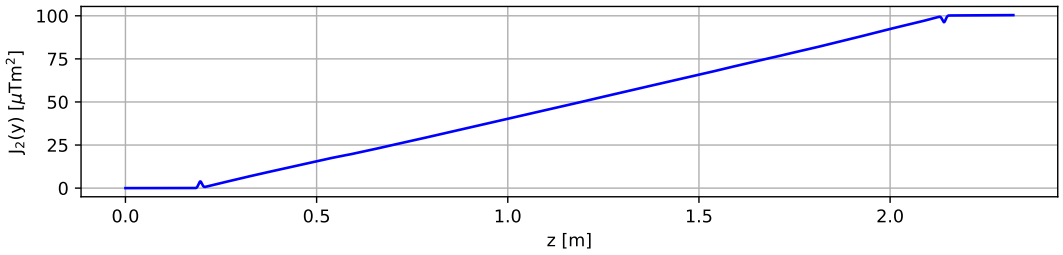

Figure 6.20 – Change of J_2 due to a rotation of the Hall probe holder.

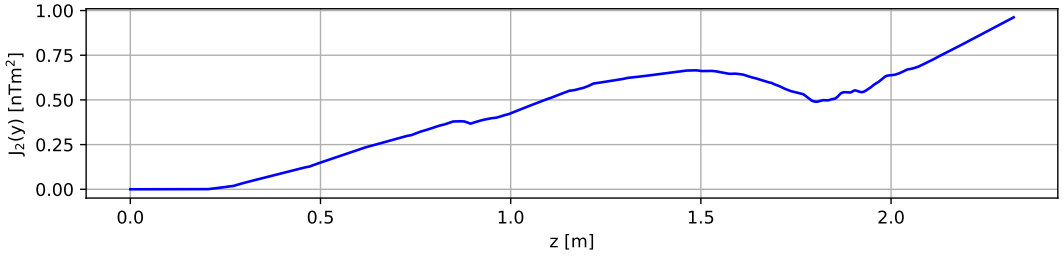

Figure 6.21 – Change of J_2 due to a rotation of the Hall probe chip.

The additional rotation of the Hall probe chip is in the nTm^2 range, so five orders of magnitudes smaller, see Fig. 6.21.

The data has to be handled with great caution, as the angles are calculated from small values with a relative high noise level and are not directly measured. The compensated distance between the data points is close to the accuracy of the Piezo stages and taking the differences between them increases the overall noise level. So, the deflection angles should be measured in future experiments. Nevertheless, the driven path length of the piezos is reproducible from run to run, which means that the impact due to angular deflections is a systematic error of the bench and manifests as an overall slope on the signal. This error can be compensated width additional magnetic coils around the undulator chamber.

6.2.5 Sampling Rate and Post Processing

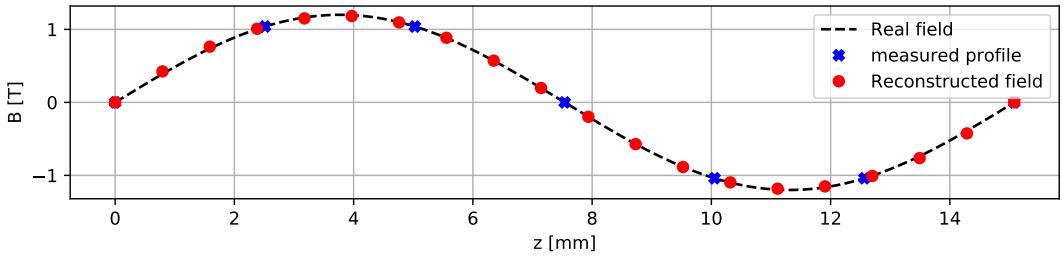

Figure 6.22 – Spline interpolation applied to the measured data to reconstruct the original field.

A large contribution to the accuracy of the vertical field integral is the sampling rate of the magnetic field due to the chosen step width of the measurement bench. For the measurements a width of 722 μm, so 22 data points per undulator period is chosen. The 22 data points per period are enough to reconstruct the magnetic field, but it is not guaranteed that the measurement points between the scans are on the same position. This will have the following effect:
In a first run the probe is moved about a length of $z = \lambda_u/4$ away from its starting point and measures the field amplitude $B_1 = B_0 \cdot \sin(k_u \cdot \lambda_u/4) = 1200$ mT. After this measurement the probe is moved back to its origin and a second scan starts. Depending on the longitudinal accuracy of the stage, the starting position of the second scan could slightly be changed about dz= 100 μm. Driving the probe now again about $z = \lambda_u/4$, the probe would measure a field of $B_2 = B_0 \cdot \sin(k_u \cdot \lambda_u/4 + dx) = 1199$ mT. It follows a 1 mT error in the peak field measurement, due to a minimal change of the starting position and with that, the sampling positions of the magnetic field. The maximum of this effect would be reached if the starting position would change about half the step width of 350 μm. Then, the difference would be 12 mT.
A way to solve this is a spline interpolation, a piecewise low degree polynomial interpolation applied to the measured data, with which the real field can be reconstructed

[79]. An example is shown in Fig. 6.22. The real sinusoidal field is shown in black. The sampling was chosen such, that 7 data points were taken over one period (blue crosses). This sampling is insufficient to retrieve the peak fields. With a spline interpolation applied to the 7 data points, the real field can be reconstructed and up-sampled, which is indicated by the red dots. After each measurement the data is interpolated to increase the accuracy of the individual scans and to make them comparable. It would also be possible to increase the sampling rate, but the amount of time to tune the machine would be disproportionally long:
The main argument for the chosen step width with 22 samples per period was the weighting between the consumed measurement time of around 3.25 h per full scan and the given accuracy. The recording of one data point lasts 1.8 seconds, where the main contributors are the longitudinal positioning ($\approx$ 1 s) and the magnetic field measurement (0.2 s). Increasing the accuracy such that an interpolation is not needed would lengthen a single measurement to days.

6.2.6 Overall Bench Performance Discussion

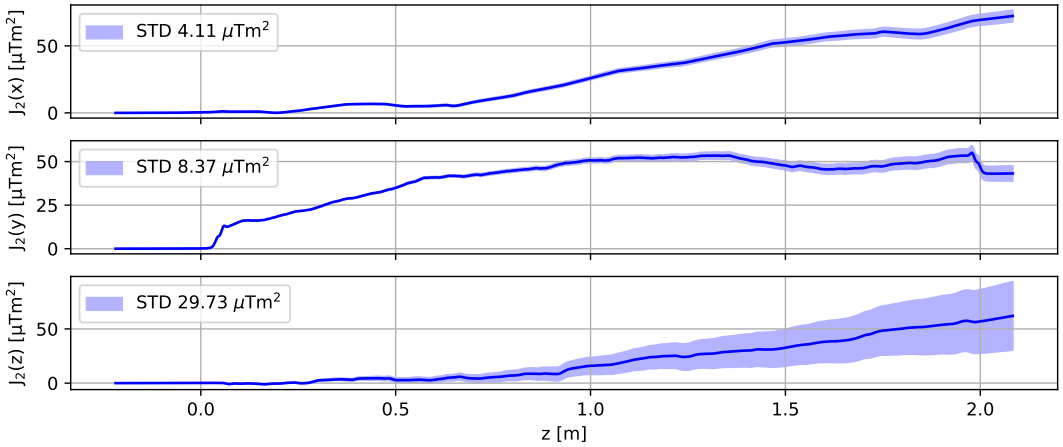

Figure 6.23 – Average field integrals and standard deviations of a reproducibility scan of 10 consecutive magnetic field measurements.

In the previous sections all error influences were discussed separately. In a last check the overall performance will be estimated by taking all error sources into account and compare them to a reproducibility scan. This scan includes 10 measurements with an active P_0 regulation and data interpolation. The resulting fluctuations of the second field integrals for all three axes are plotted in Fig. 6.23. The measurement error found in the scan are given in the Tab. 6.5.

Axis	Simulation [μTm^2]	Scan [μTm^2]
J_2(x)	0.5	4.1
J_2(y)	11	8.4
J_2(z)	50	29.7

Table 6.5 – Comparison between expected (Eq. 6.4) and measured fluctuations of the second field integrals.

According to the simulation a measurement error of $J_2(x) = 0.5\,\mu\text{Tm}^2$ is expected. The main contribution is the noise of the Hall probe, whereas positioning errors could be neglected. The error of $J_2(y)$ is $11\,\mu\text{Tm}^2$ which is dominated by longitudinal positioning and the Hall probe noise. The main contribution to $J_2(z) = 50\,\mu\text{Tm}^2$ is the vertical positioning error of the Piezo stages.
The field integrals for 10 consecutive measurements are plotted in Fig. 6.23 and the deviation is given in Tab. 6.5. All values were interpolated, as explained before.
The error for the horizontal plane is an order of magnitude higher compared to the estimation, which could come from correlations between the longitudinal position and the transverse correction, or an initially rotated Hall probe which would mix a fraction of the longitudinal error into the horizontal one. To fully understand the increased error a deeper insight into the measurement system is required. But still, this error is small enough to make reliable measurements. The measured $J_2(z)$ error is almost a factor of two smaller than the expected one. The vertical inaccuracy of 8.4 μTm^2 is of main interest and close to the estimate of 11 μTm^2. It is on the same scale as the strict limit for a K of 2 given in Tab. 6.1, but below the required shimming limit of 28 μTm^2, see Sec. 6.1. So, the bench accuracy is suitable to tune the magnetic field integrals.

Discussion

The measurement accuracy of the bench is in a tolerable range but there are still unknown influences.
For example the horizontal component is a factor of ten above the expected error. This could come from the peak field noise which changes with the longitudinal position. In Fig. 6.9 the measurement error of the magnetic field is a factor of 10 above the average within the first meter of the undulator. This effect appears in all three coordinates. A reason for that could be the cabling of the slider setup. The bench does not have a dedicated cable tray to move the cables along a defined direction. The cables from the Hall probe and the Piezo stages could have had contact on the first meter before their distance was increased. The Piezo stages run with high voltage in the kV range which could leak through the cables into the hall sensor cable. As the Hall probe has a resolution in the 10^{-6} range, those leakages could influence the recorded data. During the measurements it was observed that the displayed peak field changed about

1 mT - 2 mT depending on the distance between those cables. Although the cables were mounted in a way to minimize the effect, it could not completely be eliminated.
For the error estimation only uncorrelated errors were assumed which does not need to be true. For example, if the Piezo stages are not perfectly aligned to the geometry of the undulator field but tilted, the probe would change its position in x and y when the probe is moved with the horizontal stage. The same happens, when the Piezo stages are not mounted perpendicular to each other, or, when the camera chip is rotated around the longitudinal axis and a real change of the centroid in the horizontal dimension would be detected as a centroid change in the horizontal and the vertical. In addition, the vertical positioning has a linear correlation, see Fig. 6.16, which is not considered for the estimates, but has an impact onto the field integrals.
Also angular dependencies like small local rotations of the Hall probe holder can not be directly determined but have an impact onto the measured field.
The remaining deviations could come from the small number of samples of the measurements compared to the simulation and other error sources which could not directly be measured. These could be local temperature changes inside the laboratory which slightly change the measured field, small offsets at the beginning of each measurement which results in a different integration path, laser pointing fluctuations of the alignment laser which changes the mean centroid during the scan and therefore the transverse regulation, small fluctuations in the interferometer laser due to environmental changes, air fluctuations from the flow boxes which increase the longitudinal measurement error of the interferometer, or, a rotated probe, which changes the noise levels along the measurement and so on.

6.3 Conclusion

In this chapter the measurement bench is presented. The tuning limits of the undulator field are derived from theory and linked to accessible quantities in the laboratory, see Sec. 6.1. For the design K of 2, the tuning limits of the integrals are $J_1 = 130\,\mu\mathrm{Tm}$, $J_2 = 28\,\mu\mathrm{Tm}^2$ and a phase jitter of $\Phi = 8.4°$.
The total measurement uncertainties were estimated by simulations and found in a reproducibility scan, see Sec. 6.2.6, to be $J_2(\mathrm{x}) = 4.1\,\mu\mathrm{Tm}^2$, $J_2(\mathrm{y}) = 8.4\,\mu\mathrm{Tm}^2$ and $J_2(\mathrm{z}) = 29.7\,\mu\mathrm{Tm}^2$. For the relevant axes $J_2(\mathrm{x})$ and $J_2(\mathrm{y})$ the measurement error is below the required tuning limit. So, this bench is precise enough to tune the undulator field.
To reach those limits the measurement bench is equipped with a laser based active stabilization system of the Hall probe holder, see Sec. 6.2. The longitudinal position is determined with an uncertainty of 0.7 μm. This high measurement error is introduced by the slider mechanics of the bench itself because the slider position drifts after the motor stopped moving see Sec. 6.2.1. The transverse positioning of the probe is done

by actively measuring and regulating its position onto a defined laser line, see Sec. 6.2.3. This allows a transverse accuracy of 0.6 μm over 3.5 m length for a single measurement and a reproducibility between measurements of 1.6 μm for the horizontal and 3.2 μm in the vertical plane. The vertical plane has a linear drift in the accuracy by distance between slider and camera. This comes from a combination of decreasing resolution on the camera image with distance and a sagging of the vertical Piezo stage due to heavy load. It was shown that the implementation of the active regulation combined with a defined starting point of the measurement reduce the measurement error about more than an order of magnitude, see Fig. 6.17.

7 Undulator Field Measurements

To create a sinusoidal undulator field it is of major importance that the poles inside the magnetic arrays are aligned with a μm / μTm^2 precision relative to the magnetic axes until the overall field integrals stay within the limits derived in Sec. 6.1. The main issue here lies within the required alignment of all involved parts to one single global coordinate system in a reproducible and self-consistent way. Keeping the required accuracy in mind one can state that the poles are in an arbitrary position after their mechanical installation and also, that the measurement bench is initially arbitrary in space. This makes in total over 260 components which have to be aligned to magnetic field measurements of the Hall probe, which itself has to be considered to be in an initially arbitrary state. So, it is highly demanding to align those components with care. For example: If the Hall probe signal shows a tilted transverse undulator field it has to be possible to distinguish if this comes a) from a tilted camera which would result in a tilted regulation, b) from a Piezo stage which drives on a slope instead of a straight, c) from a tilted measurement bench, d) from a tilted Hall sensor, e) from a tilted pole inside the undulator, f) from a stray field from the surrounding, g) another source or h) from a mix of those influences. It is also very important to align the bench in a defined procedure to guarantee the reproducibility. It must be possible to reproduce the alignment and to find the undulator axes again after the bench was unplugged.
In this chapter, the procedures how to align the bench and shim the magnetic field are explained. To tune the undulator field, the measurement bench has to be aligned to the magnetic axis of the undulator. This has to be done in a consistent and reproducible procedure which will be described in section 7.1. The subsequent tuning of the undulator field is done in several steps. At first, a pillar shimming is done to reduce the global deformations of the magnetic field, see Sec. 7.1.4. In a second step a fine tuning is done by changing the pole positions to get the field integrals straight, see Sec. 7.2. The tuning of the magnetic structure is done on air and without the chamber. During the installation of the chamber the girders were exposed to vibrations which deformed the magnetic field integrals. So, the measurement procedure was repeated in the final tunnel position and the field measured again, see section 7.2.5. In a last step, the influence of the retrieved field errors are verified with simulations and discussed in Sec. 7.3.

7.1 Concept of Bench Commissioning

The bench is commissioned when the Hall probe is aligned to the undulator axes such that it only measures a vertical field component whereas the other two axes are minimized on average.
The alignment of the probe to the undulator axes is a complex task, as the coordinate systems of individual mechanical components, which are initially arranged arbitrary in space, have to be linked to one global coordinate system with some micro meters in accuracy. On this required μm precision level, it is valid to assume that all components are initially strongly misaligned and that stages do not drive exact perpendicular to each other especially when the bench was not in operation before. All components have to be mechanically aligned to values measured by the Hall probe itself, whereas each alignment step will have a direct impact onto those measurements. It has to be possible to distinguish if the probe drives on an oblique straight along the horizontal axis measuring a horizontally tapered field, or if a pole is tilted and creates a field with a horizontal taper which is measured by a probe driving on a straight horizontal line. So, one needs to solve a problem which requires great caution to not miss align due to wrong assumptions.
As the alignment is limited by the measurement accuracy of the bench one will reach a point at which the alignment can not be further improved and the shimming of the magnetic undulator axes is done along the trajectory of the Hall probe. This straight defines now the magnetic axes of the undulator which are not necessarily congruent with the mechanical axes. If the magnetic and mechanical axes are tilted with respect to each other it is possible to tilt the undulator in the accelerator tunnel such, that the magnetic axes are parallel to the accelerator geometry. This is again limited by the transfer measurement from the magnetic axes coordinates to the geometrical coordinates which are used to define the undulator inside the accelerator tunnel. Also, this correction can only be done if the tilt is small, so below a 100 μrad level, otherwise the clear aperture would be reduced such, that the electron beam could clip inside the undulator.
The list below gives an overview over all components which need to be taken care of during the alignment of the bench and, if possible, an estimate how their influence would manifest.

- **environmental conditions**: The laboratory was not temperature stabilized and fluctuations up to 13 degrees over the year and 2 degrees in the day-night cycle were measured. Those came from holes in the ceiling of the building. Flow boxes of the clean room caused additional air turbulence and local thermal hot spots. A big construction site in the surrounding area caused heavy vibrations in the measurement bench and jumps in the laser line due to which the alignment had to be repeated. A change of magnetic field amplitude and laser line pointing is, therefore, expected between the measurements. With a certain temperature

shielding and air flow distribution the temperature fluctuation was kept below 0.5 K during the day night cycle. With the temperature sensor inside the Hall probe the remaining temperature change was measured and the signal corrected.

- **Frame magnetization**: The big undulator frame is made out of magnetizable steel which influences and changes the background field along the undulator axes. Field errors of a magnetized frame will simply be shimmed out of the field, as their relative position will be the same in the lab and the experiment.
- **Motor magnetization**: The stepper motor of the bench has a magnetic field, which influences the measurement in the region around 20 cm of the motor position, so the motor is shifted far away from the undulator axes.
- **Bench deformation**: the bench needs to be aligned mechanically to the undulator axes. When the slider is driving, the bench deforms due to the weight of the slider and a local sagging occurs. An additional support is mounted below the bench to increase the stability.
- **Laser pointing**: The laser line has to be aligned mechanically to the undulator axis and the pinhole. As the motorized mirror does not have encoders this procedure has to be done iteratively and is the main limiting factor for the alignment accuracy.
- **Camera rotation**: The camera could be rotated around the longitudinal axis of the undulator. A pure vertical offset of the pinhole would be measured as a mix of vertical and horizontal offset. This would give a systematic error onto the bench alignment and the shimming, as the undulator axes would then also be shimmed in a rotated plane. This would only rotate the oscillation plane of the electrons but nothing more.
- **Probe translation**: The Piezo stages do not move perfectly perpendicular to each other and are not aligned to the undulator coordinate system. A vertical position change has to be expected when driving the probe horizontally. This fact drastically limits the horizontal and vertical motion of the Hall probe, as those effects can only be compensated when the pin hole is inside the laser. So, a valid transverse displacement is limited to the pin hole diameter and transverse scans over several mm would give false position values.
- **Probe rotation**: The Hall probe is orientated somehow in space and it has to be assumed that the magnetic undulator axes are not congruent to the mechanical undulator axes. This is a severe fact because the Hall probe is the only diagnostics to measure the undulator field. The whole alignment procedure depends on these measurements and the axes for the later tuning procedure are defined according to them. If the rotation is not measured and corrected, the real undulator axes are pointing into a different direction than the measurement suggests. Also the

amplitudes between real and measured field differ which leads to different field integrals. So, the alignment of the probe has to be done with greatest care.

- **Girder deformation**: After the girders were mounted in the frame they are not parallel. A longitudinal taper is expected. In addition a sine-like deformation due to their hanging will occur after installation. This has to be shimmed out of the structure.
- **Arbitrary pole positions**: The poles are mounted in the girder but have an offset and/or tip tilt to their ideal position after the girder mounting. A strongly disturbed field distribution after the girder installation is expected. To align the probe to this field only the average values along the undulator length can be used for a vertical or horizontal alignment.

To handle the points mentioned above the alignment of the bench has to follow a chronological sequence to achieve the desired reproducibility. The concept starts with a pure mechanical alignment of the Hall probe to the geometrical undulator axes and a subsequent referencing of the Hall probe trajectory to magnetic field measurements. So, the alignment goes in the following order:

1. Mount bench and measurement setup such, that the probe stays close to the mechanical undulator axes while it is driving along the girder (Sec. 7.1.1)
2. Align the probe holder axes to be congruent to the mechanical undulator axes (Sec. 7.1.2)
3. Align the laser to the mechanical undulator axes
4. Align the laser to the magnetic undulator axes (Sec. 7.1.3)
5. Correct and reduce magnetic undulator taper and peak field deviations by shimming the pillars (Sec. 7.1.4)
6. Align Hall probe to magnetic undulator axes and correct rotation between magnetic undulator field and Hall probe position (Sec. 7.1.5)

After the successful alignment of the probe the commissioning is completed and the fine tuning can start.

7.1.1 Mounting of Bench

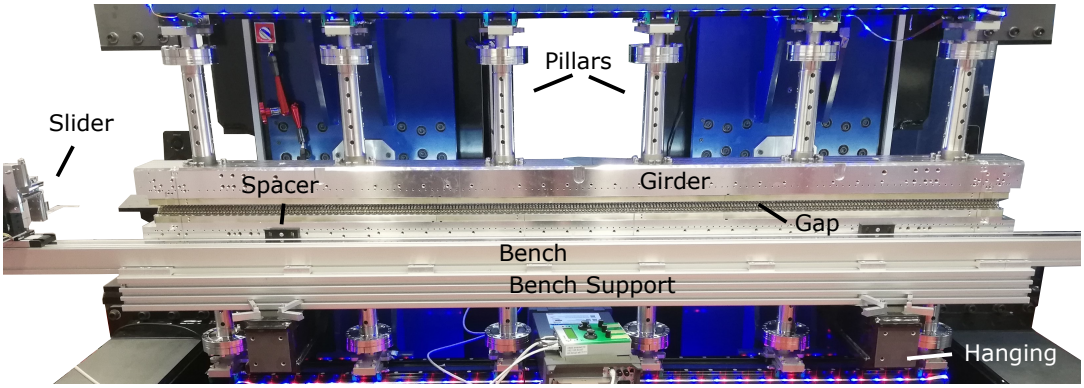

Figure 7.1 – View onto the measurement setup in front of the magnetic structure.

The magnetic girders are mounted on pillars in the frame, see Fig. 7.1. In the bottom of the picture are two black cantilever arms marked as "hanging". These supports will hold the vacuum chamber later on and are used to hold the bench during the tuning, so the bench is connected to the massive frame which reduces vibration from the surroundings. The bench is installed close to the magnetic structure which reduces the required cantilever length for the Hall probe holder to reach inside the gap.
To align the bench to the undulator, spacers are mounted onto the girder sides and the bench is slightly squeezed against them while tightening it to the support. To further position the bench, shimming plates are inserted between hanging and support to correct for rotations and offsets.
To tune the position of the bench relative to the geometrical undulator axes, the gap was closed to 5 mm and the bench was aligned such that the probe is centered at the beginning and end of the undulator. This was repeated for smaller gaps of 3 mm and 2 mm. The bench has several local deformations and a heavy motor on the right side which limited this procedure up to a 300 μm offset between undulator entrance and exit. The remaining offsets will be compensated with the active regulation.
The stepper motor has a magnetic stray field due to its inner permanent magnets, which is measurable within up to 20 cm around it. After this distance it is below the Earth's magnetic field. To reduce its impact the motor is mounted on the right side of the stage, which is out of the picture.

7.1.2 Geometrical Hall Probe Alignment

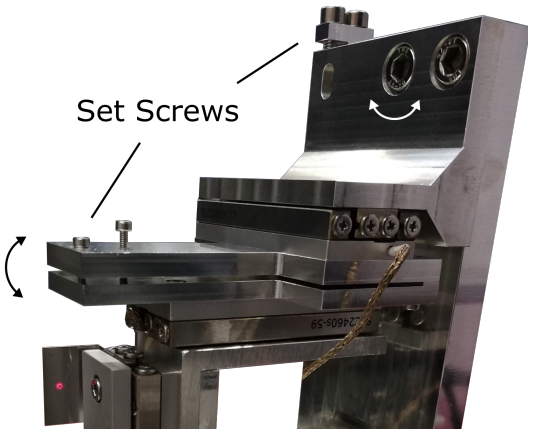

Figure 7.2 – Tip tilt support for the Hall probe. The arrows indicate the movement of the stage when the set screws are moved.

For a fine alignment of the Hall probe inside the gap, the holder is equipped with two joints which allow to rotate the probe around the horizontal (white arrows) and longitudinal axis (black arrows), see Fig. 7.2. The rotation around the horizontal axis is done by an M4 screw with 0.7 mm thread pitch which is 32.4 mm apart from the rotation center. This results in a rotated angle of ≈ 22 mrad for a full rotation. It is rather easy to turn the screw better than 15 °, so in ≈ 1 mrad steps. For the rotation around the longitudinal axis an M2 screw with 0.4 mm pitch is used. The distance between screw and rotation center is 71 mm which results in ≈ 6 mrad for a full rotation and ≈ 0.2 mrad for 15 °. After aligning the holder the screws are locked again due to which the adjusted angle slightly changes. As this setup is designed to align the Hall probe by eye to the geometry of the undulator and not onto the magnetic axes, the technically achievable accuracy is more than sufficient.
The aligned Hall probe inside the undulator gap is shown in Fig. 7.3 and Fig. 7.4. The probe is first aligned parallel to the girder and then centered inside the gap. In a second step the Hall probe is centered in the horizontal axis. When this alignment is done, the laser line (see Sec. 6.2.3) is shifted onto the pinhole.

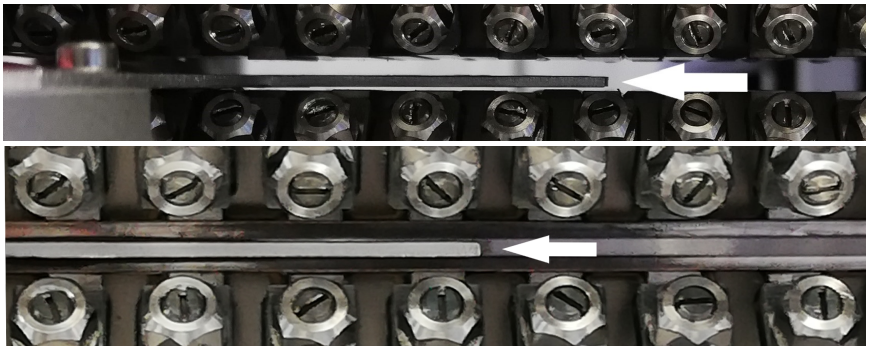

Figure 7.3 – Vertically aligned probe. The white arrows point to the Hall sensor. On the upper picture the probe is aligned parallel to the undulator, on the lower one the probe is aligned to the mechanical axis.

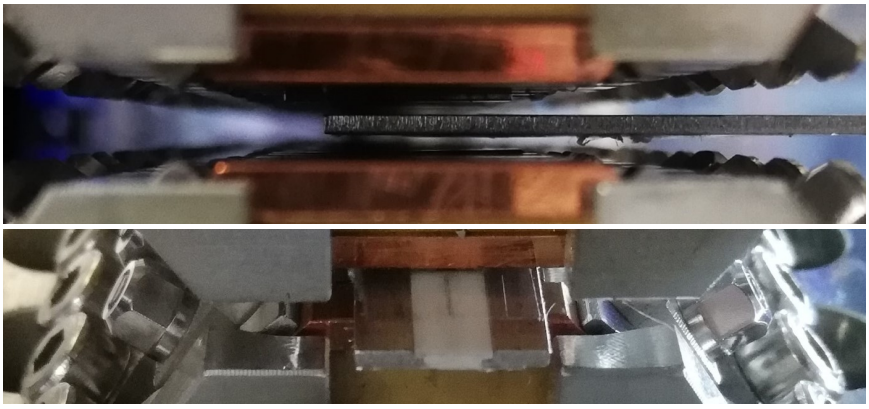

Figure 7.4 – Horizontally aligned probe to the mechanical axis.

7.1.3 Laser Alignment to the Undulator Axes

The laser alignment is done on two steps:

1. Geometrical alignment to the mechanical undulator axes
2. Geometrical alignment to the magnetic undulator axes

For the alignment it is important to know which measurable quantity has to be used as reference. By now, the girders and the poles are in an unknown state. Meaning the girders could be tapered and/or deformed and the poles in arbitrary formations. Going back to Eq. 2.9, the vertical field amplitude scales with $\left(1 - \frac{(k_x x)^2}{2} + \frac{(k_y y)^2}{2}\right)$ and it is tough to distinguish if a change of the field comes from the horizontal or vertical offset. If the probe would be aligned to the vertical field and would measure a taper it could not be distinguished if the undulator is tapered or if the Hall probe moves under an

angle away from the axis. The horizontal axis scales with x·y and is impractical as one can not measure offsets in one plane if the other offset is zero.
The best candidate is the longitudinal field component as it linearly increases with a vertical gap offset like $B_0 \cdot k_u \cdot y$ symmetrically from the undulator axis.

Geometrical Alignment

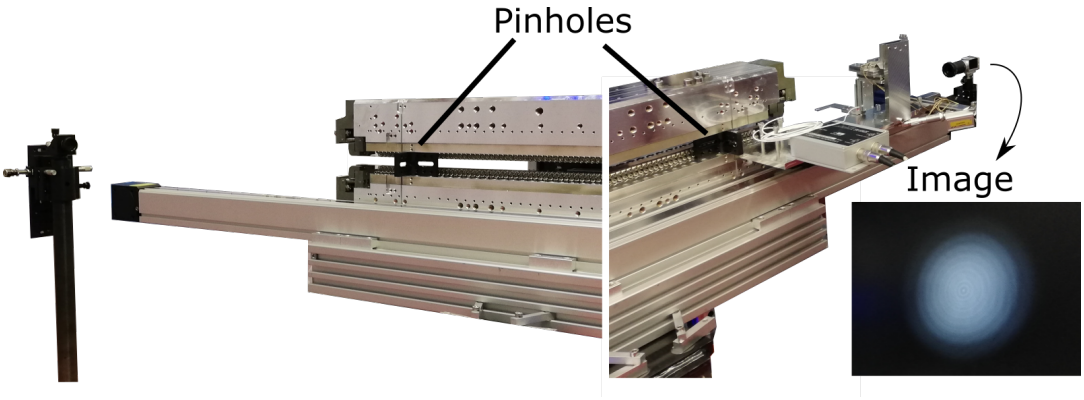

Figure 7.5 – Laser alignment setup. Two black holders with holes in it are clamped into the undulator gap. The laser (left) is guided through both holes onto the camera.

To align the laser two pinholes were slightly clamped inside the undulator gap, see Fig. 7.5. This causes both pinholes to have a fixed distance to the mechanical undulator axes and allows to guide the laser almost parallel to the mechanical axes. At each pinhole the laser is slightly clipped which will cause interference rings to appear on the camera. If the interference rings of the first and the second pinhole overlap the laser is aligned to the axis defined by the pinholes.

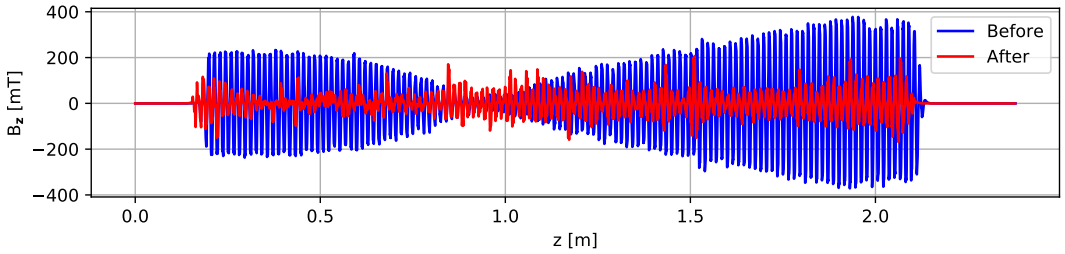

Figure 7.6 – The longitudinal field component measured before and after the geometrical alignment of the laser line to the undulator.

In Fig. 7.6 the longitudinal magnetic field is measured before and after the geometrical alignment procedure is done. The rough alignment through two pinholes increased the

straightness of the measurement system. Before the alignment, the probe started from an initial vertical offset and drove under an angle through the undulator such that it crossed the magnetic undulator axis around $z = 0.9\,m$ and stopped again on an off-axis position at the end of the undulator.
As the Hall probe is not adjusted to the magnetic axes it has to be assumed, that the Hall probe is still slightly rotated which would give a cosine like error onto the measured values. From Fig. 7.3 and Fig. 7.4 it is possible to estimate that the Hall probe is better aligned than $5\,°$ to the respective undulator axes which would give $\approx 0.38\,\%$ impact from the other two coordinates. For example, a vertical 1 T peak field would contribute with up to 4 mT to the longitudinal axis, which would be equal to a vertical Hall probe offset of $10\,\mu m$ if no contribution would be present. This means, it is only possible to align the probe such that the average B_z component is minimized, but not to get it to zero.

Magnetic Alignment

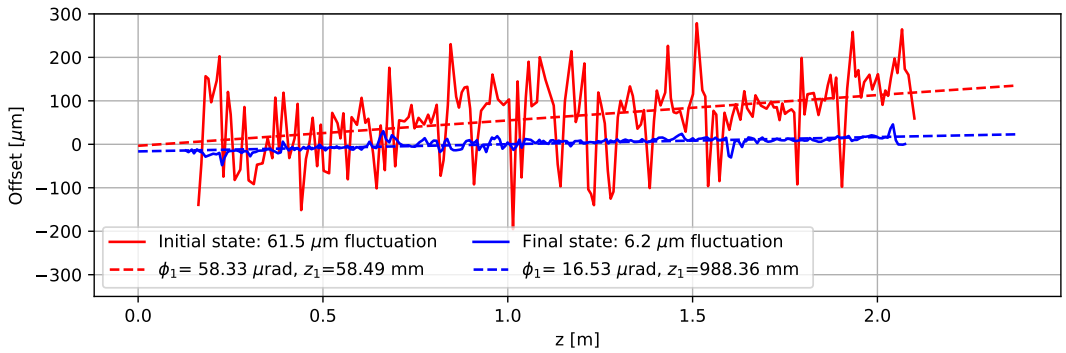

Figure 7.7 – The alignment of the laser line onto the vertical field component. In red is the data before the alignment started, in blue the final result.

To align the laser to the magnetic axes of the undulator, the longitudinal field amplitudes are converted into vertical offsets using $y = B_z/(B_0 \cdot k_u \cdot \mathrm{sign}(\cos(k_u z)))$. A linear fit is done to the peaks to retrieve the angle ϕ_1 and offset z_1 which need to be compensated by the laser line motorization by shifting and rotating the mirror. The laser is defined as aligned to the longitudinal magnetic axis, when the fluctuations of the signal is minimized.
The compensation is programmed such that it rotates the laser line around the calculated offset of the linear fit. When this is done, the laser line is shifted about the negative value of the offset to the undulator axis. The center of the motorized mirror is $z_0 = 1\,m$ away from the undulator entrance. The required steps to compensate the angle is $N_{rot} = \phi_1/0.7\mu\mathrm{rad/step}$. The rotation center is $z_2 = z_0 + z_1$ away from the

mirror center, so the mirror has to drive about $N_{vert} = z_2 \cdot \sin(\phi)/0.3\ \mu$m/step steps in the vertical direction.
This method is limited: Neither the mirror mount nor the stage have a direct encoder, so an active feedback to regulate the driven steps is not possible. In addition the Piezo motor of the mirror mount was not able to drive single steps. Several tests showed, that the driven distance overshoots up to 20 steps which would limit the angular compensation to 15 μrad. So, the alignment was automated to retrieve the best possible outcome within several iterations.
As already mentioned in the geometrical alignment section, the probe is assumed to be rotated. If the probe would be aligned to the magnetic axis the measured vertical field would consist out of contributions from the other axes due to the rotation. As a consequence, the average offset would always be non-zero which limits the routine to $\approx 10\,\mu$m. This limit is now used as a stop criterion in a way that the algorithm stops when the average absolute value of the peak offsets is below 10 μm after the linear fit is subtracted.
The red graph in Fig. 7.7 shows the initial state in which the laser axis is 60 μrad off and the average vertical offset is 60 μm. After the alignment the average vertical offset is 6 μm and well below the stop criterion of 10 μm. The zero crossing of the on axis field is centered along the undulator and the Hall probe moves under an angle of 16.5 μrad through the undulator. That means, the probe is 16.5 μm off-axis at the beginning and the end of the undulator. These offsets are below the alignment tolerances derived in Sec. 6.1. So, with this automated routine it is possible to align the Hall probe within the 10^{-4} good field region of the magnetic field in a reproducible way.
The contribution of a vertical offset of $y_{off} = 16.5\,\mu$m to the vertical magnetic field is $0.5 \cdot (k_u \cdot y_{off})^2 = 24 \cdot 10^{-6}$, see Eq. 2.9. For a 1.2 T peak field follows a contribution of 28 μT which is below the 75 μT noise level of the Hall probe signal, see Sec. 6.2.2, so, well below the possible resolution. With this measurement, the alignment of the Hall probe onto the magnetic undulator axes is finished and the tuning of the machine after the magnetic field can start.

7.1.4 Pillar Shimming

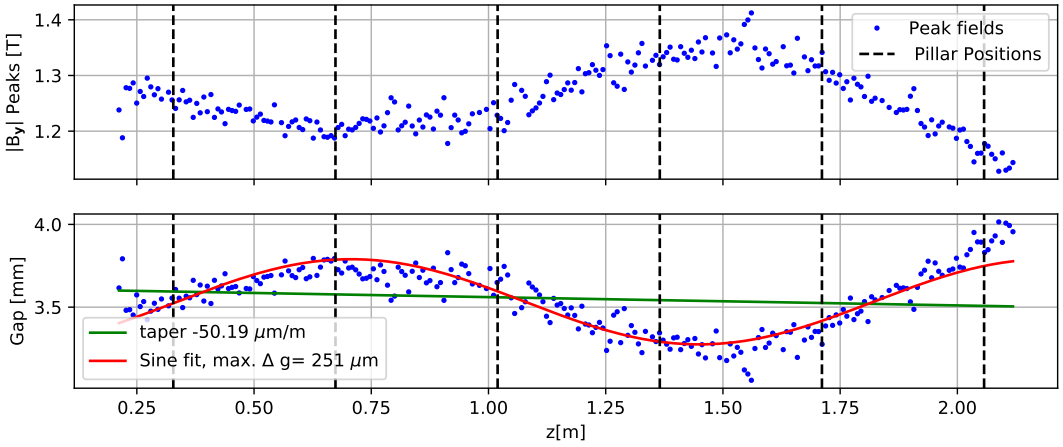

Figure 7.8 – Peak field distribution along the undulator. In the lower picture, the peak fields are converted into gap values from which the taper and the sinusoidal deformation are calculated.

By now, the Hall probe is correctly aligned to the undulator axis. Before the field can be fine tuned, a comparable rough shimming of the magnetic field has to be done by changing the pillar lengths and reducing the average taper of the magnetic distribution. These field corrections could also be done by turning every single pole, but the advantage of the pillar shimming is, that one pillar pair changes the overall magnetic field of 1/6 of the undulator. To do so, the field is measured first along its axis and the peak fields are converted to gaps values using Eq. 4.1. A taper creates a slope on the signal, whereas different pillar lengths create a long sine-like variation, see lower plot in Fig. 7.8.
The linear taper of -50 μm is removed be driving the motors of the frame. The sine-like deformation needs to be turned out by changing the length of the individual pillars. This shimming is done by putting small metal plates between the pillars and their frame connectors, see Fig. 4.39. The minimum plate thickness available is 25 μm and the shimming has to be done symmetrically on the upper and the lower girder to change the gap around the undulator axis. So, the shimming has to be stopped when the gap deviation reaches a limit of 50 μm.
To retrieve the shimming distances for each pillar pair, the sine fit in Fig. 7.8 is evaluated at each pillar position and the retrieved value is halved. The distances are then shimmed with the right amount of plates and the procedure is repeated until the desired limit is reached.
After the shimming of the pillar lengths, the maximum gap deviation of the sine fit is 34 μm. This corresponds to a shimming thickness of 17 μm which is smaller than

the available plates with 25 μm. There is also a small taper of $\approx$ 5 μm/m measurable which has to be tuned out, see Fig. 7.9.
So, the pillar shimming is finished and the fine alignment of the Hall probe to the average undulator axes can be started.

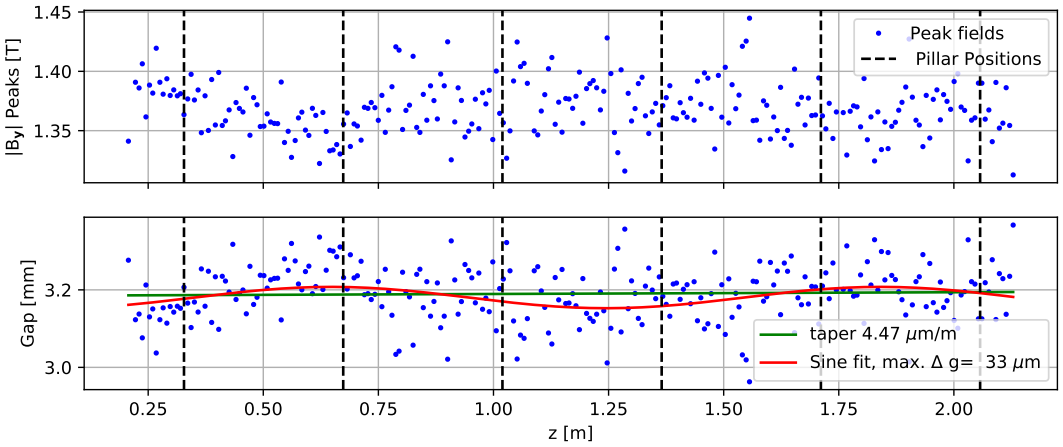

Figure 7.9 – Peak field distribution after the pillar shimming.

7.1.5 Magnetic Hall Probe Alignment

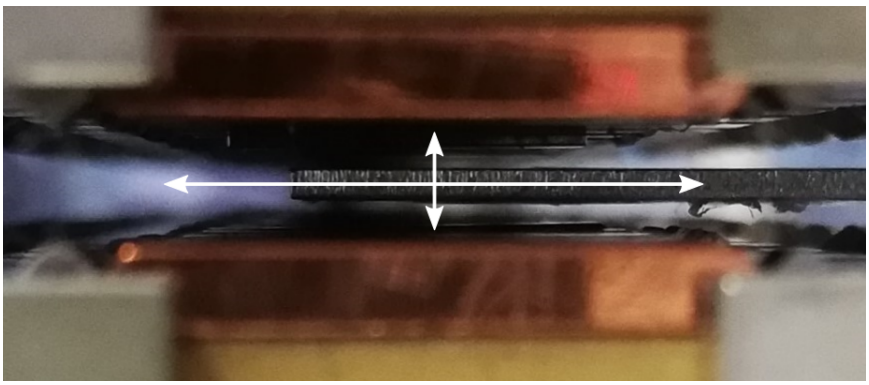

Figure 7.10 – Front view inside the gap parallel to the magnetic arrays (on top and bottom of the picture) onto the Hall probe holder. The probe is located at the crossing of the arrows. The arrows indicate the vertical and horizontal offsets for the field scans into longitudinal direction.

In Sec. 7.1.2 the Hall probe was aligned to the longitudinal field of the undulator, but the rotation of the probe with respect to the undulator axes has to be determined. This is done by scanning the magnetic field along the longitudinal direction with different

horizontal and vertical offsets, see Fig. 7.10. For this measurement three things have to be considered:

1. It is necessary to reference all individual coordinate systems of each pole and the bench to one global coordinate system with a reproducible method. As all poles are in arbitrary positions inside the girders we expect strong fluctuations from pole to pole. Therefore, the centering can only be done by averaging over all poles and to align the probe onto the average center and to find the average rotation.
2. The pinhole aperture is only 0.7 mm in diameter. Driving the probe in the mm range along the transverse plane would require to also shift the laser line due to which its alignment onto the longitudinal field component is lost. Following from this, the field scan can only happen in an area in which the camera still receives a signal from the laser without touching the laser line. So, only transverse offsets below $\pm$ 350 μm around the pinhole center can be used.
3. To calculate the rotations around the axes it has to be assumed, that the Piezo stages drive parallel to the magnetic axes and perpendicular to each other which is only approximately true. It is certain that the Piezos drive the probe on a slope with a small angle ($\ll 5\,°$) instead of a straight line along the axes. Due to the mechanical alignment, see Fig. 7.3 and Fig. 7.4, these errors should be small, especially when the offsets for the scans are kept small and below a 0.7 mm range.

Rotation around Horizontal Axis

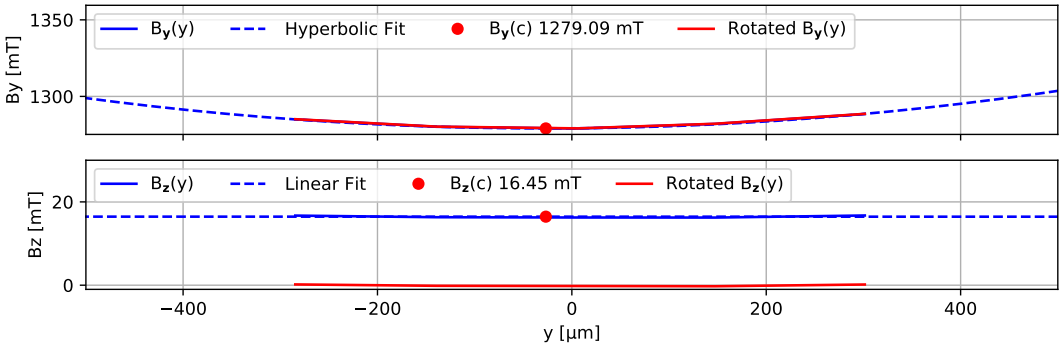

Figure 7.11 – Peak field scan of the B_y and B_z component for different vertical offsets to determine the rotation around the horizontal axis. The red lines are the rotated fields.

To measure the rotation around the horizontal axis, the undulator field is scanned with different vertical offsets. According to Eq. 2.9, a quadratic increase of the vertical field amplitude with the offset and a linear increase of the longitudinal field with the offset are expected. The vertical field oscillates with $\sin(k_u \cdot z)$ and the longitudinal with $\cos(k_u \cdot z)$. When the vertical field is at its maximum the longitudinal one should vanish. For a rotated probe non-zero values for B_z will be measure when B_y is at its maximum. By measuring the B_z component at the maximum of B_y, the rotation angle is determined.
The rotation matrix has to be evaluated at the undulator axis, to not mix a rotation and an offset into it. To calculate the on axis field, a hyperbolic fit of the form $B_0 \cdot (1 + 0.5 \cdot k_y^2 \cdot (y - c)^2)$ is used. B_0 is the minimum vertical field of the undulator, k_y the periodicity of the vertical field component, c is the position of the field minimum with respect to the Hall probe position and y is the vertical offset. To estimate the rotation angle, the fields at position c are used. There, B_y should have a minimum and B_z should be zero. The rotation angle is then $\Theta_x = \arctan(B_z(c)/B_y(c))$ and the following rotation matrix is used to rotate the data:

$$R_x = \begin{bmatrix} 1 & 0 & 0 \\ 0 & \cos(\Theta_x) & \sin(\Theta_x) \\ 0 & -\sin(\Theta_x) & \cos(\Theta_x) \end{bmatrix}$$

The scans are plotted in Fig 7.11. The Hall probe was aligned to the $y = 0\,\mu$m position by eye before, see Sec. 7.1.2. The scans show, that the average magnetic undulator axis is c = -26.7 μm below the geometrically aligned axis of the probe, which has to be adjusted. At this position, the fields are $B_y(c) = 1279.1\,$mT and $B_z(c) = 16.45\,$mT which results in a rotation angle of $\Theta_x = 0.74\,°$. The data is rotated about this angle and shown as the red graphs. For the vertical field, this change is negligible due to the small angle. The longitudinal field is now close to zero and vanishes at c. This scan is also used to determine the vertical periodicity, see Sec. 7.2.6.

Rotation around Longitudinal Axis

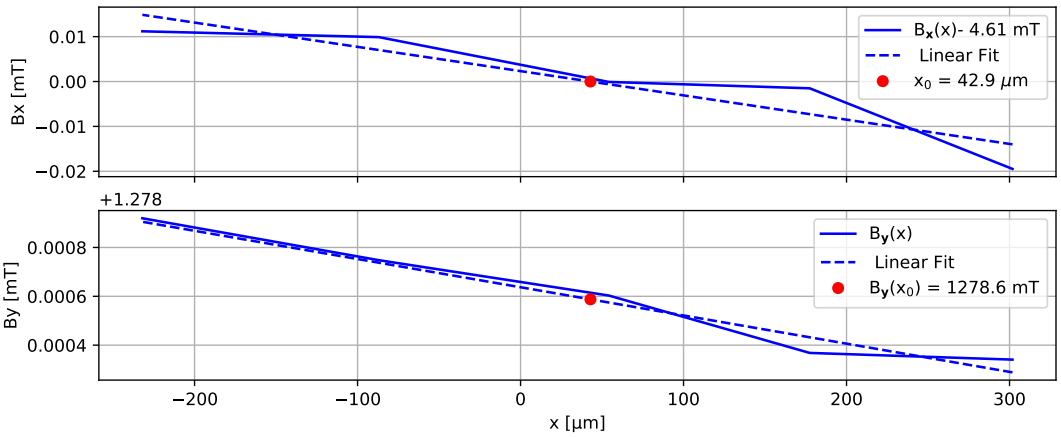

Figure 7.12 – Scan of B_x and B_y to find the horizontal center and the angular correction around the longitudinal axis.

For each horizontal scan the B_y and B_x peaks are recorded. According to Eq. 2.9, a horizontal field always vanishes as the B_x amplitude scales with x·y and is always zero for $y = 0$. A vertical offset y would introduce a linear increase of the horizontal field component with a zero crossing at $x = 0$. An additional rotation would cause an offset onto the slope. To get this offset, the mean value of the B_x component is used for the calculation of the rotation angle. After subtracting this offset, a linear fit is done to find the zero crossing x_0 of the field. As the B_y component is almost constant within this region, also a linear fit is used to get the vertical field at x_0. From the fields B_x and $B_x(x_0)$, the rotation angle is calculated using $\Theta_z = \arctan(B_x/B_y(x_0))$ and the rotation matrix is :

$$R_z = \begin{bmatrix} \cos(\Theta_z) & \sin(\Theta_z) & 0 \\ -\sin(\Theta_z) & \cos(\Theta_z) & 0 \\ 0 & 0 & 1 \end{bmatrix}$$

In the upper plot of Fig. 7.12 the average field of 4.61 mT was subtracted to evaluate the zero crossing which is 43 μm away from the Hall probe center. The rotation angle is $\Theta_z = $-0.21 °.
Both rotation matrices are combined and applied to the data during the measurements. With the final calculation of the rotation matrix the Hall probe is fully aligned and characterized to the undulator field and the fine tuning of the poles follows.

7.2 Magnetic Field Tuning

The aim of the fine tuning is to get the average particle trajectories in the vertical and horizontal plane below their tolerances, see Sec. 6.1. To do so, the magnetic field has to be modified by changing some poles in position and rotation, where the number of poles which have to be changed should be kept reasonably small. The tuning of the field is done in three major iterations and the mentioned techniques are explained in the next chapters:

1. **Field flattening:** The on-axis field is flattened first. This is done by measuring the average on-axis field at a gap of 3.5 mm. All poles will be turned such that the deviation in B_y to the average field is below a defined threshold of ± 0.5 mT. The B_x component should be zero and also below the threshold. It turned out that the additional tuning of the B_z is impossible because the accuracy of the pole hangings was not good enough, so this component was ignored for the flattening.

2. **First shimming:** After the flattening of the magnetic field, the core of the field integrals are tuned, see Sec. 7.2.1. The core is defined as the section between the in and out coupling periods. This is done by finding specific poles in the profile of the flattened field integrals with which the overall field integral can be flattened. This is repeated until the core field integrals are within their limits. What remains is a linear slope which can be changed by shimming the coupling periods, see Sec. 7.2.2.

3. **Foil shimming:** After the first shimming a CuNi foil is installed on the magnetic structure of each girder. The foil is necessary to flatten the gap sided surface. Without the foil the geometry of the magnetic lattice could form a cavity like structure inside the gap in which a fraction of the emitted radiation spectrum could potentially be captured and could radiate and interact back onto the electron bunch. The foil consists out of a Copper and a Nickel layer with 25 μm thickness each. The Ni part is magnetic and will stick to the poles to hold the copper part into position. The copper part acts as an electrical conductor for the emitted fields and or created mirror charges. Due to the Ni part the magnetic undulator field will get disturbed as now also magnetic shortcuts between neighboring poles are possible. The foil will also have some vertical offsets induced by vertically shifted poles. Due to that the foil is not flat but has some slopes in it. This increases the acting distance of the localized vertical dipole field along the longitudinal direction. During the installation it can also happen, that the position of the poles changes due to the foil, as the foil needs to be moved over the device. When poles stick to the foil while it is moving, they will change their position. So, the shimming has to be repeated after the installation.

7.2.1 Core Tuning

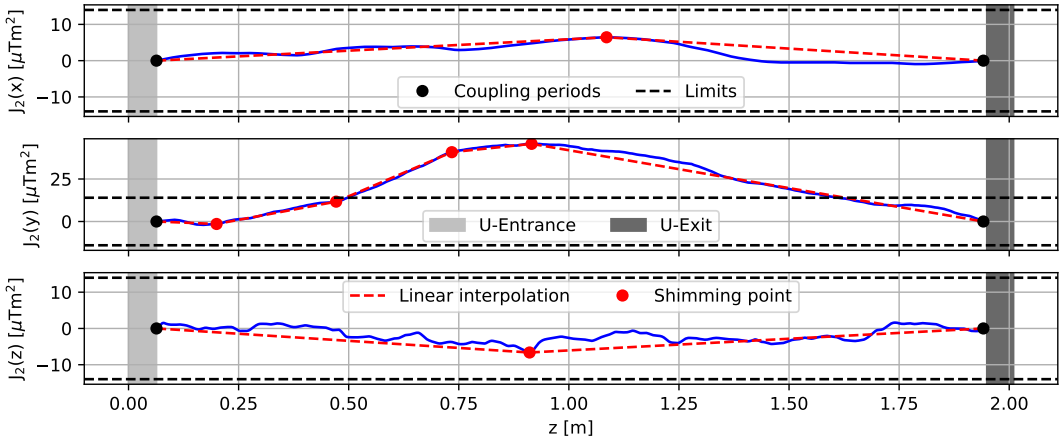

Figure 7.13 – Core part of the average second field integrals used as an example plot for the Ramer-Douglas-Peucker algorithm to find the tuning positions. The gray areas indicate the coupling periods, the red dots the periods which needs to be shimmed.

An example of the average second field integrals is plotted in Fig. 7.13. The core part refers to the magnetic field between the coupling periods. If this is flat, the coupling periods do only contribute with an overall angle to the integrals which is corrected at the end. To find the tuning positions inside the field integrals a recursive Ramer–Douglas–Peucker algorithm is used [80, 81]. This code makes a piece-wise linear interpolation between two points A and B of the core field to find the position with the largest offset P_1 to the straight $\overline{AB}$. Then, this point is added to the piece-wise linear interpolation and the largest offset P_2 between $\overline{AP_1}$ and P_3 between $\overline{P_1B}$ is calculated and so on. This algorithm stops until a user defined threshold is reached. The lower the threshold the more points are found which means more periods have to be tuned, but also about smaller amounts. A higher threshold reduces the number of periods, but increases the amplitude about which the poles have to be shifted.
An example is plotted in Fig. 7.13. The black dots are the starting points for the linear interpolation and the red dots the furthermost distance to the slope. The threshold for $J_2(z)$ is chosen such, that only one point was found. For $J_2(y)$ the threshold was lowered to increase the number of points. To retrieve the value about how much a pole has to be tuned a detour over the first field integral has to be done:
Staying in the example given before, the slope of the straight $\overline{AP_1}$ is

$$s_{AP_1} = \frac{J_2(P_1) - J_2(A)}{z(P_1) - z(A)}.$$

s_{AP_1} has now the units of the first field integral [Tm]. The difference of the slopes $\Delta s_{AB} = s_{AP_1} - s_{P_1B}$ is the amount ΔJ_1 about how much the first field integral at the period P_1 has to be changed to get the second field integral flat. The tuning is always done by changing both poles of the period in position to reduce the impact onto the phase error. So, each pole needs to be turned about $\Delta J_1/2$. The first field integral for one half period is $J_1 = B_0\lambda_u/\pi$. The peak field of each pole needs to be shifted about

$$\Delta B = \frac{\pi}{2 \cdot \lambda_u}\Delta J_1 = \frac{\pi}{2 \cdot \lambda_u}\Delta s_{AB}.$$

7.2.2 Fringe Tuning

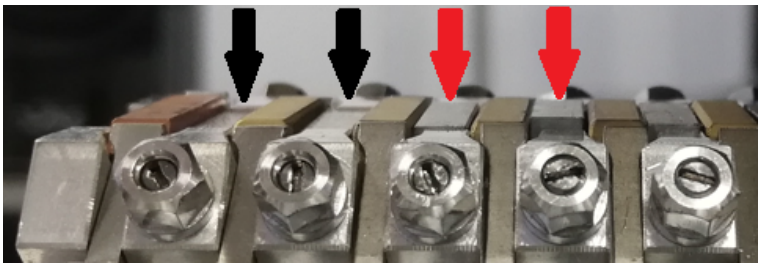

Figure 7.14 – Close up onto the coupling period of the undulator, which consists out of the first two poles from the left (black arrows). They are stuck in position and later on blocked inside the magnetic structure. The third and fourth pole are used instead to correct the initial kick (red arrows).

The mean propagation of an electron is parallel to the undulator when the boundary conditions for Eq. 2.11

$$x'(0) = \frac{1}{\gamma}K, \quad x(0) = 0.$$

are realized. This can be achieved by a suitable pair of coupling periods at the beginning and the end of the magnet array, with a non-vanishing first field integral of $J_1 = B_0/k_u$. The coupling periods have a different magnet design with an amplitude of $0.25\,B_0$ in the first and $0.75\,B_0$ in the second half period, which results in B_0/k_u for the total period.
Due to the different magnet design, the gap dependent attractive forces, see Fig. 4.9, are different for the coupling periods such that their attraction to the opposite girder is reversed for small gaps. During the tuning it was figured out, that above 4 mm gap the coupling periods are attractive, between 4 mm to 3 mm the poles are only kept in position by friction, and below 3 mm they got pushed into the girders, see Fig. 7.14 and were stuck without any controllable possibility to be moved.
By opening the gap again some poles were still stuck but one jumped out and hit the opposing magnetic lattice, which is the worst case that could happen. To keep the

poles at least in a defined position they were blocked inside the girder at their lowest point. To tune the coupling the subsequent undulator period is used. The original coupling periods will still produce a strong kick at the beginning of the undulator, which can not be completely compensated by the second coupling periods. So, the initial transverse velocity of the entering electrons has to be changed such that the average trajectory is minimized.
The periods have to be tuned in the same way as the core part. The tunable range is limited by the measurement error of $\approx 10\,\mu\mathrm{Tm}^2$ over 2 m length. This results in a peak field error of ≈ 1 mT per coupling pole, which makes their tuning quite challenging. An additional Helmholtz coil, see Sec. 5.6, or a corrector dipole magnet in front of the undulator will be used to steer the electron beam onto a straight when the coupling periods are not perfectly adjusted. So, the coupling periods were aligned as good as experimentally possible.

7.2.3 Trajectory Optimization

The tuning of the magnetic field is limited by the adjustability of the poles and the accuracy of the measurement bench. Following from that, the trajectories of the particles inside the undulator field could still be curved or tilted. To correct the tilt, the electron beam is guided into the undulator with an initial kick $\mathrm{v_0} = (\mathrm{v_x/v_z}, \mathrm{v_y/v_z})$ and position offset $\mathrm{p_0} = (\mathrm{x,y})$. To correct the curvature, an additional background field with amplitude $\mathrm{B}_f = (\mathrm{B_x}, \mathrm{B_y})$ is applied by a long Helmholtz coil, see Sec, 5.6. To find the correct fit parameters a second order polynomial of the form

$$\mathrm{P(z)} = \frac{1}{\gamma} \cdot \frac{\mathrm{e}}{\mathrm{m_e c}} \cdot \frac{1}{2} \cdot \mathrm{B_f} \cdot \mathrm{z}^2 + \mathrm{v_0} \cdot \mathrm{z} + \mathrm{p_0}$$

is used. The corrected fields will be used to calculate the electrical field of the emitted photon beam.

7.2.4 Shimming of the Undulator Field

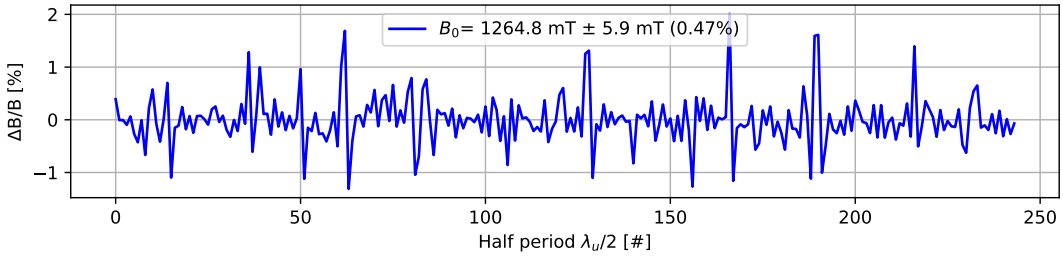

Figure 7.15 – Vertical peak field distribution along the undulator half periods.

The vertical peak field distribution of the tuned undulator field along the machine is $B_0 = 1265\,\mathrm{mT} \pm 5.9\,\mathrm{mT}$ (0.47 %), see Fig. 7.15. This results in a K-value of 1.78. The tuning limits of Tab. 6.1 are adjusted to this K-value.

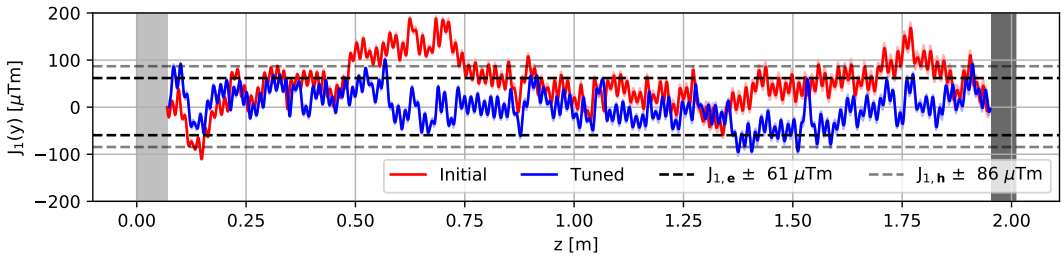

Figure 7.16 – Average vertical first field integral before and after shimming. Limits from Sec. 6.1.

The average first field integral of the vertical component is shown in Fig. 7.16 and stays within the given limits marked as the dashed lines, see Sec. 6.1. The fast oscillation from pole to pole comes from the Earth's magnetic field inside the laboratory which is amplified by the poles similar to the field of the compensation coil, see Sec. 5.6. This will not be corrected as the Earth's magnetic field will also be present in the later accelerator tunnel.

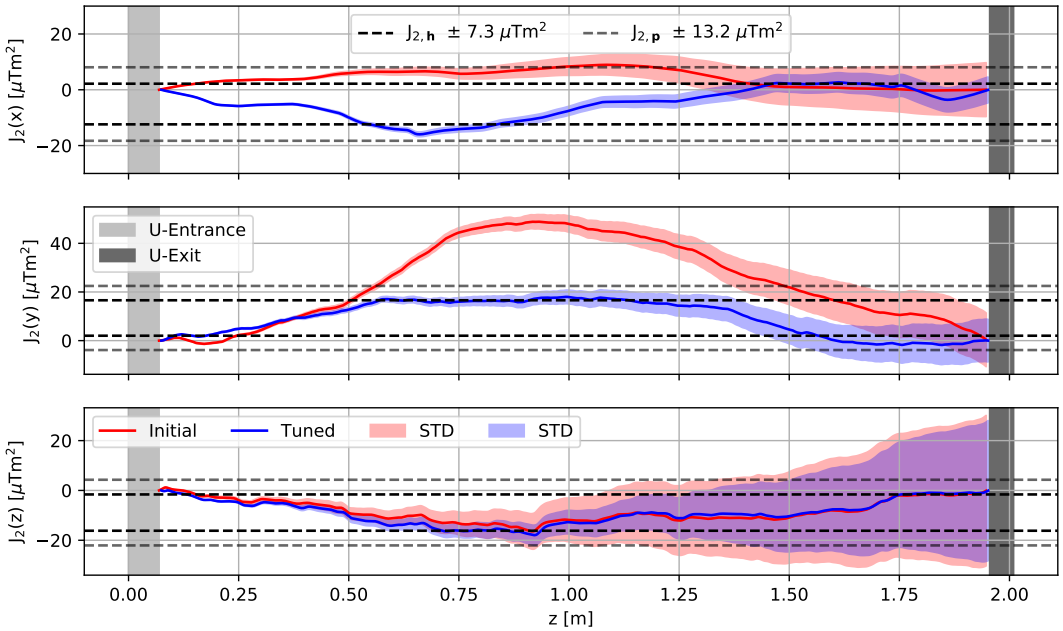

Figure 7.17 – Average second field integrals of the undulator core after the first tuning. Limits defined in Sec. 6.1.

The average second field integrals are tuned as explained in the sections before and the final field was measured ten times in a row for statistics. Fig. 7.17 shows the average core integrals before (red) and after the tuning (blue). The limits for the integrals were adjusted to the measured vertical peak field. The horizontal and longitudinal components are non-zero and have an impact onto the particle oscillation. Also, the vertical component shows a curvature in the $J_2(y)$ signal which causes a minor additional deflection in the horizontal plane. Besides that, the important integrals $J_2(y)$ and $J_2(x)$ are below the defined tuning limits, see Tab. 6.1. Due to the high measurement error, the $J_2(z)$ component is out of those limits. As mentioned, this component is not adjustable and a tuning of the field can not be done.
The resulting particle trajectory was optimized as discussed in Sec. 7.2.3 and the average position of the particle inside the undulator field is shown in Fig. 7.18.

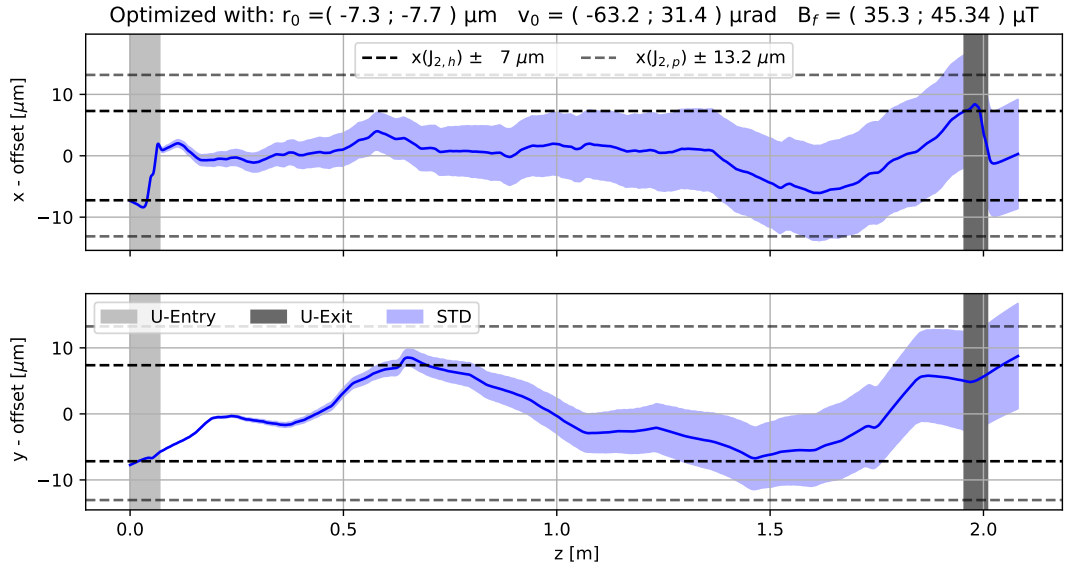

Figure 7.18 – Optimized average electron trajectory for 300 MeV. Limits (dashed lines) defined in Sec. 6.1.

The two big jumps in the horizontal trajectory come from the modified coupling periods, see Sec. 7.2.2. To the data, an additional background field in the range of the Earth's magnetic field was added: $B_x = 35\,\mu T$ and $B_y = 45\,\mu T$. With an additional steering of the electron beam of -63 μrad (horizontal) and 32 μrad (vertical) it is possible to straighten the trajectory. With an initial offset of $\approx$-7 μm in both planes, the average trajectory is closest to zero but still has a curvature on the last 75 cm of the undulator. The vertical axis has a dip around z = 60 cm which originates from the $J_2(x)$ component at this position.

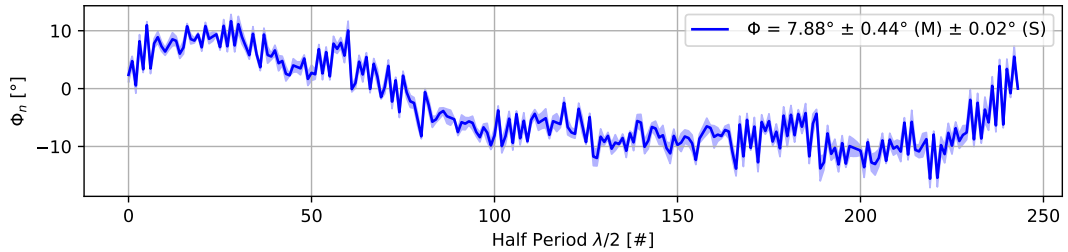

Figure 7.19 – Average phase error distribution for 10 measurements and the resulting phase jitter. For the set K-value, the limit is 8.12°.

The phase error distribution is calculated as described in Sec. 6.1 and shown in Fig. 7.19. The magnetic lattice of the undulator consists out of 257 half periods from which in total 8 periods belong to the coupling sections, see Sec. 7.2.2. These periods will not

be considered for the phase error or beam wander calculation of the core field. To calculate both the difference between the peaks of the emitted wave train has to be used, due to which the number of poles shrinks about one. So, the phase error is calculated for 124 periods instead of 128.
The fast oscillation along the signal is generated by the applied background field as this increases the amplitude of positive fields and decreases it from negative ones, resulting in a constant phase offset between the two half periods in one period. The phase jitter calculated from the emitted wave train is

$$\Phi = 7.9^\circ \pm 0.44^\circ\,(\mathrm{M}) \pm 0.02^\circ(\mathrm{S}).$$

The beam wander of the second vertical field integral is

$$\mathrm{J}_{2,\mathrm{bw}} = 19.8\,\mu\mathrm{Tm}^2 \pm 0.6\,\mu\mathrm{Tm}^2$$

and below the limit of $26.4\,\mu\mathrm{Tm}^2$.

7.2.5 Last Measurements in Tunnel

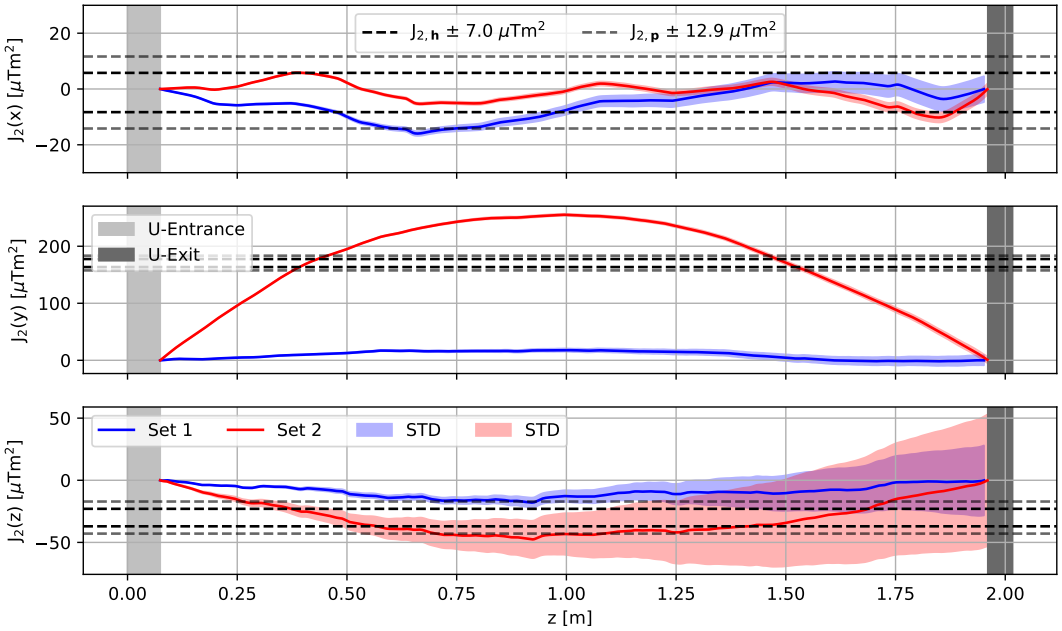

Figure 7.20 – Average core part of the 2nd field integrals of the undulator before (Set1) and after (Set2) the installation of the chamber. Limits defined in Sec. 6.1.

To install the vacuum chamber the girders had to be built out and back in after. This operation has the potential to destroy the previous shimming when a malfunction

during the installation happens, which happened as described in Sec. 5.5.:
The girders had to be dragged by force over the rails which caused vibrations inside the magnetic structure. This altered the magnetic field distribution and the field had to be measured again. This was done at the final position of the undulator in the accelerator tunnel. The alignment procedure for the bench was similar to the one described in Sec. 7.1.
The core of the second field integrals are shown in Fig. 7.20. The limits are adjusted to the tunnel field data. All three field integrals changed their shape. At the end of the $J_2(x)$ signal a strong kick appears around $z = 1.8\,\mathrm{m}$. The overall integral stays within its limits. $J_2(y)$ received a major bending and the integral reaches values far above $200\,\mu\mathrm{Tm}^2$ due to the changed positions and amplitudes of several poles, which changed the standard deviation of the vertical peak field distribution to $\pm 6.1\,\mathrm{mT}$ (0.5 %), see Fig. 7.21. This also caused a bending of the $J_2(z)$ component.

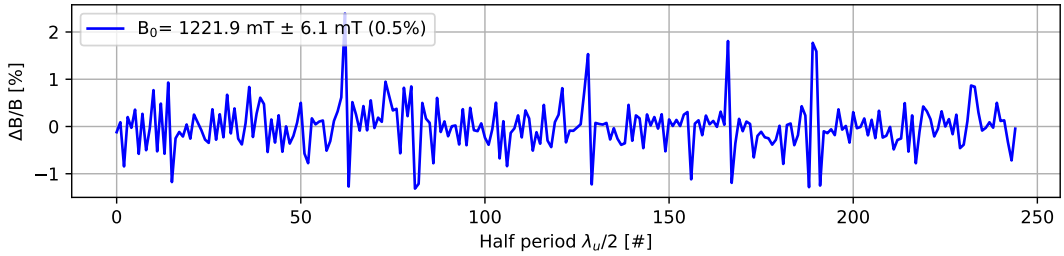

Figure 7.21 – Vertical peak field distribution of the undulator half periods after the installation of the girders inside the chamber.

To compensate the curvature of the integrals an additional field has to be applied with the compensation coil, see Sec. 5.6. With a suitable background field and an adequate steering of the electron beam into the undulator, the trajectories can be shaped such that they stay close inside the limits and the phase error within an acceptable range.

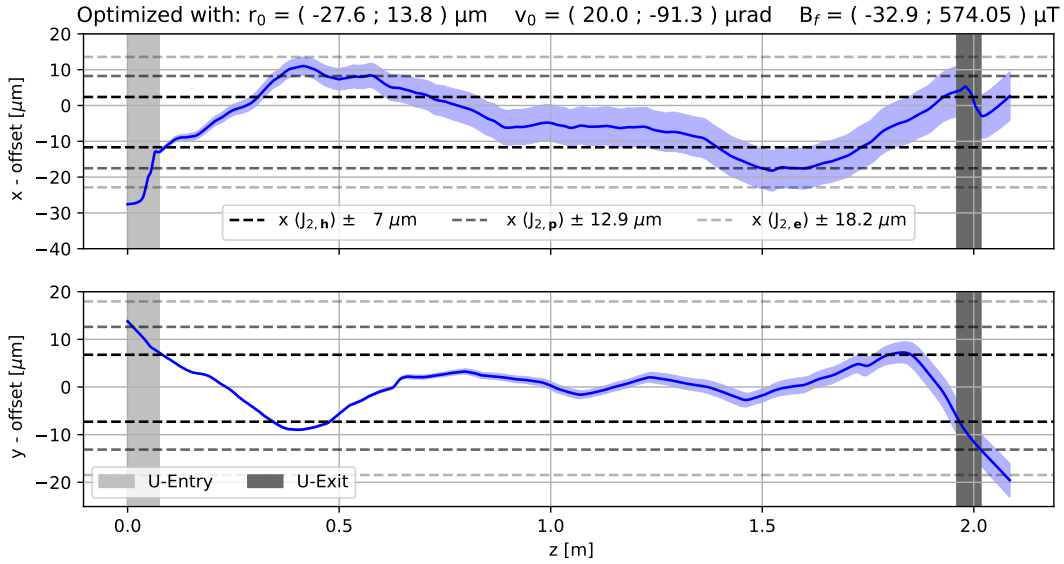

Figure 7.22 – Average modified trajectories for 300 MeV after the installation of the chamber. Limits defined in Sec. 6.1.

In Fig. 7.22 the tracking through the field is shown. The limits are adapted to the tunnel data. The background field has to be increased to 575 μT to flatten the trajectory. With this background field it is possible to keep the electrons within the defined limits, despite the fact that the chamber installation shifted several poles such that the trajectory itself has some major bendings in it. For example: in the horizontal displacement around 0.4 m and 1.5 m. As these kicks are localized at the ends of the undulator and in total only two and not a high number of kicks scattered randomly along the axis it is estimated that their impact onto the FEL performance is rather small. Especially as the field between those two positions is basically undisturbed.

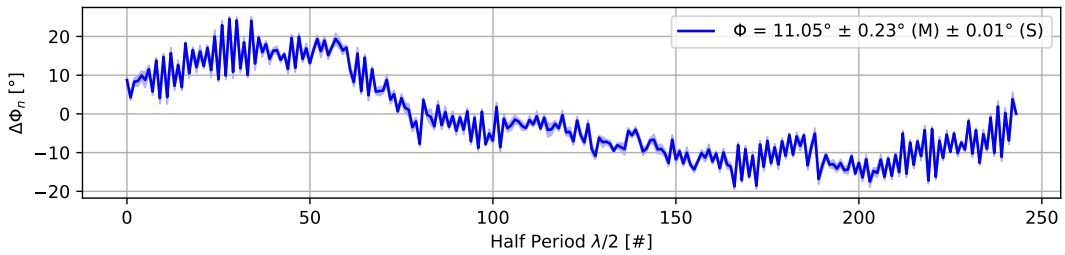

Figure 7.23 – Phase error distribution after the chamber installation and the resulting phase jitter Φ for 10 measurements. For the set K-value, the limit is 8.05°.

In Fig. 7.23 is the phase error distribution for the trajectory shown in Fig. 7.22. Due to the deformation of the trajectory the phase jitter of the photon field increased and is off the limit given in Tab. 6.1:

$$\Phi = 11.05^\circ \pm 0.23^\circ\,(\mathrm{M}) \pm 0.01^\circ\,(\mathrm{S})$$

and the beam wander increased to

$$\mathrm{J}_{2,\mathrm{bw}} = 66.3\,\mu\mathrm{Tm}^2 \pm 1.92\,\mu\mathrm{Tm}^2.$$

The main increase of the beam wander comes from the two kicks of the horizontal trajectory around 0.4 m and 1.6 m. Without those kicks the beam wander would be around $25\,\mu\mathrm{Tm}^2$, so within the acceptance discussed in Sec. 6.1.

7.2.6 Good Field Region

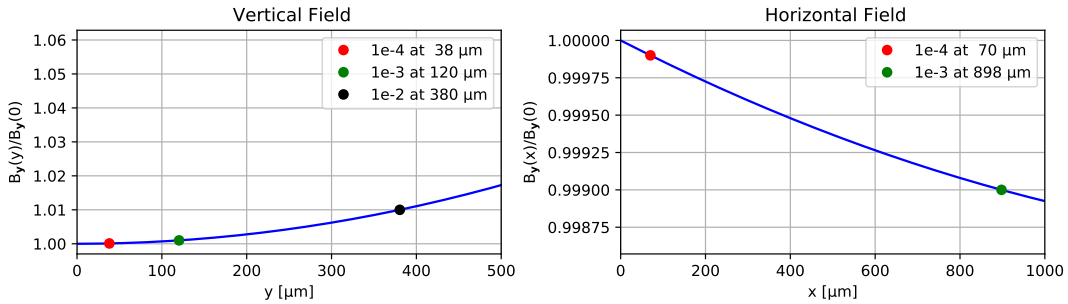

Figure 7.24 – Measured vertical and horizontal field deviation with good field regions of 10^{-4},10^{-3} and 10^{-2}. The peak field is 1279 mT.

The vertical undulator field has a minimum on axis and increases with vertical offsets. As the electron beam has a certain diameter the electrons in the outer region would receive a different deflection due to a different field amplitude than those on axis. It is convenient to define so-called good field regions of the magnetic field. These are regions within which the magnetic peak field does not change about a certain limit e.g. 0.1 %. To estimate those regions the field was measured into the vertical and horizontal direction similar to the method described in Sec. 7.1.5 and is shown in Fig. 7.24. From those measurements also the periodicities of the magnetic field axes are determined and are listed in Tab. 7.1:

Axis	Periodicity [1/m]
k_x	188.27
k_y	371.69
k_u	416.66

Table 7.1 – Measured periodicities of the individual field components.

7.2.7 Effective K - Value

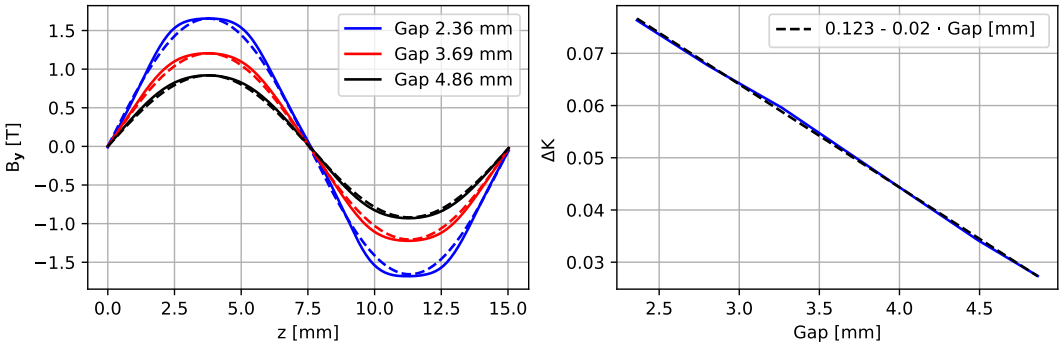

Figure 7.25 – Measured field profiles (solid) and sinusoidal approximations of the undulator field (Eq. 2.10 - dashed). With decreasing gap the field distribution changes towards a rectangular shape, which causes a shift of the K value between the measured profiles and the approximation of Eq. 2.12, as shown on the right side.

The undulator field is approximated by a pure sinusoidal function, see Eq. 2.10, which is valid for large gaps. For small gaps, especially when the pole length is longer than the gap size the magnetic field distribution converts from a sinusoidal field towards a rectangular function with a plateau at the pole height, see left in Fig. 7.25. This effect is maximized when the mechanical gap is zero and the magnetic arrays have direct contact. Then, the magnetic field can be approximated to be non-zero at the poles and zero otherwise. As a consequence of this distortion the particles will travel on a longer detour in the real field than within the sinusoidal approximations, see Sec. 2.3.1, which causes a different interference condition and, therefore, a red shift between the observed wavelength and the estimated one by Eq. 2.14.
To quantify this effect, the emitted wavelength is calculated using a particle tracking and Eq. 2.7 for different magnetic profiles measured at gaps between 2 and 5 mm. From those wavelengths the K parameter was retrieved for each field with Eq. 2.14 and compared to the K value of the sinusoidal approximation using Eq. 2.12 and Eq. 4.1. Within the measured region the difference between the K - value of the real field (K_{real})

and the approximation (K_{approx}) is close to linear, see right in Fig. 7.25, with the fit function

$$\Delta K = K_{real} - K_{approx} = 0.123 - 0.02 \cdot g \text{ [mm]}$$

and causes a correction about 2.1 % at 4.9 mm gap up to 3.2 % at 2.4 mm gap, which has to be considered when operating at small gaps. The effective K-value is then

$$K_{eff} = K + \Delta K$$

7.2.8 Spectral Analysis

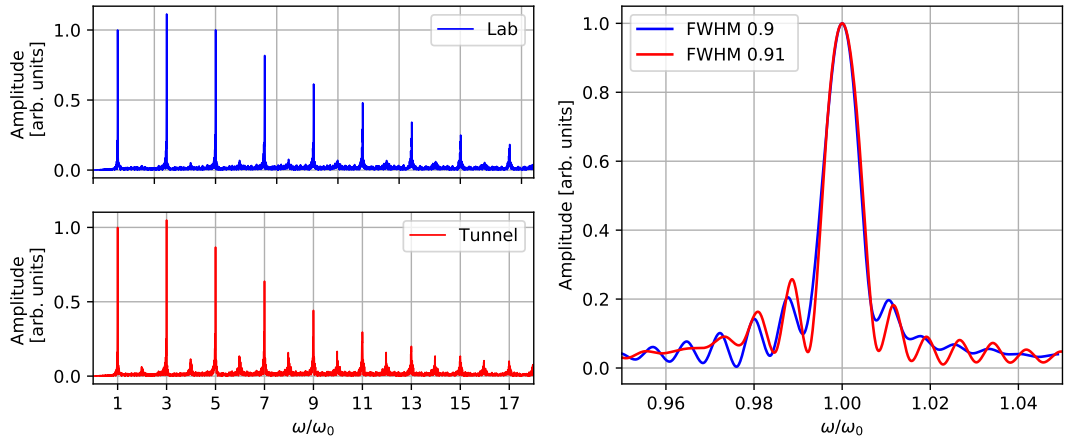

Figure 7.26 – Normalized spectral distributions of the calculated light field before (Lab) and after (Tunnel) the installation of the undulator in the tunnel. Calculated for the trajectories shown in Fig. 7.18 and Fig. 7.22.

From the measured magnetic field of the undulator before and after the installation inside the tunnel the emitted radiation for a single particle is calculated using Eq. 2.7. The fundamental bandwidth of the undulator Eq. 2.15 is increased due to peak field errors. They change the respective K-value within the periods and its effect onto the undulator bandwidht is estimated by taking the derivative of Eq. 2.14 with respect to the magnetic field:

$$\left(\frac{\Delta\lambda}{\lambda}\right)_B = \frac{K^2}{1+\frac{K^2}{2}} \cdot \frac{\Delta B}{B} \tag{7.1}$$

which contributes to the total bandwidth like

$$\left(\frac{\Delta\lambda}{\lambda}\right)_{tot} = \sqrt{\left(\frac{1}{N_u}\right)^2 + \left(\frac{\Delta\lambda}{\lambda}\right)_B^2}.$$

For the peak field errors shown in Fig. 7.15 and Fig. 7.21 and the $N_u = 128$ periods, the expected bandwidths are 0.96 % before and 0.97 % after the installation, so an increase about 0.01 %. The bandwidths of the calculated spectra are 0.9 % before and 0.91 % after the installation, see right in Fig. 7.26. The absolute values differ about 0.06 %, whereas the change of 0.01 % between both measurements are in a good agreement. The difference between the expected and measured absolute values could be caused by the distributions of the peak fields shown in Fig. 7.15 and Fig. 7.21. The peaks are not purely Gaussian distributed and the increase of the rms value is mainly caused by a small fraction which is far off the mean.
The spectra up to the 17 th harmonic are shown on the left. Due to the mentioned bumps in the electron trajectory after the installation of the girders inside the chamber, see Fig. 7.22, even harmonics will now contribute to the observed spectrum and a red shift of the radiation within each harmonic will occur. This red shift manifests in the wings of the spectrum such that the contribution of higher energies to the fundamental is suppressed whereas the lower energy side rises, see right in Fig. 7.26. But this is a small effect, because the amplitudes in the wings change within a 5 % range, whereas the main peak is close to constant.

7.3 Crosscheck with Simulations

In a last step the impact of the undulator field errors onto a possible lasing have to be determined, especially as the beam wander of the last measurement is above the estimated threshold. It is important to note that the presented FEL simulations do not show lasing of the Lux accelerator, but only the impact of the undulator field errors onto a possible lasing.
To calculate the FEL performance the Simplex [9] code is used, which allows to load measured two dimensional undulator fields, but uses approximations to estimate the FEL performance and does not allow to implement complex focusing schemes or electron bunch structures like those which will be used at Lux. An alternative is the Puffin code, an unaveraged 3D FEL code [82] which is capable of simulating those schemes and bunches but only allows to load vertical undulator fields (at the time of writing this thesis). This would neglect the vertical beam displacements caused by horizontal magnetic fields.
Nevertheless, the focus of the simulations is to show the impact of undulator errors and not electron beam parameters or complex focusing schemes onto the FEL gain. So, Simplex is a better choice here, as it allows to implement more measurement data than Puffin and the loss of field information is,therefore, lower.

Data Preparation For Simplex

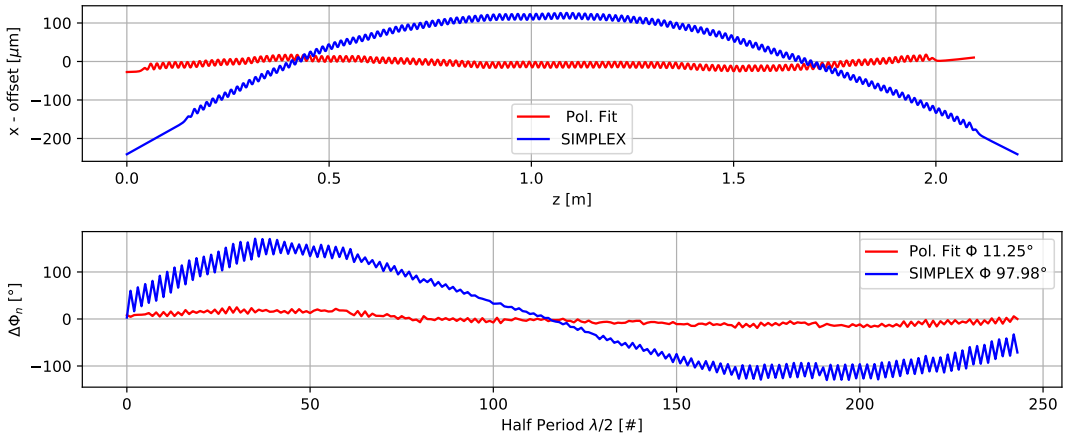

Figure 7.27 – Comparison trajectory correction by Simplex and a 2nd order polynomial.

Simplex provides an automated correction routine for the electron orbit, which is different from the one used in Sec. 7.2.3. At first, the average slope (which is the average of the first field integral) is subtracted from the loaded field data and then the average position (average of 2nd integral) is subtracted after. This is in contrast to Sec. 7.2.3 where a second order polynomial is fitted to the data to get the overall integrals closer to zero. The effects of the different corrections are shown in Fig. 7.27. To get reasonable results from Simplex the data has to be modified first. This is done by transferring the fit parameters of the second order polynomial, see Fig. 7.22, into the undulator field. The calculated background field is directly added to the data. The initial kicks dy/dz and dx/dz are implemented by artificially changing the coupling period of the undulator field such, that the average first and second field integrals are minimized. In the experiment a corrector magnet in front of the undulator produces the required initial kicks to get the average trajectory to zero. Changing the coupling periods basically mimics such a kicker in the simulation. For the modified field, a background of $\Delta B_x = $ -33 μT and $\Delta B_y = $ -575 μT was added. The coupling period was changed about 3.76 mT in x and -0.18 mT in y. To make the simulation comparable, the measured longitudinal field component is neglected.

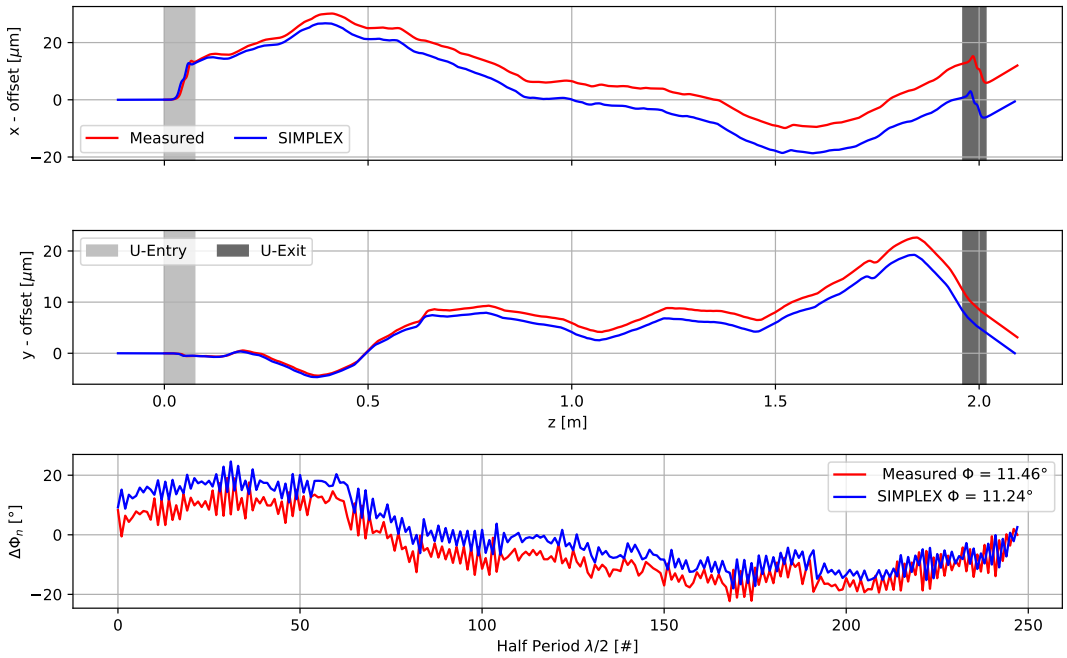

Figure 7.28 – Comparison between the modified measured field integrals and the tracking of Simplex.

The average trajectories for one modified field and the corresponding evaluation of Simplex are now comparable, see Fig. 7.28. The trajectories are close but still slightly tilted because the correction algorithm of Simplex evaluates again the modified field. Besides the small kick in both planes the phase error calculation is in an acceptable agreement and only differs about 0.2 °.

As mentioned, the Simplex simulations are used to estimate the impact of undulator errors onto the FEL performance only. Therefore, simplified and idealized parameters are used: For the simulation a 300 MeV Gaussian bunch with an rms length of 5 μm with 50 pC (1.2 kA peak current) and 2 mm mrad normalized emittance is used. The energy spread is set to zero to only see the impact of undulator field errors onto the FEL without a dominating energy spread. The trajectories of the particles are defined by two fields loaded into Simplex: the measured field of Frosty and an ideal equivalent with 128 periods with $K = 1.725$ and $\lambda_u = 15.088$ mm. Both simulations were done for 100 different seeds.

To estimate the change in the gain length, the analytical power gain curve G(z) from Eq. 2.23 is fitted to the data and the gain lengths for all seeds are plotted in Fig. 7.29. Under the assumption that the increase of the gain length is caused only by a phase error of the undulator field, the phase jitter is estimated with $\Phi_{\mathrm{FEL}} = \sqrt{3 \cdot \Delta L_G / L_G}$ [48].

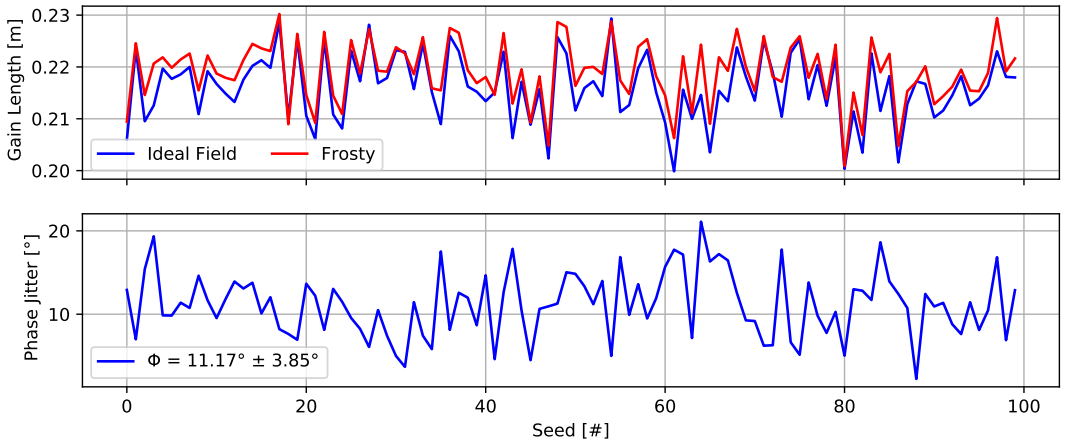

Figure 7.29 – Gain lengths for all seeds and the resulting phase jitter of the Frosty field.

The phase jitter retrieved from the simulations is:

$$\Phi_{\mathrm{FEL}} = 11.2^{\circ} \pm 3.9^{\circ}$$

which is in a good agreement with the evaluated phase jitter of Eq. 7.2.5. The simulations were done to estimate the impact of the undulator field onto the FEL performance. The only valid statements of these simulations are, that the beam wander inside Frosty has a minor effect compared to the phase error and that the gain length increase is mainly dominated by the later one.
With the right trajectory corrections in terms of initial electron pointing and undulator background field, it is possible to reduce the impact of the undulator error onto the gain length increase $\Delta \mathrm{L_G}/\mathrm{L_G} = \Phi^2_{\mathrm{FEL}}/3$, see Sec. 6.1, such, that the gain length elongates only about 1.3%.

7.4 Conclusion

Within this chapter the magnetic field tuning of the undulator was presented. The strategy to align the Hall probe to the magnetic undulator axes was shown in Sec. 7.1 and it was possible to reproducibly align the probe up to an angle of 16.5 μrad and 6.2 μm offset to the magnetic axes.
With the subsequent mechanical tuning of the magnetic field and an adequate background field correction and steering of a 300 MeV electron beam it is possible to keep the average electron trajectory deviations below $\pm 7\,\mu$m, see Sec. 7.2.4.
After the installation of the vacuum chamber inside the undulator frame the girder had to be re-installed. During this process the rail system had a malfunction and

the magnetes were exposed to vibrations which deformed the magnetic field. It was shown in Sec. 7.2.5 that the field distortions are manageable which means, that the trajectory errors can be kept with $\pm 19\,\mu$m, when applying an adequate background field of $574\,\mu$T and a right initial kick into the undulator. When this is done, the influence of the undulator onto the lasing process is reduced and completely expressed by the phase error of the trajectory:

$$\Phi = 11.05^\circ \pm 0.23^\circ(\mathrm{M}) \pm 0.01^\circ(\mathrm{S})$$

which increases a possible gain length about a factor of 1.3 %, see Sec. 7.3.

8 X-Ray Diagnostics

A single Frosty undulator is not designed to operate in the FEL saturation regime but more in the start up of the FEL. So, only a small signal compared to the background is expected. To diagnose the FEL start a high resolution around the amplified wavelength is necessary to detected the small increase. This means, the beam has to be focused in both planes onto a camera chip to maximize the number of photons per pixel and also, that the beam needs to be strongly dispersed in one plane to have a high wavelength per pixel resolution. To diagnose the FEL beam, the total flux of Frosty is gathered with a torodial mirror and focused onto a grating which diffracts the beam. The setup of the x-ray spectrometer is explained in Sec. 8.1 and its photon transmission in Sec. 8.2. The imaging system projects the end of the undulator onto the camera, so near field effects in the off-axis radiation are recorded. This causes a change in the observed bandwidth, which is discussed in Sec. 8.4.

8.1 Imaging system

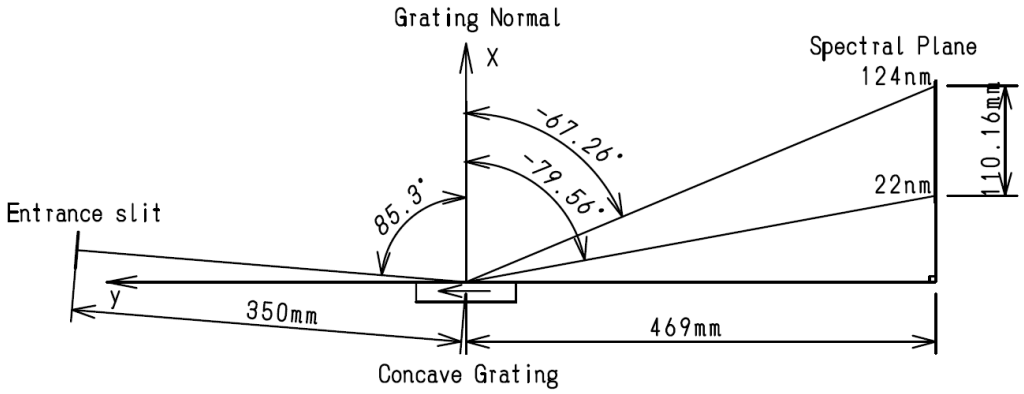

Figure 8.1 – Spectrometer grating geometry. Data provided by [11].

The photon diagnostics layout is a point to point imaging of the undulator exit onto the camera chip to maximize the photons per pixel. 5 m behind the undulator a torodial mirror with 50 mm height and 540 mm length collects and focuses the photon

beam onto a variable line space grating mounted inside the 5 m downstream x-ray chamber. The torodial mirror is rotated about 2.5 ° with respect to the photon axis which reduces the effective cross section to 50 mm x 23.6 mm. This allows to capture all radiation emitted into an angular cross section of 10 mrad x 4.7 mrad (0.57 ° x 0.27 °) behind the undulator. The optical grating disperses the beam into the vertical direction and creates itself line focii for the separated wavelengths on the camera in case of an incoming collimated beam. The grating is mounted such that it reflects the incoming photon beam in wavelength dependent angles $\beta(\lambda)$ into the vertical direction. The angle of emergence $\beta(\lambda)$ of the grating order G depends on the grating constant d given in grid lines per mm, the angle of incidence β and the wavelength λ [83]:

$$\beta(\lambda) = \arcsin(\mathrm{G} \cdot \mathrm{d} \cdot \lambda - \sin(\beta))$$

After a fixed longitudinal distance $\mathrm{d_{ccd}}$ behind the grating the vertical position of one diffracted wavelength is:

$$\mathrm{y}(\lambda) = \mathrm{d_{ccd}} \cdot \tan(\frac{\pi}{2} - \beta(\lambda)). \tag{8.1}$$

Classical planar gratings have a constant groove pattern which diffracts the incoming light without any further focusing effects. When the groove pattern is not constant but varies in a defined structure along the surface of the grating, an additional focusing of the diffracted wavelengths is achieved [83]. Those gratings are variable line space (VLS) gratings. The emitted wavelengths of Frosty are between 20 nm to 120 nm and are a comparably exotic bandwidth for spectroscopy, which limited the availability of suitable gratings up to basically one supplier and one grating [11]. So, the spectrometer was designed around the available grating and followed the geometry provided by the supplier. Fig. 8.1 shows the design of the x-ray spectrometer. The camera is mounted such, that it can drive the full vertical distance along the spectral plane shown in the figure. The resolution of the spectrometer is 0.9 nm/mm.

8.2 Efficiency Curves

When the wavelength of the emitted undulator radiation is close or equal to the electron energy levels of matter the photon's energy will be absorbed and can either be directly re-emitted or retain inside the body. This is used to an advantage by installing filter materials in front of the grating to block surrounding background light, or filter the photon beam for specific wavelength intervals. As a disadvantage this effect means, that a fraction of the beam will always be absorbed which causes losses of the observed undulator power.
Also, the grating will diffract the incoming light into several higher grating orders and not completely into the first order.

As a last part the camera (≈ 13 mm x 13 mm chip size with 1024 pixels) itself has to be taken into account. The chip does not convert the full received energy into counts. The used CCD is optimized for short wavelengths which means that the quantum efficiency of the photo-sensitive chip increases for shorter wavelength and decreases for longer ones. Also a certain amount of energy needs to be absorbed by the material to generate an electron-hole pair in the chip which can be detected by the electronics. The respective efficiency curves for all those instruments are plotted in Fig. 8.2. As a filter, a 250 nm thick aluminum foil is used.

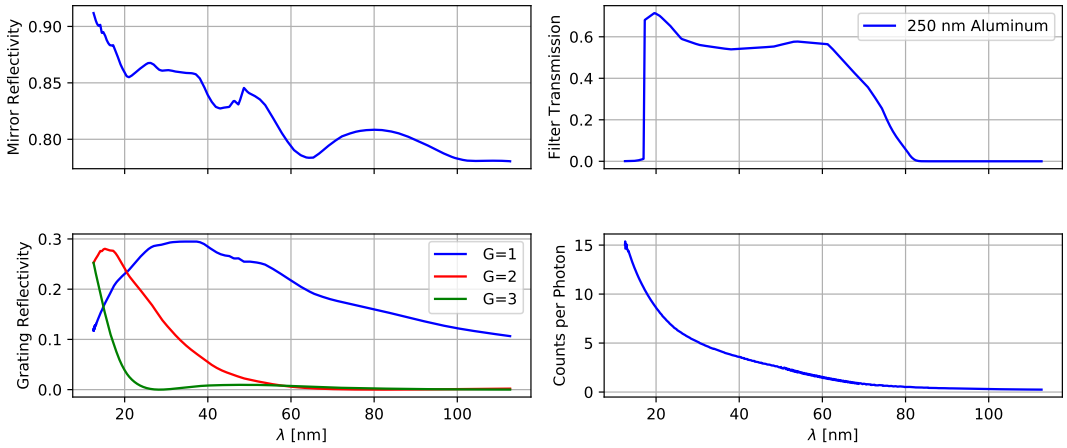

Figure 8.2 – Efficiency curves vs. incidence wavelength. Upper left is the reflectivity of the torodial mirror [12], upper right the bandpass filter used to cut out a fraction of the beam [13]. The grating efficiencies into the first, second and third diffraction order are shown in the lower left [11]. The number of counts per photon in the ccd electronics are shown in the lower right [12].

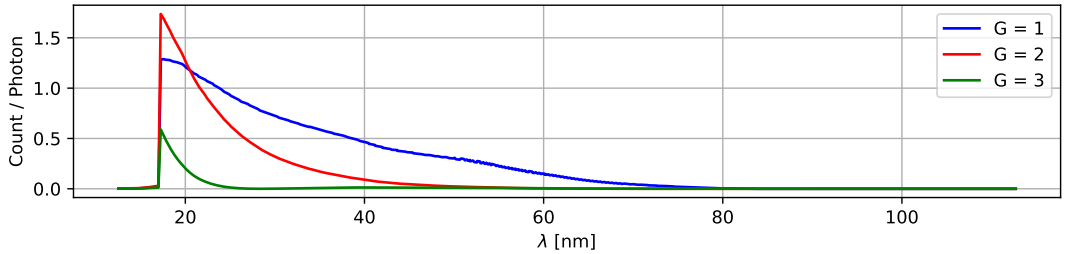

Figure 8.3 – Total efficiency curves for the first three diffraction orders.

The individual efficiency curves shown in Fig. 8.2 are combined to a total efficiency curve per diffraction order, see Fig. 8.3. The aluminum filter has a sharp cut off for wavelengths below 17 nm and as the incoming light will be filtered before the grating disperses the beam, this edge appears also in the higher diffraction orders. According

to Eq. 8.1, the diffraction orders will be separated vertically, starting with the first order at lowest position. An overlap of the diffraction orders occurs when the emitted wavelength range of the undulator is higher than the separation of the diffraction orders along the vertical axis. This is the case for a small undulator gap, so a high K value which increases the number of harmonics inside the undulator radiation. The sharp cut off lines from the aluminum filter are then used as a calibration to separate the individual diffraction orders from each other, as the sharp edges will appear as a multiple integer of the 17.1 nm cut-off. So, also at 34.2 nm and 51.3 nm and so on. The contributions of the diffraction orders to the measured spectrum along the spectrometer axis is plotted in Fig. 8.4. Between 78 mm and 105 mm (This corresponds to a wavelength range between 17.1 nm and 34.2 nm) only a signal of the first diffraction order will be measured. At 104.5 mm the rise of the second diffraction order is visible where the 17.1 nm of the second order is diffracted onto the same vertical position as the 34.2 nm line of the first order. At a height of 126 mm, the position of the 17.1 nm line of the third diffraction order overlaps with the 25.7 nm line of the second diffraction order and the 51.2 nm of the first diffraction order.

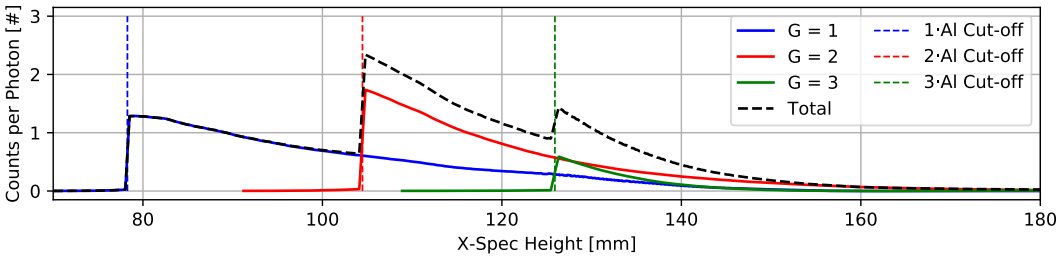

Figure 8.4 – The overlap of higher diffraction orders onto the observed undulator spectrum. The diffraction orders can be separated by the 17.13 nm cut-off of the first order.

8.3 Calibration

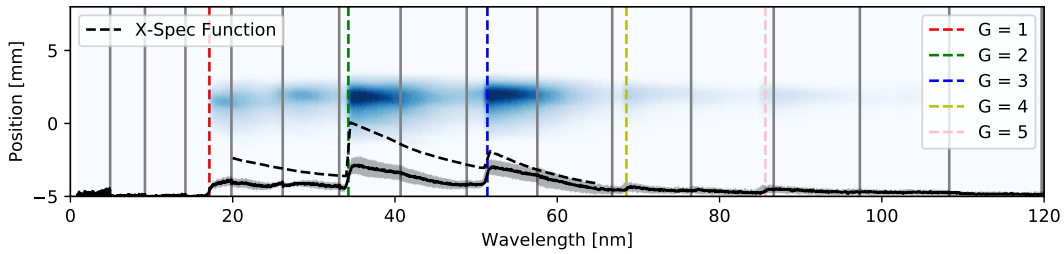

Figure 8.5 – Measured radiation spectrum for a K = 1.9 and an electron energy of ≈ 330 MeV. In the lower part the projection of the spectrum is shown in black with its deviation between the shots in gray. The black dotted line marks the x-spec function from Fig. 8.4 and the colored dotted lines mark the beginning of each grating diffraction order.

For the calibration of the x-ray spectrometer the undulator was set to a K of 1.9 and the spectrum is recorded for an electron energy of 330 MeV, see Fig. 8.5. The dotted vertical lines indicate the aluminum filter cut-off at 17.13 nm which is diffracted into the higher grating orders as discussed in Sec. 8.2. Those cut offs are used to calibrate the vertical camera position to an observed wavelength. The gray rectangles indicate the chip size of the camera. Due to the non-linear relation ship between vertical position (in the picture left to right) and observed wavelength, see Eq. 8.1 the measurable wavelength range changes for different camera positions. Recalculating the camera spectrum from vertical position to observed wavelength leads to a change of size of the boxes.

8.4 Undulator Near Field

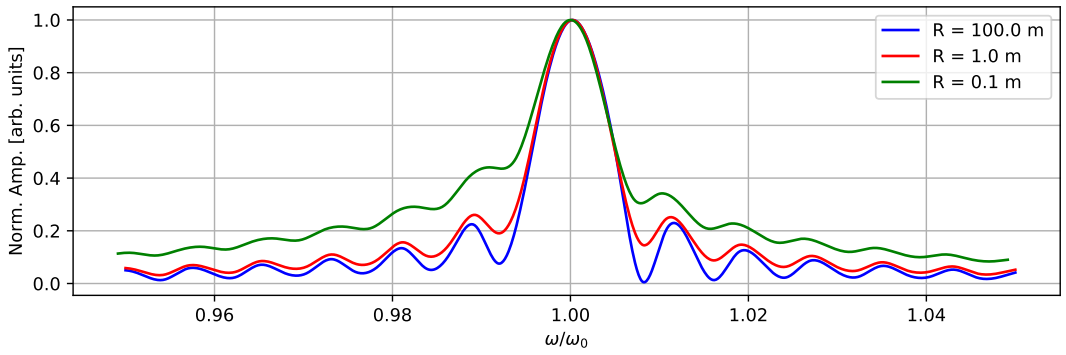

Figure 8.6 – Spectral distribution of the undulator radiation for different distances R behind the undulator. The spectrum converts to a sinc-like function in far distance, whereas a broadening of the bandwidth appears in the near field close to the undulator.

Within the paraxial approximation of the undulator far field, the observed bandwidth scales with the number of undulator periods like $1/N_u$. Getting closer to the undulator, this small angle approximation loses its validity, as the angle between the observer and the emitted light at the beginning and the end of the undulator differ. Due to the point to point imaging of the undulator end onto the x-ray camera the near field of the emitted radiation is observed, which causes a broadening of the undulator bandwidth in the off-axis radiation [1], see Fig. 8.6. A quantity to estimate the broadening is the ratio $W = L^2\,\Theta^2/(2\lambda\,D)$ between the undulator length L, the observation angle Θ, the observed wavelength λ and the distance of the observer from the undulator center D [1]. For the imaging system used for Frosty follows that D=L/2, so the criterion reduces to

$$W = \frac{L}{\lambda}\Theta^2 \tag{8.2}$$

If $W > 1$ near field effects are observed within the off-axis radiation and the bandwidth is then increased to [1]

$$\frac{\Delta\lambda}{\lambda} = \frac{W}{N_u}.$$

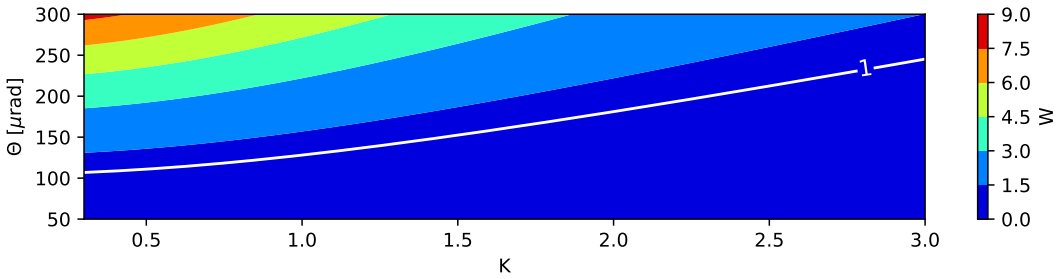

Figure 8.7 – Near field criterion W of Eq. 8.2 for different observation angles and emitted wavelengths for 300 MeV electron energy. Above W = 1 near field effects in the off-axis radiation are expected.

In Fig. 8.7 Eq. 8.2 is shown for the wavelengths emitted for a fixed energy of 300 MeV and different K-values. The observer angles above which near field effects will contribute are between 107 μrad for a K of 0.3 up to 245 μrad for a K of 3. To put this into perspective, for a K of 1 and 300 MeV electron energy (which results in 33 nm radiation), the bandwidth of the synchrotron radiation background with an opening angle of $1/\gamma \approx 1.7$ mrad would be broadened about W ≈ 176. For the opening angle of the exact fundamental undulator radiation, Eq. 2.20, follows $W = \frac{L}{\lambda}\frac{\lambda}{2L} = 1$ whereas the full angle (two times Eq. 2.16) would result in W = 4. As the full radiation cone is projected onto the camera and the full image is used for analysis, an increase of the fundamental bandwidth about a factor of 4 is expected.

8.5 Conclusion

Within this chapter the x-ray spectrometer is presented which is used to diagnose the Frosty photon beam. The imaging system, see Sec. 8.1, allows a resolution of 10 pm/pixel for wavelengths between 20 nm and 120 nm. The filter function, see Sec. 8.2, with the used aluminum shows a sharp cut off at 17.13 nm which is also diffracted into higher grating orders and used to calibrate the vertical position of the x-spec camera to the observed wavelength, see Sec. 8.3. Due to the point to point imaging of the undulator end onto the camera, near field effects contribute to the observed off-axis radiation. For the later analysis the full image data is used. That increases the observed near field bandwidth about a factor of 4 compared to the far field bandwidth, as explained in Sec. 8.4.

9 Radiation Measurements

As a final step of the commissioning of Frosty, the radiation properties of the undulator and the effect of the taper onto the radiation bandwidth are measured and characterized. The beamline setup and the measurement campaign are discussed in Sec. 9.1. To reduce the impact of deviating electron beam trajectories onto the spectrum the constrains for the measurement is explained in Sec. 9.2, which also covers the data processing of the recordings and the expected scalings of the radiation bandwidth with electron beam properties. The results of the measurement campaign are then presented in Sec. 9.3.

9.1 Beamline Overview and Measurement Campaign

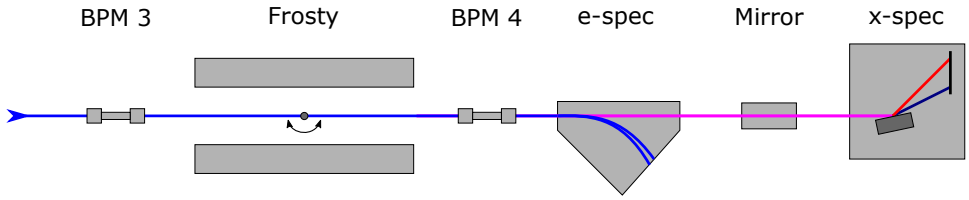

Figure 9.1 – Sketch of the measurement setup. The electrons (blue line) are coming from the left and are guided through the undulator (Frosty) in which synchrotron radiation is emitted (purple line). The electron beam properties are measured with an electron spectrometer (e-spec) and the radiation properties with an x-ray spectrometer (x-spec). Before and after the undulator beam position monitors (BPM) record the charge and center of mass of the beams. For the taper scan the girders are rotated towards each other with the rotation center marked as the gray dot in the center of Frosty.

For the commissioning of Frosty it is important to focus onto aspects which will play a major role towards the demonstration of a possible free electron lasing with the decompression concept, see Sec. 3.3, and the diagnostics / analysis of the recorded data. So, the measurements presented here are targeting the following basic correlations:

- Electron energy and central wavelength, see Sec. 9.3.3
- Electron energy spread and radiation bandwidth, see Sec. 9.3.3
- Photon flux and electron bunch charge, see Sec. 9.3.4

- Bandwidth and taper, see Sec. 9.3.5

The experimental setup is sketched in Fig. 9.1. Before and after the undulator beam position monitors (BPM) are installed, which are non-invasive diagnostics and measure the transverse center of mass and charge of a passing electron bunch. The measurement accuracy for the positioning is ≈ 10 μm, whereas the read out could be errorprone up to 100 μm. The uncertainty for the charge is 0.1% [84, 85]. However, when the accelerator is off, the BPMs show an offset from zero charge between 0.3 pC and 0.5 pC. Due to that offset the data is filtered for charges above 1 pC, double the default displayed offset. The distance between the first BPM and the undulator entrance is 1.34 m and the distance between undulator exit and the second BPM is 0.89 m which leads to a total of 4.23 m between the BPMs. After the electron bunch went through the undulator, it is focused into an electron spectrometer, in which the beam gets dispersed by a magnetic dipole field before it hits the chamber wall. On the outside of the spectrometer, a scintillator screen is attached to the chamber which starts to glow in the presence of an incoming particle shower. This glow is recorded by a camera, which measures the energy distribution. The resolution of the spectrometer depends on several aspects like the focusing into the spectrometer, the showering of the electrons inside the chamber wall, the screen granularity, camera resolution, data processing and so on. The estimated energy resolution is assumed to be 0.5 MeV, which is the minimum step size after a post process smoothing of the recorded data [12]. The emitted x-rays are focused into the x-ray spectrometer described in Sec. 8. Here, the resolution is determined by the pixel size of the camera chip. On average the resolution of the spectrometer is ≈ 0.9 nm/mm, which results in a theoretical limit of 11 pm/pixel (13 mm x 13 mm chip size with 1024 pixels).

9.2 Parameter Settings and Data Processing

For the setup of the beam line and the subsequent data processing several factors have to be considered:

- The measurements presented here were recorded before any electron beam based alignment of the undulator axes to the beam axes was done. That means, the alignment of the components mentioned in Sec. 9.1 is only accurate up to the level of their geometrical positioning inside the accelerator tunnel. This positioning is done with a laser tracker which guarantees an accuracy of 100 μm to the design position, but not better. Following from this it is certain, that the electron beams enter the undulator field with a systematic displacement and entrance angle.
- From the point above follows, that it is close to indistinguishable if the origin of a measured systematic deviation is a wrong beam trajectory through the undulator, or a displaced component inside the tunnel. E.g. if the electron beam propagates

on a tilted trajectory through the accelerator, or if one of the BPMs are off-axis and, therefore, measure a sloped orbit when the beam travels in a straight line on axis.

- The electron beam orbit is not stable on the micro meter level between the shots and the beams enter the undulator with different randomly distributed initial positions and angles, which causes a change in the radiated wavelength and bandwidth.
- A high K value increases the influence of peak field errors onto the bandwidth, see Sec. 7.2.8.
- The central wavelength should be chosen such that it does not overlap with a multiple of the 17.13 nm edge of the aluminum filters from different diffraction orders, see Fig. 8.5.
- When the emitted spectrum is broad due to a high K value, the signals of different diffraction orders can overlap, see Fig. 8.4, which complicates the analysis.

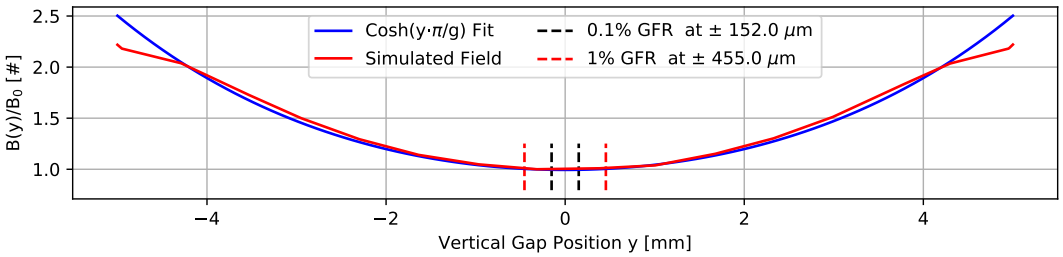

Figure 9.2 – Simulated relative change of the vertical peak field with the off-axis position at a 10 mm nominal gap. The 1 % vertical good field region is close to 1 mm.

To increase the acceptance of positioning errors and of varying initial beam positions a high gap is demanding, as it increases the good field region of the vertical field component. In the course of the measurements presented here, a gap of 10 mm is chosen which corresponds to a K-value of 0.4477. The average electron energy is 280 MeV, which corresponds to a fundamental wavelength of 27.6 nm. The beam optics were set up to transport and focus this energy into the undulator.
The central wavelength of 27.6 nm lies well between the 17.13 nm cut off line of the aluminum filter, which is diffracted into the first and into the second diffraction order of the grating. The 17.1 nm line in the second diffraction order appears at 34.26 nm. The camera is centered at 28 nm and the wavelength interval from 24 nm to 33.5 nm is recorded. This allows to measure the radiation emitted by electron energies between 254.4 MeV (corresponds to 33.5 nm) and 300 MeV (corresponds to 24 nm).
For the 10 mm gap, the vertical good field region in which the magnetic field changes about 1 % is ± 0.5 mm, see Fig. 9.2. This would cause a shift in the emitted wavelength

of 0.05 nm between a shot measured on-axis and 0.5 mm off-axis. If an electron beam enters on-axis and leaves the m long undulator 0.5 mm off-axis (0.25 mrad initial angle) the additional increase of the FWHM bandwidth would be 0.05 nm / 27. nm = 0.18 %. Adding this to the fundamental FWHM bandwidth (0.77 %) reveals that it only leads to a small increase of the total bandwidth of $\mathrm{BW_{tot}}=\sqrt{(0.18\,\%)^2+(0.77\,\%)^2}=0.79\,\%$. The influence of the electron bunch's energy spread onto the bandwidth broadening, which scales as $\mathrm{BW_{tot}}=\sqrt{(2\cdot\Delta\gamma/\gamma_0[\%])^2+(0.77\,\%)^2}$, see Eq. 9.1 has a larger impact. It increases the total FWHM bandwidth to 1.26 % for an FWHM energy spread of 0.5 %. The influence of peak field errors onto the bandwidth scales quadratically for small K values, see Eq. 7.1. Due to the low set value of 0.4477, the impact onto the total bandwidth due to this effect would be $\approx 0.8\,\%$.
The emitted flux density strongly depends on spatial electron bunch parameters like the beam size, divergence and the steering of the electron beam through the undulator. To stay independent from spatial quantities the total flux is analyzed, which is the integration of the flux density over all emission angles and, therfore, indipendent of staptial properties. It only scales with the charge, the set K-value and the phase error, see Eq. 2.18 [1, 17].
In addition, the compensation coil is set to a current of 2.2 A to reduce the systematic trajectory error, see Sec. 5.6. With this current, the field integrals are compensated such, that the mean radiation direction is close to parallel to the undulator axis. The phase jitter within this setting is 4.4 °, which leads to a reduction of the emitted power to 99.4 %, see Eq. 6.3. Within this undulator setting the influence of positioning errors, either from the components in the tunnel, or the electron beam with respect to the undulator axes are acceptably small. The remaining scaling for the observed radiation bandwidth is dominated by two effects, the electron energy spread and the increase of the observed fundamental bandwidth due to near field effects as described in Sec. 8.4.

9.2.1 Data Processing

For the analysis it is important to compare the same statistical quantities for the electron beam parameters and the undulator radiation parameters. In both cases a Gaussian distribution is fit to the data and its mean and standard deviation σ are used to calculate the energy spread and undulator bandwidth. The Gaussian statistics are denoted as σ_λ/λ (bandwidth) and σ_γ/γ (energy spread). FWHM values, which are often used through literature, are given as $\Delta\lambda/\lambda$ and $\Delta\gamma/\gamma$.

Energy Spread Calculation

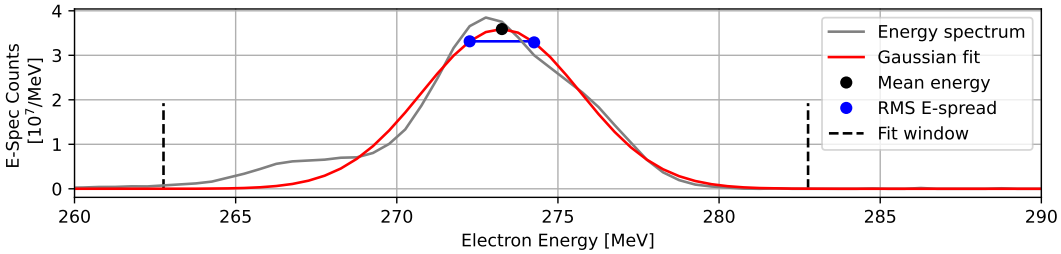

Figure 9.3 – Example of a recorded electron energy spectrum with the used Gaussian fit and the retrieved mean energy and rms energy spread.

Within the electron energy distribution several shots consists out of a main peak and a low energy tail which has no significant contribution to the observable radiation. Either, because the charge within this energy region is small compared to the main peak, or, the energy tail is below 254.4 MeV and emits wavelengths outside of the measurement interval. But this tail has an impact to measures of the descriptive statistics and has to be cut off. A fit window of ± 10 MeV around the main peak is applied to the data to improve the quality of the Gaussian fit, see Fig. 9.3. The fit parameters for the mean and the standard deviation are then used to calculate the central energy and the energy spread. The window size was chosen from the average spectrum over the whole dataset with the demand, that the intensity at the window edges is $\approx 10\,\%$ of the peak, see Fig. 9.8. A FWHM electron energy spread of 10 MeV at 280 MeV peak (3.6 %) would cause a radiation bandwidth of 7.2 %. When only measuring smaller radiation bandwidths this window is valid. The spectrum in Fig. 9.3 follows a complex structure and not a purely Gaussian distribution and it is also visible, that the mean of the Gaussian fit is not congruent with the peak of the energy spectrum. This effect leads to a general overestimation of the mean energy on the 1 MeV level, which makes the fit valid only in a first order approximation. For the commissioning of the machine, this is acceptable. As mentioned in Sec. 9.1, the estimated energy resolution of the spectrometer is 0.5 MeV, which gives an error to the calculations of $\approx 0.18\,\%$. This error is treated as a systematic measurement uncertainty.

Radiation Bandwidth Calculation

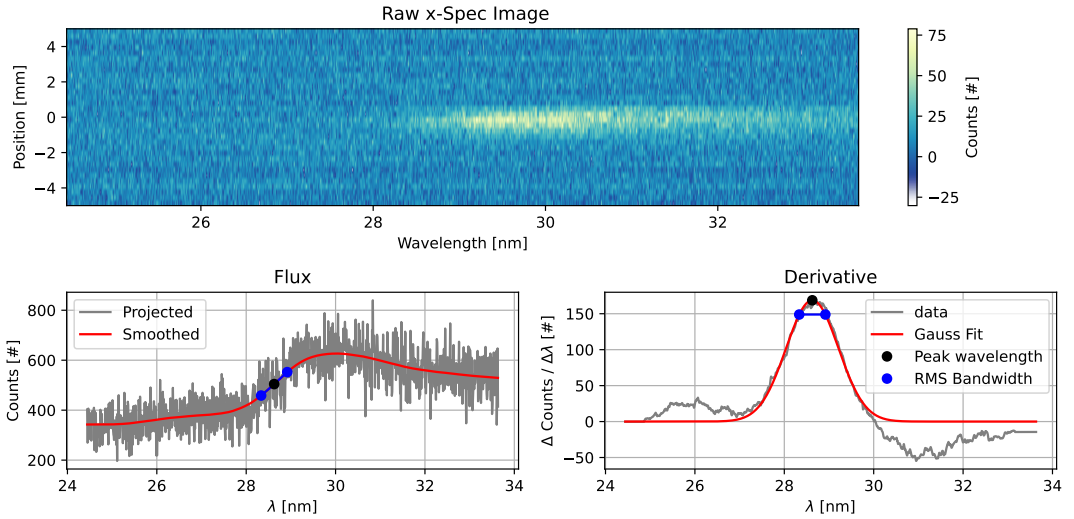

Figure 9.4 – Recorded x-ray spectrum. Top: Raw image with subtracted background. The integrated flux is the projected spectrum on the lower left. On the right is the derivative with the applied Gaussian fit to retrieve the mean wavelength and the rms bandwidth.

The total flux is the integration of the flux density over all emission angles. For a single electron, the flux density follows a sinc-like function, see Fig. 2.4. For a real beam, the distribution converts to a Gaussian shape, as the wings of the sinc-function are washed out [1, 17]. So, for a real electron beam, also the derivative of the total flux follows a Gaussian-like function with the peak at the central wavelength. To calculate the bandwidth of the undulator radiation, the integrated flux is differentiated with respect to the wavelength and the Gaussian fit is applied to this derivative. The center of the fit is the mean wavelength and the standard deviation its bandwidth. One of the recorded radiation spectra is shown in Fig. 9.4. The raw data is in the upper plot. Projecting the image to the wavelength axis, gives the integrated fux, see the lower left plot. Its differentiation with respect to the wavelength is on the lower right. Background images are subtracted to reduce stray light. Due to the small K value of 0.4477 and small electron bunch charges, the signal to noise ratio of the integrated flux is very low. Differentiating this flux would amplify the noise, which would make the signal unusable for the fit. To reduce the noise several filters are applied to the data: The signal is integrated first and smoothed with a first degree Savitzky–Golay filter [86] (polynomial regression over a sample size) with a window size of 91 pixels, which corresponds to 0.82 nm. Differentiating this signal again gives a smoothed integrated flux, see lower left in Fig. 9.4. After taking the derivative with respect to the wavelength of the smoothed flux, a second Savitzky–Golay filter with the same window size is

applied. To this, a Gaussian distribution is fitted to retrieve the mean wavelength and rms bandwidth. The Gaussian fit is shown on the lower right in Fig. 9.4. As discussed in Sec. 9.1 a spectral resolution of $\approx 11\,\mathrm{pm/pixel}$ is assumed for the systematic measurement uncertainty.

9.2.2 Radiation Bandwidth Estimate

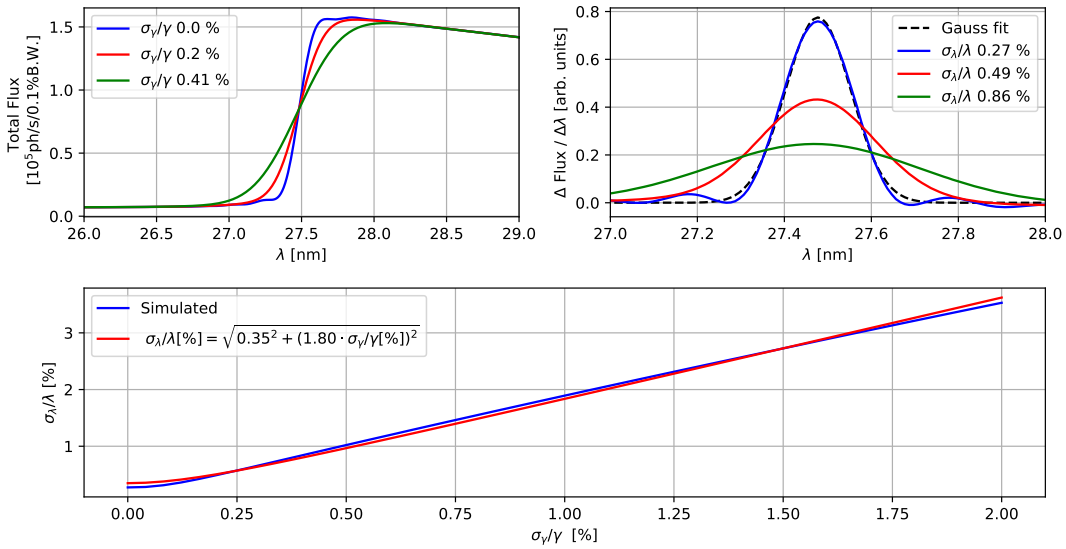

Figure 9.5 – Simulated far field flux for different electron energy spreads. The parameters discussed in Sec. 9.2 and an idealized undulator with 128 periods are used. To the derivative (upper right), a Gaussian fit is done to calculated the bandwidth. The scaling of it with the energy spread is shown in the lower part and follows close the scaling of Eq. 9.1.

For the measurements the scaling of the observed bandwidth with the energy spread is important, as it is the main contributor. The change of the wavelength, Eq.2.14, with a small energy variation of $\gamma_2 = \gamma + \Delta\gamma$ is $\Delta\lambda/\lambda = 1 - (\gamma_2/\gamma)^2 \approx 2\Delta\gamma/\gamma$ and contributes to the total bandwidth like

$$\left(\frac{\Delta\lambda}{\lambda}\right)_{\mathrm{tot}} = \sqrt{\left(\frac{1}{\mathrm{N_u}}\right)^2 + \left(2\frac{\Delta\gamma}{\gamma}\right)^2}. \tag{9.1}$$

As the equation above depends on different statistical measures (FWHM instead of σ) the total flux is simulated for different Gaussian distributed energy spreads from 0 % to 2 % and the bandwidth is calculated using the Gaussian statistics discussed in Sec. 9.2.1. The results of the simulations are shown in Fig. 9.5. The total flux for different energy spreads is on the upper left and its derivative with respect to the wavelength on the

upper right. The simulated bandwidth scaling with the electron energy spread is shown in the lower part. A function of the form $\Delta\lambda/\lambda = \sqrt{A^2 + (B \cdot \Delta\gamma/\gamma)^2}$ is fitted to the data to retrieve the actual scaling with the energy spread B and the natural undulator bandwidth A. The fit equation in the lower plot estimates a minimum bandwidth of $A = 0.35\,\% \pm 0.02\,\%$, which is above the shown minimum bandwidth of 0.2 7% in the upper right plot. As a cross check the $0.35\,\% \pm 0.02\,\%$ bandwidth is converted to a FWHM/peak value ($0.82\,\% \pm 0.05\,\%$) from which the number of undulator periods is estimated, see Eq. 2.15, to be N_u=122 ± 7. This is close to the used 128 periods used for the simulation. So, the fit parameter for the fundamental bandwidth, A, has a relative error within the 5 % range, whereas the energy scaling, B, is erroneous up to the 10 % level, as it should be 2 and is 1.8 instead. These error levels are acceptable small for the commissioning, but they make the data analysis the dominant error source.
Within the Gaussian statistics, the bandwidth for the undulator at a 10 mm gap is 0.35 % (R = 100 m data in Fig. 8.6) in the far field and is expected to increase about a factor of 4 to 1.4 % due to near field effects, see Sec. 8.4. These near field effects arise in the observed off-axis radiation. As the full image is analyzed, the expected scaling of the recorded bandwidth in the near field is

$$\left(\frac{\sigma_\lambda}{\lambda}\right)_{\text{exp}}[\%] = \sqrt{(1.4)^2 + \left(1.8\frac{\sigma_\gamma}{\gamma}[\%]\right)^2}. \tag{9.2}$$

9.3 Undulator Radiation Measurements

For the measurement campaign the accelerator is set up in a low charge mode and the undulator was set to a K of 0.4477, see Sec. 9.2.

9.3.1 Electron Beam Properties

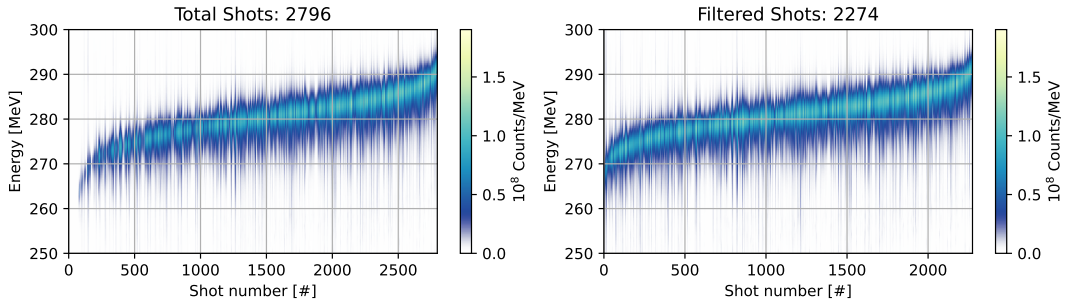

Figure 9.6 – Recorded electron energy spectra on the e-spec sorted after peak energy. On the left are all shots, on the right filtered for charges above 1 pC.

In total 2796 shots with mean energies between 270 MeV and 290 MeV were recorded. These shots are filtered for charges above 1 pC, see right in Fig. 9.6, which left 2274 shots for the analysis.

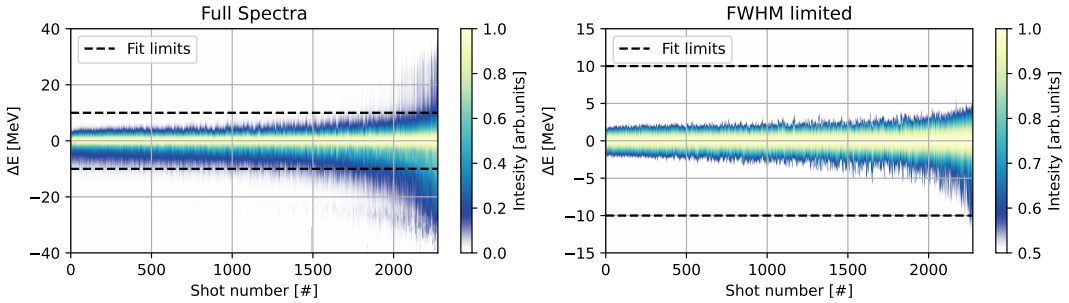

Figure 9.7 – Sorted energy deviations from the peak for each shot.

The single shot energy deviation from the mean is shown in Fig. 9.7. Left shows the normalized spectra from Fig. 9.6 with subtracted peak, on the right the same data set but cut at the FWHM.

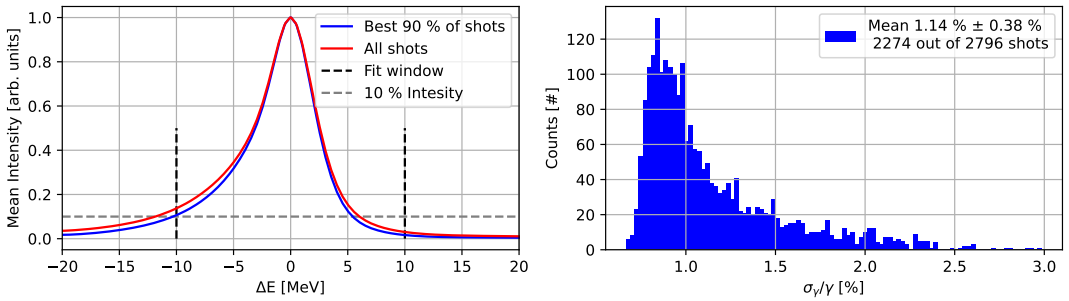

Figure 9.8 – Left: Energy deviations averaged over all runs. Right: Distribution of measured energy spreads.

The average electron spectrum is plotted on the left of Fig. 9.8. The FWHM energy distribution is well below ± 10 MeV and shows a tail towards lower energies. The mean intensity on the lower fit window side (-10 MeV) is 13.8 % for all shots and 10.7 % for the best 90 % of the shots. On the high energy side (+10 MeV), the mean intensities are 3.1 % for all shots and 1.7 % for the best 90 % of shots. So, the size of the used fit window, see Sec. 9.2.1, covers the majority of the energy distribution and cuts off only a small fraction of the spectrum. The energy spread distribution is calculated as

explained in Sec. 9.2.1 and is plotted on the right. The energy spread distribution over the dataset is shown on the right of Fig. 9.8 and is on average

$$\left\langle \frac{\sigma_\gamma}{\gamma} \right\rangle = 1.14\% \pm 0.38\%.$$

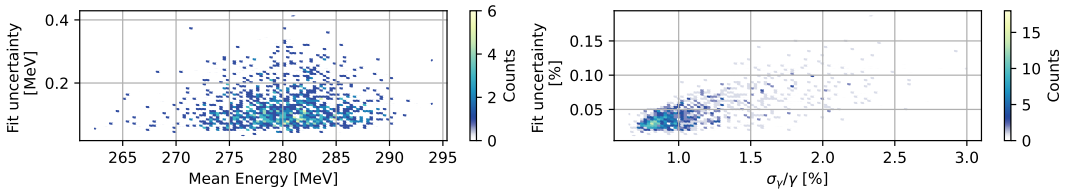

Figure 9.9 – 2D histograms of the Gaussian fit uncertainties.

To estimate the reliability of the method to determine the energy spread, the uncertainties of the Gaussian fits have to be evaluated. Averaged over the dataset, the mean electron energy is 280.21 MeV with an absolute fit inaccuracy of 0.13 MeV (0.05 % relative error). The fit inaccuracy for the mean energy is added to the estimated 0.5 MeV resolution of the electron spectrometer to get a total systematic measurement error for the mean energy, which includes the analysis algorithm. The uncertainty is

$$\mathrm{u}_\gamma = 0.63\,\mathrm{MeV}, \tag{9.3}$$

which is a 0.22 % relative error for 280.21 MeV electron energy. For the energy spread follows, again averaged over the full data set, a mean of 1.14 % with an absolute uncertainty of

$$\mathrm{u}_{\sigma_\gamma/\gamma} = 0.05\,\%, \tag{9.4}$$

which is a relative error of 4.39 %.

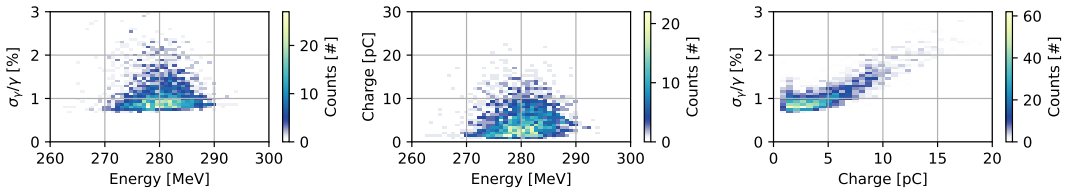

Figure 9.10 – 2D histograms of the correlations between measured peak energies, energy spreads and charge.

Fig. 9.10 shows the correlations between the electron beam parameters. The accelerator is setup such, that the beam loading compensates the acceleration gradient inside the plasma for ≈ 3 pC, which results in a low projected energy spread.

For different charges the bunch is chirped, which results in an increase of the projected energy spread, as described in Sec. 3.2. Right in Fig. 9.10 this correlation is shown as the increase of the energy spread for increasing charge.

9.3.2 Electron Beam Stability

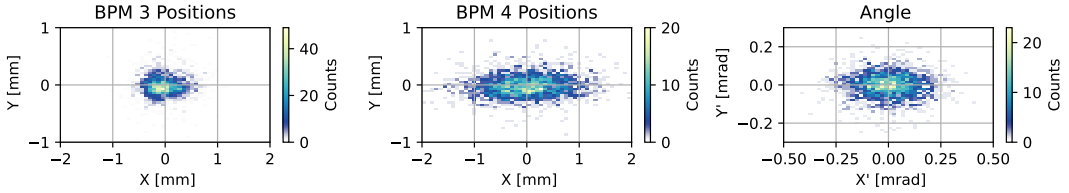

Figure 9.11 – 2D histograms of the transverse positions at BPM 3 and BPM 4 and the calculated angular fluctuation.

As mentioned in Sec. 9.2 it is important that the influence of the electron beam trajectory deviations onto the radiated bandwidth is small. The beam positions measured at the BPMs show, that the positions in BPM 3 deviate about 274 μm rms in x and 174 μm in y. In BPM 4 about 600 μm rms in x and 174 μm in y. For all BPM positions the angle through the undulator is calculated and the angular fluctuations are 112 μrad rms in the horizontal x plane and 60 μrad rms in the vertical y plane. The important fluctuation of the vertical offsets would cause a FWHM bandwidth broadening of $\approx 0.1\,\%$, which is well below the 0.18 % threshold described in see Sec. 9.2 and, therefore, negligible.

9.3.3 Undulator Radiation and Bandwidth

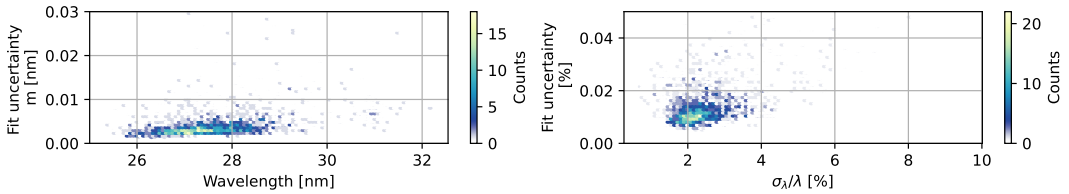

Figure 9.12 – 2D histograms of the Gaussian fit uncertainties. Left: calculated peak wavelength, right: radiation bandwidth.

From the radiation spectra the fundamental wavelengths and the bandwidths are calculated as explained in Sec. 9.2.1. Averaged over the dataset, the mean wavelength is 27.59 nm with an absolute fit inaccuracy of 4.0 pm (0.01 % relative error).

The fit uncertainty of the mean wavelength is added to the spectrometer resolution of 11 pm, which results in a total systematic measurement accuracy of

$$u_\lambda = 15\,\text{pm}. \tag{9.5}$$

This corresponds to a relative error of 0.05 % for a 27.56 nm wavelength. The bandwidth is, on average 2.5 %. The absolute inaccuracy is

$$u_{\sigma_\lambda/\lambda} = 0.01\,\%, \tag{9.6}$$

which corresponds to a relative error of 0.58 %.

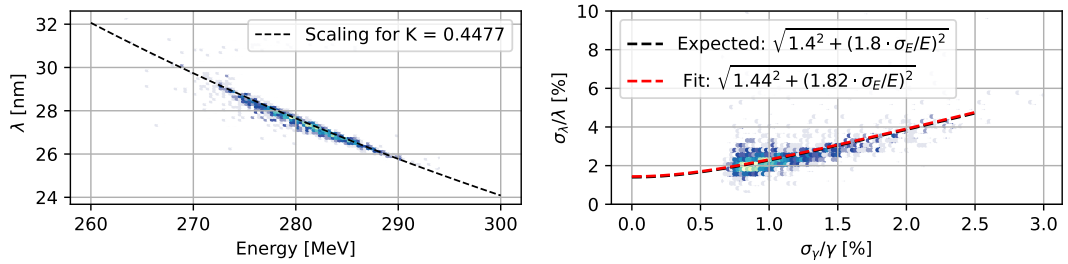

Figure 9.13 – Measured fundamental wavelengths on the left with an estimate for the set K-value during the run, see Eq. 2.14. The calculated bandwidth is on the right with the expected near field scaling of Eq. 9.2 and a fit to the data.

For the set K-value the expected wavelength is shown in Fig. 9.13 as the dashed line. The mean difference between the measured wavelengths and the theoretical expected wavelengths of Eq. 2.14 is -0.08 nm ± 0.19 nm. As stated in Sec. 9.2.1 the mean energy calculation is overestimated with the Gaussian fit, as shown in Fig. 9.3. Under the assumption that the measured mean deviation originates from an offset caused by the energy spectrum analysis, this offset is -0.42 MeV. Subtracting the error of the spectrometer resolution, 15 pm see Eq. 9.5, from the wavelength fluctuation and also converting this into an electron energy fluctuation would result in ± 0.88 MeV. This level is close, but above the estimated spectrometer resolution of 0.63 MeV, see Eq. 9.3. The recorded wavelengths and electron energies fit close to the resolution limit except a small offset in the 0.25 MeV range. This offset mainly comes from the simplified data analysis, which is based on Gaussian distributions. Also, the systematic errors are calculated over average values, which simplifies their impact.
On the right of Fig. 9.13 the bandwidth is shown with the estimate of Eq. 9.2 (black-dashed) and a fit (red-dashed). The fundamental near field undulator bandwidth is calculated to be 1.44% ± 0.05 % (rel. error 3.5 %) and the energy spread scaling to be 1.8 ± 0.03 (rel. error 1.7 %). Here, the standard deviation errors of the fit functions where used as uncertainties. As already discussed in Sec. 9.2.1 the fit itself

does only recover the scaling up to 5 % for the undulator bandwidth. As a conservative estimate, the relative errors are added up to 8.5 % (0.122 % absolute) for the calculated fundamental bandwidth. The systematic inaccuracies of the energy spread (4.39 % rel.error, see Eq. 9.4) and radiation bandwidth (0.58 % rel.error, see Eq. 9.6) calculations are summarized to a total relative systematic error of 5 % (0.072 % absolute error) and denoted as (S).
From the near field bandwidth (NF) the far field bandwidth (FF) is calculated by dividing the values by 4, see Sec 8.4. It follows for both bandwidths:

$$\left(\frac{\sigma\lambda}{\lambda}\right)_{\mathrm{NF}} = 1.44\% \pm 0.122\% \pm 0.072\%(\mathrm{S}) \tag{9.7}$$

$$\left(\frac{\sigma\lambda}{\lambda}\right)_{\mathrm{FF}} = 0.36\% \pm 0.03\% \pm 0.018\%(\mathrm{S}) \tag{9.8}$$

which are in a good agreement with the expected Gaussian far field bandwidth of 0.35% and near field bandwidth of 1.4 %, see Sec. 9.2.2.

9.3.4 Flux Scaling

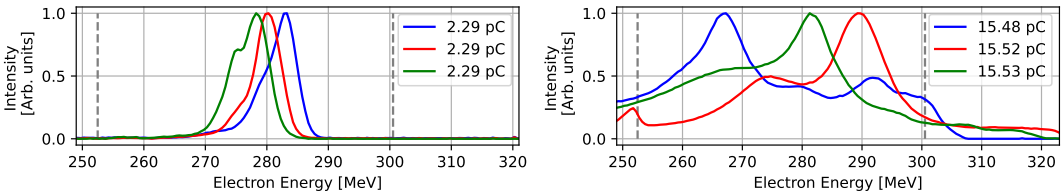

Figure 9.14 – Energy distribution for different shots. Optimum beam loading is at ≈ 3 pC. Lower charged beams are on the left and high charged beams on the right. The vertical dashed lines mark the limit between which emitted wavelengths can be measured, see Sec. 9.2.

The flux at the fundamental wavelength scales linear with the charge, see Eq. 2.18. With increasing charge, also the calculated energy spreads increase due to a strong beam loading which overcompensates the acceleration field inside the plasma and chirps the energy spectrum as described in Sec. 3.2. Optimal beam loading is given for ≈ 3 pC, so beams with charges close to 3 pC have a peaked energy spectrum and bunches with charges well above this level have a broad energy spectrum, see Fig. 9.14. A Gaussian fit to those high charge profiles does not represent the measured spectra with an adequate accuracy and gives falsified values. Also, a fraction of the charge radiates on wavelengths which can not be measured within the chosen spectrometer settings and is far off the fundamental of the peak at which the photon count is evaluated. This effect is visible on the left plot of Fig. 9.15 in which the linear scaling decreases

with charges above ≈ 6 pC. The dataset is filtered for charges below 6 pC and a linear regression is used to find the scaling, see middle plot. From the spectra shown there, the linear fit is subtracted and the mean and standard deviation of the remaining distribution are used as a lower (mean-std) and higher (mean+std) cut out level to further reduce the influence of broad electron energy spectra onto the fit, see right on Fig. 9.15. The dataset was recorded with one shot per second, so the scaling of the photons per second on the fundamental wavelength and a K of 0.4477 with the charge is $(5.61 \pm 0.05) + (25.64 \pm 0.03) \cdot q\,[\mathrm{pC}]$, see right in Fig. 9.15. It is common in literature to normalize this property to a radiation bandwidth of 0.1 % [17, 1]. Here, the near field increase of the bandwidth about a factor of 4 has to be taken into account. The integrated flux scaling is then

$$\dot{\mathrm{N}}[\mathrm{ph/s/0.1\%B.W.}] = (224.4 \pm 2.0) + (1025.6 \pm 1.2) \cdot q\,[\mathrm{pC}]. \tag{9.9}$$

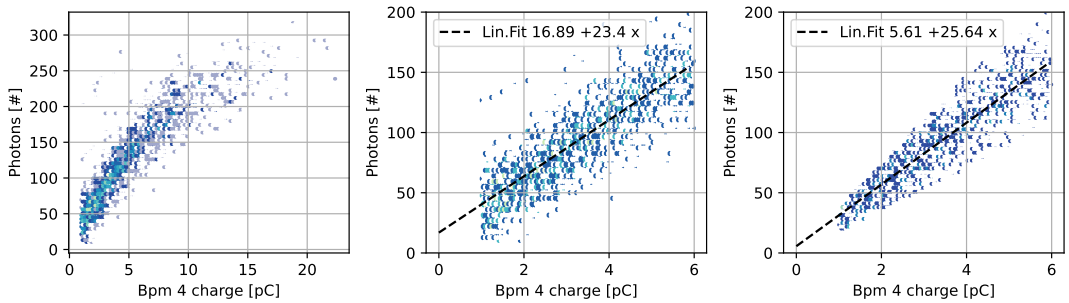

Figure 9.15 – Scaling of the photons per second at the fundamental wavelength with the charge. Left is the full recording, in the middle filtered for charge. On the right, the data was filtered to reduce the impact of broad energy spread beams.

As already mentioned in Sec. 2.3.2, the definitions of the basic undulator radiation properties vary between the peak flux and the flux of the exact harmonic. Here, the definition for the total flux in the central cone (Eq. 2.18 as defined in [1]) and the on axis radiation (as defined in [17]) differ about a factor of two. For the correlation shown in Fig. 9.15, the number of photons emitted on the exact harmonic are used. The flux definition in Eq. 2.18 has to be divided by two to get the theoretical flux at the exact harmonic. For the used settings during the measurements, the K-value of 0.4477 and the 128 undulator periods, the predicted flux (half value of Eq. 2.18) scales like $\dot{\mathrm{N}}[\mathrm{ph/s/0.1\%B.W.}] = 1590.3 \cdot q[\mathrm{pC}]$. The measured flux of Eq. 9.9 is ≈ 66% of the theoretically expected flux, so 1/3 of the photons is lost. The reasons for this are manifold. The BPMs could measure dark current, or lower energetic electron beam tails which contribute to the total charge measurement, but not to the recorded photon spectrum, similar to the discussion at the beginning of this subsection. The photon transport beam line is not yet aligned to the undulator axis and the emitted photon

beam diameters could be so big, that they clip along the beam line. For example at the mirror, the entrance slit of the x-spec, or the grating. Such clips are visible in the spectra shown in Fig. 10.1 close to the 3 mm position of the upper plot. The efficiency curves of the spectrometer could slightly differ from the data presented in Sec. 8.2. For the data preparation a background is subtracted. This background is the mean image of all shots with charges below 0.4 pC. It is assumed that no electrons are present below this measured level, as this is the default BPM display when the accelerator is off, as discussed in Sec. 9.1. This assumption could be wrong which would have a high impact, as the measured charges are in the low one digit pC range. Also, the data preparation requires a lot of filtering which could have an influence.
However, the most likely explanation for this loss is the power supply of the compensation coil. It should have been set to +2.2 A to fit to the evaluations shown in Sec. 5.6, but it is possible that the polarity is switched and -2.2 A are applied in reality. Instead of compensating field errors and reducing the overall phase jitter to 4.4 °, it would then increase the phase jitter to 34.5 °, which would lead to a reduction of the emitted power to ≈ 70 %, see Eq. 6.3. This would fit very well to the observed flux reduction of ≈ 33 %. The coil current versus partial flux scan presented in Fig. 10.1, in which the flux increases for negative coil currents, supports the statement that the polarity is switched.

9.3.5 Taper Scan

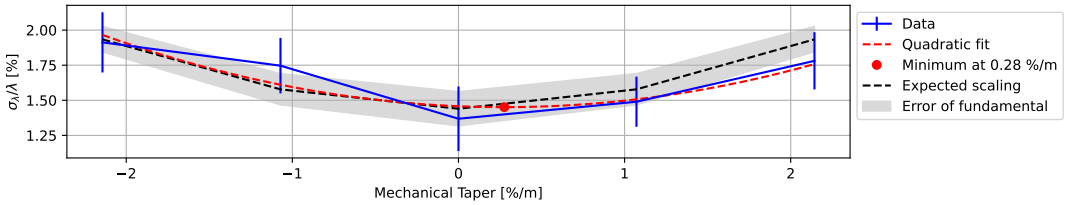

Figure 9.16 – Calculated undulator near field bandwidths (blue) for different taper settings. The vertical bars denote the measurement uncertainty. The expected bandwidth scaling of Eq. 9.10 is shown as a reference for the bandwidth of Eq. 9.8.

To measure the taper, see Sec. 4.2.4, the undulator girders are tilted around the longitudinal center of the machine, as indicated in Fig. 9.1. The nominal gap at the undulator center is fixed to 10 mm and the girders are rotated symmetrically up to $\Delta g = 200\,\mu$m in 5 steps. A Δg of $+200\,\mu$m means, the gap is 10.2 mm at the beginning and 9.8 mm at the end of the undulator. The gap measurement systems are separated about 1.87 m, so the mechanical adjusted taper values are ± 2.14 %/m, ± 1.07 %/m, 0 %/m, which directly translate into different K values at the beginning of the undulator

and its end with respect to the nominal K-value K_0 at the center. The resulting FWHM bandwidth increase is [87]

$$\left(\frac{\Delta\lambda}{\lambda}\right)_T = \frac{K_0^2}{1+K_0^2/2}\frac{\pi}{\lambda_u}\cdot\Delta g. \tag{9.10}$$

which is transformed into an rms σ value (FWHM $\approx 2.35\cdot\sigma$), multiplied by 4 due to the near field scaling , see Sec. 8.4, and convoluted with the fundamental bandwidth of Eq. 9.7 to the total bandwidth like $\sigma_\lambda/\lambda = \sqrt{(\sigma_\lambda/\lambda)^2_{NF} + (\sigma_\lambda/\lambda)^2_T}$. For the nominal 10 mm gap and the above mentioned mechanical tapers, the expected bandwidths are 1.44 % for 0 %/m taper, 1.58 % for ± 1.07%/m taper and 1.93 % for ± 2.14 %/m taper.

For each taper setting 500 shots are recorded, filtered for charges above 1 pC and a high signal to noise ratio in the x-spec profiles and then analyzed as described in Sec. 9.2.1. The retrieved fundamental bandwidth for each taper setting is shown in Fig. 9.16. As a measurement error the fit errors are used. Within the uncertainty of the measurements and the error of the calculated fundamental near field bandwidth, see Eq. 9.8, the scaling of the bandwidth with the taper is in a good agreement with the theoretical expected behavior of Eq. 9.10. The minimum of the bandwidth is found with a quadratic fit for a taper setting of +0.28 %/m which corresponds to $\Delta g = 51.5\,\mu$m. That means, at the assumed 0 %/m taper position the gap at the upstream gap measurement system is $\approx 26\,\mu$m too high and at the downstream side $\approx 26\,\mu$m to small. This offset could be readjusted software wise to match the measured 0 %/m taper position from this scan with the recorded 0 %/m taper position of the gap measurement system.

9.4 Conclusion

Within this chapter the basic properties of the undulator radiation are measured. To reduce the impact of electron trajectory errors onto the x-ray spectrum the undulator is set to a low K value of 0.4477 which increases the vertical good field region to one mm, due to which trajectory instabilities up to ± 0.5 mm offset and ± 0.25 mrad angle into the undulator are strongly suppressed, see Sec. 9.2. In addition, the integrated flux was used as basis for calculations as it is independent of the beam shape and orbit, and only scales with the charge and broadens with the energy spread.
For the measurement of the fundamental wavelengths 2274 shots were used with an average energy spread of $\langle\sigma\gamma/\gamma\rangle = 1.14\,\% \pm 0.38\,\%$ and electron energies between 270 MeV and 290 MeV.

From the scaling of the bandwidth with the energy spread, the fundamental near field and far field bandwidth of the undulator was found to be:

$$\left(\frac{\sigma\lambda}{\lambda}\right)_{\mathrm{NF}} = 1.44\% \pm 0.122\% \pm 0.072\%(\mathrm{S})$$
$$\left(\frac{\sigma\lambda}{\lambda}\right)_{\mathrm{FF}} = 0.36\% \pm 0.03\% \pm 0.018\%(\mathrm{S})$$

with the systematic measuremnt uncertainty denoted as (S). The retrieved values are in a good agreement with the calculated bandwidth from the magnetic undulator field, see Sec. 9.2.2, which is 0.35% in the near field and 1.4% in the far field, see Sec. 9.3.3. The integrated flux at the harmonic wavelength was determined to scale with the charge as

$$\dot{\mathrm{N}}[\mathrm{ph/s/0.1\%B.W.}] = (224.4 \pm 2.0) + (1025.6 \pm 1.2) \cdot q\,[\mathrm{pC}],$$

which is $\approx 66\%$ of the expected scaling. It is assumed, that the polarity of the compensation coil power supply is switched, which would increase the phase error to 34.5°, causing a emission power reduction to 70 % see Sec. 9.3.4.
In a second run the undulator was tapered symmetrically around its center and a symmetric increase of the fundamental bandwidth was observed. Within the uncertainties of the measurements the symmetric increase matches the analytical expressions, see Sec. 9.3.5. It was found, that a remaining taper of 0.28 %/m is at the assumed 0 %/m taper position which could be turned out software wise by recalibrating the read out values of the gap measurement systems about 26 μm.

10 Conclusion and Outlook

This thesis describes the design, characterization and commissioning of a cryogenic in-vacuum undulator in detail. The tunable and taperable gap undulator was commissioned up to a state which allows to demonstrate the start of a possible free electron lasing with electron bunches generated by the laser plasma accelerator Lux.

To maximize the acceptance of the electron energy spread and simultaneously shorten the overall machine length, the undulator is designed with a high on-axis undulator field of 2.04 T at a 2 mm gap combined with a short undulator period of 15 mm in the cryo state with a total of 130 periods. Within the cryo state, a K value of would be 2.8 possible.

When cooling the undulator down to its operating temperature below 77 K, the structure contracts and mechanical stresses appear between the individual components. Also, the magnetic field increases which changes the forces acting onto the support structure. It was shown that the tolerance chain of the Frosty design compensates stress peaks within the mechanics and that the support structure deforms about 1 μm to 2 μm between the forces acting in the warm and cold condition. An open task for future devices is the adjustability of the poles. During the tuning of the machine it was found, that the B_z component of the undulator field could not be tuned. A possible explanation for this effect could be a dent in the contact area between the poles and the adjustment screws, which formed due to the high acting forces of the point support. This dent would act as a joint connection and would move the pole in an undefined motion when the screw is wobbling around its axis when it gets turned. The same effect would appear if the point support is not centered at the screw head.

The used cooling scheme, localized cold heads at the ends of the girders, does introduce a thermal gradient along the magnetic structure, which deforms the undulator field at its design gap such, that a systematic phase advance of -645 ° at the fundamental wavelength occurs. This phase advance shifts the average wavelength about 1.7 % to the red and reduces the intensity of the average wavelength to 70 % compared to the case without a thermal gradient. This phase advance could be compensated by tuning the undulator field respectively, but the cooling concept has the high potential to make Frosty to a dominant degradation factor of the FEL performance and has to be reworked in the future. A desired solution is a uniform cooling concept with which

the thermal gradients are kept small. An upgrade could be to directly connect the cryo heads to the bayonet enclosures. Doing so would cause the heat to flow from the out-of-vacuum contact surfaces to the cold head without traversing the girder.

For the magnetic field measurements a 3.5 m long bench was built which actively regulates the transverse Hall probe position onto a defined laser axis. The reproducibility of the system is 1.6 μm in the horizontal, 3.2 μm in the vertical and 0.7 μm in the longitudinal direction, which produces uncertainties of the measured second field integrals of $J_2(x) = 4.1\,\mu\mathrm{Tm}^2$, $J_2(y) = 8.4\,\mu\mathrm{Tm}^2$ and $J_2(z) = 29.7\,\mu\mathrm{Tm}^2$ over the full measurement range of 3 m. The main contributors to the measurement errors are a too heavy load on the vertical Piezo stage and a drift of the longitudinal slider position caused by the timing belt inside the bench. Also, the bench is only capable of measuring and compensating positions but not angular deviations. One has to say here, that the measurement bench was designed, constructed and commissioned within three months and a lot of regulations and mechanics are not optimized to the maximum, but only to a state in which the measurement accuracy allows to make qualified statements of the measured field and to tune the undulator field integrals below its limits. Which succeeded for the above mentioned accuracies of the stage, but still there is room for improvements. For the future, the bench has to be upgraded by implementing a second laser line to measure the rotation around the longitudinal axis and a 5 axes interferometer to regulate the rotation around the vertical and horizontal axes. The timing belt of the longitudinal mover system has to be exchanged with a cable pull and a drag chain has to be installed to separate the high voltage supply of the Piezo stages from the sensitive Hall probe cables. It is estimated, that those improvements would reduce the uncertainties of the field integrals about a factor of 3 to 5. Also, the system has to be upgraded to measure on the fly and not in a step by step mode, which would reduce the measurement time from 3.5 hours to 30 minutes.

During the installation of the girders inside the vacuum vessel a malfunction of the rail system caused vibrations and a accompanying reduction of undulator field quality. With an additional corrector coil around the undulator chamber the field integrals can be flattened again, but the remaining phase error increased from $7.9\,^\circ \pm 0.44\,^\circ$ to $11.05\,^\circ \pm 0.23\,^\circ$ and two localized bendings inside the average second field integrals increased the beam wander from $19.8\,\mu\mathrm{Tm}^2 \pm 0.6\,\mu\mathrm{Tm}^2$ to $66.3\,\mu\mathrm{Tm}^2 \pm 1.92\,\mu\mathrm{Tm}^2$. It was verified with simulations, that the effect of the disturbed undulator field onto the FEL performance is dominated by the phase error and causes an increase of the gain length of 1.3 %, which is acceptable small for the application. Nevertheless, the magnetic field of Frosty should be optimized again at some time in the future, when the influence of undulator field errors onto the lasing dominate the influence of electron beam deviations.

For the commissioning, the undulator was installed in the Lux beamline, connected to the vacuum system and first measurements of the spontaneous undulator radiation were performed. From the measured spectra, the FWHM far field bandwidth was experimentally determined to be $0.85\,\% \pm 0.07\,\%$, which is close to the calculated bandwidth of $0.82\,\%$ from magnetic field measurements, but a relative increase of $10\,\%$ compared to the bandwidth of an ideal undulator which is $0.78\,\%$ for 128 periods. Also, a functionality test shows the expected increase of the fundamental bandwidth with the taper. It was found, that the a taper of $0.28\,\%/\mathrm{m}$ is present at the assumed $0\,\%/\mathrm{m}$ taper position, which has to be readjusted in the motion control software.

Path towards Lasing

While the undulator is ready for operation its adjustment and alignment to the accelerator coordinate system and to the electron beam orbit is still pending. Besides that, an additional optimization of the compensation coil could be performed to increase the signal on the FEL diagnostics. Both cases, the additional calibration and the electron beam based alignment are shortly discussed.

Coil vs Flux Scan

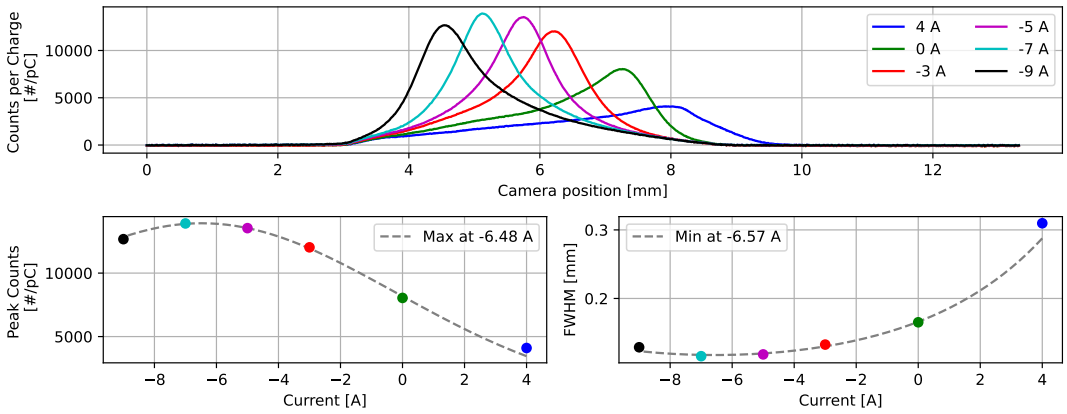

Figure 10.1 – Showcase measurement of the spatial photon flux distribution for different currents of the compensation coil. Each distribution is averaged over 100 shots and normalized to the recorded charge. The K is ≈ 2 and the average energy 270 MeV.

The purpose of the compensation coil is to correct the overall trajectory of the electron beam to a state in which the pointing of the particles is the same before and after the undulator. The coil manipulates the average trajectory of the electrons inside the field,

but is not capable of compensating local errors.
The Frosty field shows a local horizontal kick to one side at the end of the machine which would be compensated by steering the average trajectory to the other side in a way that the deflection at the end of the undulator is compensated. The electrons would exit the undulator without an additional kick, but would travel along a curved trajectory inside the device. An example of this effect is shown in the lower part of Fig. 5.18. As the undulator flux depends on the trajectory inside the undulator, its maximum flux would be radiated along the tilted trajectory and not parallel to the longitudinal undulator axis. As an additional calibration the coil current should be scanned versus the maximum flux and minimum bandwidth in the 0th diffraction order, in which the grating acts as a mirror and does not diffract the beam. This allows to measure a spatial resolved image. Such a first proof of principle measurement is shown in Fig. 10.1 for an undulator gap of 3 mm. As the coil deflects in the horizontal plane, also the camera image is projected to the horizontal plane. The upper part shows the count distributions for different applied coil currents. The maximum signal corresponds to the most straightest average trajectory of the electrons inside the undulator field. For an applied current of ≈ -6.5 A the flux is maximized and the bandwidth minimized, which means the average emission direction points towards the camera. In contrast, a coil current of -5.1 A would be required to compensate the overall kick of the electrons. Such scans should be repeated for all gaps and could also be used to align the emission direction towards the camera before each run.

Beam Based Alignment

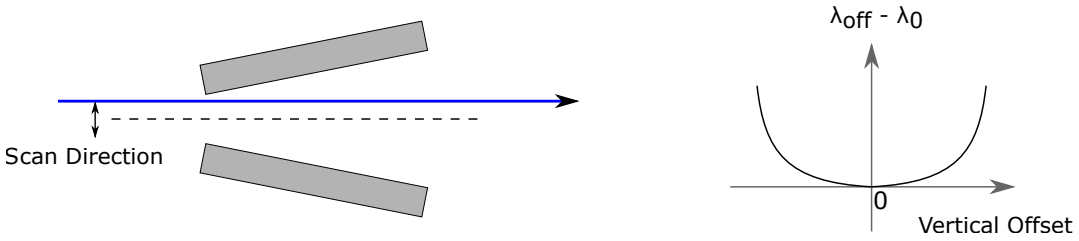

Figure 10.2 – Sketch for the vertical beam based alignment scan and the expected red shift of the fundamental wavelength with the vertical offset.

A beam based alignment of the electron beam orbit to the undulator axes has to be done, as mechanical alignment errors on the 0.1 mm scale between the electron beam diagnostics and the magnetic undulator axes are possible. These positioning errors are above the vertical good field region at the design gap and would cause a broadening of the radiated spectra, which decreases the peak performance.
To find the undulator axes, taper scans can be used, as illustrated in Fig. 10.2. When adjusting the taper such that the peak field is maximized at the undulator entrance,

the longest recorded wavelength is emitted at the beginning of the undulator. Scanning the vertical entrance position of the undulator with the electron beam causes a red shift of the measured radiation due to the increasing peak field. Scanning horizontally causes a blue shift, as the magnetic field degrades. The shortest wavelength for the vertical scan and the longest wavelength for the horizontal scan is recorded on axis, so the magnetic center at the entrance is determined. Repeating this measurement for the undulator exit gives the center position at the end. With this procedure the electron beam orbit could be adjusted to the magnetic undulator axes. A subsequent symmetric taper scan around the undulator center could now be used to find the minimum radiation bandwidth at which the taper of the magnetic field is minimized and close to 0 %/m.

When this beam based alignment is completed, this thesis states that the undulator is ready for operation. The impact of the trajectory errors inside the magnetic field onto a possible free electron lasing with a laser plasma generated electron bunch manifests by an increase of the FEL gain length about 1.3 %, which is negligible small.

Bibliography

[1] J. A. Clarke, *The Science and Technology of Undulators and Wigglers*, vol. 1st edition. Oxford University Press, 2004.

[2] P. Schmüser, M. Dohlus, J. Rossbach, and C. Behrens, *Free-Electron Lasers in the Ultraviolet and X-Ray Regime: Physical Principles, Experimental Results, Technical Realization.* Springer Tracts in Modern Physics, Springer International Publishing, 2014.

[3] M. Kirchen, S. Jalas, P. Messner, P. Winkler, T. Eichner, L. Hübner, T. Hülsenbusch, L. Jeppe, T. Parikh, M. Schnepp, and A. R. Maier, "Optimal beam loading in a laser-plasma accelerator," *Phys. Rev. Lett.*, vol. 126, p. 174801, Apr 2021.

[4] T. Seggebrock, *Conceptual design of a laser-plasma accelerator driven free-electron laser demonstration experiment.* PhD thesis, Ludwig-Maximilians-Universität München, 2015.

[5] J. Bahrdt. Private Communication.

[6] F.-J. Boergermann, C. Brombacher, and K. Uestuener, "Properties, Options and Limitations of PrFeB-magnets for Cryogenic Undulators," in *Proceedings, 5th International Particle Accelerator Conference (IPAC 2014): Dresden, Germany, June 15-20, 2014*, p. TUPRO085, 2014.

[7] E. D. Marquardt, J. P. Le, and R. Radebaugh, *Cryogenic Material Properties Database*, pp. 681–687. Boston, MA: Springer US, 2002.

[8] SHI Cryogenics Group, *RDK-400B 40K Cryocooler Series manual*, July 2022. www.shicryogenics.com.

[9] T. Tanaka, "Simplex: Simulator and postprocessor for free-electron laser experiments," *Journal of Synchrotron Radiation*, vol. 22, 2015.

[10] M. Misakian, "Equations for the magnetic field produced by one or more rectangular loops of wire in the same plane," *Journal of Research of the National Institute of Standards and Technology*, vol. 105, 07 2000.

[11] Hitachi High-Technologies Corporation, *Aberration - corrected concave grating. Part. No. 01-0639 Manual*, July 2022. www.hitachi-hightech.com.

[12] "Lux team." Internal Communication.

[13] B. Henke, E. Gullikson, and J. Davis, "X-ray interactions: Photoabsorption, scattering, transmission, and reflection at e = 50-30,000 ev, z = 1-92," *Atomic Data and Nuclear Data Tables*, vol. 54, no. 2, pp. 181–342, 1993.

[14] METALCOR, *Titan Grade 5 Ti6Al4V Datasheet*, July 2022. www.metalcor.de.

[15] VACUUMSCHMELZE GMBH & CO.KG, *Rare Earth Permanent Magnets VACODYM - VACOMAX*, July 2022. www.vacuumschmelze.com.

[16] A. F. . P. Association, "Beam design formulas with shear and moment diagrams," 2005.

[17] K.-J. Kim, Z. Huang, and R. Lindberg, *Synchrotron Radiation and Free-Electron Lasers: Principles of Coherent X-Ray Generation*. Cambridge University Press, 2017.

[18] H. Onuki and P. Elleaume, *Undulators, Wigglers and Their Applications*, vol. 1st edition. CRC Press, 2002.

[19] F. Duarte, *Tunable Laser Applications*. Optical Science and Engineering, CRC Press, 2008.

[20] "European xfel homepage," March 2022. `https://www.xfel.eu`.

[21] "Linac coherent light source lcls homepage," June 2022. `https://lcls.slac.stanford.edu/`.

[22] "Flash homepage," June 2022. `https://flash.desy.de/`.

[23] "Fels of europe homepage," June 2022. `https://www.fels-of-europe.eu/`.

[24] D. Strickland and G. Mourou, "Compression of amplified chirped optical pulses," *Optics Communications*, vol. 56, no. 3, pp. 219–221, 1985.

[25] M. Perry and G. Mourou, "Terawatt to petawatt subpicosecond lasers," *Science (New York, N.Y.)*, vol. 264, p. 917—924, May 1994.

[26] T. Tajima and J. M. Dawson, "Laser electron accelerator," *Phys. Rev. Lett.*, vol. 43, pp. 267–270, Jul 1979.

[27] J. Faure, Y. Glinec, A. Pukhov, S. Kiselev, S. Gordienko, E. Lefebvre, J. Rousseau, F. Burgy, and V. Malka, "A laser-plasma accelerator producing monoenergetic electron beams," *Nature*, vol. 431, p. 541—544, September 2004.

[28] S. Mangles, C. Murphy, Z. Najmudin, A. Thomas, J. Collier, A. Dangor, E. Divall, P. Foster, J. Gallacher, C. Hooker, D. Jaroszynski, A. Langley, W. Mori, P. Norreys, F. Tsung, R. Viskup, B. Walton, and K. Krushelnick, "Monoenergetic beams of relativistic electrons from intense laser-plasma interactions," *Nature*, vol. 431, pp. 535–8, 10 2004.

[29] E. Esarey, C. B. Schroeder, and W. P. Leemans, "Physics of laser-driven plasma-based electron accelerators," *Rev. Mod. Phys.*, vol. 81, pp. 1229–1285, Aug 2009.

[30] W. Leemans and E. Esarey, "Esarey, e.: Laser-driven plasma-wave electron accelerators. phys. today 62(3), 44," *Physics Today - PHYS TODAY*, vol. 62, 03 2009.

[31] C. Geddes, C. Toth, J. Tilborg, E. Esarey, C. Schroeder, D. Bruhwiler, C. Nieter, J. Cary, and W. Leemans, "High quality electron beams from a plasma channel guided laser wakefield accelerator," *Nature*, vol. 431, 07 2004.

[32] S. Karsch, J. Osterhoff, A. Popp, T. P. Rowlands-Rees, Z. Major, M. Fuchs, B. Marx, R. Hörlein, K. Schmid, L. Veisz, S. Becker, U. Schramm, B. Hidding, G. Pretzler, D. Habs, F. Grüner, S. M. Hooker, and F. Krausz, "GeV-scale electron acceleration in a gas-filled capillary discharge waveguide," *New Journal of Physics*, vol. 9, pp. 415–426, 2007.

[33] J. Osterhoff, A. Popp, Z. Major, B. Marx, T. P. Rowlands-Rees, M. Fuchs, M. Geissler, R. Hörlein, B. Hidding, S. Becker, E. A. Peralta, U. Schramm, F. Grüner, D. Habs, F. Krausz, S. M. Hooker, and S. Karsch, "Generation of stable, low-divergence electron beams by laser-wakefield acceleration in a steady-state-flow gas cell," *Phys. Rev. Lett.*, vol. 101, p. 085002, Aug 2008.

[34] A. R. Maier, N. M. Delbos, T. Eichner, L. Hübner, S. Jalas, L. Jeppe, S. W. Jolly, M. Kirchen, V. Leroux, P. Messner, M. Schnepp, M. Trunk, P. A. Walker, C. Werle, and P. Winkler, "Decoding sources of energy variability in a laser-plasma accelerator," *Phys. Rev. X*, vol. 10, p. 031039, Aug 2020.

[35] W. Wang, K. Feng, and L. Ke, "Free-electron lasing at 27 nanometres based on a laser wakefield accelerator," *Nature*, vol. 595, pp. 516 – 520, 2021.

[36] "Laser plasma driven light source lux," March 2022. `http://lux.cfel.de/`.

[37] N. Delbos, C. Werle, I. Dornmair, T. Eichner, L. Hübner, S. Jalas, S. Jolly, M. Kirchen, V. Leroux, P. Messner, M. Schnepp, M. Trunk, P. Walker, P. Winkler, and A. Maier, "Lux – a laser–plasma driven undulator beamline," *Nuclear Instruments and Methods in Physics Research Section A: Accelerators, Spectrometers, Detectors and Associated Equipment*, vol. 909, pp. 318–322, 2018. 3rd European Advanced Accelerator Concepts workshop (EAAC2017).

[38] F. Grüner, S. Becker, U. Schramm, T. Eichner, M. Fuchs, R. Weingartner, D. Habs, J. M. ter Vehn, M. Geissler, M. Ferrario, L. Serafini, B. van der Geer, H. Backe, W. Lauth, and S. Reiche, "Design considerations for table-top, laser-based VUV and x-ray free electron lasers," *Applied Physics B*, vol. 86, pp. 431–435, jan 2007.

[39] A. R. Maier, A. Meseck, S. Reiche, C. B. Schroeder, T. Seggebrock, and F. Grüner, "Demonstration scheme for a laser-plasma-driven free-electron laser," *Phys. Rev. X*, vol. 2, p. 031019, Sep 2012.

[40] J. Bahrdt, W. Frentrup, A. Gaupp, M. Scheer, R. Weingartner, F. O'Shea, and F. Gruener, "Cryogenic undulator for a table top fel," *AIP Conference Proceedings*, vol. 1234, 06 2010.

[41] F. Holy, *Research and Development towards Undulator Designs Dedicated to Laser Plasma Accelerator Beam Lines.* PhD thesis, Universität Hamburg, 2018.

[42] K. Uestuener, M. Katter, R. Blank, D. Benedikt, J. Bahrdt, A. Gaupp, B. Klemke, F. Gruener, and R. Weingartner, "Sintered (pr, nd)-fe-b permanent magnets with (bh) max of 520. kj/m^3 at 85 k for cryogenic applications," 01 2010.

[43] W. Heisenberg, "Über den anschaulichen inhalt der quantentheoretischen kinematik und mechanik," *Zeitschrift für Physik*, vol. 43, p. 172–198, March 1927.

[44] G. Margaritondo and P. Rebernik Ribic, "A simplified description of X-ray free-electron lasers," *Journal of Synchrotron Radiation*, vol. 18, pp. 101–108, Mar 2011.

[45] Z. Huang and K.-J. Kim, "Review of x-ray free-electron laser theory," *Phys. Rev. ST Accel. Beams*, vol. 10, p. 034801, Mar 2007.

[46] Q.-K. Jia, "Analytical formula of free electron laser exponential gain for a non-resonant electron beam," *Chinese Physics C*, vol. 39, p. 048101, apr 2015.

[47] M. Xie, "Exact and variational solutions of 3d eigenmodes in high gain fels," *Nuclear Instruments and Methods in Physics Research Section A: Accelerators, Spectrometers, Detectors and Associated Equipment*, vol. 445, no. 1, pp. 59–66, 2000.

[48] Q.-K. Jia, D.-H. He, S.-K. Lu, S.-C. Zhang, Y. Cao, Z.-M. Dai, Z.-T. Zhao, C. Yun, and Q.-G. Zhou, "Design of undulator for the Shanghai DUV-FEL," in *26th International Free Electron Laser Conference and 11th FEL User Workshop (FEL 04)*, pp. 494–497, 8 2004.

[49] A. R. Maier, S. W. Jolly, V. Leroux, and M. Schnepp, "Integration of the angus 200 tw laser-system into the accelerator infrastructure at desy," in *Conference on Lasers and Electro-Optics*, p. JTu3L.4, Optica Publishing Group, 2017.

[50] J. Faure, "Plasma injection schemes for laser–plasma accelerators," *CERN Yellow Reports*, pp. Vol 1 (2016): Proceedings of the 2014 CAS–CERN Accelerator School: Plasma Wake Acceleration, 2016.

[51] E. L. Saldin, E. A. Schneidmiller, and M. V. Yurkov, "Self-amplified spontaneous emission fel with energy-chirped electron beam and its application for generation of attosecond x-ray pulses," *Phys. Rev. ST Accel. Beams*, vol. 9, p. 050702, May 2006.

[52] VACUUMSCHMELZE GMBH & CO.KG, *VACODYM 131 TP / VACODYM 131 DTP for low temperature applications*, July 2022. www.vacuumschmelze.com.

[53] VACUUMSCHMELZE GMBH & CO.KG, *Soft magnetic Cobalt Iron alloys - vacoflux*, July 2022. www.vacuumschmelze.com.

[54] H. Fujii, H. Nagata, Y. Uwatoko, T. Okamoto, H. Yamamoto, and M. Sagawa, "Heat capacity and thermal expansion of r2fe14b compounds (r = y, nd and tm)," *Journal of Magnetism and Magnetic Materials*, vol. 70, no. 1, pp. 331–333, 1987.

[55] H. Bethe, "Zur theorie des durchgangs schneller korpuskularstrahlen durch materie," *Annalen der Physik*, vol. 397, no. 3, 1930.

[56] H. Bethe, "Bremsformel für elektronen relativistischer geschwindigkeit," *Zeitschrift für Physik*, vol. 76, 1932.

[57] R. M. Sternheimer, "The density effect for the ionization loss in various materials," *Phys. Rev.*, vol. 88, pp. 851–859, Nov 1952.

[58] R. M. Sternheimer, S. M. Seltzer, and M. J. Berger, "Density effect for the ionization loss of charged particles in various substances," *Phys. Rev. B*, vol. 26, pp. 6067–6076, Dec 1982.

[59] M. Berger, J. Coursey, M. Zucker, and J.Chang, "ESTAR, PSTAR, and ASTAR: Computer Programs for Calculating Stopping-Power and Range Tables for Electrons, Protons, and Helium Ions," 2022.

[60] *CST Studio*, July 2022. www.3ds.com.

[61] METALCOR, *Stainless Steel AISI 316 LN Datasheet*, July 2022. ww.metalcor.de.

[62] Nedal Aluminium BV, *Aluminum EN AW 5083 Datasheet*, July 2022. www.nedal.com.

[63] Deutsches Kupferinstitut, *Cu HCP Datasheet*, July 2022. www.kupferinstitut.de.

[64] U. Hahn and K. Zapfe, "Technische Spezifikation, Richtlinien fuer UHV-Komponenten bei DESY," 2010. www.edmsdirect.desy.de.

[65] J. P. Kolb, "Model of a cryogenic undulator tapered by a thermal gradient," b.s. thesis, Ludwig-Maximilians-Universität München, 2010.

[66] V. Läpple, *Loesungsbuch zur Einfuehrung in die Festigkeitslehre: Ausfuehrliche Loesungen und Formelsammlung.* Wiesbaden: Vieweg, 2007.

[67] Steinmeyer, *Precision rolled ball screw - internal specification*, July 2022. www.steinmeyer.com.

[68] Vogel, *Gearing mksh2 Manual*, July 2022. www.vogel-antriebe.de.

[69] Keyence, *Keyence - ls 7070 Manual*, July 2022. www.keyence.de.

[70] Wittur, *Wittur dum6-b1 manual*, July 2022. www.wittur.com.

[71] F. Incropera, D. DeWitt, T. Bergman, and A. Lavine, *Fundamentals of Heat and Mass Transfer*. Wiley, 2007.

[72] M. Bahrami, J. Culham, M. Yovanovich, and F. Asme, "Modeling thermal contact resistance: A scale analysis approach," *Journal of Heat Transfer*, vol. 126, 01 2003.

[73] Y. Li, B. Faatz, and J. Pflueger, "Undulator system tolerance analysis for the European x-ray free-electron laser," *Phys. Rev. ST Accel. Beams*, vol. 11, p. 100701, 2008.

[74] Y. Li, B. Ketenoglu, and J. Pflueger, "Girder deformation related phase errors on the undulators for the european x-ray free electron laser," *Phys. Rev. ST Accel. Beams*, vol. 18, p. 060704, Jun 2015.

[75] ENNOLOGIC, *Emissivity Table for Infrared Thermometer Readings*, July 2022. www.ennologic.com.

[76] Micro-Epsilon, *scanCONTROL 2910-25 Manual*, July 2022. www.micro-epsilon.de.

[77] J. Pflüger, H. H. Lu, D. Köster, and T. Teichmann, "Magnetic measurements on the undulator prototype for the vuv-fel at the tesla test facility," *Nuclear Instruments & Methods in Physics Research Section A-accelerators Spectrometers Detectors and Associated Equipment*, vol. 407, pp. 386–391, 1998.

[78] SENIS AG, *3MH6 Manual*, July 2022. www.senis.swiss.

[79] R. Plato, *Numerische Mathematik kompakt: Grundlagenwissen für Studium und Praxis*. Vieweg Studium, Vieweg+Teubner Verlag, 2010.

[80] U. Ramer, "An iterative procedure for the polygonal approximation of plane curves," *Computer Graphics and Image Processing*, vol. 1, no. 3, pp. 244–256, 1972.

[81] D. H. Douglas and T. K. Peucker, "Algorithms for the reduction of the number of points required to represent a digitized line or its caricature," *Cartographica: The International Journal for Geographic Information and Geovisualization*, vol. 10, pp. 112–122, 1973.

[82] L. T. Campbell and B. W. J. McNeil, "Puffin: A three dimensional, unaveraged free electron laser simulation code," *Physics of Plasmas*, vol. 19, no. 9, p. 093119, 2012.

[83] C. Palmer, *Diffraction Grating Handbook, eighth edition.* MKS Instruments, 03 2020.

[84] N. Joshi, *Design and Analysis Techniques for Cavity Beam Position Monitor Systems for Electron Accelerators.* PhD thesis, Royal Holloway, U. of London, 2013.

[85] R. Lorenz, "Cavity beam position monitors," *AIP Conference Proceedings*, vol. 451, no. 1, pp. 53–73, 1998.

[86] A. Savitzky and M. J. E. Golay, "Smoothing and differentiation of data by simplified least squares procedures.," *Analytical Chemistry*, vol. 36, no. 8, pp. 1627–1639, 1964.

[87] B. Lai, A. Khounsary, R. Savoy, L. Moog, and E. Gluskin, "Undulator a characteristics and specifications," 2 1993.

11 Acknowledgments

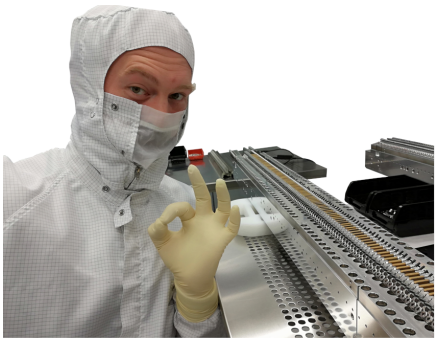

First of all I would like to thank my supervisor Andreas R. Maier who gave me the opportunity to guide this difficult and long lasting project towards a successful end. Due to the unusual high number of encountered problems during the design and assembling, he had to serve as a valve for my frustration once in a while, but always found the right words to cheer me up and keep me on moving. I am grateful that you were my supervisor!

The project is based on a BWMF funded collaboration initiated by Florian Grüner back in 2009. Without his initiative, the undulator would not be here. Thank you for this!

The whole project would have been impossible without the team around Johannes Bahrdt and Bodo Schulz from HZB Berlin, who were the driving force behind the Frosty development before I became in charge. With their scientific expertise and know-how they developed the new magnetic alloy and tested its cryogenic performance on several prototypes until the technology was so well understood that a final prototype version of Frosty 3 was designed, which formed the basis for my thesis. Here one has to mention Florian Holy who did a majority of simulations and optimizations of the magnet dimensions for Frosty. My greatest respect and thanks to your work!

A special thanks goes out to the Lux crew. Paul, Philipp, Lars and Soeren helped me a lot during the installation of the chamber and took care of the transport into the accelerator tunnel and the final field measurements there. Our former member Laurids Jeppe helped me a lot with his incredible programming skills to set up the measurement bench into a fully automated state. I would also like to thank Niels

Delbos who was in charge of Frosty before I received the project. Niels took greatest care to implement the DESY vacuum standard into the undulator and managed the design and fabrication of the Frosty frame and the vacuum chamber. He had a lot of trouble and many unloved tasks on his desk which caused a lot of painstakingly work. Thank you very much for your meticulous care and planning (and keeping those tasks away from me). The measurement data presented here were recorded within a single beam time. Cora, Lars, Manu and Soeren helped me a lot to set up the accelerator to produce those wonderful spectra. Thanks a lot! Also, a big thanks goes out to the rest of the team who built up such a wonderful laser plasma accelerator. Thanks to all of you!

Lars Gumprecht from DESY helped me a lot to get into the topic of CAD modeling and always had an open door when it came to technical and design questions related to the existing Frosty design. One of my favorite lessons learned from him was, that you should always have a model of your tools, screwdrivers and stuff, in your design to check if you can assemble it.

To get the design into reality I had a lot of support from the University workshop around Stephan Fleig, who helped me building prototypes of each component and taught me a lot about how to modify the existing designs into a state in which they are also economically producible. The same goes out to Tim Tobiassen from the company VAB - Vakuum - Anlagenbau GmbH in Elmshorn, who supported me with all his know how and manufacturing skills of his company to get the required vacuum components into a working state. The technical support from the workshop and from VAB was incredible helpful and can not be honored too much.

Last but not least, I would like to thank my undulator colleges. With Thomas Schmidt from PSI and Suren Karabekyan from European XFEL I had a lot of helpful discussions to get a deeper insight into the whole topic and the broad field of undulators and their applications. Thank you very much for the warm welcome and also for the nice lab tours! I will never forget the Swiss cheese fondue with the extra shot of schnapps. During the simulations with Simplex and Spectra, I had very intense support from Takashi Tanaka from Spring 8. He helped me a lot to rule out several issues. The DESY undulator team around Markus Tischer gave me a lot of support and insight into their strategies to model the physics and to design, manufacture and measure undulators and SAFALI benches. A big thanks goes out to Pavel Vagin, who helped me out with equipment, software and know-how wherever he could. Frosty is a puzzle out of 28752 individual components which all have to be aligned with greatest care with a μm precision, which requires a lot of experience, patience and personal skills which have to be learned. This would have been hardly achievable for me without your expertise. Thank you very very much!